

---

# Counterions at Charged Polymers

Ali Naji

---



Munich, 2005



---

# Counterions at Charged Polymers

Ali Naji

---

Dissertation  
der Fakultät für Physik  
der Ludwig–Maximilians–Universität  
München

vorgelegt von  
Ali Naji  
geboren am 11. September 1976 in Karaj (Tehran)

München, August 2005

Erstgutachter: Prof. Dr. Roland R. Netz  
Zweitgutachter: Prof. Dr. Joachim O. Rädler  
Tag der mündlichen Prüfung: 10. November 2005

*To my wife–Hoda–,  
my parents–Masoumeh and Sohrab–,  
my brothers–Majid and Hamid–,  
and the memory of  
my grandfather, Razzagh*



# Contents

<b>Abstract</b>	<b>xi</b>
<b>Zusammenfassung</b>	<b>xiii</b>
<b>1 Introduction</b>	<b>1</b>
<b>2 Counterion at Charged Objects: General aspects</b>	<b>7</b>
2.1 Length scales in a classical charged system . . . . .	7
2.1.1 From mean-field to strong-coupling regime . . . . .	8
2.2 Counterion distribution at a charged surface . . . . .	10
2.2.1 Weak-coupling or mean-field regime . . . . .	10
2.2.2 Strong-coupling (SC) regime . . . . .	11
2.3 The role of curvature . . . . .	12
2.3.1 Binding-unbinding transition of counterions . . . . .	13
2.4 Interactions between like-charged surfaces . . . . .	14
2.4.1 Mean-field regime: Repulsion . . . . .	15
2.4.2 Strong-coupling regime: Attraction . . . . .	16
2.4.3 Rouzina-Bloomfield criterion . . . . .	17
<b>3 Counterion-Condensation Transition (CCT) at Charged Cylinders</b>	<b>19</b>
3.1 Cell model for charged rod-like polymers . . . . .	21
3.1.1 Dimensionless description . . . . .	22
3.2 CCT as a generic binding-unbinding process . . . . .	23
3.2.1 Onsager instability . . . . .	24
3.2.2 Beyond the Onsager instability . . . . .	25
3.3 Mean-field theory for the CCT . . . . .	25
3.3.1 Non-linear Poisson-Boltzmann (PB) equation . . . . .	25
3.3.2 Onset of the CCT within mean-field theory . . . . .	27
3.3.3 Critical scaling-invariance: Mean-field exponents . . . . .	28
3.4 Strong-coupling theory for the CCT . . . . .	32
3.5 Monte-Carlo study of the CCT in 3D . . . . .	33
3.5.1 The centrifugal sampling method . . . . .	33
3.5.2 Simulation model and parameters . . . . .	35
3.6 Simulation results in 3D . . . . .	35
3.6.1 Overall behavior in the infinite-system-size limit . . . . .	35
3.6.2 Critical Manning parameter $\xi_c$ . . . . .	41
3.6.3 Scale-invariance near the critical point . . . . .	44

3.6.4	Critical exponents: the CCT universality class . . . . .	47
3.7	Conclusion and discussion . . . . .	50
<b>4</b>	<b>Counterion-Condensation Transition in Two Dimensions</b>	<b>53</b>
4.1	The 2D model . . . . .	54
4.1.1	Rescaled representation . . . . .	54
4.2	Simulation results in 2D . . . . .	55
4.2.1	The order parameters . . . . .	55
4.2.2	Energy and heat capacity . . . . .	56
4.2.3	Condensation singularities in 2D: an analytical approach . . . . .	57
4.2.4	Critical point and the continuum limit . . . . .	60
4.2.5	The condensed fraction . . . . .	61
<b>5</b>	<b>Strong-Coupling Interactions</b>	<b>63</b>
5.1	Strong-coupling theory: General formalism . . . . .	64
5.1.1	The strong-coupling free energy . . . . .	65
5.2	Two like-charged rods . . . . .	67
5.2.1	Threshold of attraction . . . . .	68
5.2.2	Equilibrium axial distance . . . . .	70
5.2.3	Comparison with numerical simulations . . . . .	72
5.3	Two like-charged spheres . . . . .	74
5.3.1	Attraction threshold . . . . .	77
5.3.2	Comparison with numerical simulations . . . . .	77
5.4	Conclusion and discussion . . . . .	79
<b>6</b>	<b>Polyelectrolyte Brushes: Non-linear osmotic regime</b>	<b>83</b>
6.1	Non-linear scaling theory for the osmotic brush . . . . .	85
6.1.1	Comparison with Molecular Dynamics simulations . . . . .	88
6.1.2	Comparison with experiments . . . . .	90
6.2	Non-linear mean-field theory for the osmotic brush . . . . .	91
6.2.1	The cell model . . . . .	91
6.2.2	The electrostatic free energy . . . . .	92
6.2.3	The elastic free energy . . . . .	94
6.2.4	Optimal brush height and its limiting behavior . . . . .	95
6.2.5	Comparing mean-field results with simulations . . . . .	99
6.3	Conclusion and Discussion . . . . .	101
<b>7</b>	<b>Charged Polymers in Electric Field</b>	<b>105</b>
7.1	Model and methods . . . . .	106
7.1.1	Interactions . . . . .	107
7.1.2	Rescaled parameters . . . . .	108
7.1.3	Langevin Brownian Dynamics . . . . .	109
7.1.4	Models for charge pattern . . . . .	112
7.2	Simulations results . . . . .	113
7.2.1	Counterion distribution . . . . .	113
7.2.2	Hydrodynamic “evaporation” mechanism . . . . .	114
7.2.3	Electrophoresis: Mobility in an external field . . . . .	116



7.2.4	Counterion condensation and electrophoretic mobility . . . . .	120
7.2.5	Self-diffusion at a charge array: An analytical approach . . . . .	122
7.3	Conclusion and discussion . . . . .	125
<b>A</b>	<b>Field Theory for Macroions in an Ionic Solution</b>	<b>127</b>
A.1	Weak-coupling limit: Mean-field theory . . . . .	129
A.2	Strong-coupling limit . . . . .	131
<b>B</b>	<b>Notes on the Onsager instability</b>	<b>133</b>
<b>C</b>	<b>Mean-Field Theory for Charged Cylinders: Asymptotic results</b>	<b>135</b>
C.1	Limiting behavior of $\beta$ for large $\Delta$ . . . . .	135
C.2	Finite-size scaling for $\beta$ close to $\xi_c^{\text{PB}}$ : . . . . .	136
C.3	The PB cumulative density profile . . . . .	136
C.4	Asymptotic behavior of $S_n$ within PB theory . . . . .	137
C.5	PB potential, counterion density and free energy . . . . .	138
C.6	PB solution in an unbounded system ( $\Delta = \infty$ ) . . . . .	139
<b>D</b>	<b>Periodic Cell Model: Summation techniques for simulations in 3D</b>	<b>141</b>
D.1	Counterions at charged cylinders: MC simulations . . . . .	141
<b>E</b>	<b>Strong-Coupling Interactions: Asymptotic analysis</b>	<b>145</b>
E.1	Two like-charged rods . . . . .	145
E.2	Two like-charged spheres . . . . .	146
<b>F</b>	<b>Free Energy of a Charged Brush</b>	<b>149</b>
F.1	Freely-jointed-chain model . . . . .	149
F.2	PB free energy: Asymptotic results . . . . .	150
	<b>Bibliography</b>	<b>153</b>
	<b>List of Publications</b>	<b>165</b>
	<b>Acknowledgment</b>	<b>167</b>
	<b>Curriculum Vitae</b>	<b>169</b>



# Abstract

This work explores the equilibrium and non-equilibrium statistical mechanics of small charged particles (counterions) at oppositely charged polymers and cylindrical surfaces. Processes involving charged polymers and their neutralizing counterions are ubiquitous in soft-matter and biological systems, where electrostatic interactions result in an impressive variety of phenomena. The interplay between electrostatic interactions, that attract counterions towards charged polymers, and the entropy gained by counterions upon dissolution leads to a critical counterion-condensation transition, which is the central theme of this thesis.

The universal and critical features of this transition are investigated in equilibrium conditions using both analytical approaches and a novel Monte-Carlo simulation method. The critical exponents as well as the singular behavior associated with thermodynamic quantities are determined and demonstrated to be universal and in accord with mean-field theory in two and three spatial dimensions. The statistical correlation between counterions comes into play below the critical temperature, where counterions are strongly bound to the oppositely charged surface of the polymer (condensation phase). It is shown using asymptotic analysis that in the strong-coupling limit, which is realized by high-valency counterions or highly charged surfaces, electrostatic correlations dominate and result in an effective electrostatic attraction between two like-charged cylinders. Such attractive pair interactions are in striking contrast with the standard, purely repulsive mean-field interactions, and can trigger aggregation and phase instability in solutions of highly charged macroions.

Another relevant system, in which counterions play a decisive role and will be subject of theoretical investigation in the present work, are charged polymer brushes, that consist of densely end-grafted polymer chains onto a surface. It is shown that the coupling between osmotic pressure of counterions trapped inside the brush and the polymer length variation due to the chain elasticity leads to a weak grafting-density dependence for the brush layer thickness. This behavior goes beyond the standard scaling theories. It has been observed in recent experiments and simulations, which are compared with the present theoretical results.

Finally, to investigate the non-equilibrium dynamics of counterions at charged polymers, Brownian Dynamics simulation techniques are employed both in the presence and absence of hydrodynamic interactions between constituent particles. In particular, the influence of counterion condensation on the electrophoretic mobility of a charged polymer and its counterions is studied under the action of small and large external electric fields. It is shown that hydrodynamic interactions enhance the polymer mobility but substantially reduce the mobility of counterions. In fact, counterions located in the immediate vicinity of the charged polymer are found to be dragged along with the polymer. It is shown using different charge pattern models that the local structural details of the polymer chain, such as the charge spacing, can drastically affect the mobility of counterions and the charged polymer itself.



# Zusammenfassung

Diese Arbeit untersucht die statistische Mechanik für Gleichgewichts- und Nichtgleichgewichtszustände kleiner geladener Teilchen (Gegenionen) in der Nähe von entgegengesetzt geladenen Polymeren und zylindrischen Oberflächen. Prozesse, die geladene Polymere und ihre ladungskompensierenden Gegenionen beinhalten, sind allgegenwärtig in weicher Materie und biologischen Systemen, in denen elektrostatische Wechselwirkungen sich in einer beeindruckenden Vielfalt von Phänomenen niederschlagen. Das Zusammenspiel von elektrostatischen Wechselwirkungen, die Gegenionen zu den geladenen Polymeren ziehen, mit der Entropie, die die Gegenionen dadurch gewinnen, dass sie in Lösung gehen, führt zu einem kritischen Gegenionen-Kondensationsübergang. Dieser ist das zentrale Thema der vorliegenden Arbeit.

Die universellen und kritischen Eigenschaften dieses Übergangs werden im Gleichgewicht sowohl durch analytische Ansätze als auch durch eine neue Monte-Carlo-Simulationsmethode untersucht. Die kritischen Exponenten und das singuläre Verhalten, das in den thermodynamischen Größen sichtbar wird, werden mit Hilfe von Simulationen bestimmt, und es wird gezeigt, dass diese universell und in Übereinstimmung mit der *mean-field*-Theorie sind, sowohl in zwei als auch in drei Raumdimensionen. Statistische Korrelation der Gegenionen tritt unterhalb der kritischen Temperatur auf, also in der Kondensationsphase, bei der die Gegenionen sich in großer Anzahl um die entgegengesetzt geladene Oberfläche des Polymers ansammeln. Anhand einer asymptotischen analytischen Theorie wird gezeigt, dass im Grenzfall starker Kopplung – beispielsweise bedingt durch hochvalente Gegenionen oder stark geladene Oberflächen – die elektrostatischen Korrelationen dominieren und sich in einer effektiven elektrostatischen Anziehung zwischen zwei gleichnamig geladenen Zylindern niederschlagen. Solche attraktiven Paar-Wechselwirkungen stehen im Gegensatz zu den gewöhnlichen, ausschließlich repulsiven *mean-field* Wechselwirkungen und können Aggregation und Phaseninstabilität in Lösungen von hochgeladenen Makro-Ionen auslösen.

Ein anderes relevantes System, bei dem Gegenionen eine entscheidende Rolle spielen, sind sogenannte geladene Polymer-Bürsten, die aus dichtgepackten Polymerketten bestehen, welche mit einem Ende auf einer Oberfläche befestigt sind. In dieser Arbeit wird gezeigt, dass die Kopplung zwischen dem osmotischen Druck der in der Bürste gefangenen Gegenionen und der durch die Elastizität des Polymers hervorgerufenen Variation der Polymerlänge zu einer schwachen Abhängigkeit der Dicke der Bürstenschicht von der Bedeckungsdichte führt. Dieses Verhalten geht über die Standard-Skalentheorie hinaus und wurde vor kurzem in Experimenten und Simulationen beobachtet, die mit den vorliegenden theoretischen Ergebnissen verglichen werden.

Um die Nichtgleichgewichtsdynamik von Gegenionen an geladenen Polymeren zu untersuchen, wurden Brownsche-Dynamik-Simulationstechniken verwendet, sowohl mit als auch ohne hydrodynamische Wechselwirkungen zwischen den einzelnen Partikeln. Insbesondere wurde der Einfluss der Gegenionen-Kondensation auf die (elektrophoretische) Mobilität eines gela-

denen Polymers und seiner Gegenionen in einem äußeren Feld untersucht. Es wird gezeigt, dass die hydrodynamischen Wechselwirkungen die Mobilität des Polymers erhöhen, aber die Beweglichkeit der Gegenionen wesentlich reduzieren. Tatsächlich werden Gegenionen, die sich in der unmittelbaren Nähe des geladenen Polymers befinden, mit dem Polymer mitgezogen. Desweiteren wird mit Hilfe verschiedener Ladungsverteilungsmodelle gezeigt, dass die lokalen Details der Struktur der Polymerkette, zum Beispiel der Abstand der geladenen Monomere, die elektrophoretische Mobilität sowohl der Gegenionen als auch des Polymers selbst stark beeinflussen können.

# Chapter 1

## Introduction

Electric charges and electrostatic interactions are ubiquitous in soft-matter and biological systems. Soft materials, such as polymers, colloids and proteins acquire surface charges when dissolved in a polar solvent such as water. This is often due to dissociation of surface chemical groups, which leaves permanent charges on the surface and releases microscopic ions into the solution. Soft materials are easily deformed or re-arranged by potentials comparable to thermal energy. It thus becomes clear that electrostatic interactions caused by permanent (or even induced) charges, that are typically of long-range and large strength, constitute a prominent factor determining the behavior and properties of these materials. This makes charged materials central to many technological applications and on the other hand, a challenging subject for fundamental research in inter-disciplinary sciences. In what follows, I briefly review a few examples to demonstrate the diversity of phenomena associated with charged soft-matter systems.

### Colloids and polymers: The mesoscopic scale

Colloids are abundant in nature and industry: Smoke, fog, milk, paint and ink are only a few examples of colloidal systems. They comprise tiny solid or liquid particles that are suspended in another medium such as air or another liquid. An important factor, which makes colloidal solutions in many ways different from molecular or simple electrolyte solutions (such as sugar or salt solution), is the large asymmetry in size and mass between the colloidal particles and solvent molecules (or microscopic ions): Colloids are *mesoscopic* particles with sizes in the range of few nanometers to microns that are indeed made of many atoms, but not yet sufficiently many (i.e. much less than a mole) to make them behave like macroscopic bodies. In colloidal dispersions, the total area that is in contact with solvent is tremendously large: For nanometer-size colloids, nearly half of the atoms (of Angstrom size) are at the surface. This ratio reduces to only a minor fraction of one for micron-size particles, and tends to “zero” for macroscopic objects. Therefore contrary to the typical situation in the macroscopic world, the physics here is dominated by “surface” properties [1, 2, 3].

Another relevant mesoscopic or *macromolecular* system are polymers (with everyday-life examples like chewing gum, dough, or egg white), in which many repeating subunits (monomers) are chemically connected to form a flexible chain. Flexible polymers are distinguished by their many degrees of freedom associated with conformational arrangement of monomers that are easily excited by thermal energy at room temperature. The coexistence

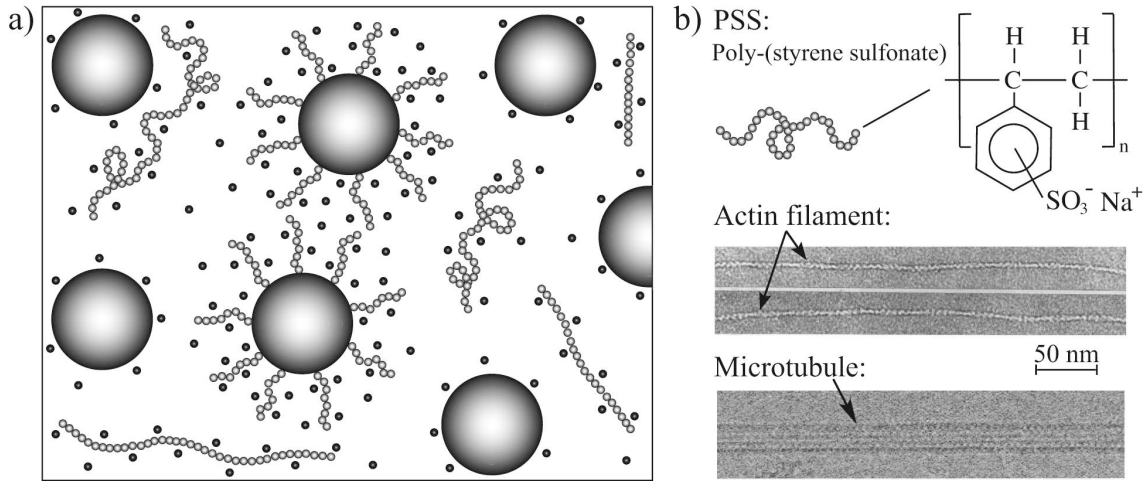


Figure 1.1: a) Schematic view of a charged solution consisting of charged colloids (dark spheres), charged polymer chains and microscopic neutralizing counterions (small black spheres). Colloids may be covered by charged polymer brushes, which are typically highly swollen in aqueous solutions and generate an additional repulsive interaction between colloids. b) Charged polymers may be classified as flexible (such as PSS), semi-flexible (such as DNA or actin filaments) and rigid (such as microtubules) depending on the ratio between their contour length and their persistence length. Actin filaments (two-stranded helical polymers of the actin protein with diameter of 5-9 nm) and microtubules (long hollow cylinders of outer diameter 25 nm made of the protein tubulin) have relatively large persistence lengths of the order of  $10 \mu\text{m}$  and  $1 \text{ mm}$  respectively.

between thermal fluctuations and the stringent constraint of connectivity imposed by covalent binding between subunits (which is characteristic of the solid state) leads to a diverse phase behavior [4, 5, 6]: Polymer chains can have large extensions in the solution and be strongly entangled, or even collapse into a compact globular state (and thus form a colloidal system as it is, for instance, realized with proteins). The entanglement of chains in polymeric liquids gives rise to mechanical and rheological properties that differ dramatically from those of normal liquids or solids. Depending on their chemical structure, polymer chains can have a large mechanical stiffness as well, in which case they behave like rigid rods at length scales smaller than a characteristic persistence length (Figure 1.1a). Two famous examples of stiff polymers are provided by Nature: Actin filaments and microtubules that are known by their important role in biological processes occurring in the cell [7] (see Figure 1.1b).

The mesoscopic scale exhibits a distinct regime of time scales as well: The processes involving macromolecules in a solvent are quite slow as compared with microscopic phenomena. Any motion in a solvent, such as water, is bounded by frequent collisions with microscopic solvent particles, that transfer the energy to the solvent heat bath, and generate an erratic movement, the prominent Brownian motion [8, 9, 10, 11]. While the collisions and molecular processes occur at very short time scales (of the order  $10^{-14} - 10^{-10}$  seconds), the *diffusion* of polymers and colloids occurs in time scales that are larger by orders of magnitude spanning the range of microseconds to seconds. Within this time scale, one deals with a dissipative stochastic dynamics [12, 13] that will be considered later in this thesis.



---

## Charges: from industry to biology

In the mesoscopic world, only electromagnetic interactions, that emerge in a variety of forms, are capable of overcoming thermal fluctuations, which are characterized by an energy scale of about  $0.025eV$  at room temperature [2]. Here other fundamental forces of nature, such as gravity that rules the macroscopic large-scale world, play a marginal role or no role at all.

In general, colloids dissolved in an aqueous solvent attract each other due to ubiquitous van-der-Waals dispersion forces that result from induced charges (via spontaneous polarization of atoms) on their surfaces [2]. As a result, colloidal particles tend to form aggregates. Large aggregates typically sediment and destroy the dispersion. In many applications (for example in food emulsions such as milk), however, stability of a colloidal dispersion is a desirable property. One way to stabilize dispersions against aggregation is to generate long-range repulsive interactions between colloidal particles by imparting permanent like-charges to their surfaces, which leads to the celebrated DLVO mechanism for the stability of colloidal dispersions [1, 14]. Another method is to end-graft polymer chains (or *polymer brushes*) to the particle surfaces [15]. For this task, charged polymers are ideal since they swell substantially in aqueous solutions and inhibit close contact between colloids (see Figure 1.1a). This latter mechanism has the advantage that it is highly stable against the addition of electrolyte or salt ions [16], a common ingredient of colloidal solutions, which screen the long-range Coulomb forces resulting thus in exponentially decaying interactions between particles [18, 17]. But since dense charged polymer brushes trap a large amount of oppositely charged ions (counterions) inside, the structure of the brush layer, and thereby the repulsive force generated between colloids, remains highly insensitive to the amount of additional salt.

Charged polymers, or the so-called *polyelectrolytes*, and their synthesis have attracted a lot of attention in recent years thanks to their significant role in the production of cheap, non-toxic and environmentally friendly materials [19, 20]. In contrast to water-insoluble hydro-carbon chains, polyelectrolytes typically show high affinity for water and heavy metal ions, which makes them useful in applications such as super-absorbing diapers, waste water purifiers and washing detergents and their additives.

In biology, on the other hand, charged polymers and electrostatic effects emerge in many striking examples [21]. Almost all proteins, as well as the DNA and the RNA, are charged polymers. DNA, for instance, is a long, highly negatively charged biomolecule with a total length of about two meters in human cells: It bears one elementary charge per  $1.7\text{\AA}$ , which for human DNA adds up to  $10^{10}$  elementary charges overall. Yet the DNA is densely packed inside the micron-size cell nucleus. In eucaryotic cells, this storage process involves a hierarchical structure on the lowest level of which short segments of DNA are tightly wrapped around positively charged proteins (histones) of few nanometers in diameter [7]. The complexation of DNA with histone proteins is believed to be highly influenced by electrostatic interactions [23, 24, 25]. Electrostatic effects also play a key role in complexes of DNA with cationic lipids [26, 27, 28], which are considered as promising synthetically based non-viral carriers of DNA for gene therapy [29].

Another notorious example (which is closely related to the works presented later in this thesis) is DNA condensation [21, 30, 31], where electrostatic effects enter in a counter-intuitive fashion: Here like-charged segments of DNA strongly attract each other! In the *in vitro* experiments, the condensation of DNA is realized using bacteriophages—viruses that infect bacteria and consist of a rigid shell (the capsid) accommodating a single molecule of viral DNA. These viruses can inject their DNA into a cell (or a lipid vesicle) with appropriate

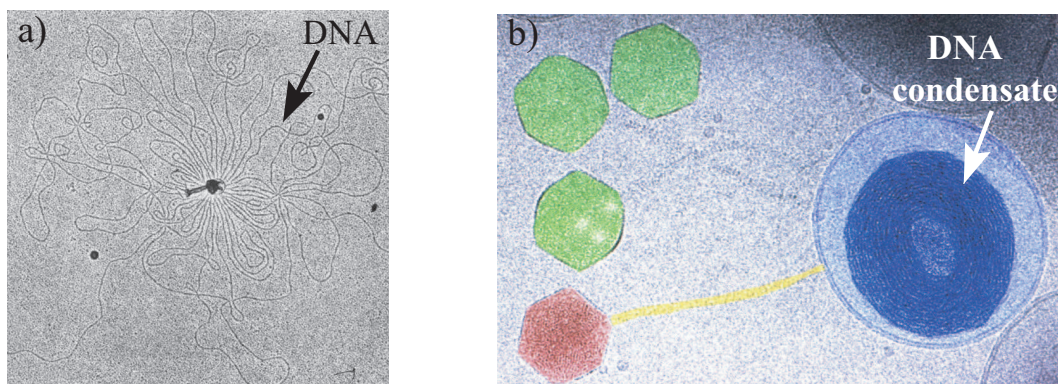


Figure 1.2: a) Single DNA molecule of the bacteriophage T2 (about  $50 \mu\text{m}$  long) is tightly packed into the viral capsid (shown in the middle). When exposed to distilled water, the capsid shell is ruptured due to the excess internal osmotic pressure (osmotic shock) and the DNA is pushed out [22]. b) Three now-empty T5 bacteriophages, shown on the top left, have injected their DNA into a liposome (a model bacterial cell). The remaining bacteriophage, bottom left, is about to inject its DNA [30, 32]. The subtle electrostatic effects inside the liposome have caused the three viral DNA molecules (of total length of about  $124 \mu\text{m}$ ) to form a tightly wound toroidal condensate (for comparison note that the capsid size is about  $70 \text{ nm}$ ). The medium contains  $50 \text{ mM}$  of spermidine chloride that yields a sufficient concentration of trivalent cations to condense the DNA.

receptor proteins in its outer membrane (see Figure 1.2). As a result, large lengths of DNA (up to hundred microns) are fitted and condensed into a tightly packed, circumferentially wound torus with a diameter of about hundred nanometers. But this packaging process, which works against the Coulombic self-repulsion and the conformational entropy of the DNA chain, is made possible because of the presence of high-valency cations (counterions) in the medium. Similarly, other highly charged polymers, such as negatively charged F-actin, a principal structural protein in cells and muscle tissues, can aggregate into closely packed rod-like bundles when small amounts of multivalent cations are added to the solution [33, 34]. It turns out that, in general, when particles are strongly charged, the role of electrostatic interactions dramatically changes (or, indeed, reverses as compared with weakly charged systems) [35]: Here electrostatic interactions themselves govern the destabilization of charged solutions by mediating attractive like-charge interactions!

## Theoretical challenge and coarse-grained models

From a theoretical point of view, charged systems pose a many-body problem: *Macroions*, such as charged colloids or polymers, are always surrounded by neutralizing oppositely charged microscopic ions, called *counterions*, and also in general by *coions*. These particles form loosely bound ionic clouds around macroions and tend to screen their charges. In particular, counterions, that are attracted towards macroion surfaces, predominantly determine static or dynamic properties of macroionic solutions in many instances. Understanding the interaction between macroions across an ionic medium, or their transport properties (such as their mobility in response to a driving electric field, or *electrophoresis*), requires an understanding of the counterionic clouds first.

---

In the case of charged polymers, the conformational degrees of freedom, as well as the long-range electrostatic interactions between charged monomers, add to the complexity of the problem. While these factors can all be incorporated to some extent within numerical simulation approaches, analytical understanding of charged systems is less developed and is mainly based on simplified models. A common theoretical approximation to disentangle the coupling between various degrees of freedom is to fix the chain conformation and focus on a detailed description of the counterion distribution. Insofar as the *counterionic properties* are concerned, this approach provides a good approximation, particularly because charged polymers are typically highly stretched due to mutual repulsions between monomers. On the other hand, many important charged polymers such as DNA, actin filaments, microtubules and fd-viruses, as well as many synthetic polymers, are intrinsically stiff and rod-like. Likewise, in densely grafted brushes, charged polymers appear to be highly stretched and with relatively small lateral wiggling. Therefore, as a first step towards understanding counterionic properties on an analytical level, one may represent charged polymers with rigid straight cylinders or lines of discrete charges [20, 36, 37, 38, 39].

In the most common theoretical approaches known also as *primitive models*, the molecular nature of solvent is neglected and it is represented by a continuum dielectric medium. In reality, the solvent structure is locally perturbed around particles, which can give rise to additional short-range solvent-induced interactions between particles [2]. On the other hand, the microscopic features of the colloidal particles and polymers are taken into account using coarse-grained models that incorporate only a few effective parameters. For instance, the charge pattern of colloids or polymers (that may be ordered or highly irregular) is represented by a uniform distribution, characterized by an effective surface charge density. In most cases, the specific effects associated with ions (which represent their quantum-chemical properties) as well as the image charge effects (due to the dielectric mismatch at the boundaries) are also neglected. These models therefore represent a crude simplification of reality, yet given those simplifications, establishing a systematic and clear understanding of electrostatic effects turns out to be a challenging route.

## Overview of this work

The central goal in this thesis is to establish unambiguous results based on simple well-defined models for those aspects of charged polymers that are associated with counterions. I have therefore adopted the aforementioned approximations except in Chapter 7, where structural details of polymer chains are incorporated in a simple fashion and within numerical simulations. In this work, I focus on the one-component counterion-only systems and neglect coions and the additional salt. The possible effects associated with additional salt will be discussed qualitatively. However, for the specific problems (or the regimes of parameters) considered in this work, the additional salt is expected to matter only when present in large amounts. The organization of this thesis is as follows:

Chapter 2 gives an overview of the two basic phenomena that are central to the problems discussed in the forthcoming chapters, namely, counterion condensation at charged curved boundaries and strong-coupling effects such like-charge attraction. Here I will make use of qualitative arguments to demonstrate the gross physical picture behind these phenomena.

In Chapters 3 and 4, I will focus on the asymptotic properties of counterions at a single charged cylinder in the limit where outer confining boundaries tend to infinity (the so-called

infinite-dilution limit). In this limit, counterions display a peculiar critical behavior referred to as the counterion-condensation transition, which has become one of the central issues in understanding the static and dynamic properties of charged polymers. The chief goal here is to determine the critical and universal aspects of this transition. To this end, I employ extensive Monte-Carlo simulations (using a novel sampling technique for large system sizes) as well as asymptotic analytical methods in both three and two spatial dimensions. By introducing the mean inverse localization length of counterions as the relevant order parameter, I will demonstrate that the critical behavior of counterions is governed by universal scaling relations, and thereby determine the so-called critical exponents of this transition. The precise location of the critical point, the role of electrostatic correlations and the singular behavior of thermodynamic quantities are among other issues that will be addressed in detail.

In Chapter 5, I will focus on the interaction between a pair of like-charged cylinders in the strong-coupling limit (i.e. when counterions are multivalent or surfaces are highly charged), where, as it will be shown, correlation effects give rise to strong effective attraction between like-charged cylinders. The analytical studies in this chapter are based on the asymptotic strong-coupling theory. I will also discuss the effective interaction between two like-charged spheres. These results will be compared with recent numerical simulations on strongly coupled systems displaying a good quantitative agreement.

Chapter 6 deals with charged polymer (or polyelectrolyte) brushes, in which many like-charged polymers are grafted by one end to a planar surface. The main issue here is the behavior of the brush thickness as a function of the grafting density (number of chains per unit area) in the so-called osmotic regime. In this regime, counterions are strongly trapped inside the brush layer and their osmotic pressure generates the dominant pressure swelling the polymer chains. While previous scaling theories predict that the osmotic brush height is independent of the grafting density, recent experiments and simulations exhibit a weakly increasing brush height with grafting density. I will present a non-linear scaling theory as well as a systematic mean-field cell-model study, which can explain the observed behavior in experiments and simulations on a semi-quantitative level.

Chapter 7 considers the non-equilibrium stationary-state dynamics of extended charged polymers in an external electric field. I investigate the electrophoretic mobility of a charged polymer and its counterions using Brownian Dynamics simulations methods as well as simple analytical considerations. In particular, I will discuss the role of hydrodynamic interactions and counterion condensation in electrophoresis of counterions and the charged polymer. Here I shall consider several polymer models that differ in the specific form of the charge distribution along the backbone but all have identical effective charge parameters (such as the linear charge density). It will be thus shown that the electrophoretic mobility is substantially influenced by such structural details as also demonstrated recently by capillary electrophoresis experiments.

## Chapter 2

# Counterion at Charged Objects: General aspects

This chapter provides a general overview of the physical mechanism behind some of the basic phenomena in charged systems that one frequently encounters throughout this thesis. Emphasis is made on equilibrium statistical behavior of counterions at uniformly charged surfaces that may be planar or curved.

I will first focus on a system of counterions at one and two opposing like-charged planes and introduce two main regimes of weak and strong coupling, where counterions adopt distinctly different distribution functions. Strong-coupling effects lead to effective interactions between like-charged surfaces that qualitatively differ from what one would expect based on the standard mean-field arguments. At charged curved surfaces, on the other hand, counterions exhibit a dramatic unbinding transition, which varies in nature depending on geometrical symmetries of bounding surfaces, and influences the effective interaction between charged surfaces as well. The main ideas presented here will be corroborated using systematic analytical and numerical methods, and will be applied to other related systems, in the following chapters.

### 2.1 Length scales in a classical charged system

Consider a system of fixed charged objects (macroions) with uniform surface charge density  $-\sigma_s e$  (with  $e$  being the elementary charge) that are surrounded by their neutralizing counterions of charge valency  $+q$ . (I conventionally assume that macroions are negatively charged and counterions are positively charged, thus  $\sigma_s$  and  $q$  are both positive by definition.) The solvent is assumed to be a continuum medium of dielectric constant,  $\varepsilon$ , independent of the temperature,  $T$ .

One of the most basic characteristic length scale in a charged system is set by the ratio between the thermal energy scale,  $k_B T$ , and the bare Coulombic interaction energy between two elementary charges at separation  $r$ , that is  $V(r) = e^2/(4\pi\varepsilon\varepsilon_0 r)$ , where  $\varepsilon_0$  is the permittivity of vacuum. This ratio may be written as  $V/(k_B T) = \ell_B/r$ , where

$$\ell_B = \frac{e^2}{4\pi\varepsilon\varepsilon_0 k_B T} \quad (2.1)$$

is the *Bjerrum length*, which measures the distance at which two elementary charges interact

with thermal energy  $k_B T$  [40]. In water and at room temperature, one has  $\ell_B \simeq 7.1 \text{ \AA}$ . Likewise, the rescaled Bjerrum length,

$$\tilde{\ell}_B = q^2 \ell_B, \quad (2.2)$$

characterizes the strength of mutual counterionic repulsions against thermal fluctuations in the system.

Other length scales are set by the charge distribution and the specific geometry of macroions. For simplicity, I shall concentrate here on a system composed of a *planar* charged wall of infinitely large extension with neutralizing counterions confined to one half-space, the so-called planar electrical double layer [1, 2, 41, 42] (Figure 2.1).

A different length scale may be identified by comparing the thermal energy  $k_B T$  with the energy scale of the counterion-wall attraction,  $U(z) = q\sigma_s e^2 z / (2\epsilon\epsilon_0)$ , where  $z$  is the vertical distance from the wall. Hence the ratio  $U/(k_B T) = z/\mu$ , where

$$\mu = \frac{1}{2\pi q \ell_B \sigma_s} \quad (2.3)$$

is known as the *Gouy-Chapman length* [41, 42], which measures the distance at which the thermal energy equals the counterion-wall interaction energy. The Gouy-Chapman length gives a measure of the thickness of the counterionic layer at a charged wall as will be shown later.

In principle, one may tune the system parameters in such a way that either of the two length scales,  $\ell_B$  and  $\mu$ , become arbitrarily large or small. In fact, only the dimensionless ratio between these two quantities, namely,

$$\Xi = \frac{\tilde{\ell}_B}{\mu} = 2\pi q^3 \ell_B^2 \sigma_s, \quad (2.4)$$

which is known as the *electrostatic coupling parameter*, is relevant and uniquely describes different physical regimes that may be found for counterions at a planar charged wall [35, 43, 44, 45, 46]. In fact, one could show on purely dimensional grounds that such a system has only two independent length scales (which are taken here as the Bjerrum length and the Gouy-Chapman length) and thus only one independent dimensionless parameter.

### 2.1.1 From mean-field to strong-coupling regime

For small coupling parameter  $\Xi \ll 1$ , equation (2.4) indicates that the counterion-wall system has a relatively large Gouy-Chapman length (or small Bjerrum length), which reflects a loosely bound counterion cloud at the charged wall (Figure 2.1a). For large coupling parameter  $\Xi \gg 1$ , in contrast, the Gouy-Chapman length is relatively small (or the Bjerrum length is large) and counterions are strongly attracted toward the wall (Figure 2.1b).

Further insight into the structure of the counterionic layer may be obtained by considering the typical distance between counterions at the charged surface. For counterions residing near the surface, the local electroneutrality condition implies a typical lateral separation of

$$a_\perp \sim \sqrt{\frac{q}{\sigma_s}}, \quad (2.5)$$

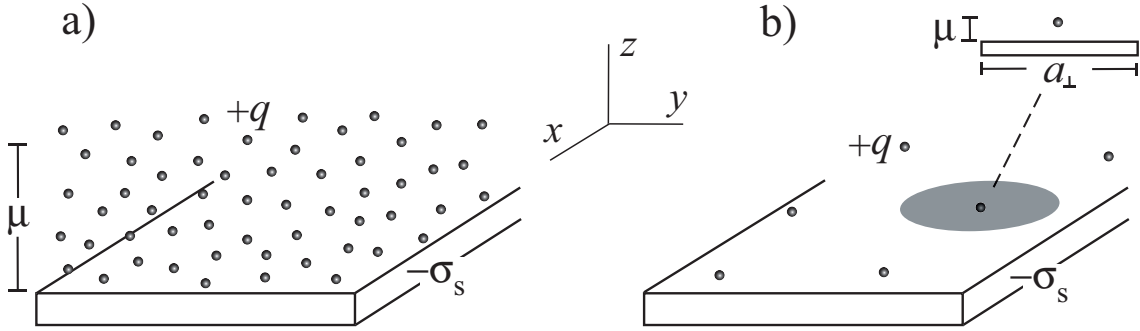


Figure 2.1: a) For small coupling parameter,  $\Xi \ll 1$ , counterions form a diffuse three-dimensional layer. b) For large coupling parameter,  $\Xi \gg 1$ , the counterionic layer is essentially two dimensional since the typical lateral distance between counterions,  $a_{\perp}$ , becomes much larger than the Gouy-Chapman length,  $\mu$ . In this regime, counterions are strongly correlated and surrounded by a correlation hole of size  $\sim a_{\perp} \gg \mu$ .

since each counterion neutralizes the charge of an area given by  $a_{\perp}^2 \sim q/\sigma_s$ , up to a geometrical prefactor of the order one. Counterion spacing  $a_{\perp}$  is not an independent length scale and may be written in units of the Gouy-Chapman length as

$$\frac{a_{\perp}}{\mu} \sim \sqrt{\Xi}. \quad (2.6)$$

In the *weak-coupling regime*  $\Xi \ll 1$ , equation (2.6) indicates that the lateral separation of counterions at surface is small compared with  $\mu$  (layer thickness) implying a diffuse fluid-like counterionic layer at the surface as depicted in Figure 2.1a.<sup>1</sup> This regime is dominated by mean-field-like features, i.e. counterions become independent from each other in a statistical sense, as can be verified using a systematic approach (Appendix A).

In the *strong-coupling regime*  $\Xi \gg 1$ , lateral separation of counterions becomes larger than the Gouy-Chapman length indicating a quasi two-dimensional structure for the counterionic layer as depicted in Figure 2.1b. Such a layer is dominated by strong mutual repulsions between counterions as can be seen by considering the effective 2D plasma parameter [47]

$$\Gamma \equiv \frac{\tilde{\ell}_B}{a_{\perp}} \sim \Xi^{1/2}, \quad (2.7)$$

which gives the ratio between mutual Coulombic repulsions against thermal fluctuations (in the 2D one-component plasma of counterions at a neutralizing surface). Coulombic repulsions for large  $\Gamma$  tend to freeze out lateral fluctuations of counterions on the surface, inducing strong *correlations* and a trend toward crystallization in the ionic structure [48, 49]. Individual counterions thus become surrounded by a *correlation hole* of size  $a_{\perp}$  from which neighboring counterions are statistically depleted. The Wigner crystallization of the 2D one-component plasma is known to occur for  $\Gamma > \Gamma_c \simeq 125$  [47], corresponding to the range of coupling parameters  $\Xi > \Xi_c \simeq 3.1 \times 10^4$  [46].

<sup>1</sup>A more accurate estimate of the typical distance,  $a$ , between counterions in an extended three-dimensional layer gives  $a/\mu \sim \Xi^{1/3}$  [43].

Charged object	$\sigma_s$ ( $e/\text{nm}^2$ )	$R$ ( $\text{\AA}$ )	$q$	$\mu$ ( $\text{\AA}$ )	$\Xi$	$\tilde{R}$
charged membranes	$\sim 1$	–	1	2.2	3.1	–
			2	1.1	24.8	–
			3	0.7	83.7	–
DNA	0.9	10	1 ( $\text{Na}^+$ )	2.4	2.8	4.1
			2 ( $\text{Mn}^{2+}$ )	1.2	22.4	8.2
			3 (spermidine)	0.8	75.6	12.3
			4 (spermine)	0.6	179	16.4
highly charged colloids (surfactant micelles)	$\sim 1$	20	3	0.7	85	28
weakly charged colloids (polystyrene particles)	$\sim 0.1$	$\sim 10^3$	1	$\sim 2$	$\sim 0.1$	$\sim 5 \times 10^2$

Table 2.1: Typical values of physical parameters for realistic charged systems:  $\sigma_s$  and  $R$  denote the surface charge density and the radius of curvature of charged objects.  $q$  is the charge valency of counterions,  $\mu = 1/(2\pi q\ell_B\sigma_s)$  is the Gouy-Chapman length,  $\Xi = q^2\ell_B/\mu$  is the coupling parameter, and  $\tilde{R} = R/\mu$  is the Manning parameter (Section 2.3). The Bjerrum length is taken here as  $\ell_B \simeq 7.1\text{\AA}$  corresponding to an aqueous medium of dielectric constant  $\epsilon = 80$  at room temperature.

In brief, the two asymptotic regimes of weak coupling ( $\Xi \ll 1$ ) and strong coupling ( $\Xi \gg 1$ ) are distinguished physically by different structures arising for counterionic layers at charged surfaces (these results hold for charged curved surfaces as well). The quantitative form of the counterionic distribution function is considered in the following section. Before proceeding further, it is useful to consider the typical values of the coupling parameter in realistic systems. Table 2.1 shows few typical examples of both weakly coupled and strongly coupled systems. As already seen from Eq. (2.4), the coupling strength grows quite rapidly with the counterion valency ( $\Xi \sim q^3$ ), which agrees with experimental and numerical evidence indicating rapidly growing correlation effects for increasing counterion valency (see Chapter 5 and references cited therein). Note that a typical coupling strength of  $\Xi \sim 10^2$  (or larger) already reflects strong-coupling regime and a value of  $\Xi \sim 1$  (or smaller) typically corresponds to the weak-coupling regime.

## 2.2 Counterion distribution at a charged surface

### 2.2.1 Weak-coupling or mean-field regime

For small coupling strength  $\Xi \ll 1$ , as mentioned before, one may employ the mean-field approximation in order to describe the counterionic layer because each counterion in the layer interacts with a diffuse cloud of other counterions (Figure 2.1a). The mean-field theory systematically neglects inter-particle correlations. It can formally be derived in the limit of  $\Xi \rightarrow 0$  [50] (see Appendix A). It is governed by the so-called mean-field Poisson-Boltzmann (PB) equation [1, 2]

$$\nabla^2 \psi_{\text{elec}}(\mathbf{x}) = \frac{\sigma(\mathbf{x})e}{\epsilon\epsilon_0} - \frac{qe\rho_0}{\epsilon\epsilon_0} \Omega(\mathbf{x}) \exp(-qe\psi_{\text{elec}}/k_B T), \quad (2.8)$$



for the mean electrostatic potential in space,  $\psi_{\text{elec}}$ . Note that  $\sigma(\mathbf{x})$  on the right hand side of Eq. (2.8) represents the charge distribution of macroions (which are assumed to be fixed), and the second term corresponds to the mean-field PB counterion density profile (Appendix A), i.e.

$$\rho_{\text{PB}}(\mathbf{x}) = \rho_0 \Omega(\mathbf{x}) \exp(-qe\psi_{\text{elec}}/k_{\text{B}}T), \quad (2.9)$$

where  $\rho_0$  is a normalization prefactor, and the geometry function  $\Omega(\mathbf{x})$  specifies the space accessible to counterions.

For point-like counterions at a single uniformly charged wall (Figure 2.1a), the PB solution yields an algebraically decaying density profile of the form [1, 2]

$$\frac{\rho_{\text{PB}}(z)}{2\pi\ell_{\text{B}}\sigma_{\text{s}}^2} = \frac{1}{(z/\mu + 1)^2}, \quad (2.10)$$

where  $z \geq 0$  is the distance from the wall. In agreement with qualitative considerations in Section 2.1, the mean-field profile (2.10) represents an extended counterionic layer with diverging moments  $\langle z^n \rangle = \int_0^\infty dz z^n \rho_{\text{PB}}(z)$  for  $n > 1$ . Yet, the density profile is itself normalizable to the total number of counterions (as necessary to neutralize the surface charge) reflecting the fact that a charged wall binds *all* its counterions. The Gouy-Chapman length,  $\mu$ , in this case equals the height of a layer at the wall which contains *half* of the counterions, and may thus be associated with the typical layer thickness.

The density of counterions at contact with the charged wall is obtained as  $\rho_{\text{PB}}(z = 0) = 2\pi\ell_{\text{B}}\sigma_{\text{s}}^2$ . This result is in fact exact (i.e. valid beyond the mean-field level) within the present model [51].

### 2.2.2 Strong-coupling (SC) regime

At intermediate to large coupling strength  $\Xi > 1$ , counterionic correlations render the mean-field theory an invalid description of the system. It becomes exceedingly difficult to obtain a full analytical description for the system due to the liquid-like behavior of counterions at surface. But for very large coupling parameter  $\Xi \gg 1$ , one can obtain a simple analytical theory as explained below [43, 48, 49].

For  $\Xi \gg 1$ , counterions are highly separated from each other and one may consider the layer as a collection of laterally frozen *correlation cells*, each consisting of a single counterion interacting with an area of the wall of size  $\sim a_{\perp}$ , Eq. (2.5) (Figure 2.1b). Since the lateral extension of the cells is much larger than the layer thickness  $a_{\perp}/\mu = \sqrt{\Xi} \gg 1$ , the dominant contribution to the density profile of counterions comes from the vertical degree of freedom,  $z$ , through which single counterions are coupled to the wall with the interaction potential  $U/(k_{\text{B}}T) \simeq z/\mu$ . Hence using the Boltzmann weight, one finds the (laterally averaged) density profile

$$\rho_{\text{SC}}(z) = \rho_0 \exp(-z/\mu). \quad (2.11)$$

The prefactor in the above expression (the contact density) may be fixed from the normalization condition and using the global electroneutrality of the system as  $\rho_0 = 2\pi\ell_{\text{B}}\sigma_{\text{s}}^2$ . Unlike the weak-coupling case, the strong-coupling profile,  $\rho_{\text{SC}}(z)$ , decays exponentially as one moves away from the charged wall. Moreover, the average distance of counterions is finite and equal to the Gouy-Chapman length,  $\langle z \rangle_{\text{SC}} = \mu$ , reflecting the quasi-2D form of the layer.

It can be shown using a series expansion in powers of  $1/\Xi$  that when  $\Xi \rightarrow \infty$ , the main contribution to the partition function of a charged system comes from *single-particle* interaction terms (i.e. the terms representing interactions between single mobile counterions with

fixed macroions) [43] (see Appendix A). This leads to a leading-order analytical theory for  $\Xi \rightarrow \infty$ , which is known as the *asymptotic strong-coupling (SC) theory*. As indicated by the preceding argument, the strong-coupling single-particle results correspond physically to the situation with an infinitely large correlation hole size,  $a_{\perp}/\mu$ , around counterions at the surface. For a *finite* coupling parameter, one expects that the SC results, such as Eq. (2.11), that are strictly valid for  $\Xi \rightarrow \infty$ , still hold at distances smaller than the correlation hole size, i.e. for  $z < a_{\perp}$ . This yields a criterion identifying the strong-coupling regime for finite coupling strength as

$$\frac{z}{\mu} < \Xi^{1/2} \quad (2.12)$$

using Eq. (2.5). This criterion has been verified using numerical and analytical studies on charged walls [43, 44, 46]. At distances larger than the correlation hole size  $z > a_{\perp}$ , multi-particle interactions play a role and modify the form of the density profile. For  $z \gg a_{\perp}$ , correlation effects weaken and the system exhibits mean-field-like behavior [43, 44, 46, 52].

### 2.3 The role of curvature

In the preceding sections, I discussed the two asymptotic regimes of weak and strong coupling for counterions at a planar charged wall. In realistic situations, charged surfaces often have an intrinsic curvature. The general results discussed before remain valid also for the structure of the counterionic layers at charged curved surfaces. But charged curved boundaries can trigger a striking binding-unbinding transition for counterions which leads to drastically different features. For simplicity, I consider only charged spherical and cylindrical macroions characterized by a single radius of curvature  $R$ .

The relevant dimensionless parameter identifying curvature of macroions is given by the ratio between the radius of curvature,  $R$ , and the Gouy-Chapman length,  $\mu$ , that is

$$\tilde{R} = \frac{R}{\mu}, \quad (2.13)$$

which will be referred to as the *Manning parameter* (see below). Intuitively, one expects that for  $\tilde{R} \gg 1$ , properties of the system remain *qualitatively* close to those of planar charged walls. On the contrary, the curvature of the surface is expected to become important for small  $\tilde{R}$ . In fact, the geometrical symmetries of macroions, e.g., whether they are cylindrical or spherical, also play an important role as they enforce the generic form of the long-range counterion-surface interactions.

Using a uniform surface charge density  $\sigma_s$ , the Gouy-Chapman length (2.3) reads

$$\mu = \frac{1}{2\pi q\ell_B\sigma_s} = \begin{cases} R/(q\ell_B\tau) & \text{for charged cylinders,} \\ 2R^2/(q\ell_B Z) & \text{for charged spheres,} \end{cases} \quad (2.14)$$

where  $\tau = 2\pi\sigma_s R$  is the linear charge density (in units of the elementary charge  $e$ ) in the case of charged cylinders, and  $Z = 4\pi\sigma_s R^2$  is the total charge valency for charged spheres. For charged *cylinders*, the rescaled radius  $\tilde{R}$ , Eq. (2.13), is identical with the well-known Manning parameter,  $\xi$ , introduced originally for charged rod-like polymers [39], i.e.

$$\tilde{R} = \xi \equiv q\ell_B\tau, \quad (2.15)$$

while for charged *spheres*, one has

$$\tilde{R} = \frac{q\ell_{\text{B}}Z}{2R}. \quad (2.16)$$

In the following chapters, I may occasionally use  $\xi$  or  $\tilde{R}$  to denote the Manning parameter.

### 2.3.1 Binding-unbinding transition of counterions

At equilibrium, counterions tend to diffuse away in order to maximize the entropy of the system, while at the same time, they are attracted energetically toward the macroion surfaces. In the planar limit  $\tilde{R} \rightarrow \infty$ , as seen from the limiting results in Section 2.2, counterions retain a finite density profile,  $\rho(z)$ , normalized to the total number of counterions (i.e., to the amount necessary to neutralize the surface charge). This reflects complete counterion-binding in the planar limit as intuitively expected, since counterion attraction to the surface,  $\sim z$ , grows faster than the entropic gain,  $\sim \ln z$ , with distance,  $z$ .

#### Charged spheres

At a charged *sphere*, the energetic attraction scales like  $1/r$ , which is always weaker than the *entropic repulsion* ( $\sim \ln r$ ) experienced by counterions at large distances,  $r$ , from the sphere center. Hence, counterions tend to unbind completely and diffuse to infinity in the absence of confining boundaries. This behavior may be demonstrated on a single-particle level using the partition function,  $\mathcal{Z}_1$ , of a single counterion attracted to an oppositely charged sphere via the interaction energy  $U(r)/(k_{\text{B}}T) = -qZ\ell_{\text{B}}/r = -2\tilde{R}^2\mu/r$ , i.e.

$$\mathcal{Z}_1 = 4\pi \int_R^D r^2 dr \exp \left[ 2\tilde{R}^2 \left( \frac{\mu}{r} \right) \right], \quad (2.17)$$

where it is assumed that the counterion-sphere system is bounded by an outer spherical shell of radius  $D > R$ . Since the integrand in Eq. (2.17) is always large than unity,  $\mathcal{Z}_1$  diverges as  $\mathcal{Z}_1 \sim (D/R)^3$  when  $D/R \rightarrow \infty$ . Consequently, the single-particle distribution function,  $\rho_1(r) = \exp[-U(r)/k_{\text{B}}T]/\mathcal{Z}_1$ , vanishes indicating complete unbinding (or de-condensation) of counterions. The role of a confining volume thus becomes important in keeping counterions in the proximity of charged spheres. Note that the confinement volume per sphere is inversely related to the concentration of spherical macroions in a solution, and the infinite-volume limit in fact represents the *infinite-dilution limit* of a macroionic solution.

#### Charged cylinders

Charged *cylinders* represent a situation intermediate to planar charged walls and spheres in that the energetic attraction of counterions to a charged cylinder grows logarithmically with the radial distance from the cylinder axis,  $r$ , that is in the same way as the entropic gain increases,  $\sim \ln r$ . The competition between these two effects can result in a threshold binding-unbinding process, known as the *counterion-condensation transition* (CCT) at charged cylinders.

On a single-particle level, this threshold behavior can be characterized using the single-counterion interaction energy,  $U/(k_{\text{B}}T) = 2(q\ell_{\text{B}}\tau) \ln(r/R) = 2\xi \ln(r/R)$ , with an infinite cylinder in an outer confining cylindrical shell of radius  $D > R$ . The single-particle partition

function may thus be written as

$$\mathcal{Z}_1 = 2\pi \int_R^D r dr e^{-2\xi \ln(r/R)} \sim \int_0^\Delta dy e^{-2(\xi-1)y}, \quad (2.18)$$

where I have used a logarithmic transformation for the radial coordinate as  $y = \ln(r/R)$ , and defined

$$\Delta = \ln(D/R) \quad (2.19)$$

as the *lateral extension parameter* of the system. The relevant infinite-volume limit (infinite-dilution limit) for cylinders is determined by this factor as  $\Delta \rightarrow \infty$ , where  $\mathcal{Z}_1$  may remain finite or it may diverge depending on the Manning parameter  $\xi$ : For  $\xi < 1$ ,  $\mathcal{Z}_1$  diverges and the single-particle distribution function,  $\rho_1(r) \sim \exp(-2\xi \ln r)/\mathcal{Z}_1$ , tends to zero reflecting *complete de-condensation* of counterions. For  $\xi > 1$ , on the contrary,  $\mathcal{Z}_1$  remains finite indicating *condensation* of counterions that adopt a finite density profile at the cylinder (the condensation is not complete in the sense that a fraction of (neutralizing) counterions always escapes to infinity—see Chapter 3). The above argument suggests a threshold of  $\xi_c = 1$  for the counterion-condensation transition.

Strictly speaking, the threshold behavior emerges only at an infinitely long cylinder (or approximately when the cylinder length, say  $H$ , is larger than  $D$ ). For finite cylinders, one can distinguish two regimes of radial distances, namely,  $r < H$ , where the cylindrical symmetry assumed above (and the results for the threshold behavior) approximately holds, and  $r > H$ , where counterions experience an almost-spherically-symmetric potential and thus tend to diffuse away.

It is important to note that the preceding discussion, though useful in bringing out the peculiar behavior of counterions at curved surfaces, is only based on single-particle considerations: the counterionic interactions and the role of the coupling parameter,  $\Xi$ , are not taken into account. In Chapters 3 and 4, I present systematic analysis of the counterion-condensation transition (CCT) at a charged cylinder incorporating the full interaction Hamiltonian. As will be demonstrated, many-body effects give rise to qualitatively different features as compared to these single-particle predictions. Indeed, the logarithmic transformation,  $y = \ln(r/R)$ , introduced above turns out to be the key to establish a full analysis of the CCT in the limit  $\Delta \rightarrow \infty$ .

## 2.4 Interactions between like-charged surfaces

Macroions in solution are often like-charged and thus repel each other by their bare Coulombic interaction. The overall effective interaction is however different from this bare interaction due to the presence of counterions, which can mediate both repulsive and *attractive* effective forces between two like-charged surface as will be demonstrated in this section. Obviously, the counterion-mediated interactions depend strongly on the distribution of counterions around macroions. For instance for two spherical or cylindrical macroions, the effective interaction reduces to the bare (repulsive) value in the regime where counterions completely de-condense and diffuse away (e.g., for two unconfined spheres or for two unconfined cylinder with sufficiently small Manning parameter). In the regime where counterions bind to the surface, the nature of effective interaction varies from pure repulsion to attraction as electrostatic

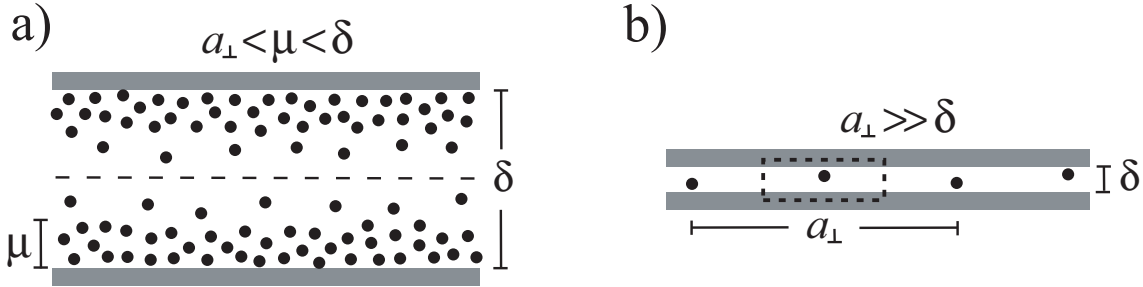


Figure 2.2: Schematic representation of the asymptotic interaction regimes of a) mean field and b) strong coupling for two like-charged walls. The mean-field regime is obtained for large separations between the walls (compared to other length scales) and is dominated by the repulsive osmotic pressure of counterions. For small separations (compared with the typical counterion spacing), the walls attract each other due to a dominant single-particle attraction mediated by counterions that are isolated in correlation cells of large lateral extension  $\sim a_{\perp}/2 \gg \delta$  (shown by a dotted loop).

correlations become stronger by increasing the coupling parameter,  $\Xi$ .<sup>2</sup>

In order to demonstrate the gross physical picture, I shall focus on the interaction between two planar like-charged walls of uniform surface charge density  $-\sigma_s e$  at separation  $\delta$  from each, where  $q$ -valent counterions fill only the space between the walls—see Figure 2.2 (the dielectric constant is assumed to be uniform in space). In this system, an extra length scale is set by the wall separation,  $\delta$ . Two limiting regimes of repulsion and attraction may be distinguished qualitatively by comparing  $\delta$  with other length scales of the system as follows.

### 2.4.1 Mean-field regime: Repulsion

First consider the limit where the wall separation,  $\delta$ , is *large* compared with all other length scales in the system and also that the system is weakly coupled,  $\Xi \ll 1$  (Figure 2.2a). In this case, counterions form a diffuse layer at each wall, but due to large wall separation, the system is approximately decoupled into two *nearly neutral* sub-systems, each consisting of a charged wall and its counterionic cloud. The effective pressure acting between the walls is dominated by the osmotic pressure of counterions across the mid-plane, since the overall electrostatic field at the mid-plane is zero due to the charge neutrality of each sub-system. This osmotic pressure is positive and therefore yields an effective *repulsion* between the walls.

The mid-plane osmotic pressure is proportional to the local density of counterions,  $\rho_{\text{mid}}$ , following the ideal-gas equation of state,  $P = \rho_{\text{mid}} k_B T$ , where  $\rho_{\text{mid}}$  drops roughly with the inverse square of the wall separation for large  $\delta$  as indicated by Eq. (2.10). This yields the

<sup>2</sup>Note that for charged spheres and cylinders, the coupling parameter,  $\Xi$ , and the Manning parameter,  $\tilde{R}$ , can in principle be varied independently from each other. In other words, de-condensation of counterions may occur in all ranges of the coupling parameter,  $\Xi$  (see Chapter 3). Therefore, the strong correlations regime, where like-charge attraction emerges, is achieved by taking a large coupling parameter,  $\Xi \gg 1$  (see a more accurate criterion in Section 2.4.3), and also a sufficiently large Manning parameter to ensure substantial counterion binding at macroions. It is however difficult to establish this latter condition even for the simplest interesting cases of *two* spheres and *two* cylinders, as it requires a detailed analysis of the binding-unbinding process, which is available only in the asymptotic limits of mean field ( $\Xi \rightarrow 0$ ) [39, 53] and strong coupling ( $\Xi \rightarrow \infty$ ) [54]. The mean-field theory is irrelevant for our purpose (as it does not include correlations). The strong-coupling condition on the Manning parameter is discussed in Chapter 5.

scaling form of the repulsive pressure between the walls as  $P(\delta) \sim \delta^{-2}$ . The formal derivation of the pressure based on the PB equation gives [1, 2, 43]

$$\frac{P_{\text{PB}}(\delta)/(k_{\text{B}}T)}{2\pi\ell_{\text{B}}\sigma_{\text{s}}^2} = \Lambda, \quad (2.20)$$

where  $\Lambda$  is determined from the transcendental equation  $\Lambda^{1/2} \tan[\Lambda^{1/2}(\delta/2\mu)] = 1$ . For large  $\delta/\mu \gg 1$ , the PB solution yields

$$\frac{P_{\text{PB}}(\delta)/(k_{\text{B}}T)}{2\pi\ell_{\text{B}}\sigma_{\text{s}}^2} \simeq \left(\frac{\pi\mu}{\delta}\right)^2, \quad (2.21)$$

which is expectedly independent of the surface charge density of the walls.

### 2.4.2 Strong-coupling regime: Attraction

Now consider a different asymptotic regime in which the system is strongly coupled,  $\Xi \gg 1$ , and the distance between the walls is smaller than the lateral spacing between counterions at each wall, i.e.  $a_{\perp} \gg \delta$  (Figure 2.2b). Since counterions are highly separated from each other, the two opposite layers of counterions tend to form an inter-locking pattern in equilibrium and at small separations.

The system may be thought of as a collection of laterally frozen “correlation cells”, each consisting of a single counterion sandwiched between two opposing sections of the walls with lateral size of about  $a_{\perp}/2$  (Figure 2.2b). Since  $a_{\perp} \gg \delta$ , the effective pressure (or interaction free energy) between the walls is dominated by the contribution from individual counterions fluctuating in each correlation cell, and lateral interactions may be neglected. The electrostatic energy of the system per cell is the sum of the bare interaction between the two surfaces with each other and with the single counterion, which—using the electroneutrality condition per cell and the fact that the wall separation is small—follows as  $u_{\text{elec}}/(k_{\text{B}}T) \simeq 2\pi\ell_{\text{B}}\sigma_{\text{s}}^2\delta$  per unit area. This *energetic* contribution gives an attractive pressure as  $P_{\text{elec}}/(k_{\text{B}}T) \simeq -2\pi\ell_{\text{B}}\sigma_{\text{s}}^2$  between the walls. On the other hand, the entropic contribution due to counterion confinement is of the order  $S_{\text{ci}} \sim k_{\text{B}} \ln \delta$  (per cell), which generates a repulsive component. The total pressure between strongly coupled walls is then obtained by combining these two effects and may be written as

$$\frac{P_{\text{SC}}(\delta)/(k_{\text{B}}T)}{2\pi\ell_{\text{B}}\sigma_{\text{s}}^2} = -1 + \frac{2\mu}{\delta}. \quad (2.22)$$

This expression clearly predicts a closely packed *bound-state* for the like-charged walls with the equilibrium surface separation,  $\delta_*$ , being equal to twice the Gouy-Chapman length, i.e.

$$\delta_* = 2\mu. \quad (2.23)$$

The like-charged walls therefore attract each other for  $\delta > \delta_*$  and repel at smaller distances.

As noted before, for  $\Xi \rightarrow \infty$ , the partition function of a charged system is in general reduced to a single-particle form (Appendix A). Indeed, the single-particle expression (2.22) represents an exact asymptotic result for planar walls [43, 45, 46].

### 2.4.3 Rouzina-Bloomfield criterion

In a system with *finite* coupling parameter,  $\Xi$  (and thus with a finite  $a_{\perp}/\mu$  ratio, Eq. (2.5)), the asymptotic strong-coupling results (strictly valid for  $\Xi \rightarrow \infty$ ) hold approximately as long as the surface separation,  $\delta$ , is smaller than the typical lateral distance between counterions at surface,  $a_{\perp}$ , i.e. for

$$\delta < a_{\perp}. \quad (2.24)$$

This condition in fact yields a simple and generic criterion identifying the regime where strong-coupling attraction is expected to emerge between two like-charged macroions. It was originally suggested by Rouzina and Bloomfield [48] and verified later using analytical and numerical methods for two charged planar walls [43, 45, 46], and also for other systems such as charged cylinders [55] as will be discussed in Chapter 5. For planar walls and in units of the Gouy-Chapman length, the Rouzina-Bloomfield criterion (2.24) reads

$$\left(\frac{\delta}{\mu}\right)^2 < \Xi. \quad (2.25)$$

For  $\delta < a_{\perp}$ , single-particle contributions are dominant and give rise to attraction of purely energetic origin between like-charged surfaces, a direct consequence of structural correlations among counterions (Figure 2.2b). For larger separations between opposing macroion surfaces  $\delta > a_{\perp}$ , mean-field features become increasingly important and the strength of attraction reduces. Eventually at very large separations, the interaction becomes repulsive [43, 45, 46]. This is the reason why correlation-induced attractive interactions in systems with (realistic) finite coupling parameter appears to be short-ranged.





## Chapter 3

# Counterion-Condensation Transition (CCT) at Charged Cylinders

Electrostatics of charged polymers is often dominated by small oppositely charged ions (counterions), which maintain the global electroneutrality of charged solutions. Many charged polymers, such as tubulin, actin and DNA are stiff and may be represented by straight cylinders (on length scales smaller than the persistence length). Neglecting many-ion effects, a single counterion is attracted by an electrostatic potential that grows logarithmically with the radial distance from the central cylinder axis. But since the counterion confinement entropy also shows a logarithmic size dependence, it was suggested early by Onsager [39] that a counterion delocalization transition occurs at a threshold cylinder charge or equivalently, at a critical temperature. Onsager's argument, which is strictly valid for a single particle, was soon corroborated by mean-field studies [20, 39, 56, 57, 58, 59, 60, 61, 62, 63, 64, 65, 66], which demonstrate that a charged cylinder can indeed bind or condense a finite fraction of counterions below a critical temperature (and even in the limit of infinite system size with no confining boundaries), while above the critical temperature, all counterions de-condense and diffuse to infinity.

This *counterion-condensation transition* (CCT) dramatically affects a whole number of static and dynamic quantities as observed in recent experiments on charged polymers [20, 59, 60, 67, 68, 69, 70, 71, 72, 73]: upon condensation, the bare polymer charge is screened leading, for instance, to a significant reduction in electrophoretic mobility [70, 73] and conductivity of polymers [72]; it also triggers striking static properties such as counterion-induced attraction between like-charged polymers, which gives rise to compact phases of F-actin [33, 34] and DNA [31]. Since its discovery, the CCT has been at the focus of numerical [74, 75, 76, 77] and analytical [78, 79, 80, 81, 82, 83, 84, 85, 86, 87, 88, 89, 90, 91, 92, 93, 94, 95] studies. Under particular dispute has been the connection between CCT and the celebrated Kosterlitz-Thouless transition of logarithmically interacting particles in two dimensions [82, 97, 98, 99].

The CCT at charged cylinders is regulated by a dimensionless control parameter,  $\xi = q\ell_B\tau$ , known as the Manning parameter [39], which depends on the linear charge density of the cylinder,  $-\tau e$ , charge valency of counterions,  $+q$ , and the Bjerrum length  $\ell_B = e^2/(4\pi\epsilon\epsilon_0k_B T)$  accommodating the ambient temperature  $T$  and the medium dielectric constant  $\epsilon$ . The Manning parameter plays the role of the *inverse rescaled temperature* and can be varied experimentally

by changing the linear charge density (using synthetic chains or various  $pH$ ) [69, 71, 72, 73] or by varying the dielectric media (mixing different solvents) [70, 73]. According to mean-field theory [20, 39, 62, 63, 64, 65, 66], condensation occurs above the critical value  $\xi_c = 1$ . In experiments, the critical Manning parameter appears to be about unity, but large deviations have also been reported [72, 73, 100], and the precise location of the critical point is still debated [73].

On the other hand, it is known that the critical temperature may in general be influenced by correlations and fluctuations, which are not captured within the mean-field theory [101]. These effects typically cause deviations from mean-field predictions in both non-universal and universal quantities below the upper critical dimension. Surprisingly, the mean-field prediction for the CCT threshold,  $\xi_c$ , has not been questioned in literature and apparently assumed to be exact. Likewise, the existence of universal scaling relations and critical (scaling) exponents associated with the CCT has not been addressed, neither on the mean-field level nor in the presence of correlations.

The chief goal in this chapter is to address the following issues: i) what is the exact threshold of the CCT,  $\xi_c$ , and ii) what are the critical scaling exponents associated with this transition in three spatial dimensions (3D). I shall also determine the type of singularities that emerge in thermodynamic quantities as the CCT criticality sets in (these issues will be addressed for the CCT in two dimensions in the following chapter). To establish a systematic investigation of the correlation effects, I will employ Monte-Carlo simulations for counterions at a single charged cylinder using a novel sampling method (centrifugal sampling), which is realized by mapping the radial coordinate to a logarithmic scale. This enables us to investigate the critical limit of infinite system size (that is when the outer boundaries confining counterions tend to infinity) within tractable equilibration times in the simulations. The importance of taking very large system sizes becomes evident by noting that lateral finite-size effects, which mask the critical unbinding behavior of counterions, depend on the *logarithm* of system size in the cylindrical geometry [39, 57, 62, 63, 64, 65, 66, 75, 82, 83, 87, 89, 94, 37, 38], causing a quite weak convergence to the critical infinite-size limit.

The present simulations [95, 96] provide the first numerical results for the asymptotic critical behavior of CCT and systematically incorporate correlation effects. The relevance of electrostatic correlations is in general identified by a dimensionless coupling parameter,  $\Xi = 2\pi q^3 \ell_B^2 \sigma_s$  with  $\sigma_s = \tau/(2\pi R)$  being the surface charge density and  $R$  the radius of the cylinder. The mean-field theory represents the limit  $\Xi \rightarrow 0$  [43, 46, 50], while in the converse limit of strong coupling,  $\Xi \gg 1$ , correlations become significant and typically lead to drastic changes [35, 43, 46, 49, 54, 55]. In order to investigate scaling properties of the CCT in various regimes of the coupling parameter, I shall focus on the inverse moments of the counterionic density profile, which play the role of the “order parameters” for this transition and represent the mean inverse localization length of counterions. Using a combined finite-size-scaling analysis with respect to both lateral size of the system and the number of counterions, I show that the order parameters adopt scale-invariant forms in the vicinity of the critical point. The critical scaling exponents associated with the reduced temperature and the size parameters are determined both within the simulations and also analytically within two limiting theories of mean field and strong coupling. As a main result, I demonstrate that the critical exponents of the CCT are *universal* (that is independent of the coupling parameter varied over several decades  $0.1 < \Xi < 10^5$ ) and appear to be in close agreement with the mean-field prediction. Surprisingly, the critical Manning parameter is also found to be universal and given by the mean-field value  $\xi_c = 1$ . The transition threshold,  $\xi_c$ , is

determined with high accuracy from the asymptotic behavior of the location of a singular peak emerging in the internal energy of the system. The excess heat capacity is found to vanish at small Manning parameters (de-condensation phase) and exhibits a universal jump at the transition point indicating that the CCT may be regarded as a second-order transition as also suggested in a previous mean-field study [89].

As will be shown, the validity of mean-field predictions in 3D breaks down as the Manning parameter increases beyond the critical value (i.e. in the condensation phase), where inter-particle correlations become significant at large coupling. This leads to an enhanced accumulation of counterions near the cylinder surface and a crossover to the strong-coupling theory predictions [35, 43, 46].

The organization of this chapter is as follows: In Sections 3.1 and 3.2, I shall introduce the model and outline the general method proposed for the investigation of the CCT. In Section 3.3, I will derive the scaling relations for order parameters and determine the asymptotic behavior of thermodynamic quantities within mean-field theory, which is valid in all dimensions. In Section 3.4, analytical results are obtained within the strong-coupling theory. The numerical analysis of the CCT for various coupling strengths will be presented in Sections 3.5 and 3.6.

### 3.1 Cell model for charged rod-like polymers

I shall consider a primitive cell model [37, 38, 104], which consists of a single charged cylinder of radius  $R$  and point-like neutralizing counterions of charge valency  $+q$  that are confined laterally in an outer (co-axial) cylindrical box of radius  $D$ —see Figure 3.1. The cylinder has infinite length,  $H$ , and a uniform (surface) charge distribution,  $-\sigma(\mathbf{x})e$ , where  $\sigma(\mathbf{x}) = \sigma_s \delta(r - R)$ . (Note that  $q$  and  $\sigma_s$  are given in units of the elementary charge,  $e$ , and are positive by definition.) The cylinder is assumed to be rigid and impenetrable to counterions and the dielectric medium is represented by a uniform dielectric constant,  $\epsilon$ . In three dimensions, electric charges interact via bare Coulombic interaction

$$v(\mathbf{x}) = 1/|\mathbf{x}|. \quad (3.1)$$

The electroneutrality condition holds globally inside the cell and entails the relation

$$qN = \tau H, \quad (3.2)$$

where  $N$  is the number of counterions per cell and  $\tau = 2\pi R\sigma_s$  represents the linear charge density of the cylinder. The system is described by the Hamiltonian

$$\frac{\mathcal{H}_N}{k_B T} = q^2 \ell_B \sum_{\langle ij \rangle} v(\mathbf{x}_i - \mathbf{x}_j) - q \ell_B \sum_{i=1}^N \int v(\mathbf{x} - \mathbf{x}_i) \sigma(\mathbf{x}) d\mathbf{x} + \frac{\ell_B}{2} \int \sigma(\mathbf{x}) v(\mathbf{x} - \mathbf{x}') \sigma(\mathbf{x}') d\mathbf{x} d\mathbf{x}', \quad (3.3)$$

which comprises mutual repulsions between counterions located at  $\{\mathbf{x}_i\}$  (first term), the counterion-cylinder attraction (second term) and the self-energy of the cylinder (last term). It can be written as

$$\frac{\mathcal{H}_N}{k_B T} = q^2 \ell_B \sum_{\langle ij \rangle} v(\mathbf{x}_i - \mathbf{x}_j) + 2\xi \sum_{i=1}^N \ln \left( \frac{r_i}{R} \right) + C_0, \quad (3.4)$$

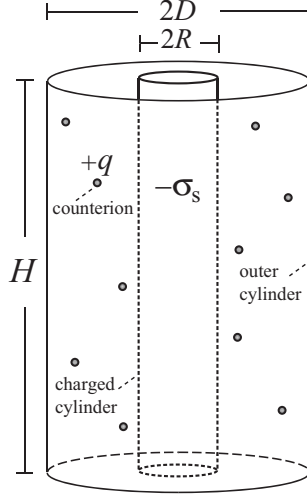


Figure 3.1: The three-dimensional model consists of a charged cylinder of infinite length,  $H$ , and its neutralizing counterions confined in an outer cylindrical box (see the text for parameters).

where  $\xi$  is the Manning parameter of the system [39, 57],

$$\xi = q\ell_B\tau \quad (3.5)$$

with  $\ell_B = e^2/(4\pi\epsilon\epsilon_0k_B T)$  being the Bjerrum length (in water and at room temperature  $\ell_B \simeq 7\text{\AA}$ ), and  $r_i = (x_i^2 + y_i^2)^{1/2}$  being the radial coordinate of the  $i$ -th counterion from the cylinder axis, which coincides with  $z$ -axis. The additive term  $C_0$  in Eq. (3.4) is related to the cylinder self-energy, which will be important in obtaining a convergent energy expression for the system in the simulations (Section 3.5.2 and Appendix D.1).

### 3.1.1 Dimensionless description

The parameter space of the system may be spanned by a minimal set of independent dimensionless parameters obtained from the ratios between characteristic length scales. These length scales are the rescaled Bjerrum length,  $q^2\ell_B$ , the Gouy-Chapman length

$$\mu = \frac{1}{2\pi q\ell_B\sigma_s}, \quad (3.6)$$

and the radius of the charged cylinder,  $R$ , and that of the outer boundary,  $D$ . The rescaled cylinder radius

$$\tilde{R} = \frac{R}{\mu} = \xi \quad (3.7)$$

equals the Manning parameter,  $\xi$ . The ratio between the rescaled Bjerrum length and the Gouy-Chapman length,  $\mu$ , gives the electrostatic coupling parameter (Chapter 2),

$$\Xi = \frac{q^2\ell_B}{\mu} = 2\pi q^3\ell_B^2\sigma_s, \quad (3.8)$$

which can identify the importance of electrostatic correlations in a charged system [35, 43, 44, 46, 54, 55], and the ratio between  $D$  and  $R$ , which enters only through the *lateral extension parameter*

$$\Delta \equiv \ln \left( \frac{D}{R} \right) \quad (3.9)$$

characterizing lateral finite-size effects. The relevant infinite-system-size limit is obtained for  $\Delta \rightarrow \infty$  [66, 37, 38].

I shall use the dimensionless form of the Hamiltonian obtained by rescaling the spatial coordinates as  $\tilde{\mathbf{x}} = \mathbf{x}/\mu$  [43], that is

$$\frac{\mathcal{H}_N}{k_B T} = \Xi \sum_{\langle ij \rangle} v(\tilde{\mathbf{x}}_i - \tilde{\mathbf{x}}_j) + 2\xi \sum_{i=1}^N \ln \left( \frac{\tilde{r}_i}{\tilde{R}} \right) + C_0. \quad (3.10)$$

The electroneutrality condition (3.2) in rescaled units reads

$$2\pi\xi\tilde{H} = 2\pi\Xi N, \quad (3.11)$$

where the left hand side is simply the rescaled area of the cylinder covered by the electric charge. The thermodynamic limit is obtained for  $N \rightarrow \infty$  and  $H \rightarrow \infty$ , but keeping  $N/H = \tau/q$  (or equivalently,  $N/\tilde{H} = \xi/\Xi$ ) fixed.

## 3.2 CCT as a generic binding-unbinding process

The statistical physical properties of the system may be investigated using the canonical partition function,

$$\mathcal{Z}_N = \frac{\mu^{3N}}{N!} \int_{\tilde{V}} \left[ \prod_{i=1}^N d\tilde{z}_i d\phi_i d\tilde{r}_i \tilde{r}_i \right] \exp \left\{ - \frac{\mathcal{H}_N}{k_B T} \right\} \quad (3.12)$$

represented in cylindrical coordinates  $\tilde{\mathbf{x}}_i = (\tilde{r}_i, \phi_i, \tilde{z}_i)$ , with the spatial integral running over the volume,  $\tilde{V}$ , of the space accessible for counterions, i.e.  $\tilde{R} \leq \tilde{r} \leq \tilde{D}$ .

Naively, one may conjecture that the partition function (3.12) diverges in a certain range of Manning parameters, when the upper boundary of the radial integrals,  $\tilde{D}$ , tends to infinity, as may be indicated by the logarithmic form of the counterion-cylinder interaction, which gives rise to algebraic prefactors of the form  $\tilde{r}_i^{1-2\xi}$  in the integrand. The possible emergence of a divergency in a charged cylindrical system was first pointed out by Onsager and the connection with the counterion-condensation transition was discussed by Manning [39].

Here I shall demonstrate this peculiar point using a transformation of coordinates, which provides the basis for the numerical simulations considered later in Section 3.5. The radial coordinate is transformed as

$$y = \ln \left( \frac{\tilde{r}}{\tilde{R}} \right), \quad (3.13)$$

upon which the partition function in (3.12) transforms as

$$\mathcal{Z}_N = \frac{\mu^{3N} \tilde{R}^{2N}}{N!} \int_{\tilde{V}} \left[ \prod_{i=1}^N d\tilde{z}_i d\phi_i dy_i \right] \exp \left\{ - \frac{\mathcal{H}_N^*}{k_B T} \right\}, \quad (3.14)$$

where the volume integral runs over the region  $0 < y < \Delta = \ln(D/R)$ , and

$$\frac{\mathcal{H}_N^*}{k_B T} = \sum_{i=1}^N W(y_i) + \Xi \sum_{\langle ij \rangle} v(\tilde{\mathbf{x}}_i - \tilde{\mathbf{x}}_j) + C_0 \quad (3.15)$$

is the transformed Hamiltonian of the system with

$$W(y) = 2(\xi - 1)y. \quad (3.16)$$

As seen, the original partition function is now mapped to the partition function of a system of interacting (repelling) particles in a *linear* potential well,  $W(y)$ . This latter quantity includes the contributions associated with the cylindrical boundary, namely, the bare counterion-cylinder attraction (i.e.  $2\xi y$ ) and an entropic (repulsive) term from the measure of the radial integral (i.e.  $-2y$ ), which may be regarded as an induced *centrifugal* component.

For small Manning parameter,  $\xi < 1$ , the potential well,  $W(y)$ , becomes purely repulsive suggesting that counterions *unbind* (or “de-condense”) from the central cylinder departing to infinitely large distances as the outer confining boundary tends to infinity,  $\Delta = \ln(D/R) \rightarrow \infty$ . In contrast for  $\xi > 1$ , the potential well exerts an attractive force upon counterions, which might lead to *partial binding* (or “condensation”) of counterions even in the absence of confining walls. The new representation of  $\mathcal{Z}_N$  in Eq. (3.14), therefore, reflects the interplay between energetic and entropic factors on a microscopic level.

Note that the rigorous analytical derivation of the aforementioned properties for counterions based on the full partition function is still an open problem, and only approximate limiting cases have been examined analytically (Section 3.2.2).

### 3.2.1 Onsager instability

As a simple illustrative case, let us consider a “hypothetical” system, in which mutual counterionic repulsions are switched off. The partition function (3.12) thus factorizes as  $\mathcal{Z}_N \sim \mathcal{Z}_1^N$ , where

$$\mathcal{Z}_1 = \int_0^\Delta dy e^{(2-2\xi)y} = \frac{e^{(2-2\xi)\Delta} - 1}{2 - 2\xi} \quad (3.17)$$

is the single-particle partition function. It diverges for  $\xi < 1$ , when the lateral extension parameter,  $\Delta$ , tends to infinity, which implies complete de-condensation of counterions, i.e. the probability,  $P(r) \sim \exp(-2\xi \ln r)/\mathcal{Z}_1$ , of finding counterions at any finite distance,  $r$ , from the cylinder tends to zero (equivalent to a vanishing density profile,  $\rho(r) = NP(r)$ ). But  $\mathcal{Z}_1$  and the counterionic density profile remain finite for  $\xi > 1$ , indicating that the Manning parameter  $\xi_c = 1$  is the onset of the CCT on the *one-particle* level, which will be termed here as the *Onsager instability* (in the spirit of Onsager’s original argument [39]). Onsager instability captures the basic features of the CCT. It exhibits the weak logarithmic convergence (via  $\Delta = \ln D/R$ ) to the critical limit as the volume per polymer ( $\sim D^2$ ) goes to infinity,<sup>1</sup> and as shown in Appendix B, displays algebraic singularities in energy and heat capacity (at  $\xi_c = 1$ ) that may be identified by a set of scaling exponents. Such scaling relations are crucial in the analysis of the critical behavior in the following sections.

I emphasize here that the results obtained within Onsager instability are by no means conclusive as soon as inter-counterionic interactions are switched on, which, as will be shown,

<sup>1</sup>The Onsager divergency may equivalently occur when the lower bound of the integral (cylinder radius) tends to zero  $R \rightarrow 0$  [39], since only the ratio  $D/R$  is relevant.

lead to qualitative differences. In particular, it turns out that a diverging partition function is *not* necessarily an indication of the *onset* of the CCT as asserted by the single-particle argument [39].

### 3.2.2 Beyond the Onsager instability

Many-body terms involved in the full partition function (3.12) render the systematic analysis of the CCT quite difficult. The analytical results are available in the asymptotic limits of i) vanishing coupling parameter  $\Xi \rightarrow 0$ , which leads to the mean-field or Poisson-Boltzmann (PB) theory, and ii) infinite coupling parameter  $\Xi \rightarrow \infty$ , which leads to the strong-coupling (SC) theory [43]. In the mean-field approximation (case i), statistical correlations among counterions are systematically neglected. In the opposite limit of strong coupling (case ii), the leading contribution to the partition function takes a very simple form comprising only the one-particle (counterion-cylinder) contributions [35, 43, 54, 55]. I will derive the mean-field predictions for the CCT in Section 3.3. The SC description ( $\Xi \rightarrow \infty$ ) resembles the Onsager instability and will be discussed in Section 3.4 and Appendix B. The perturbative improvement of these two limiting theories in a system of *finite* coupling parameter,  $\Xi$ , is formally possible by computing higher-order correction terms as previously performed for planar charged walls [43, 44, 46], but will not be considered here.

Interestingly, in both limits, the onset of the CCT is obtained as  $\xi_c = 1$ , which is due to the simplified form of the counterionic correlations. An important question is whether the critical value,  $\xi_c$ , varies with the coupling parameter. Such a behavior may be expected since the Manning parameter represents the rescaled inverse temperature of the system (i.e.  $\xi = T_*/T$  with  $T_* \equiv q\tau e^2/(4\pi\epsilon\epsilon_0 k_B)$ ), which, as known from bulk critical phenomena [101], can be shifted from its mean-field value due to inter-particle correlations for large couplings. Also it is interesting to examine whether the CCT exhibits scale-invariant properties near  $\xi_c$  and if it can be classified in terms of a universal class of exponents. Such scaling relations are known to represent relevant statistical characteristics of systems close to continuous phase transitions [101].

To address these issues, one has to define quantities which can serve as *order parameters* of the CCT. In the following section, I shall introduce such quantities and, by considering the mean-field theory, I will show that the order parameters indeed exhibit scaling behavior near the CCT threshold. I will return to the influence of electrostatic correlations on the threshold Manning parameter and scaling exponents of the CCT in the subsequent sections.

## 3.3 Mean-field theory for the CCT

### 3.3.1 Non-linear Poisson-Boltzmann (PB) equation

The mean-field theory can be derived systematically using a saddle-point analysis in the limit  $\Xi \rightarrow 0$  [43]. It is governed by the well-known Poisson-Boltzmann (PB) equation [37, 38], which, in rescaled units, reads (Appendix A)

$$\nabla_{\tilde{\mathbf{x}}}^2 \psi = 2\tilde{\sigma}(\tilde{\mathbf{x}}) - \tilde{\kappa}^2 \tilde{\Omega}(\tilde{\mathbf{x}}) e^{-\psi(\tilde{\mathbf{x}})} \quad (3.18)$$

for the dimensionless potential field  $\psi(\tilde{\mathbf{x}})$ . Here

$$\tilde{\sigma}(\tilde{\mathbf{x}}) = \delta(\tilde{r} - \tilde{R}) \quad (3.19)$$

is the rescaled charge distribution of the cylinder and

$$\tilde{\Omega}(\tilde{\mathbf{x}}) = \tilde{\Omega}(\tilde{r}) = \begin{cases} 1 & \tilde{R} \leq \tilde{r} \leq \tilde{D}, \\ 0 & \text{otherwise} \end{cases} \quad (3.20)$$

specifies the volume accessible to counterions. In the canonical ensemble, one has

$$\frac{\tilde{\kappa}^2}{2} = \frac{2\pi\xi\tilde{H}}{\int d\tilde{\mathbf{x}} \tilde{\Omega}(\tilde{\mathbf{x}}) \exp(-\psi)}. \quad (3.21)$$

Assuming the cylindrical symmetry (for an infinitely long cylinder) and using Eq. (3.18) and the global electroneutrality condition (3.11), one obtains

$$\left( \tilde{r} \frac{d\psi}{d\tilde{r}} \right)_{\tilde{r}=\tilde{R}} = 2\xi \quad \text{and} \quad \left( \tilde{r} \frac{d\psi}{d\tilde{r}} \right)_{\tilde{r}=\tilde{D}} = 0, \quad (3.22)$$

which are used to solve the PB equation (3.18) in the non-trivial region  $\tilde{R} \leq \tilde{r} \leq \tilde{D}$  [37, 38]. Thereby, one obtains both the free energy (Section 3.3.3) and the rescaled radial density profile of counterions around the charged cylinder

$$\tilde{\rho}(\tilde{r}) = \frac{\tilde{\kappa}^2}{2} \tilde{\Omega}(\tilde{r}) e^{-\psi(\tilde{r})}. \quad (3.23)$$

The rescaled density profile,  $\tilde{\rho}(\tilde{r})$ , is related to the actual *number* density of counterions,  $\rho(r)$ , through  $\tilde{\rho}(\tilde{r}) = \rho(r)/(2\pi\ell_B\sigma_s^2)$  [43] (see also Appendix A).

As shown by Alfrey et al. [37] and Fuoss et al. [38], the PB solution takes different functional forms depending on whether  $\xi$  lies below or above the Alfrey-Fuoss threshold

$$\Lambda_{\text{AF}} = \frac{\Delta}{1 + \Delta}, \quad (3.24)$$

that is

$$\psi_{\text{PB}}(\tilde{r}) = \begin{cases} \ln\left[\frac{\tilde{\kappa}^2\tilde{r}^2}{2\beta^2} \sinh^2\left(\beta \ln \frac{\tilde{r}}{\tilde{R}} + \coth^{-1} \frac{\xi-1}{\beta}\right)\right] & \xi \leq \Lambda_{\text{AF}}, \\ \ln\left[\frac{\tilde{\kappa}^2\tilde{r}^2}{2\beta^2} \sin^2\left(\beta \ln \frac{\tilde{r}}{\tilde{R}} + \cot^{-1} \frac{\xi-1}{\beta}\right)\right] & \xi \geq \Lambda_{\text{AF}}, \end{cases} \quad (3.25)$$

where  $\beta$  is given by the transcendental equations

$$\xi = \begin{cases} \frac{1-\beta^2}{1-\beta \coth(-\beta\Delta)} & \xi \leq \Lambda_{\text{AF}}, \\ \frac{1+\beta^2}{1-\beta \cot(-\beta\Delta)} & \xi \geq \Lambda_{\text{AF}}. \end{cases} \quad (3.26)$$

The PB density profile of counterions, Eq. (3.23), is then obtained for  $\tilde{R} \leq \tilde{r} \leq \tilde{D}$  as

$$\tilde{\rho}_{\text{PB}}(\tilde{r}) = \frac{\beta^2}{\tilde{r}^2} \times \begin{cases} \sinh^{-2}\left(\beta \ln \frac{\tilde{r}}{\tilde{R}} + \coth^{-1} \frac{\xi-1}{\beta}\right) & \xi \leq \Lambda_{\text{AF}}, \\ \sin^{-2}\left(\beta \ln \frac{\tilde{r}}{\tilde{R}} + \cot^{-1} \frac{\xi-1}{\beta}\right) & \xi \geq \Lambda_{\text{AF}}, \end{cases} \quad (3.27)$$



where I have arbitrarily chosen  $\psi_{\text{PB}}(\tilde{r} = \tilde{R}) = 0$  to fix the reference of the potential. This condition also fixes  $\tilde{\kappa}$  in Eq. (3.25) as well as the radial density of counterions *at contact* with the cylinder using Eq. (3.23), i.e.

$$\frac{\tilde{\kappa}^2}{2} = \tilde{\rho}_{\text{PB}}(\tilde{R}) = \frac{1}{\xi^2} \times \begin{cases} (\xi - 1)^2 - \beta^2 & \xi \leq \Lambda_{\text{AF}}, \\ (\xi - 1)^2 + \beta^2 & \xi \geq \Lambda_{\text{AF}}. \end{cases} \quad (3.28)$$

The density profiles given in Eq. (3.27) are in fact normalized to the total number of counterions,  $N$ , a condition imposed via Eq. (3.21). Using Eq. (3.23), the normalization condition in rescaled units reads

$$\int_{\tilde{R}}^{\tilde{D}} d\tilde{r} \tilde{r} \tilde{\rho}_{\text{PB}}(\tilde{r}) = \xi. \quad (3.29)$$

### 3.3.2 Onset of the CCT within mean-field theory

The threshold of CCT within the mean-field PB theory was considered by several workers [62, 63, 64, 65, 66, 37, 38]. It may be obtained from the asymptotic behavior of the density profile ( $\Delta \rightarrow \infty$ ) as reviewed below.

First note that for  $\Delta \gg 1$ , the Alfrey-Fuoss threshold  $\Lambda_{\text{AF}}$ , Eq. (3.24), tends to unity from below, i.e.

$$\Lambda_{\text{AF}} = 1 - \frac{1}{\Delta} + \mathcal{O}(\Delta^{-2}). \quad (3.30)$$

Therefore, for Manning parameter  $\xi < 1$ , one may use the first relation in Eq. (3.26) to obtain the limiting behavior of the integration constant  $\beta$  as (Appendix C.1)

$$\beta = (1 - \xi) + \mathcal{O}\left(e^{-2\Delta(1-\xi)}\right), \quad (3.31)$$

when  $\Delta \rightarrow \infty$ . Using this into Eq. (3.28), one finds that the density of counterions at contact,  $\tilde{\rho}_{\text{PB}}(\tilde{R})$ , asymptotically vanishes. Hence, the density profile (3.23) at any finite distance from the cylinder tends to zero for  $\xi \leq 1$ , i.e.

$$\tilde{\rho}_{\text{PB}}(\tilde{r}) \rightarrow 0, \quad (3.32)$$

representing the de-condensation regime in the limit  $\Delta \rightarrow \infty$ . For  $\xi \geq 1$ , on the other hand, one has  $\beta \rightarrow 0$  for increasing  $\Delta$  (Appendix C.1), and thus using Eq. (3.28),

$$\tilde{\rho}_{\text{PB}}(\tilde{R}) \rightarrow \frac{(\xi - 1)^2}{\xi^2}. \quad (3.33)$$

Using the second relation in Eq. (3.27) and expanding for small  $\beta$ , the radial density profile follows as [63, 105]

$$\tilde{\rho}_{\text{PB}}(\tilde{r}) \rightarrow \frac{(\xi - 1)^2}{\xi^2} \left[ \frac{\tilde{r}}{\tilde{R}} \right]^{-2} \left[ 1 + (\xi - 1) \ln \frac{\tilde{r}}{\tilde{R}} \right]^{-2} \quad (3.34)$$

in the limit  $\Delta \rightarrow \infty$  (see also Appendix C.6), which is finite and indicates condensation of counterions. This proves that the mean-field critical point is given by

$$\xi_c^{\text{PB}} = 1, \quad (3.35)$$

corresponding to the mean-field critical temperature

$$T_c^{\text{PB}} = \frac{q\tau e^2}{4\pi\epsilon\epsilon_0 k_B}. \quad (3.36)$$

### 3.3.3 Critical scaling-invariance: Mean-field exponents

It is readily seen from Eqs. (3.33) and (3.34) that the asymptotic density of counterions adopts a scale-invariant or homogeneous form with respect to the *reduced Manning parameter*,

$$\zeta = 1 - \frac{\xi_c^{\text{PB}}}{\xi}, \quad (3.37)$$

close to the critical value  $\xi_c^{\text{PB}} = 1$ . Note that the reduced Manning parameter equals the *reduced temperature* of the system,  $t = 1 - (T/T_c^{\text{PB}})$ , when other quantities such as the dielectric constant,  $\varepsilon$ , and the linear charge density of the cylinder,  $\tau$ , are kept fixed. (Experimentally, however, the Manning parameter may be varied by changing  $\varepsilon$  [70, 73] or  $\tau$  [69, 71, 72, 73] at constant temperature, in which case,  $\zeta$  can be related to the reduced dielectric constant or the reduced linear charge density.)

In a finite confining volume (finite  $\Delta$ ), such scaling forms with respect to  $\zeta$  do not hold since the true CCT is suppressed. Yet as a general trend [101], one expects that for *sufficiently large*  $\Delta$ , the reminiscence of such scaling relations appears in the form of finite-size-scaling relations near the transition point. These relations would involve both  $\zeta$  and the lateral extension parameter,  $\Delta$ , (as the only relevant parameters in the mean-field limit) in a scale-invariant fashion as will be shown below.

#### The CCT order parameters

As possible candidates for the CCT “order parameter”, I use the inverse moments of the counterionic density profile

$$S_n(\xi, \tilde{D}) \equiv \left\langle \frac{1}{\tilde{r}^n} \right\rangle = \frac{\int_{\tilde{R}}^{\tilde{D}} \tilde{r} \, d\tilde{r} \, \tilde{r}^{-n} \tilde{\rho}(\tilde{r})}{\int_{\tilde{R}}^{\tilde{D}} \tilde{r} \, d\tilde{r} \, \tilde{\rho}(\tilde{r})} \quad (3.38)$$

where  $n > 0$ .<sup>2</sup> Note that these quantities reflect *mean inverse localization length* of counterions. In the condensation phase (where counterions adopt a finite density profile), one has  $S_n > 0$ , reflecting a finite localization length. But at the critical point and in the decondensation phase (with vanishing counterionic density profile), one has  $S_n = 0$  in the limit of infinite system size  $\Delta \rightarrow \infty$ , which indicates a diverging counterion localization length.

In order to derive the mean-field finite-size-scaling relations for  $S_n$  near  $\xi_c^{\text{PB}} = 1$ , I will focus on the PB solution in the regime of Manning parameters  $\xi \geq \Lambda_{\text{AF}}$ , since for any finite  $\Delta$ , one has  $\Lambda_{\text{AF}} \leq \xi_c^{\text{PB}} = 1$  from Eq. (3.30). Inserting the first relation in Eq. (3.27) into Eq. (3.38), I obtain

$$S_n^{\text{PB}} = \frac{\beta^2}{\xi} \int_{\tilde{R}}^{\tilde{D}} d\tilde{r} \, \tilde{r}^{-n-1} \sin^{-2}(\beta \ln \frac{\tilde{r}}{\tilde{R}} + \cot^{-1} \frac{\xi - 1}{\beta}). \quad (3.39)$$

Changing the integration variable as  $y = \ln(\tilde{r}/\tilde{R})$ , I obtain

$$S_n^{\text{PB}} = \frac{\beta^2}{\xi^{n+1}} \int_0^\Delta dy \, e^{-ny} \sin^{-2}(\beta y + \cot^{-1} \frac{\xi - 1}{\beta}). \quad (3.40)$$

---

<sup>2</sup>The density moments for  $n < 0$  are divergent since for finite  $\xi$ , a finite fraction of the counterions is always de-condensed.

For  $\Delta \gg 1$ , the above relation may be approximated by a simple analytic expression as (Appendix C.4)

$$S_n^{\text{PB}}(\zeta, \Delta) \simeq \frac{1}{n} \left[ \zeta^2 + \beta^2(\zeta, \Delta) \right] \quad (3.41)$$

for  $\xi$  being sufficiently close to the critical value  $\xi_c^{\text{PB}} = 1$ .

Using the above result, one may distinguish two limiting cases, where different scaling relations are obtained, namely, i) when  $\Delta \rightarrow \infty$  but  $\zeta = 1 - \xi_c^{\text{PB}}/\xi$  is *finite* and close to the critical value  $\zeta^{\text{PB}} = 0$ , and ii) when  $\Delta$  is finite and large, but the system tends towards the critical point,  $\zeta \rightarrow \zeta_c^{\text{PB}} = 0$ .

In the first case, as stated before, one has  $\beta \rightarrow 0$  for the above-threshold regime,  $\zeta \geq 0$ ; thus using Eq. (3.41), I obtain

$$S_n^{\text{PB}}(\zeta, \Delta \rightarrow \infty) \simeq \frac{\zeta^2}{n}. \quad (3.42)$$

On the other hand,  $S_n^{\text{PB}}$  vanishes for  $\zeta \leq 0$  (Appendix C.4). Hence, the following scaling relation is obtained in the infinite-system-size limit  $\Delta \rightarrow \infty$ ,

$$S_n^{\text{PB}}(\zeta, \infty) \simeq \begin{cases} \zeta^{\chi_{\text{PB}}}/n & 0 \leq \zeta \ll 1, \\ 0 & \zeta \leq 0, \end{cases} \quad (3.43)$$

which introduces the mean-field critical exponent associated with the reduced Manning parameter,  $\zeta$  (or the reduced temperature,  $t$ ) as

$$\chi_{\text{PB}} = 2. \quad (3.44)$$

The mean-field counterion-condensation transition is therefore characterized by a diverging (localization) length scale  $1/S_1^{\text{PB}} \sim \zeta^{-2}$ , as the critical point is approached from above. The scaling relation (3.43) may also be derived in a direct way by considering a strictly infinite system ( $\Delta = \infty$ ) as shown in Appendix C.6.

In the limiting case (ii) with  $\zeta \rightarrow \zeta_c^{\text{PB}} = 0$ , one has from Eq. (3.26) that  $\beta \simeq \pi/(2\Delta)$  when  $\Delta$  is finite but large,  $\Delta \gg 1$  (Appendix C.1). Therefore, using Eq. (3.41) I obtain

$$S_n^{\text{PB}}(0, \Delta) \simeq \frac{\pi^2}{4n\Delta^2}, \quad (3.45)$$

which introduces a new scaling relation

$$S_n^{\text{PB}}(0, \Delta) \sim \Delta^{-\gamma_{\text{PB}}} \quad (3.46)$$

with the mean-field exponent

$$\gamma_{\text{PB}} = 2 \quad (3.47)$$

associated with the lateral extension parameter,  $\Delta$ . This relation shows that the approach to the true CCT limit (when  $S_n^{\text{PB}}$  vanishes at the critical point) is *logarithmically* weak as the box size,  $D$ , increases to infinity, i.e.  $S_n^{\text{PB}}(\zeta = 0) \sim 1/(\ln D/R)^2$ .

The scaling relations (3.42) and (3.45) indicate that  $S_n^{\text{PB}}$  takes a general scale-invariant form with respect to  $\zeta$  and  $\Delta$  as

$$S_n^{\text{PB}} \simeq \Delta^{-\gamma_{\text{PB}}} \mathcal{D}_n(\zeta \Delta^{\gamma_{\text{PB}}/\chi_{\text{PB}}}) \quad (3.48)$$

for sufficiently large  $\Delta$  and in the vicinity of the mean-field threshold. The scaling function,  $\mathcal{D}_n(u)$ , has the following asymptotic behavior

$$\mathcal{D}_n(u) \sim \begin{cases} \text{const.} & u \rightarrow 0, \\ u^{\chi_{\text{PB}}/n} & u \rightarrow +\infty. \end{cases} \quad (3.49)$$

In general, the scale-invariant relations such as Eq. (3.48) may be obtained within the PB frame-work using the fact that the integration constant  $\beta(\zeta, \Delta)$  takes a scale-invariant form as

$$\beta \simeq \Delta^{-1} \mathcal{B}(\zeta \Delta). \quad (3.50)$$

Here  $\mathcal{B}(u)$  is a scaling function which behaves asymptotically as (Appendix C)

$$\mathcal{B}(u) \sim \begin{cases} \text{const.} & u \rightarrow 0, \\ \sqrt{u} & u \rightarrow +\infty. \end{cases} \quad (3.51)$$

Combining Eqs. (3.41) and (3.50), the scaling function  $\mathcal{D}_n(u)$  is obtained in terms of  $\mathcal{B}(u)$  as

$$\mathcal{D}_n(u) \simeq \frac{1}{n} [u^2 + \mathcal{B}^2(u)], \quad (3.52)$$

which reproduces Eq. (3.49) when combined with Eq. (3.51).

The mean-field exponents  $\chi_{\text{PB}}$  and  $\gamma_{\text{PB}}$  appear to be independent of the index of the density moments,  $n$ . They may be used to characterize the mean-field universality class of the CCT in all dimensions, since the PB results are independent of the space dimensionality.

### Mean-field energy and heat capacity

The mean-field canonical free energy of the counterion-cylinder system may be obtained using a saddle-point analysis from the field-theoretic representation of the partition function when  $\Xi \rightarrow 0$  [103] (Appendix A). The rescaled PB free energy defined as  $\tilde{\mathcal{F}}^{\text{PB}} \equiv \mathcal{F}_N^{\text{PB}}/(Nk_B T)$  is given by (up to the trivial kinetic energy part)

$$\tilde{\mathcal{F}}^{\text{PB}} = -\frac{1}{\xi} \int \tilde{r} d\tilde{r} \left[ \frac{1}{4} \left( \frac{d\psi_{\text{PB}}}{d\tilde{r}} \right)^2 + \delta(\tilde{r} - \tilde{R}) \psi_{\text{PB}}(\tilde{r}) \right] - \ln \left[ \frac{1}{\xi} \int_{\tilde{R}}^{\tilde{D}} \tilde{r} d\tilde{r} e^{-\psi_{\text{PB}}(\tilde{r})} \right] - \ln \left( \frac{2V_{\text{cyl}}}{N\xi} \right), \quad (3.53)$$

where  $V_{\text{cyl}} = \pi R^2 H$  is the actual volume of the cylinder. In the thermodynamic limit  $N \rightarrow \infty$ , the ratio  $V_{\text{cyl}}/N$  is a constant and will be dropped in what follows.

Inserting the PB potential field, Eq. (3.25), into the free energy expression (3.53), I find that for  $\xi > \Lambda_{\text{AF}}$

$$\tilde{\mathcal{F}}^{\text{PB}} = -\frac{1}{\xi} \left[ (1 - \beta^2) \Delta + \ln \left( \frac{(\xi - 1)^2 + \beta^2}{1 + \beta^2} \right) + \xi \right] + \ln[(\xi - 1)^2 + \beta^2] - \ln(2\xi). \quad (3.54)$$

While for  $\xi < \Lambda_{\text{AF}}$ , I obtain

$$\tilde{\mathcal{F}}^{\text{PB}} = -\frac{1}{\xi} \left[ (1 + \beta^2) \Delta + \ln \left( \frac{(\xi - 1)^2 - \beta^2}{1 - \beta^2} \right) + \xi \right] + \ln[(\xi - 1)^2 - \beta^2] - \ln(2\xi). \quad (3.55)$$

These expressions (up to some additive constants) have also been obtained by Lifson et al. [104] using a charging process method.

The rescaled (internal) energy,  $\tilde{E}^{\text{PB}} \equiv E_N^{\text{PB}}/(Nk_{\text{B}}T)$ , and the rescaled excess heat capacity,  $\tilde{C}^{\text{PB}} \equiv C_N^{\text{PB}}/(Nk_{\text{B}})$ , can be calculated using the thermodynamic relations

$$\tilde{E}^{\text{PB}} = \xi \frac{\partial \tilde{\mathcal{F}}^{\text{PB}}}{\partial \xi}, \quad (3.56)$$

$$\tilde{C}^{\text{PB}} = -\xi^2 \frac{\partial^2 \tilde{\mathcal{F}}^{\text{PB}}}{\partial \xi^2}, \quad (3.57)$$

where the derivatives are taken at fixed volume, number of particles, and also for fixed charges and dielectric constant. A closed-form expression may be obtained for energy using the relation  $E = (\varepsilon\varepsilon_0/2) \int \mathbf{d}\mathbf{x} (\nabla\psi_{\text{elec}})^2$ , where  $\psi_{\text{elec}} = k_{\text{B}}T\psi_{\text{PB}}/qe$  is the potential field in actual units. In rescaled units, the result is

$$\tilde{E} = \frac{1}{4\xi} \int_{\tilde{R}}^{\tilde{D}} \tilde{r} d\tilde{r} \left( \frac{d\psi}{d\tilde{r}} \right)^2 = \frac{1}{\xi} \times \begin{cases} (1 + \beta^2)\Delta + \ln \left[ \frac{(\xi-1)^2 - \beta^2}{1 - \beta^2} \right] + \xi & \xi \leq \Lambda_{\text{AF}}, \\ (1 - \beta^2)\Delta + \ln \left[ \frac{(\xi-1)^2 + \beta^2}{1 + \beta^2} \right] + \xi & \xi \geq \Lambda_{\text{AF}}. \end{cases} \quad (3.58)$$

In general, the above quantities can be calculated numerically using the transcendental equation (3.26). But in the limit of  $\Delta \rightarrow \infty$ , I employ the asymptotic results obtained for  $\beta$  (Appendix C) to derive the asymptotic form of the rescaled PB free energy as [103]

$$\tilde{\mathcal{F}}^{\text{PB}} = \begin{cases} (\xi - 2)\Delta & \xi \leq \xi_c^{\text{PB}} = 1, \\ -\Delta/\xi & \xi \geq \xi_c^{\text{PB}} = 1. \end{cases} \quad (3.59)$$

The rescaled PB energy asymptotically behaves as

$$\tilde{E}^{\text{PB}} = \begin{cases} \xi\Delta & \xi \leq \xi_c^{\text{PB}}, \\ \Delta/\xi & \xi \geq \xi_c^{\text{PB}}, \end{cases} \quad (3.60)$$

and the rescaled PB excess heat capacity as

$$\tilde{C}^{\text{PB}} = \begin{cases} 0 & \xi < \xi_c^{\text{PB}}, \\ 2\Delta/\xi & \xi > \xi_c^{\text{PB}}. \end{cases} \quad (3.61)$$

The above results show that both energy and excess heat capacity develop a singular peak at the Manning parameter  $\xi_c^{\text{PB}} = 1$  when the critical limit  $\Delta \rightarrow \infty$  is approached. The PB results also show that the free energy diverges with  $\Delta$  *both* above and below the mean-field critical point, in contrast with the behavior obtained within the (one-particle) Onsager instability [39], which suggests a connection between the onset of the counterion condensation and the divergence of the partition function (Section 3.2 and Appendix B).

Another important point is that the PB heat capacity exhibits a discontinuity at  $\xi_c^{\text{PB}} = 1$ . Therefore, the CCT may be considered as a second-order transition as also pointed out in a previous mean-field study [89]. I shall return to the singular behavior of energy and heat capacity later in the numerical studies.

### 3.4 Strong-coupling theory for the CCT

In the limit of large coupling parameter,  $\Xi \rightarrow \infty$ , the partition function of a charged system adopts an expansion in powers of  $1/\Xi$ , the leading term of which comprises only single-particle contributions, i.e. a single counterion interacting with fixed charged objects [43, 44, 44] (see Appendix A). This leading-order theory, referred to as the asymptotic strong-coupling (SC) theory, describes the complementary limit to the mean-field regime,  $\Xi \gg 1$ , where inter-particle correlations are expected to become important [35, 43, 48, 49].

The rescaled SC density profile for counterions is obtained as (Appendix A)

$$\tilde{\rho}_{\text{SC}}(\tilde{r}) = \Lambda_0 \tilde{\Omega}(\tilde{r}) e^{-\tilde{u}(\tilde{r})} \quad (3.62)$$

where  $\tilde{u}(\tilde{r}) = 2\xi \ln(\tilde{r}/\tilde{R})$  is the single-particle interaction energy and  $\Lambda_0$  is a normalization factor, which is fixed with the total number of counterions. Thus one has

$$\Lambda_0 = \frac{2(\xi - 1)}{\xi} \left[ 1 - e^{-2(\xi-1)\Delta} \right]^{-1}, \quad (3.63)$$

in the cell model considered here. Note that for  $\Delta \rightarrow \infty$ ,  $\Lambda_0$ , and therefore the whole density profile, vanishes for  $\xi \leq 1$ . But for  $\xi \geq 1$ , one obtains  $\Lambda_0 \rightarrow 2(\xi - 1)/\xi$  and hence a finite limiting density profile as

$$\tilde{\rho}_{\text{SC}}(\tilde{r}) \rightarrow \frac{2(\xi - 1)}{\xi} \left( \frac{\tilde{r}}{\tilde{R}} \right)^{-2\xi}. \quad (3.64)$$

This shows that the CCT is reproduced within the SC theory as well, and surprisingly, the threshold value is found to be  $\xi_c^{\text{SC}} = 1$  in coincidence with the mean-field prediction. Note however that the SC profile for  $\xi > 1$  indicates a *larger* contact density for counterions as compared with the mean-field theory, e.g., for  $\Delta \rightarrow \infty$ , one has

$$\tilde{\rho}_{\text{SC}}(\tilde{R}) = \frac{2(\xi - 1)}{\xi}, \quad (3.65)$$

which is larger than the PB value (3.33) by a factor of  $\tilde{\rho}_{\text{SC}}(\tilde{R})/\tilde{\rho}_{\text{PB}}(\tilde{R}) = 2(1 - 1/\xi)^{-1}$ . The SC density profile also decays faster than the PB profile indicating a more compact counterionic layer at the cylinder. This reflects strong ionic correlations in the condensation phase ( $\xi > 1$ ) for  $\Xi \gg 1$  as will be discussed further in the numerical studies below.

Using Eq. (3.62), the SC order parameters can be calculated as

$$S_n^{\text{SC}}(\xi, \Delta) = \frac{2(\xi - 1)}{\xi^n(2\xi - 2 + n)} \frac{1 - e^{-(2\xi-2+n)\Delta}}{1 - e^{-2(\xi-1)\Delta}} \quad (3.66)$$

for arbitrary  $\xi$  and  $\Delta$ . For  $\Delta \rightarrow \infty$ ,  $S_n^{\text{SC}}$  vanishes for  $\xi \leq \xi_c^{\text{SC}} = 1$ , but tends to

$$S_n^{\text{SC}}(\zeta, \infty) = \frac{2(\xi - 1)}{\xi^n(2\xi - 2 + n)} \quad (3.67)$$

for  $\xi \geq \xi_c^{\text{SC}} = 1$ . In the vicinity of the critical point,  $S_n^{\text{SC}}$  exhibits the scaling relation

$$S_n^{\text{SC}}(\zeta, \infty) \simeq 2\zeta/n, \quad (3.68)$$

which gives the SC scaling exponent associated with the reduced Manning parameter,  $\zeta = 1 - \xi_c/\xi$ , as  $\chi_{\text{SC}} = 1$ . In a finite system and right at the threshold  $\xi = \xi_c^{\text{SC}}$ ,  $S_n^{\text{SC}}$  shows the finite-size-scaling relation

$$S_n^{\text{SC}}(0, \Delta) \simeq \frac{1}{n\Delta}, \quad (3.69)$$

which gives the SC scaling exponent associated with the lateral extension parameter,  $\Delta$ , as  $\gamma_{\text{SC}} = 1$ .

These exponents are different from the corresponding mean-field values, Eqs. (3.44) and (3.47). As will be shown later, the SC predictions, which coincide with the Onsager instability results, in fact break down *near* the CCT critical point.

## 3.5 Monte-Carlo study of the CCT in 3D

The preceding analysis within the mean-field and the strong-coupling theory reveals a set of new scaling relations associated with the counterion-condensation transition (CCT) in the limit of infinitely large (lateral) system size. In the following sections, I shall use numerical methods to examine the critical behavior in various regimes of the coupling parameter, and thereby, to examine the validity of the aforementioned analytical results.

### 3.5.1 The centrifugal sampling method

The major difficulty in studying the CCT numerically goes back to the lack of an efficient sampling technique. Poor sampling problem arises for counterions at charged curved surfaces in the infinite-confinement-volume limit because, contrary to charged plates, a finite fraction of counterions always tends to unbind from curved boundaries and diffuse to infinity as the system relaxes toward its equilibrium state. This situation is, of course, not tractable in numerical simulations; hence to achieve proper equilibration within a reasonable time, charged cylinders are customarily considered in a confining box (in lateral directions) of *practically* large size. As well known [57, 63, 64, 65, 75, 77], lateral finite-size effects are quite small for sufficiently large Manning parameter ( $\xi > \xi_c$ ). But at small Manning parameters ( $\xi \sim \xi_c$ ), these effects become significant and suppress the de-condensation of counterions.

The mean-field results already reveal a very weak asymptotic convergence to the true critical transition limit controlled by the logarithmic size of the confining box  $\Delta = \ln(D/R)$ . Hence one needs to consider a confinement volume of extremely large radius,  $D$ , to establish the large- $\Delta$  regime, where the scaling (and possibly universal) properties of the CCT emerge. For this purpose, clearly, the simple-sampling methods within Monte-Carlo or Molecular Dynamics schemes [74, 75, 76, 77, 106, 107, 108] are not useful at *low* Manning parameter as they render an infinitely long relaxation time.

I shall therefore introduce a novel sampling method within the Monte-Carlo scheme, which enables one to properly span the relevant parts of the phase space for large confining volumes. In three dimensions, I use the configurational Hamiltonian (3.10) in rescaled coordinates. The sampling method, which I will refer to as the *centrifugal sampling*, is obtained by mapping the radial coordinate to a logarithmic scale according to Eq. (3.13), i.e.  $y = \ln(\tilde{r}/\tilde{R})$ , which leads to the transformed partition function (3.14). As explained before (Section 3.2), the entropic (centrifugal) factor,  $\exp(2y)$ , is absorbed from the measure of the radial integrals into the Hamiltonian, yielding the transformed Hamiltonian  $\mathcal{H}_N^*$  in Eq. (3.15).

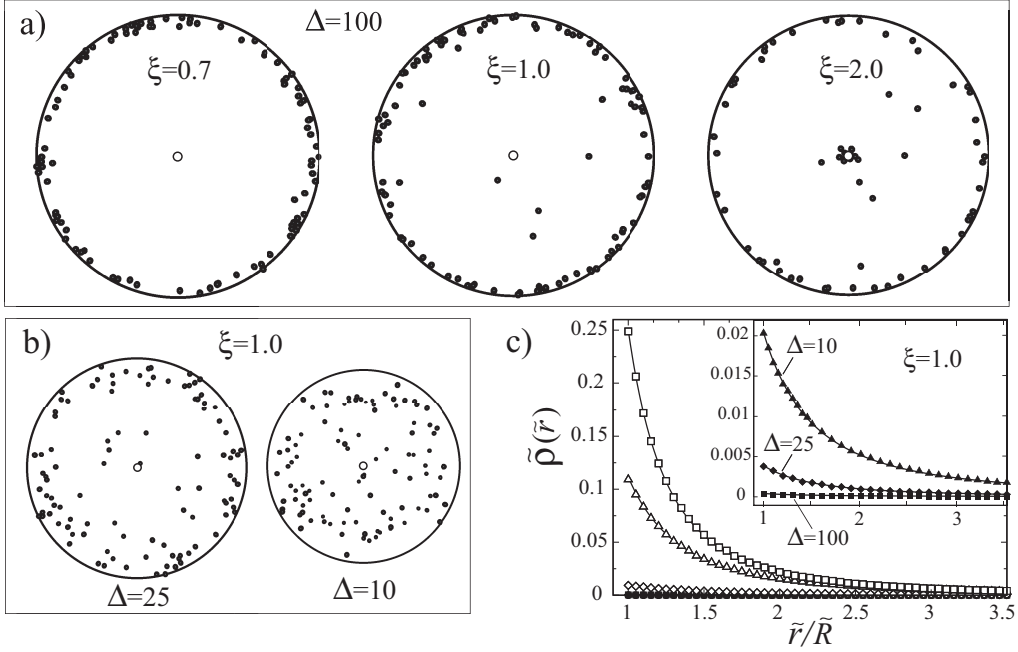


Figure 3.2: Typical snapshots from the simulations on the counterion-cylinder system in 3D for a) lateral extension parameter  $\Delta = \ln(D/R) = 100$  and three different Manning parameters  $\xi = 0.7, 1.0$  and  $2.0$  as indicated on the graph, and b) for Manning parameter  $\xi = 1.0$  and smaller lateral extension parameters  $\Delta = 10$  and  $25$ . The snapshots show top-views of the simulation box (see Section 3.5.2 and Figure 3.1) with radial distances shown in logarithmic scale  $y = \ln(\tilde{r}/\tilde{R})$ . Point-like counterions are shown by black spheres and the charged cylinder by a circle in the middle. Figure c) gives the simulated radial density of counterions in rescaled units,  $\tilde{\rho}(\tilde{r}) = \rho(r)/(2\pi\ell_B\sigma_s^2)$ , as a function of the (linear) distance from the cylinder axis. Main set shows the data for  $\Delta = 100$  and Manning parameters  $\xi = 2.0$  (open square),  $1.5$  (open triangle-ups),  $1.1$  (open diamonds),  $1.0$  (filled squares) and  $0.7$  (filled circles) from top to bottom. Inset shows the same for  $\xi = 1.0$ , but for various lateral extension parameters  $\Delta = 10, 25$  and  $100$  (top to bottom). Solid curves are the mean-field PB prediction obtained numerically from Eq. (3.27). Number of counterions here is  $N = 100$  and the coupling parameter  $\Xi = 0.1$ . Error-bars are smaller than the size of symbols.

I thus simulate the system using Metropolis algorithm [109], but making use of the transformed Hamiltonian (3.15). The entropic factors, which cause unbinding of counterions, are hence incorporated into the transition probabilities of the associated Markov chain of states, that generates equilibrium states with the distribution function  $\sim \exp(-\beta\mathcal{H}_N^*)$ . The averaged quantities, say  $\bar{Q}$ , follow by extracting a set of  $T$  values  $\{Q_1, \dots, Q_T\}$  in the course of the simulations as  $\bar{Q} = \sum_{t=1}^T Q_t/T$ , which, for sufficiently large  $T$ , produces the desired ensemble average  $\langle Q \rangle$ , i.e.

$$\bar{Q} = \frac{1}{T} \sum_{t=1}^T Q_t \simeq \frac{\mu^{3N} \tilde{R}^{2N}}{N! \mathcal{Z}_N} \int_{\tilde{V}} \left[ \prod_{i=1}^N d\tilde{z}_i d\phi_i dy_i \right] Q(y_i, \phi_i, \tilde{z}_i) e^{-\beta\mathcal{H}_N^*} = \langle Q \rangle, \quad (3.70)$$

up to relative corrections of the order  $1/\sqrt{T}$ .



### 3.5.2 Simulation model and parameters

The geometry of the counterion-cylinder system in the following simulations is similar to what I have sketched in Figure 3.1. I use typically between  $N = 25$  to 300 counterions (most of the results in are obtained with  $N=100$  and 200 particles) and increase the lateral extension parameter,  $\Delta = \ln(D/R)$ , up to  $\Delta = 300$ . I also vary the Manning parameter,  $\xi$ , and consider a wide range of values for the electrostatic coupling parameter,  $\Xi$ , from  $\Xi = 0.1$  (close to the mean-field regime) up to  $\Xi = 10^5$  (close to the strong-coupling regime).

The cylindrical simulation box has a finite height,  $\tilde{H}$ , which is set by the electroneutrality condition (3.11), i.e.  $\tilde{H} = N\Xi/\xi$ . In order to mimic the thermodynamic limit and reduce the finite-size effects due to the finiteness of the cylinder height, I apply periodic boundary conditions in  $z$  direction (parallel to the cylinder axis) by replicating the main simulation box infinitely many times in that direction. The long-range character of the Coulomb interaction in such a periodic system leads to summation of infinite series over all periodic images. These series are not generally convergent, but in an electroneutral system, the divergencies cancel and the series can be converted to fast-converging series. I use the summation techniques due to Lekner [110] and Sperb [111], which are utilized for the one-dimensionally periodic system considered here—see Appendix D.1 (similar methods are developed in Ref. [112]). Finally in order to obtain reliable values for the error-bars, the standard block-averaging scheme is used [113]. The simulations typically run for  $\sim 1.1 \times 10^6$  Monte-Carlo steps per particle with  $\sim 10^5$  steps used for the equilibration purpose.

## 3.6 Simulation results in 3D

### 3.6.1 Overall behavior in the infinite-system-size limit

#### Distribution of counterions

I start by demonstrating the results for the distribution of counterions as generated by the centrifugal sampling method. In Figure 3.2, typical simulation snapshots are shown together with the counterionic density profile for small coupling parameter  $\Xi = 0.1$ . Counterion distribution is shown for large ( $\Delta = 100$ ), intermediate ( $\Delta = 25$ ) and small ( $\Delta = 10$ ) lateral extension parameter. The counterion-condensation transition is clearly reproduced for large  $\Delta$  (Figure 3.2a): counterions are “de-condensed” and gather at the outer boundary at small Manning parameter (shown for  $\xi = 0.7$ ), while they partially “condense” and accumulate near the cylinder surface for large Manning parameter (shown for  $\xi = 2$ ). The Manning parameter  $\xi = 1$ , as seen, represents an intermediate situation. This trend is demonstrated on a quantitative level by the radial density profile of counterions  $\tilde{\rho}(\tilde{r})$  (Figure 3.2c, main set), which tends to zero by decreasing  $\xi$  down to about unity. Note that relatively large fluctuations occur at low  $\xi$  making  $\tilde{\rho}(\tilde{r})$  an inconvenient quantity to precisely locate the critical value  $\xi_c$ , which will be considered later. The data moreover follow the mean-field PB density prediction, Eq. (3.27), shown by solid curves, as expected since the chosen coupling parameter is small.

The transition regime at intermediate  $\xi$  exhibits strong finite-size effects. As may be seen from the snapshots in Figure 3.2b, the de-condensation process at  $\xi = 1$  is strongly suppressed for small logarithmic sizes  $\Delta = \ln(D/R) = 10$  and 25. The corresponding density profiles (inset of Figure 3.2c) indicate a sizable accumulation of counterions near the cylinder

surface, which is washed away only by taking a sufficiently large  $\Delta$ . Such finite-size effects at low  $\xi$  are also observed in previous numerical studies, which have devised simulations in linear scale and thus considered only small confinement volumes per polymer (typically  $\Delta < 10$ ) [75, 77, 106, 107, 108]. In some studies [114], these effects have been interpreted as an evidence for counterion condensation at *small*  $\xi$ , leading to the incorrect conclusion that no condensation transition exists.

### Condensed fraction of counterions

The preceding results for large  $\xi$  exhibit a counterionic density profile that extends continuously from the cylinder surface to larger distances. This indicates that making a distinction between two layers of condensed and de-condensed counterions, in the sense of two-fluid models frequently used in literature [20, 39, 56, 57, 58, 59, 60, 61, 80, 82, 83, 84, 85, 86, 91, 92], requires a criterion.

The two-fluid description predicts a fraction of

$$\alpha_M = \begin{cases} 0 & \xi \leq 1 \\ 1 - 1/\xi & \xi \geq 1 \end{cases} \quad (3.71)$$

of counterions to reside in the condensed layer (which is considered as a layer with small thickness at the polymer surface), when the infinite-dilution limit is reached. Previous studies [62, 63, 64, 66, 75, 94] show that the Manning condensed fraction,  $\alpha_M$ , may also be identified systematically within the Poisson-Boltzmann theory by employing an *inflection-point criterion* [75, 94]. This can be demonstrated using the PB cumulative density (the number of counterions inside a cylindrical region of radius  $r$ ),  $n_{\text{PB}}(r)$ , obtained as

$$\frac{n_{\text{PB}}(r)}{N} = \frac{2\pi H}{N} \int_R^r r' dr' \rho_{\text{PB}}(r') = \frac{1}{\xi} \times \begin{cases} (\xi - 1) - \beta \coth \left[ \beta y + \coth^{-1} \frac{\xi - 1}{\beta} \right] & \xi \leq \Lambda_{\text{AF}}, \\ (\xi - 1) - \beta \cot \left[ \beta y + \cot^{-1} \frac{\xi - 1}{\beta} \right] & \xi \geq \Lambda_{\text{AF}}, \end{cases} \quad (3.72)$$

using Eq. (3.27). For  $\xi \geq \Lambda_{\text{AF}}$ ,  $n_{\text{PB}}(r)$  exhibits an inflection point at a radial distance  $r_*$  when plotted as a function of  $y = \ln(r/R)$  [75]. One can show that for  $\Delta \rightarrow \infty$ , only the fraction of counterions, that lie within the cylindrical region  $r \leq r_*$ , remains associated with the cylinder and tends to the Manning condensed fraction, i.e.

$$\frac{n_{\text{PB}}(r_*)}{N} \rightarrow \alpha_M. \quad (3.73)$$

In other words, only this fraction of counterions contribute to the asymptotic density profile and the rest ( $1/\xi$  of all) is pushed to infinity (Appendix C.6).

The simulation results for the cumulative density as a function of the logarithmic radial distance  $y = \ln(\tilde{r}/\tilde{R})$  are shown in Figure 3.3 for various Manning parameters (solid and dot-dashed curves). Here I have chosen a very large lateral extension parameter  $\Delta = \ln(D/R) = 300$ , which exhibits the concept of condensed fraction more clearly. The data show an inflection point, which is located approximately at  $y_* = \ln(r_*/R) \simeq \Delta/2$  for large  $\xi$  (for small  $\xi \rightarrow 1$ , the location of the inflection point,  $r_*$ , tends to  $R$ —see Appendix C.3). The rapid increase of  $n(\tilde{r})$  at small ( $r \sim R$ ) and at large distances ( $r \sim D$ ) reflects the two counterion-populated regions at the inner and outer boundaries, which are separated by an extended

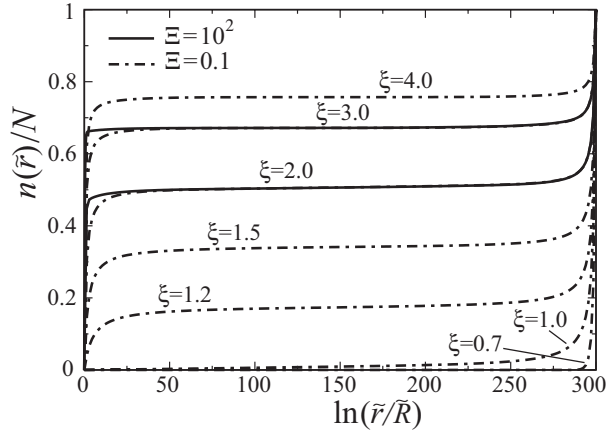


Figure 3.3: Cumulative density,  $n(\tilde{r})$ , per total number  $N$ , of counterions as a function of the logarithmic distance from the charged cylinder,  $\ln(\tilde{r}/\tilde{R})$ . The dot-dashed curves are simulation results for  $\Xi = 0.1$ ,  $N = 70$ , and  $\Delta = 300$  and for various Manning parameters as shown on the graph. These curves also closely represent the PB prediction (3.72), which are not explicitly shown. The solid curves show the simulation data for the large coupling parameter  $\Xi = 10^2$  and for  $\xi = 3.0$  and  $\xi = 2.0$ .

plateau (compare with Figure 3.2). For small  $\Delta$ , the inflection point has a non-vanishing slope and the two regions are not quite separated (data not shown) [75, 91].

Using the inflection-point criterion, the condensed fraction,  $\alpha$ , may be estimated as  $\alpha = n(r_*)/N$  [75], which roughly corresponds to the plateau level in Figure 3.3. Simulation results are shown in Figure 3.4 for large  $\Delta = 300$ . Let us first consider the case of a small coupling parameter  $\Xi = 0.1$ , where the simulated cumulative density,  $n(\tilde{r})$  (dot-dashed curves in Figure 3.3), closely follows the PB prediction (3.72) (PB curves are not explicitly shown). The calculated condensed fraction (diamonds in Figure 3.4) agrees already quite well (within  $< 1\%$ ) with the Manning or PB limiting value  $\alpha_M$  (solid curve in Figure 3.4).

An important question is whether the form of the cumulative density profile,  $n(\tilde{r})$ , and the condensed fraction are influenced by electrostatic correlations for increasing coupling parameter  $\Xi$ . In Figure 3.3, I show  $n(\tilde{r})$  from the simulations for  $\Xi = 10^2$  and for two values of Manning parameter  $\xi = 2.0$  and  $3.0$  (solid curves). This coupling strength generally falls into the strong-coupling regime for charged systems, where electrostatic correlations are expected to matter [35, 54, 55] (note that DNA with trivalent counterions represents  $\Xi \sim 10^2$ , but with a larger  $\xi \sim 12$ ). As seen,  $n(\tilde{r})$  shows a more rapid increase at small distances from the cylinder (condensed region) indicating a stronger accumulation of counterions near the surface. This trend is also observed in previous simulations [75, 107, 106, 108] and in experiments with multivalent counterions [115], and will be analyzed in more detail later in this section.

However, in contrast to previous conclusions (obtained based on small values of  $\Delta$ ) [75, 91], the aforementioned behavior for large  $\Xi$  does not imply a larger condensed fraction as defined within the inflection-point criterion. Since as seen in Figure 3.3, the *large-distance* behavior of the density profile is not influenced by electrostatic correlations, and so remains the condensed fraction (plateau level) unaffected for increasing coupling strength (inset of Figure 3.4). This result can be appreciated only when the asymptotic behavior for  $\Delta \gg 1$  is considered.

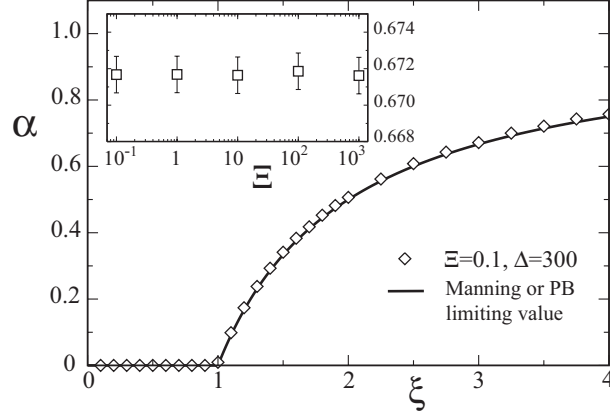


Figure 3.4: Main set: Simulated condensed fraction of counterions,  $\alpha$ , as defined via the inflection-point criterion (see the text), as a function of Manning parameter,  $\xi$ , for  $\Xi = 0.1$  (diamonds). Solid curve displays Manning (or the PB) limiting value,  $\alpha_M$ , for  $\Delta = \ln(D/R) \rightarrow \infty$ ; see Eq. (3.71). Inset: Condensed fraction as a function of the coupling parameter,  $\Xi$ , for  $\xi = 3.0$ . These data are obtained for  $\Delta = 300$  and  $N = 70$ .

### The order parameters $S_n$

The  $n$ -th-order inverse moment of the counterionic density profile may be calculated numerically using

$$S_n = \frac{1}{N} \sum_{i=1}^N \overline{\tilde{r}_i^{-n}} \quad (3.74)$$

for  $n > 0$ , where  $\tilde{r}_i$  is the radial distance of the  $i$ -th counterion from the cylinder axis and the bar sign denotes the Monte-Carlo time average after proper equilibration of the system. The overall behavior is shown in Figure 3.5 for  $S_1$  as a function of Manning parameter,  $\xi$ . Recall that a vanishing order parameter,  $S_1$ , indicates the complete de-condensation of counterions, while a finite  $S_1$  reflects a finite degree of counterion binding to the charged cylinder (corresponding to a finite localization length  $\sim 1/S_1$ ).

As seen from the figure, de-condensation can occur in all relevant regimes of the coupling parameter  $\Xi$ . For large Manning parameter, electrostatic coupling effects become important and shift the order parameter to larger values exhibiting a crossover from the mean-field prediction (solid curve), which is verified for small  $\Xi < 1$ , to the strong-coupling prediction (dashed curve) at very large values of  $\Xi$  [35, 43, 46]. The mean-field result follows from Eq. (3.40) and the strong-coupling prediction is obtained using Eq. (3.66). As seen, in the transition regime  $\xi \sim 1$ , the order parameter data remain close to the mean-field curve and deviate from the SC prediction. A close examination of correlation effects as well as finite-size effects in this region is quite important in determining the scaling behavior and will be considered later. Here I will concentrate on the correlation-induced crossover behavior in the condensation phase.

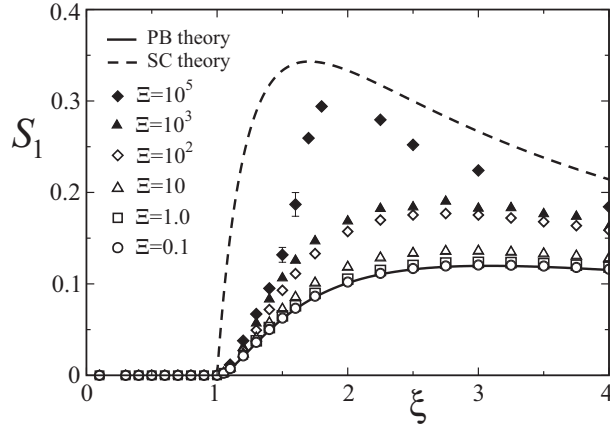


Figure 3.5: Simulation data for the order parameter  $S_1 = \langle 1/\tilde{r} \rangle$  as a function of Manning parameter,  $\xi$ , for various coupling parameters  $\Xi = 0.1$  up to  $10^5$  as indicated on the graph. The mean-field PB and the strong-coupling predictions are calculated from Eqs. (3.40) and (3.66) (solid and dashed curves respectively). The lateral extension parameter is  $\Delta = 300$  and the number of counterions is  $N = 200$  for  $\Xi = 0.1$ ,  $N = 50$  for  $\Xi = 10^5$ , and  $N = 70$  for other coupling parameters.

### Electrostatic correlations at surface and for large $\xi$

In Figure 3.6, I plot the simulated radial density profile of counterions,  $\tilde{\rho}(\tilde{r})$ , for  $\xi = 3.0$  and consider several different coupling parameters. In agreement with the preceding results, the counterionic density in the immediate vicinity of the charged cylinder increases for increasing  $\Xi$  exhibiting large deviations from the mean-field prediction (see Ref. [116] for a similar trend at charged plates). For a given surface charge density  $\sigma_s$ , the observed trend is predicted, e.g., for increasing counterion valency,  $q$ , since the coupling parameter scales as  $\Xi \sim q^3$  (Eq. (3.8)). The crossover from the mean-field PB prediction (solid curve) to the strong-coupling prediction (dashed curve) appears to be quite weak, in agreement with the situation observed for counterions at planar charged walls [44, 46]. These limiting profiles are calculated from Eqs. (3.27) and (3.62) respectively, and both exhibit an *algebraic* decay with the radial distance,  $\tilde{r}$ . But the SC profile shows a faster decay and thus a more compact counterion layer near the surface at large coupling strength (compare Eqs. (3.34) and (3.64)).

An interesting point is that the simulated density at contact with the cylinder shows a more rapid increase when the coupling parameter increases from  $\Xi = 10$  to  $\Xi = 100$  as compared with other ranges of  $\Xi$  (Figure 3.6). This is in fact accompanied by the formation of correlation holes around counterions near the surface as shown below.

In order to examine counterion-counterion correlations at the surface, I consider the one-dimensional pair distribution of counterions,  $g_{1D}(\tilde{z})$ , which measures the probability of finding two counterions lined-up along  $z$ -axis (i.e. along the cylinder axis with equal azimuthal angles  $\phi$ ) at a distance  $\tilde{z}$  from each other. In Figure 3.7, I plot the unnormalized pair distribution function defined via

$$g_{1D}(\tilde{z}) \equiv \frac{1}{N} \sum'_{i \neq j} \left\langle \delta(\tilde{z}_i - \tilde{z}_j - \tilde{z}) \delta(\phi_i - \phi_j) \right\rangle, \quad (3.75)$$

where the prime mark indicates that the sum runs only over counterions at the surface (defined

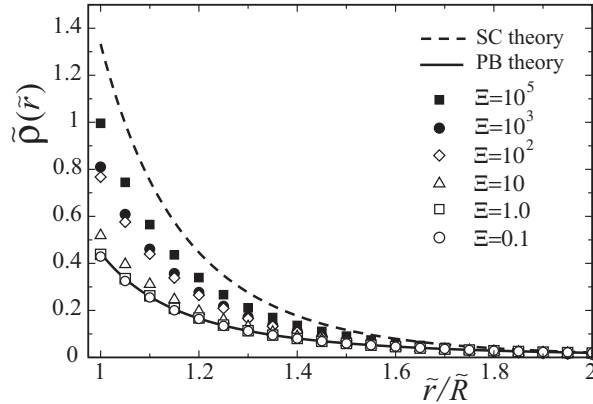


Figure 3.6: Radial density of counterions in rescaled units,  $\tilde{\rho}(\tilde{r}) = \rho(r)/(2\pi\ell_B\sigma_s^2)$ , as a function of the (linear) distance from the cylinder axis for Manning parameter  $\xi = 3.0$  and various coupling parameters ( $\Xi = 0.1$  up to  $10^5$ ) as shown on the graph. Here  $\Delta = 300$  and the number of counterions is  $N = 50$  for  $\Xi = 10^5$ , and  $N = 70$  for other values of  $\Xi$ . The mean-field (solid curve) and the strong-coupling (dashed curve) predictions are obtained from Eqs. (3.27) and (3.62), which, for  $\Delta = 300$ , roughly coincide with the asymptotic expressions (3.34) and (3.64).

in the simulations as counterions residing in a shell of thickness about the Gouy-Chapman length,  $\mu$ , around the cylinder). At small coupling parameter ( $\Xi = 10$ , cross symbols), the pair distribution function only shows a very weak depletion zone at small distances along the cylinder axis. For larger values of  $\Xi$ , one observes a pronounced correlation hole at small distances around counterions, where the distribution function vanishes over a finite range. This correlation hole develops in the range of coupling parameters  $10 < \Xi < 100$ , which marks the crossover regime between the mean-field and the strong-coupling regime (compare cross symbols and filled triangle-ups) [46]. The correlation hole appears only for sufficiently large Manning parameter  $\xi$  (large enough number of condensed counterions) and is distinguishable in the present simulations for  $\xi > 1.2$ .

The small-separation correlation hole is followed by an oscillatory behavior for elevated  $\xi$  indicative of a short-ranged liquid-like order among counterions line-up along the cylinder axis (distinguishable from the data for  $\xi > 2.0$  in the large-coupling regime  $\Xi > 100$ ). The location of the first peak of  $g_{1D}$  gives a rough measure of the typical distance between lined-up counterions,  $a_z$ , at the cylinder surface. This distance is set by the local electroneutrality condition  $a_z\tau = q$ . In rescaled units, one obtains

$$\tilde{a}_z \equiv \frac{a_z}{\mu} = \frac{\Xi}{\xi}, \quad (3.76)$$

from Eqs. (3.5), (3.6) and (3.8), which is used to rescale the horizontal axis of the graph in Figure 3.7.

Note that the correlation hole size increases with the coupling parameter and thus counterions at the surface become highly isolated, reflecting dominate single-particle contributions for  $\Xi \gg 1$  [43, 46]. In fact, as discussed in Chapter 2, the single-particle form of the SC theory (obtained formally for  $\Xi \rightarrow \infty$ ) is a direct consequence of large correlation hole size around counterions at the surface [35, 43, 46, 54, 55]. Clearly, for the counterion-cylinder system,

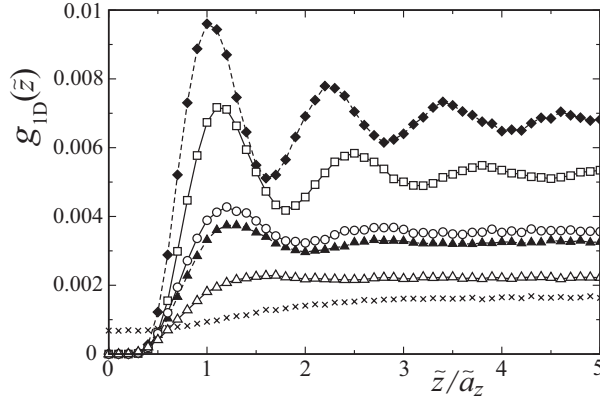


Figure 3.7: The one-dimensional pair distribution function of counterions at contact with cylinder as defined in Eq. (3.75). Symbols show simulation data for  $\Xi = 10^5$  and  $\xi = 4.0$  (filled diamonds),  $\Xi = 10^3$  and  $\xi = 2.0, 3.0$  and  $4.0$  (open symbols from bottom to top), and for coupling parameters  $\Xi = 10$  and  $\Xi = 100$  with Manning parameter  $\xi = 3.0$  (cross symbols and filled triangle-ups respectively).

this can be the case only for sufficiently large Manning parameter, where a sizable fraction of counterions can gather near the surface. Consequently in this regime, the data tend to the strong-coupling predictions for elevated  $\Xi$  (Figures 3.5 and 3.6) as also verified in the simulations of charged plates, where all counterions are bound to the surface [46], and two charged cylinders with large  $\xi$  [54, 55]. This also explains why the SC theory, though being able to reproduce the CCT on a qualitative level, fails to capture the quantitative features *near the critical point* (except for the value of the critical Manning parameter), where counterion are mostly de-condensed.

### 3.6.2 Critical Manning parameter $\xi_c$

I will now consider the behavior of counterions near the critical point and begin with determining the precise location of the critical Manning parameter,  $\xi_c$ .

To this end, I shall employ a procedure similar to the method of locating the transition temperature in bulk critical phenomena [101, 117, 121]. Namely, one expects that the transition point is reflected by a singular behavior in thermodynamic quantities such as energy or heat capacity as already indicated by the mean-field results obtained in Section 3.3.3. The mean (internal) energy,  $E_N$ , and the excess heat capacity,  $C_N$ , may be obtained directly from the simulations and in rescaled units as

$$\tilde{E} = \frac{E_N}{Nk_B T} = \left\langle \frac{\mathcal{H}_N}{Nk_B T} \right\rangle, \quad (3.77)$$

$$\tilde{C} = \frac{C_N}{Nk_B} = N \left\langle \left( \frac{\delta \mathcal{H}_N}{Nk_B T} \right)^2 \right\rangle, \quad (3.78)$$

where the configurational Hamiltonian  $\mathcal{H}_N$  is defined through Eq. (3.10) and  $\delta \mathcal{H}_N = \mathcal{H}_N - \langle \mathcal{H}_N \rangle$ .

Simulation results for the rescaled energy,  $\tilde{E}$ , and the rescaled excess heat capacity,  $\tilde{C}$ , in Figure 3.8 (symbols) show a non-monotonic behavior as a function of  $\xi$ . The energy develops a

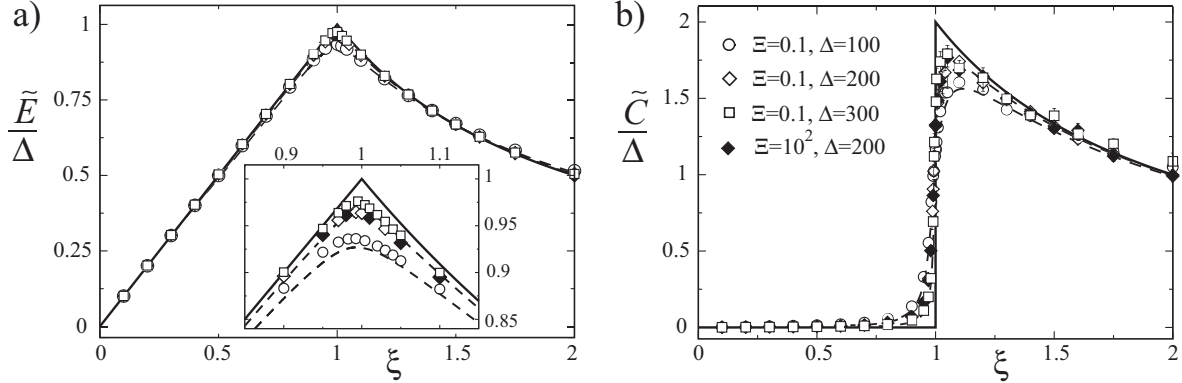


Figure 3.8: a) The rescaled internal energy,  $\tilde{E} = E_N/(Nk_B T)$  and b) the rescaled excess heat capacity,  $\tilde{C} = C_N/(Nk_B)$ , of the counterion-cylinder system as a function of Manning parameter,  $\xi$ . Open symbols show the data for small coupling parameter  $\Xi = 0.1$  and for lateral extension parameters  $\Delta = 100, 200$  and  $300$  as indicated on the graph. Filled symbols are the data for large coupling  $\Xi = 10^2$  and  $\Delta = 200$ . Here number of counterions is  $N = 100$ . Solid curves show the asymptotic PB prediction for  $\Delta \rightarrow \infty$ , Eqs. (3.60) and (3.61). Dashed curves are the full PB result for  $\Delta = 100$  and  $300$  (from bottom to top), which are calculated numerically using Eqs. (3.58) and (3.80). The inset shows a closer view of the energy peak.

pronounced peak and the heat capacity exhibits a jump at intermediate Manning parameters, which become singular for  $\Delta$  increasing to infinity. The general behavior of energy and heat capacity can be understood using simple arguments as follows.

For sufficiently small  $\xi$ , counterions are all unbound and the electrostatic potential in space is roughly given by the bare potential of the charged cylinder, i.e.  $\psi(\tilde{r}) \simeq 2\xi \ln(\tilde{r}/\tilde{R})$ . This yields the rescaled internal energy,  $\tilde{E}$ , (via integrating over the square electric field, see Eq. (3.58)) as

$$\tilde{E} = \frac{1}{4\xi} \int_{\tilde{R}}^{\tilde{D}} \tilde{r} d\tilde{r} \left( \frac{d\psi}{d\tilde{r}} \right)^2 \simeq \xi \Delta \quad (3.79)$$

for  $\Delta = \ln(D/R) \gg 1$ . Intuitively, this result may be obtained also by assuming that counterions experience the potential of the cylinder at the outer boundary; thus one simply has  $\tilde{E} \simeq \psi(\tilde{D})/2 \simeq \xi \Delta$ , which explains the linear increase of the left tail of the energy curve with both  $\xi$  and  $\Delta$  (Figure 3.8a). Now using the following thermodynamic relation

$$\xi \frac{\partial \tilde{E}}{\partial \xi} = \tilde{E} - \tilde{C}, \quad (3.80)$$

the excess heat capacity is obtained to vanish in the de-condensation regime, i.e.  $\tilde{C} \simeq 0$  (Figure 3.8b). Hence, the heat capacity reduces to that of an ideal gas of particles.

For large  $\xi$ , the electrostatic potential of the cylinder is screened due to counterionic binding. If one estimates the screened electrostatic potential of the cylinder as  $\psi(\tilde{r}) \simeq 2 \ln(\tilde{r}/\tilde{R})$ , which can be verified systematically within the PB theory [38, 105], one obtains the energy and the heat capacity as

$$\tilde{E} \simeq \Delta/\xi \quad \text{and} \quad \tilde{C} \simeq 2\Delta/\xi. \quad (3.81)$$



These results may also be obtained by noting that only the fraction  $1/\xi$  of de-condensed counterions (Section 3.6.1) contributes to the energy on the leading order; thus  $\tilde{E} \simeq \psi(\tilde{D})/(2\xi) \simeq \Delta/\xi$ . The above asymptotic estimates in fact coincide with the asymptotic ( $\Delta \rightarrow \infty$ ) PB results (3.60) and (3.61), which are shown by solid curves in Figure 3.8.

The preceding considerations demonstrate that the non-monotonic behavior of the energy and excess heat capacity results directly from the screening effect due to the condensation of counterions as  $\xi$  increases. Hence, the singular peaks emerging in both quantities reflect the onset of the counterion-condensation transition,  $\xi_c$ , which occurs in the thermodynamic infinite-system-size limit  $N \rightarrow \infty$  and  $\Delta \rightarrow \infty$ . Within the PB theory (solid and dashed curves in Figure 3.8), the location of the peak of energy,  $\xi_*^{E,\text{PB}}(N, \Delta)$ , tends to the mean-field threshold  $\xi_c^{\text{PB}} = 1$  from *below* as  $\Delta$  increases obeying the finite-size-scaling relation

$$\xi_c^{\text{PB}} - \xi_*^{E,\text{PB}}(\Delta) \simeq \frac{1}{\Delta}, \quad (3.82)$$

which is obtained using the full PB energy (3.58). On the other hand, the location of the peak of the PB heat capacity approaches  $\xi_c^{\text{PB}}$  from *above*.

I locate the critical point from the asymptotic behavior of the energy peak,  $\xi_*^E$ , as  $N$  and  $\Delta$  increase. (The heat capacity peak is found to be located further away from the critical point than the energy peak, resembling the well-known behavior of the heat capacity peak in finite Magnetic systems [117], which makes it inconvenient for determining the critical point). In Figure 3.9, I show the simulation results for  $\xi_*^E$  (symbols) as a function of  $\Delta^{-1}$  for  $\Xi = 0.1$  and for various number of particles (main set). These data are obtained using the thermodynamic relation (3.80), which allows us to calculate the first derivative of the energy,  $\partial\tilde{E}/\partial\xi$ , including its error-bars, directly from the energy and the heat capacity data without referring to numerical differentiation methods which typically generate large errors near the peak. As seen, for increasing  $N$ , the data converge to and closely follow the mean-field prediction (solid curve) within the estimated error-bars; for  $N > 100$ ,  $\xi_*^E$  lies within about 1% of the PB threshold  $\xi_c^{\text{PB}} = 1$ . Since in the simulations I have used  $\Delta \leq 300$ , the behavior of  $\xi_*^E$  for very small  $\Delta^{-1} \rightarrow 0$  is not obtained, nevertheless, the excellent convergence of the data for  $\Xi = 0.1$  to the PB prediction gives an accurate estimate for the critical Manning parameter as

$$\xi_c = 1.00 \pm 0.002. \quad (3.83)$$

The results for larger values of the coupling parameter,  $\Xi$ , in the inset of Figure 3.9 show that the location of the energy peak does not vary with the coupling parameter. Therefore, the critical Manning parameter is found to be *universal* and given by the mean-field value  $\xi_c = 1.0$ . Recall that the same threshold is obtained within the Onsager instability and the strong-coupling analysis (Sections 3.2.2 and 3.4).

Another important result is that the CCT is not associated with a diverging singularity, in contrast to the Onsager instability prediction [39]. But, the energy at any finite value of  $\xi$ , and also the heat capacity for  $\xi > 1$ , tend to infinity (as  $\sim \Delta$ ) when the lateral extension parameter,  $\Delta$ , increases to infinity, which, as illustrated before, reflects the logarithmic divergency of the effective electrostatic potential in a charged cylindrical system. The CCT, however, exhibits a *universal* discontinuous jump for the excess heat capacity at  $\xi_c$ , and thus indicates a second-order phase transition (Figure 3.8).

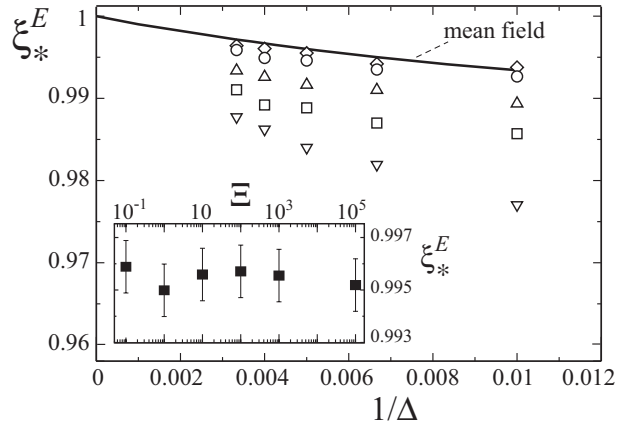


Figure 3.9: Main set: Location of the peak of energy,  $\xi_*^E$ , as a function of the inverse lateral extension parameter,  $1/\Delta = 1/\ln(D/R)$ . Open symbols are simulation results for small coupling parameter  $\Xi = 0.1$  and for various number of counterions (from bottom):  $N = 25$  (triangle-downs), 50 (squares), 100 (triangle-ups), 200 (circles) and 300 (diamonds). Solid curve shows the mean-field PB prediction for the peak location as obtained by numerical evaluation of the full PB energy, Eq. (3.58). Inset: Location of the energy peak as a function of the coupling parameter,  $\Xi$ , for  $N = 200$  and  $\Delta = 300$ .

### 3.6.3 Scale-invariance near the critical point

Now that the precise location of the critical Manning parameter is determined, a finite-size analysis, similar to what I presented within the mean-field theory, may be used to determine the near-threshold properties of the CCT order parameters from the simulation data.

Note that in the simulations, finite size effects arise both from the finiteness of the system size (via the lateral extension parameter,  $\Delta$ ), and also from the finiteness of the number of counterions,  $N$ ; the latter being related to the finiteness of the height of the main simulation box  $H = Nq/\tau$  (Section 3.5), which has a sizable influence on the transition, although the implemented periodic boundary condition already reduces its effects. In what follows, I present the numerical evidence for scaling relations with respect to both  $N$  and  $\Delta$ . The asymptotic behavior for increasing  $N$  and  $\Delta$  to infinity provides us with the scaling behavior with respect to the reduced Manning parameter,  $\zeta$  (or the reduced temperature,  $t$ ), which characterizes the CCT universality class in 3D.

#### Finite-size effects near $\xi_c$

In Figure 3.10 (main set), I show the order parameter  $S_1$  as a function of  $1/\Delta$  and in the vicinity of the critical point  $\xi_c = 1$  (number of counterions  $N = 100$  is fixed).  $S_1$ , which represents the mean inverse localization length of counterions, gradually decreases with decreasing  $1/\Delta$  as they become gradually more de-condensed, but for Manning parameters as large as  $\xi = 1.05$  (open circles), the data quickly saturate to a finite value as  $\Delta \rightarrow \infty$ . For sufficiently small Manning parameter (e.g.  $\xi < 0.97$ ), on the other hand,  $S_1$  converges to zero. In the vicinity of the threshold ( $\xi = 1$ , diamonds), a non-saturating behavior is found suggesting a power-law decay as  $S_1 \sim \Delta^{-\gamma}$ , where  $\gamma > 0$ . As seen, the data at  $\xi = 1$  roughly coincide for both small coupling ( $\Xi = 0.1$ , open diamonds) and large coupling ( $\Xi = 10^2$ , filled diamonds)

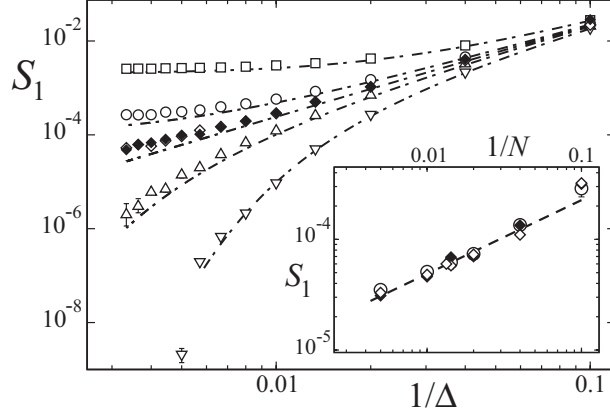


Figure 3.10: Main set: Order parameter  $S_1 = \langle 1/\tilde{r} \rangle$  as a function of the inverse lateral extension parameter  $1/\Delta$ . Open symbols are data for  $\Xi = 0.1$  and Manning parameters (from top):  $\xi = 1.05$  (squares),  $1.01$  (circles),  $1.0$  (open diamonds),  $0.99$  (triangle-ups) and  $0.97$  (triangle-downs). Filled diamonds are the data for large coupling parameter  $\Xi = 10^2$  and  $\xi = 1.0$ . Number of counterions  $N = 100$  is fixed. Dot-dashed curves are the full PB prediction, Eq. (3.40), for the corresponding  $\xi$ . Inset:  $S_1$  as a function of the inverse number of counterions  $1/N$  for  $\xi = 1.0$  and for the coupling parameters  $\Xi = 0.1$  (open diamonds),  $10^2$  (filled diamonds) and  $10^3$  (open circles). Dashed line shows the power-law exponent  $2/3$ . Here  $\Delta = 300$ .

indicating that electrostatic correlations do not influence the scaling behavior (see below). There still remain non-negligible deviations between the simulation data at the critical point (diamonds) and the PB power-law prediction (3.45) with  $\gamma_{\text{PB}} = 2$ , which is shown in the figure by a straight dot-dashed line. These deviations arise from the finiteness of the number of particles.

Interestingly, the data obtained for various number of counterions,  $N$  (at fixed lateral extension parameter,  $\Delta$ ), also indicate a power-law decay near the critical point, i.e. as  $S_1 \sim N^{-\nu}$ , where  $\nu > 0$ . This is shown in the inset of Figure 3.10, where the scaling exponent  $\nu$  appears to be about  $2/3$  (represented by a dashed line). In fact, for sufficiently large  $N$ , the data deviate from this power-law behavior since finite-size effects due to lateral extension of the system,  $\Delta$ , are simultaneously present. Thus in order to determine the exponents  $\gamma$  and  $\nu$ , a more systematic approach is required, which should incorporate both lateral-size and ion-number effects.

### Generalized finite-size-scaling relations

In brief, the simulation data suggest that at the critical point ( $\zeta = 1 - \xi_c/\xi = 0$ ) and for a bounded system (finite  $\Delta$ ) in the thermodynamic limit  $N \rightarrow \infty$ , the order parameter  $S_n(\zeta, \Delta, N) = \langle 1/\tilde{r}^n \rangle$  decays as

$$S_n(0, \Delta, \infty) \sim \Delta^{-\gamma}, \quad (3.84)$$

while in an unbounded system ( $\Delta \rightarrow \infty$ ) and for finite  $N$ , one expects a power-law decay as

$$S_n(0, \infty, N) \sim N^{-\nu}. \quad (3.85)$$

In thermodynamic infinite-system-size limit ( $\Delta \rightarrow \infty$  and  $N \rightarrow \infty$ ), the true critical transition sets in with  $S_n(\zeta < 0, \infty, \infty) = 0$ , and one anticipates the scaling behavior with the reduced Manning  $\zeta$  as

$$S_n(\zeta, \infty, \infty) \sim \zeta^\chi \quad (3.86)$$

in a sufficiently small neighborhood *above*  $\xi_c = 1$ .

These scaling relations may all be deduced from a general finite-size-scaling hypothesis for  $S_n$ , i.e. assuming that  $S_n(\zeta, \Delta, N)$  takes a *homogeneous scale-invariant* form with respect to its arguments in the vicinity of the transition point,  $\xi_c$ , when both  $N$  and  $\Delta$  are sufficiently large. In other words, for any positive number  $\lambda > 0$ ,

$$S_n(\lambda\zeta, \lambda^{-b}\Delta, \lambda^{-c}N) = \lambda^a S_n(\zeta, \Delta, N), \quad (3.87)$$

where  $a, b$  and  $c$  are a new set of exponents associated with  $\zeta, \Delta$  and  $N$  respectively. The above relation implies that when the reduced Manning parameter,  $\zeta$ , is rescaled with a factor  $\lambda$ , the size parameters,  $N$  and  $\Delta$ , can be rescaled such that the order parameter remains invariant up to a scaling prefactor. Finite-size scale-invariance is a common feature in critical phase transitions [101, 118, 119] and provides an accurate tool to estimate the critical exponents in numerical simulations [117, 120, 121, 122]. The exponents in Eq. (3.87) can be calculated directly from MC simulations. These exponents are in fact related to and give the values of the desired critical exponents  $\gamma, \nu$  and  $\chi$ , as will be shown below. Note that the exponents may in general depend on  $n$  (the index of  $S_n$ ), the coupling parameter,  $\Xi$ , or the space dimensionality, which are not explicitly incorporated in the proposed scaling hypothesis, but their influence will be determined later.

Given Eq. (3.87), the following relations are obtained by suitably choosing  $\lambda$ . For  $\lambda = N^{1/c}$ , one finds

$$S_n(\zeta, \Delta, N) = N^{-a/c} \mathcal{C}_n(\zeta N^{1/c}, \Delta N^{-b/c}), \quad (3.88)$$

where  $\mathcal{C}_n(u, v)$  is the scaling function corresponding to a system with both finite  $N$  and  $\Delta$ . The above expression is useful for a system with finite  $N$  in the limit  $\Delta \rightarrow \infty$ . Thus assuming that  $\mathcal{C}_n(u, v)$  exists for  $v = \Delta N^{-b/c} \rightarrow \infty$ , the relation (3.88) reduces to

$$S_n(\zeta, \infty, N) = N^{-a/c} \mathcal{N}_n(\zeta N^{1/c}), \quad (3.89)$$

where the scaling function  $\mathcal{N}_n(u) = \mathcal{C}_n(u, \infty)$ . The critical exponent  $\nu$  follows by considering this relation right at the critical point,  $\zeta = 0$ , i.e.

$$S_n(0, \infty, N) = \mathcal{N}_n(0) N^{-\nu}, \quad (3.90)$$

where  $\nu$  is obtained as

$$\nu = \frac{a}{c}. \quad (3.91)$$

On the other hand, I assume that in the vicinity of (and above) the critical point (i.e. for small but finite  $\zeta$ ),  $S_n(\zeta, \infty, N)$  is only a finite function of the reduced Manning parameter  $\zeta$  when the limit  $N \rightarrow \infty$  is taken. Hence the scaling function  $\mathcal{N}_n(u)$  is required to behave as  $\mathcal{N}_n(u) \sim u^a$  for  $u \rightarrow \infty$ , which yields

$$S_n(\zeta, \infty, \infty) \sim \zeta^a, \quad (3.92)$$

where the critical exponent associated with  $\zeta$  reads

$$\chi = a. \quad (3.93)$$

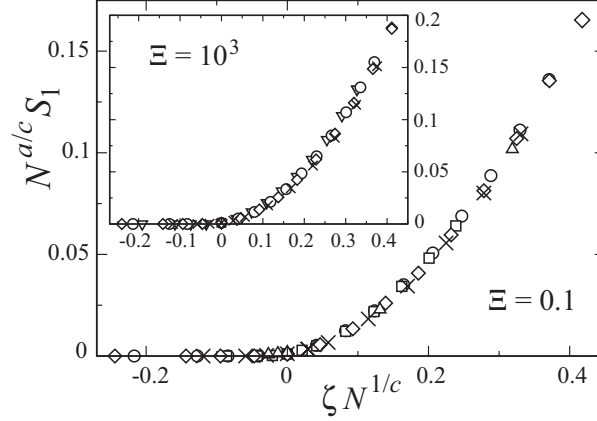


Figure 3.11: Rescaled order parameter,  $N^{a/c} S_1$ , as a function of the rescaled reduced Manning parameter,  $\zeta N^{1/c}$ , in the vicinity of the critical point,  $\xi_c = 1.0$ , and for small and large coupling parameters  $\Xi = 0.1$  (main set) and  $\Xi = 10^3$  (inset). Symbols show data for various number of particles  $N = 50$  (triangle-downs), 70 (circles), 75 (squares), 100 (diamonds), 200 (cross symbols), 300 (triangle-ups), and fixed  $\Delta = 300$ . In these plots, the exponents are chosen as  $a/c = 2/3$  and  $1/c = 1/3$ . Error-bars are smaller than the symbol size.

To determine the critical exponent associated with  $\Delta$  in terms of the exponents  $\{a, b, c\}$ , one needs to consider Eq. (3.87) for  $\lambda = \Delta^{1/b}$ . One thus has

$$S_n(\zeta, \Delta, N) = \Delta^{-a/b} \mathcal{C}'_n(\zeta \Delta^{1/b}, N \Delta^{-c/b}), \quad (3.94)$$

where  $\mathcal{C}'_n(u, v)$  is a new scaling function. This relation is useful for a system with finite  $\Delta$  in the limit  $N \rightarrow \infty$ , where assuming that  $\mathcal{C}'_n(u, v)$  exists, one obtains

$$S_n(\zeta, \Delta, \infty) = \Delta^{-a/b} \mathcal{D}_n(\zeta \Delta^{1/b}) \quad (3.95)$$

with a new scaling function  $\mathcal{D}_n(u) = \mathcal{C}'_n(u, \infty)$ . The critical exponent  $\gamma$  follows by considering this relation right at the critical point,  $\zeta = 0$ , that yields

$$S_n(0, \Delta, \infty) = \mathcal{D}_n(0) \Delta^{-\gamma}, \quad (3.96)$$

where  $\gamma$  reads

$$\gamma = \frac{a}{b}. \quad (3.97)$$

Therefore, one has a complete set of relations (3.91), (3.93) and (3.97) from which the critical scaling exponents  $\gamma$ ,  $\nu$  and  $\chi$  may be obtained using the exponents  $a, b$  and  $c$ .

Equation (3.95) compares directly with the mean-field result, Eq. (3.45), where I showed that  $\gamma_{\text{PB}} = 2$  and  $\chi_{\text{PB}} = 2$ . Note also that the exponent  $\nu$  is not defined within mean-field theory.

### 3.6.4 Critical exponents: the CCT universality class

#### The exponents $\chi$ and $\nu$

In order to verify the generalized finite-size scaling hypothesis (3.87) and estimate the critical exponents numerically, I adopt the standard data-collapse scheme used widely in literature [120, 121, 122].

I begin with the exponents  $\chi$  and  $\nu$  that can be calculated using Eq. (3.88), which involves a scaling function  $\mathcal{C}_n(u, v)$  of two arguments  $u = \zeta N^{1/c}$  and  $v = \Delta N^{-b/c}$ . In the present simulations,  $N$  ranges from 25 up to 300 and  $\Delta$  ranges from 50 up to 300; thus assuming that the exponent  $b/c$  is small, which will be verified later on, one deals with a typically large value for  $v \sim 10 - 10^2$ . Therefore the limiting relation (3.89) is approximately valid and yields

$$N^{a/c} S_n \simeq \mathcal{N}_n(\zeta N^{1/c}). \quad (3.98)$$

Now if the data for  $S_n$  are plotted as function of  $\zeta = 1 - \xi_c/\xi$  for *various*  $N$  (but at fixed sufficiently large  $\Delta$ ), equation (3.98) predicts that by rescaling the reduced Manning parameter  $\zeta$  by the factor  $N^{1/c}$  and the order parameter by the factor  $N^{a/c}$ , all data should collapse onto a single curve. Numerically, this procedure allows to determine the exponents  $a/c$  and  $1/c$  in such a way that the best data collapse is achieved. I show the results in Figure 3.11 for various  $N$  (symbols) and for the coupling parameter  $\Xi = 0.1$  (main set). The collapse of the data onto each other is indeed achieved within the numerical error-bars for the exponents in the range  $1/c \simeq 1/3 \pm 0.05$  and  $a/c \simeq 2/3 \pm 0.1$ . This yields the critical scaling exponents  $\nu$  and  $\chi$  from Eqs. (3.91) and (3.93) as

$$\nu \simeq 2/3 \pm 0.1, \quad (3.99)$$

$$\chi \simeq 2.0 \pm 0.4, \quad (3.100)$$

where the errors are estimated using the standard error propagation methods. The value obtained for  $\chi$  agrees with the mean-field result, Eq. (3.44).

In order to check whether the exponents vary with the electrostatic coupling parameter,  $\Xi$ , I repeat this procedure for a wide of range of values for  $\Xi$ . I find the same values for the exponents for coupling parameters up to  $\Xi = 10^5$ . For comparison, the results for  $\Xi = 10^3$  are shown in the inset of Figure 3.11, where the data collapse is demonstrated for  $1/c = 1/3$  and  $a/c = 2/3$ .

### The exponent $\gamma$

Given the exponents  $a$  and  $c$  calculated above and making use of the finite-size scaling relation (3.94), one can estimate the exponent  $b$ , and thereby the scaling exponent  $\gamma$ , associated with the lateral extension parameter. In this case, however, the second argument  $v = N\Delta^{-c/b}$  in the scaling function  $\mathcal{C}'_n(u, v)$  defined in Eq. (3.94) may not be considered as large within the present simulations (since as shown below the ratio  $c/b$  is large). But it turns out that the dependence of  $\mathcal{C}'_n(u, v)$  on  $v$  is quite weak such that the finite-size scaling relation (3.95) is approximately valid and can thus give the desired exponent. To examine this latter property of  $\mathcal{C}'_n(u, v)$ , I consider the relation (3.94) right at the threshold Manning parameter ( $\zeta = 0$ ), i.e.

$$S_n(0, \Delta, N) = \Delta^{-a/b} \mathcal{C}'_n(0, N\Delta^{-c/b}). \quad (3.101)$$

In Figure 3.12,  $S_n(0, \Delta, N)$  is plotted as a function of  $\Delta$  in a log-log plot for increasing  $N$  from 70 up to 300 and for  $\Xi = 0.1$ . As clearly seen, the order parameter varies quite weakly with the number of particles, and the variations are already within the error-bars (equal to symbol size) for  $N > 100$ .

Thus multiplying both sides of Eq. (3.95) with  $\Delta^{a/b}$ , one has

$$\Delta^{a/b} S_n \simeq \mathcal{D}_n(\zeta \Delta^{1/b}), \quad (3.102)$$

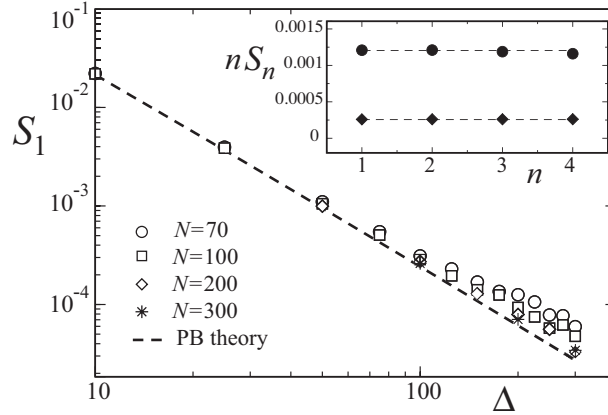


Figure 3.12: Main set: Order parameter  $S_1$  as a function of the lateral extension parameter,  $\Delta$ , for increasing number of counterions from  $N = 70$  up to 300 as indicated on the graph (Manning parameter here is  $\xi = 1.0$  and the coupling parameter  $\Xi = 0.1$ ). Dashed line shows the PB power-law, Eq. (3.45). Inset: Rescaled order parameters  $S_n = \langle \tilde{r}^{-n} \rangle$  as a function of  $n$  for Manning parameters close to the threshold (from top):  $\xi = 1.03$  (filled circles) and  $\xi = 1.01$  (filled diamond). Here the coupling parameter is  $\Xi = 0.1$ , the number of counterions  $N = 100$ , and  $\Delta = 300$ . Error-bars are smaller than the symbol size.

in which the exponent  $a$  is previously determined as  $a = \chi = 2.0 \pm 0.4$ . I thus plot the order parameter  $S_n$  as a function of  $\zeta$  for *various*  $\Delta$  (but at fixed sufficiently large  $N$ ), and rescale both  $S_n$  and  $\zeta$  values with the scaling factors  $\Delta^{a/b}$  and  $\Delta^{1/b}$  respectively; the exponent  $b$  is chosen in such a way that the best data collapse is obtained within the error-bars. The result is shown in Figure 3.13 for  $\Delta^{a/b} S_1$  as a function of  $\zeta \Delta^{1/b}$ , where the coupling parameter is chosen as  $\Xi = 0.1$ . The collapse of the data onto each other is obtained only for the exponent  $1/b$  in the range  $1/b \simeq 1.0 \pm 0.2$ , yielding the critical scaling exponent  $\gamma$  from Eq. (3.97) as

$$\gamma \simeq 2.0 \pm 0.6, \quad (3.103)$$

which agrees with the mean-field exponent, Eq. (3.47). I find the same value for  $\gamma$  by repeating the above procedure for larger coupling parameters. For instance, the results for  $\Xi = 10^5$  are shown in the inset of Figure 3.13, where I have chosen  $1/b = 1.0$ .

Note that the estimated values of  $b$  and  $c$  show that the ratio  $b/c$  is as small as 0.3, which is consistent with the assumption made in using the asymptotic forms (3.89) and (3.95) in the foregoing data-collapse procedure.

As a main result, the present numerical data confirm the existence of characteristic scaling relations associated with the counterion-condensation transition in 3D and show that the values of the critical exponents are *universal*, i.e. independent of the coupling parameter,  $\Xi$ , and agree with the mean-field universality class.

Also, in agreement with mean-field results, the exponents are found to be independent of  $n$ , the index of the order parameters  $S_n = \langle 1/\tilde{r}^n \rangle$ . In fact, I find that the higher-order moments are related to the first-order moment,  $S_1$ , via

$$S_n \simeq \frac{S_1}{n} \quad (3.104)$$

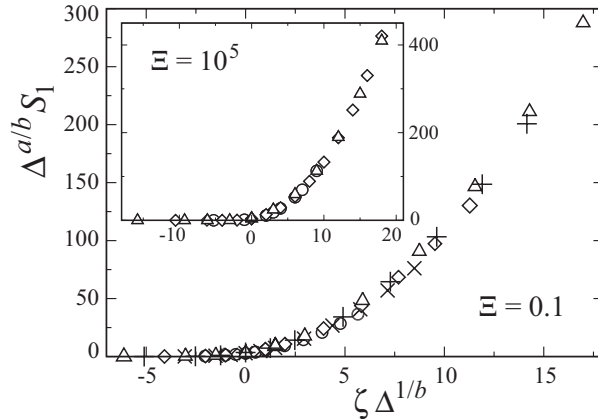


Figure 3.13: Rescaled order parameter,  $\Delta^{a/b} S_1$ , as a function of the rescaled reduced Manning parameter,  $\zeta \Delta^{1/b}$ , in the vicinity of the critical point,  $\xi_c = 1.0$ , and for small and large coupling parameters  $\Xi = 0.1$  (main set) and  $\Xi = 10^5$  (inset). Symbols show data for various lateral extension parameters  $\Delta = 100$  (circles), 150 (cross symbols), 200 (diamonds), 250 (plus symbols) and 300 (triangle-ups). Number of counterions is fixed ( $N = 200$  for the coupling parameter  $\Xi = 0.1$  and  $N = 100$  for  $\Xi = 10^5$ ), and the exponents are here chosen as  $a/b = 2.0$  and  $1/b = 1.0$ . Error-bars are smaller than the symbol size.

in the *vicinity* of the critical point, which indicates that  $nS_n$  is independent of  $n$ , as demonstrated in the inset of Figure 3.12 (compare with the mean-field relation (3.41)).

### 3.7 Conclusion and discussion

In this chapter, I present an extensive numerical analysis of the critical behavior of counterions at a charged cylinder in three spatial dimensions [95, 96]. I also investigate the critical behavior analytically in the asymptotic limits of mean field (Poisson-Boltzmann) and strong coupling.

The counterion-condensation transition (CCT) is regulated by the dimensionless Manning parameter (rescaled inverse temperature),  $\xi = q\ell_B\tau$ , and occurs at a critical threshold  $\xi_c$ , below which counterions completely unbind (de-condense) to infinity, but above  $\xi_c$ , a finite fraction of counterions binds (or condenses) in the vicinity of the charged cylinder. Since the CCT criticality emerges asymptotically in the limit of infinite system size and infinitely many particles, I have employed Monte-Carlo (MC) simulation of a periodic cylindrical cell model in the *logarithmic radial coordinate*, which gives rise to a powerful (centrifugal) sampling method for extremely large lateral system sizes within reasonable equilibration times. This constitutes the key part of the present numerical investigation, since the critical and universal aspects of the CCT within the cell model can only be captured for large *logarithmic* system size  $\Delta = \ln(D/R) \gg 1$  (with  $D$  and  $R$  being the outer boundary and the charged cylinder radii respectively).

As main results, I have determined the precise location of the critical Manning parameter,  $\xi_c$ , the scaling universality class of the CCT and the singular behavior of energy and heat capacity on a systematic level and without suppressing inter-particle correlations. As shown both the mean internal energy and the excess heat capacity become singular at the critical



point. The excess heat capacity, which vanishes in the de-condensation phase, shows a universal discontinuity (jump) at the critical point indicating that the CCT is a second-order transition, as also suggested in a recent mean-field study [89]. In a finite system, these singularities appear in the form of pronounced peaks, the asymptotic behavior of which is used to determine the critical Manning parameter,  $\xi_c$ , in the simulations. On the other hand, the critical scaling exponents associated with the CCT are obtained using a combined finite-ion-number,  $N$ , and finite-size,  $\Delta$ , analysis of the order parameters  $S_n = \langle \tilde{r}^{-n} \rangle$  (with  $\tilde{r} = r/\mu$  being the radial distance from the cylinder axis in units of the Gouy-Chapman length,  $\mu$ ). These order parameters represent the inverse localization length of counterions. For  $\xi < \xi_c$  and in an infinitely large system,  $S_n$  vanishes, but takes a finite value above  $\xi_c$ , which exhibits the scaling relation  $S_n \sim \zeta^\chi$ , where  $\zeta = 1 - \xi_c/\xi$  is the reduced Manning parameter (the reduced temperature) and the exponent  $\chi$  is determined as  $\chi = 2.0 \pm 0.4$  from the simulations. In finite systems,  $S_n$  does not vanish at  $\xi_c$  and displays a power-law decay with increasing size parameters,  $\Delta$  and  $N$ , as  $S_n(\xi = \xi_c) = \Delta^{-\gamma}$  (when number of particles,  $N$ , is fixed) and  $S_n(\xi = \xi_c) = N^{-\nu}$  (when lateral extension parameter,  $\Delta$ , is fixed), where the critical exponents are determined as  $\gamma = 2.0 \pm 0.6$  and  $\nu = 2/3 \pm 0.1$ .

The critical exponents are demonstrated to be universal, i.e. independent of the coupling strength,  $\Xi$  (varied over several decades  $0.1 < \Xi < 10^5$ ), and agree with the values obtained from the mean-field PB theory as  $\chi_{\text{PB}} = 2.0$  and  $\gamma_{\text{PB}} = 2.0$  (note that the exponent  $\nu$  is not defined within mean-field theory). Interestingly, the critical Manning parameter in 3D is also found to be universal and given by the mean-field value  $\xi_c = 1$ . Therefore, in contrast with the typical situation in bulk critical phenomena, the CCT criticality is found to be described by the mean-field universality class in 3D. Correlation effects in fact become important above the critical Manning parameter (in the condensation phase) and lead to strong deviations from mean-field theory and support the strong-coupling predictions characterized by an excessive accumulation of counterions near the cylinder surface, in agreement with previous numerical studies [75, 91, 106, 107, 108] and experiments [115]. An important result is that the large-distance form of the density profile remains unaffected by these correlations and thereby a universal condensed fraction is obtained when the inflection-point criterion is applied.

The rigorous analytical derivation of the critical Manning parameter or the scaling exponents of the CCT in 3D is not yet available and the present study provides the first numerical results for the universal and critical features of this transition in the large-system-size limit. The present predictions for order parameters and thermodynamic quantities can be examined in experiments. In particular, the order parameters may be obtained from the distribution of counterions around charged polymers, which has been directly measured using anomalous scattering techniques [124].

In this study, I have made use of a standard cell model in order to bring out main *universal* aspects of the CCT. It is interesting to examine possible effects due to additional specific factors that exist in realistic situations, namely, the discrete charge pattern of polymers [76, 77, 80, 88, 91, 107, 125], chain flexibility and finite contour length [64, 65, 74, 76, 77, 80, 84, 85, 92, 125, 126] as well as the influence of non-uniform dielectric boundaries [92] on the critical behavior. However, the present results already indicate that short-range effects such as electrostatic correlations do not affect the properties of the system near the critical region ( $\xi \sim \xi_c$ ), since most of counterions are de-condensed and the critical behavior is predominately determined by long-range features.

In this work, I have not investigated the role of additional salt and co-ions, which lead to screening of electrostatic interactions (see, e.g., Refs. [75, 76, 107, 108]). It is known that

the Debye screening length,  $r_s$ , plays the role of an upper bound cut-off (similar to the outer boundary  $D$  in the cell model): the CCT occurs for vanishing salt concentration, i.e. when  $\ln(r_s/R) \rightarrow \infty$  [39, 62, 63, 94]. Thus one can expect similar asymptotic behavior to arise near  $\xi_c = 1$  and within a similar model as used here, when the vanishing-salt limit is approached.

## Chapter 4

# Counterion-Condensation Transition in Two Dimensions

In this chapter, I shall investigate the asymptotic and critical properties of the counterion-cylinder system in two spatial dimensions (2D). In two dimensions, the Coulomb interaction between a pair of point-like particles depends logarithmically on their distance. The 2D counterion-cylinder system is thus equivalent to a 3D system composed of a central charged cylinder and parallel cylindrical “counterions”. This model may be applicable to an experimental system of oriented cationic and anionic polymers such as DNA with polylysine [102].

From a fundamental point of view, the study of such a 2D system is important because the effects of fluctuations typically grow with diminishing dimension [101]. Fluctuations are known to play a significant role near critical phase transitions, and may lead to deviations from mean-field theory below an upper critical dimension. However, as shown in the preceding chapter, the counterion-condensation transition (CCT) at charged cylinders falls into the mean-field universality class in three spatial dimensions: While the regime above the critical Manning parameter  $\xi_c$  (condensation phase) is dominated by correlation effects at elevated electrostatic coupling strength,  $\Xi$ , the critical region itself shows universal scale-invariant and singular features independent of the coupling parameter. It is interesting to determine whether these results will be altered in a lower spatial dimension.

As will be shown using Monte-Carlo simulations [95, 96], the 2D counterion-cylinder system exhibits certain peculiarities that arise due to the long-range logarithmic interactions between particles. Namely, for finite number of counterions, a set of singular points emerge in thermodynamic quantities (as well as in the order parameters) that reflect delocalization events of individual counterions as the Manning parameter varies. For increasing particle number, the singular points tend to merge and eventually in the thermodynamic limit, the 2D results tend to the universal values determined by mean-field theory. Therefore, the striking result in 2D is that the mean-field theory is found to be *exact* for the whole range of Manning parameters (including the critical region) when the number of counterions tends to infinity. I will show that these results can be understood using an approximate analytical theory based on the 2D partition function.

## 4.1 The 2D model

In two dimensions, I shall use an analogue of the cell model described in Chapter 3, which consists of a 2D central charged cylinder (central “disk”) of radius  $R$  confined co-axially and together with its neutralizing point-like counterions in an outer cylinder (outer “ring”) of radius  $D$ . In order to construct the two-dimensional interaction Hamiltonian, I use the fact that the Coulomb interaction between two elementary charges in 2D (the 2D Green’s function) is of the form

$$v(\mathbf{x}) = -\ln |\mathbf{x}|. \quad (4.1)$$

This follows directly from the solution of the 2D Poisson equation for a point charge, that is

$$\nabla^2 v(\mathbf{x}) = -2\pi\delta^2(\mathbf{x}). \quad (4.2)$$

The configurational Hamiltonian of the 2D system may thus be written as

$$\frac{\mathcal{H}_N}{k_B T} = \lambda_c \lambda_r \sum_{i=1}^N \ln \left( \frac{r_i}{R} \right) - \lambda_c^2 \sum_{\langle ij \rangle} \ln \left| \frac{\mathbf{x}_i - \mathbf{x}_j}{R} \right| \quad (4.3)$$

with  $\mathbf{x}_i = (r_i, \phi_i)$  being the position vector of the  $i$ -th counterion (in polar coordinates), and  $\lambda_c$  and  $\lambda_r$  being dimensionless charges of the counterions and the cylinder respectively. The first term gives the counterion-cylinder attraction and the second term gives mutual repulsions between counterions. Clearly, the present 2D model is equivalent to a 3D system comprising an infinitely long central cylinder (of radius  $R$ ) in the presence of mobile *parallel* lines of opposite charge as “counterions”. Using this 3D analogy, the prefactors  $\lambda_r$  and  $\lambda_c$  may be related to the linear charge density of the cylinder and counterion lines respectively.

Taking the logarithmic interaction (4.1) will also ensure that the general form of the field-theoretic representation for the system remains the same as in the 3D case [170], and in particular, the mean-field Poisson-Boltzmann theory, which follows from a saddle-point analysis (Appendix A), is represented exactly by the same equations and results as discussed in Section 3.3.

### 4.1.1 Rescaled representation

In analogy with the 3D system, I shall refer to the dimensionless prefactor of the counterion-cylinder interaction in Eq. (4.3) as the *Manning parameter*, that is

$$\xi = \lambda_c \lambda_r / 2. \quad (4.4)$$

Also the prefactor of the counterion-counterion interaction is defined as the *coupling parameter*

$$\Xi = \lambda_c^2 / 2. \quad (4.5)$$

These definitions can be justified systematically when the Hamiltonian of the system is mapped to an effective field theory, where  $\Xi$  and  $\xi$  formally appear in the same role as in 3D. I shall conventionally rescale the spatial coordinates as  $\tilde{\mathbf{x}} = \mathbf{x} / \mu_{2D}$  using the length scale  $\mu_{2D} \equiv R / \xi$ , which is the 2D analogue of Eq. (3.7).

The Hamiltonian in rescaled units reads

$$\frac{\mathcal{H}_N}{k_B T} = 2\xi \sum_{i=1}^N \ln \left( \frac{\tilde{r}_i}{\tilde{R}} \right) - 2\Xi \sum_{\langle ij \rangle} \ln \left| \frac{\tilde{\mathbf{x}}_i - \tilde{\mathbf{x}}_j}{\tilde{R}} \right|. \quad (4.6)$$

The electroneutrality condition implies  $\lambda_r = N\lambda_c$ , where  $N$  is the number of counterions in the system. This relation may also be written as

$$\xi = N\Xi. \quad (4.7)$$

Thus an important consequence of electroneutrality in 2D is that the coupling parameter and the Manning parameter are related only via the number of counterions. In particular, in the thermodynamic limit  $N \rightarrow \infty$ , the coupling parameter tends to zero,  $\Xi \rightarrow 0$ , suggesting that the mean-field prediction should become exact!

I use a similar simulation method as devised for the 3D system using the transformed coordinates  $(y, \phi)$  with  $y = \ln(\tilde{r}/\tilde{R})$  being the logarithmic radial distance of particles from the central cylinder. As explained in Section 3.5, this transformation leads to the centrifugal sampling method appropriate for equilibration of systems with large lateral extension parameter  $\Delta = \ln(D/R) \gg 1$ , where the critical behavior associated with the CCT emerges. The 2D partition function thus reads

$$\mathcal{Z}_N = \frac{R^{2N}}{N!} \int_{\tilde{V}} \left[ \prod_{i=1}^N d\phi_i dy_i \right] \exp \left\{ -\frac{\mathcal{H}_N^*}{k_B T} \right\}, \quad (4.8)$$

where  $0 \leq y \leq \Delta$  and the transformed Hamiltonian,

$$\frac{\mathcal{H}_N^*}{k_B T} = (2\xi - 2) \sum_{i=1}^N y_i - 2\Xi \sum_{\langle ij \rangle} \ln \left| \frac{\tilde{\mathbf{x}}_i - \tilde{\mathbf{x}}_j}{\tilde{R}} \right|. \quad (4.9)$$

The minimal set of dimensionless parameters in 2D is given by Manning parameter,  $\xi$ , total number of counterions,  $N$ , and the lateral extension parameter,  $\Delta$ . The range of simulation parameters and other details are consistent with those given in Section 3.5.2.

## 4.2 Simulation results in 2D

### 4.2.1 The order parameters

I will consider the same set of order parameters  $S_n = \langle 1/\tilde{r}^n \rangle$  as defined in Eq. (3.38) to characterize the CCT in 2D. They can be measured in the simulations as

$$S_n = \frac{1}{N} \sum_{i=1}^N \overline{\tilde{r}_i^{-n}} \quad (4.10)$$

for  $n > 0$ , where the bar sign denotes the MC time average after proper equilibration of the system. Of particular interest is the behavior of  $S_n$  as a function of Manning parameter,  $\xi$ , which identifies the two regimes of complete de-condensation (with vanishing  $S_n$ ) and partial condensation (with  $S_n > 0$ ) as  $\Delta \rightarrow \infty$ . Unlike in 3D, where  $\Xi$  can be varied as an independent parameter, various coupling regimes in the 2D system are spanned by changing the number of particles,  $N$ , for a given  $\xi$  (see Eq. (4.7)).

The 2D simulation results for the order parameter  $S_1$  are shown in Figure 4.1 for various number of particles  $N = 1, 2, 3, 5, 10$  and 100 (symbols) and for a large lateral extension parameter  $\Delta = 300$ . As seen for the smallest number of counterions,  $N = 1$ , the data trivially follow the strong-coupling prediction, Eq. (3.66), shown by the dashed curve (Section

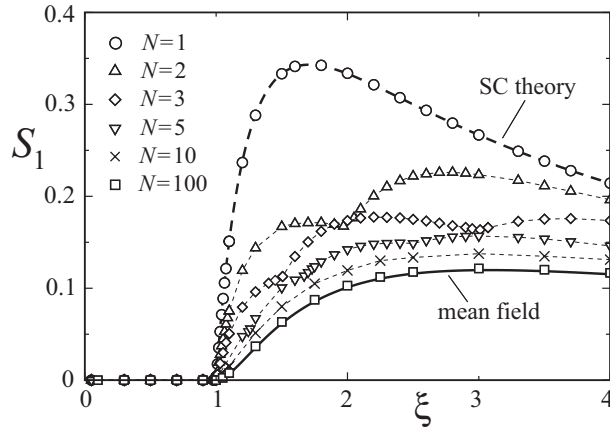


Figure 4.1: Order parameter  $S_1 = \langle 1/\bar{r} \rangle$  as a function of Manning parameter,  $\xi$ , for the 2D counterion-cylinder system. Symbols show simulation data for different number of particles as indicated on the graph. The mean-field PB (solid curve) and the strong-coupling (dashed curve) predictions are obtained from Eqs. (3.40) and (3.66) respectively, which are valid in 2D as well. The lateral extension parameter here is  $\Delta = 300$ . Thin dashed curves are guides to the eyes.

3.4). As  $N$  increases,  $S_1$  decreases and for sufficiently large values, the data converge to the mean-field PB prediction, Eq. (3.40), shown by the solid curve. This in fact occurs for the whole range of Manning parameters and thus confirms the trend predicted from the 2D electroneutrality condition (4.7). Accordingly, scaling analysis of the order parameters for large  $N$  gives identical results for the scaling exponents as in 3D (Sections 3.6.3 and 3.6.4) and thus in agreement with the mean-field theory, which I shall not discuss here any further. The result that the mean-field theory for the counterion-cylinder system is *exact* in 2D for  $N \rightarrow \infty$  is in striking contrast with the typical trend in bulk phase transitions [101], and also with the situation in 3D, where the strong-coupling effects become important in the condensation phase ( $\xi > 1$ ) for growing  $\Xi$  (Section 3.6.1).

The order-parameter data in Figure 4.1, on the other hand, reveal a peculiar set of cusplike singularities, that are quite pronounced for small number of particles. These points become strictly singular in the limit  $\Delta \rightarrow \infty$  and represent the Manning parameters at which individual counterions successively condense (or de-condense). I will demonstrate this point using an analytical approach in Section 4.2.3. (A similar singular behavior is also found in 3D for small  $N$ , but the behavior in 3D appears to be more complex and will not be considered in this work).

#### 4.2.2 Energy and heat capacity

The singularities at small particle number,  $N$ , appear also in the internal energy and the heat capacity. In Figures 4.2 and 4.3, I plot the rescaled energy,  $\tilde{E} = E_N/(Nk_B T)$ , and excess heat capacity,  $\tilde{C} = C_N/(Nk_B)$ , obtained from the simulations using Eqs. (3.77) and (3.78) and the 2D Hamiltonian (4.6), as a function of  $\xi$  and for  $N = 1, 2, 3, 4$  and 5. As seen, the energy shows a sawtooth-like structure consisting of wide regular regions, in which the energy almost linearly increases, and narrow singular regions, where the energy rapidly drops. Recalling the

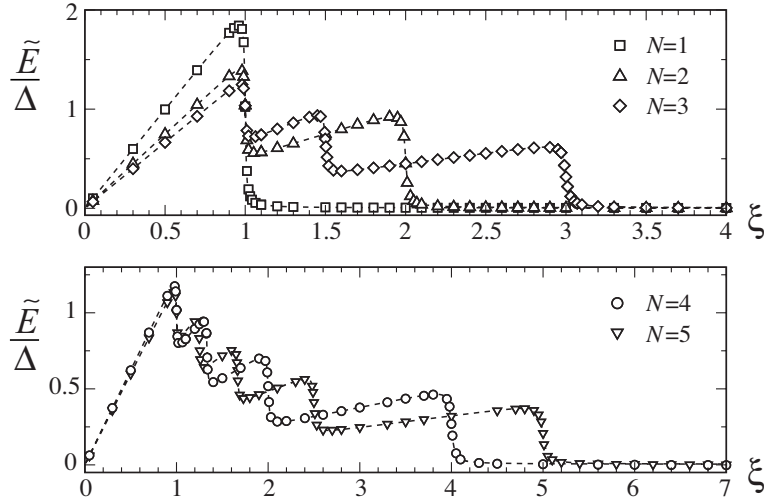


Figure 4.2: The rescaled (internal) energy of the 2D counterion-cylinder system,  $\tilde{E} = E_N/(Nk_B T)$ , as a function of Manning parameter,  $\xi$ , for different number of particles as indicated on the graph. Singular regions represent successive condensation (de-condensation) of counterions—see Section 4.2.3. The lateral extension parameter for these data is  $\Delta = 300$ . The dashed curves are the analytical results given by Eq. (4.19).

thermodynamic relation

$$\xi \frac{\partial \tilde{E}}{\partial \xi} = \tilde{E} - \tilde{C}, \quad (4.11)$$

it follows that the excess heat capacity vanishes in the regular regions, but develops highly localized peaks in the singular regions, as also seen from the simulation data in Figure 4.3.

### 4.2.3 Condensation singularities in 2D: an analytical approach

In what follows, I present an approximate (asymptotic) analysis of the 2D partition, which elucidates the physical mechanism behind the singular behavior in 2D. (The rigorous analysis of the 2D problem is still missing and more systematic approximations are recently developed [123].)

#### The partition function

Suppose that the Manning parameter is such that  $N - m$  counterions are firmly bound to the central cylinder (disk), while  $m$  counterions have de-condensed to infinity, where  $m = 1, \dots, N$ . Using the 2D Hamiltonian (4.6), the partition function can exactly be written as

$$\mathcal{Z}_N = \int \left[ \prod_{i=m+1}^N dx_i \right] \exp \left\{ -\frac{\mathcal{H}_{N-m}}{k_B T} \right\} \times \prod_{l=1}^m \mathcal{Z}_N^{(l)} \quad (4.12)$$

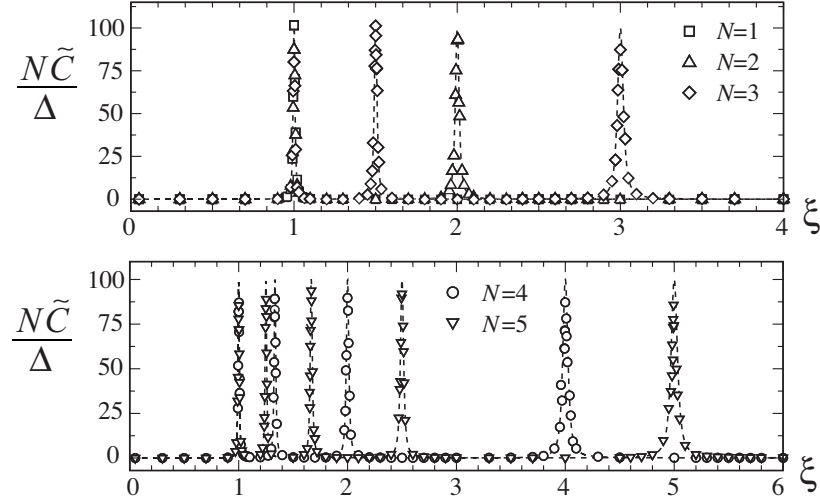


Figure 4.3: The rescaled excess heat capacity of the 2D system,  $\tilde{C} = C_N/(Nk_B)$ , as a function of Manning parameter,  $\xi$ , for different number of particles,  $N$ , as indicated on the graph (for clarity, the data are here multiplied by  $N$ ). The peaks represent successive condensation (de-condensation) of counterions—see Section 4.2.3. For these data  $\Delta = 300$ . The dashed curves are the analytical results given by Eq. (4.20).

in actual units, where  $\mathcal{H}_{N-m}$  represents interactions among condensed counterions (labeled by  $i = m + 1, \dots, N$ ), and

$$\mathcal{Z}_N^{(l)} = \int d\mathbf{x}_l \exp \left\{ -2\xi \ln \left( \frac{r_l}{R} \right) + \frac{2\xi}{N} \sum_{i=l+1}^N \ln \left| \frac{\mathbf{x}_i - \mathbf{x}_l}{R} \right| \right\} \quad (4.13)$$

is the contribution from individual de-condensed counterions (labeled by  $l = 1, \dots, m$ ). Assuming that the de-condensed counterions are de-correlated from each other and also from the condensed counterions as they diffuse to infinity for  $\Delta \rightarrow \infty$  (i.e. using  $|\mathbf{x}_i - \mathbf{x}_l| \simeq r_l$ ),  $\mathcal{Z}_N^{(l)}$  approximately factorizes as

$$\begin{aligned} \mathcal{Z}_N^{(l)} &\simeq 2\pi \int r_l dr_l \exp \left\{ -2\xi \ln \left( \frac{r_l}{R} \right) + \frac{2\xi}{N} \sum_{i=l+1}^N \ln \left( \frac{r_l}{R} \right) \right\} \\ &= 2\pi R^2 \frac{\exp [2(1 - \xi l/N)\Delta] - 1}{2(1 - \xi l/N)}. \end{aligned} \quad (4.14)$$

In the limit  $\Delta \rightarrow \infty$ ,  $\mathcal{Z}_N^{(l)}$  diverges for Manning parameters

$$\xi \leq \xi_l^s \equiv \frac{N}{l}, \quad (4.15)$$

which indicates de-condensation of the  $l$ -th counterion from the charged cylinder (see Section 3.2.1). Repeating the above argument for various number of de-condensed counterions, one finds a set of singular Manning parameters,

$$\xi_l^s = \frac{N}{l} \quad \text{for } l = 1, \dots, N, \quad (4.16)$$



$N$	$\{\xi_N^s, \dots, \xi_1^s\}$
1	1
2	1 2
3	1 3/2 2
4	1 4/3 $\simeq 1.33$ 2 4
5	1 5/4 = 1.25 5/3 $\simeq 1.67$ 5/2 5

Table 4.1: Numerical values of the location of the singularities, Eq. (4.16), for the 2D counterion-cylinder system for different numbers of particles,  $N$  (compare Figures 4.1-4.3).

at which individual counterions de-condense from the charged cylinder. These singular points coincide with the values obtained from the simulations based on the full partition function (4.8) for very large  $\Delta$  (see Figures 4.1-4.3 and Table 4.1 for the numerical values).

### Energy and heat capacity

In general the partition function (4.12) can also exactly be written as

$$\mathcal{Z}_N = \prod_{l=1}^N \mathcal{Z}_N^{(l)}, \quad (4.17)$$

where  $\mathcal{Z}_N^{(l)}$  is defined in Eq. (4.13). For  $\Delta \gg 1$ , the dominant contribution to the internal energy and the heat capacity comes from de-condensed counterions. Thus, in order to derive analytical expressions for energy and heat capacity on the leading-order for large  $\Delta$ , I shall use Eq. (4.17) together with the approximate expression (4.14) for  $\mathcal{Z}_N^{(l)}$ . Hence, I obtain the leading-order contribution to the free energy  $\mathcal{F}_N/(k_B T) = -\ln \mathcal{Z}_N$  as

$$\tilde{\mathcal{F}} \equiv \frac{\mathcal{F}_N}{N k_B T} \simeq -\frac{1}{N} \sum_{l=1}^N \ln \frac{e^{2(1-\xi/\xi_l^s)\Delta} - 1}{2(1-\xi/\xi_l^s)} \quad (4.18)$$

for  $\Delta \gg 1$ , and thereby the (rescaled) internal energy,  $\tilde{E} = \xi \partial \tilde{\mathcal{F}} / \partial \xi$ , and the rescaled heat capacity,  $\tilde{C} = -\xi^2 \partial^2 \tilde{\mathcal{F}} / \partial \xi^2$ , are obtained as

$$\tilde{E} \simeq \sum_{l=1}^N \frac{\xi}{N \xi_l^s} \left( \frac{2\Delta \exp[2(1-\xi/\xi_l^s)\Delta]}{\exp[2(1-\xi/\xi_l^s)\Delta] - 1} - \frac{1}{1-\xi/\xi_l^s} \right), \quad (4.19)$$

$$\tilde{C} \simeq \sum_{l=1}^N \left( \frac{\xi}{\xi_l^s} \right)^2 \left( \frac{1}{(1-\xi/\xi_l^s)^2} - \frac{\Delta^2}{\sinh^2[2(1-\xi/\xi_l^s)\Delta]} \right). \quad (4.20)$$

The above expressions are shown in Figures 4.2 and 4.3 for  $\Delta = 300$  and for various number of particles (dashed curves), which as seen closely reproduce the behavior obtained in the simulations (symbols).

Note that as an individual counterion de-condenses at  $\xi_l^s$ , the internal energy suddenly jumps, since the de-condensing counterion gains a large amount of energy due to its logarithmic interaction with the central cylinder. The *regular* regions (between two successive jumps)

in the energy curve are dominated by de-condensed counterions and thus exhibit linear scaling with  $\Delta = \ln(D/R)$ . The asymptotic form of the energy in these regions for  $\Delta \rightarrow \infty$  is obtained from Eq. (4.19) as

$$\lim_{\Delta \rightarrow \infty} \frac{\tilde{E}}{\Delta} = \frac{l(l+1)}{N^2} \xi \quad \text{for } \xi_{l+1}^s < \xi < \xi_l^s. \quad (4.21)$$

The *singular* part of the energy corresponds to a narrow region around each  $\xi_l^s$ , which (except for the uppermost singularity) is bounded between a local minimum (slightly above  $\xi_l^s$ ) and a local maximum (slightly below  $\xi_l^s$ ). The approximate locations of these extrema are obtained as

$$\frac{\xi_l^{\min}}{\xi_l^s} \simeq 1 + \frac{1}{\sqrt{\Delta(l-1)}} \quad \text{and} \quad \frac{\xi_l^{\max}}{\xi_l^s} \simeq 1 - \frac{1}{\sqrt{\Delta(l+1)}} \quad (4.22)$$

using Eq. (4.19), and for large  $\Delta$ . The *energy jump*,  $\delta\tilde{E}_l$ , upon de-condensation of a counterions at  $\xi = \xi_l^s$  is then given by

$$\delta\tilde{E}_l \equiv \tilde{E}(\xi_l^{\max}) - \tilde{E}(\xi_l^{\min}) \simeq \frac{2\Delta}{N}. \quad (4.23)$$

Note that this value can also be obtained directly from Eq. (4.21). For  $\Delta \rightarrow \infty$  but at *fixed* and *finite*  $N$ , the energy curve tends to a sharp sawtooth-like form as both  $\xi_l^{\min}$  and  $\xi_l^{\max}$  tend to  $\xi_l^s$  producing  $N$  strictly step-like singular points, at which the limiting energy jump is

$$\lim_{\Delta \rightarrow \infty} \frac{\delta\tilde{E}_l}{\Delta} = \frac{2}{N}. \quad (4.24)$$

The heat capacity expression (4.20), on the other hand, exhibits  $N$  isolated peaks for  $\Delta \gg 1$ . The heat capacity at  $\xi_l$  diverges as  $\tilde{C}(\xi = \xi_l^s) \simeq \Delta^2/3$  with increasing  $\Delta$ , giving rise to  $N$  limiting algebraic divergencies as

$$\lim_{\Delta \rightarrow \infty} \tilde{C} = \sum_{l=1}^N \left(1 - \frac{\xi_l^s}{\xi}\right)^{-2}. \quad (4.25)$$

#### 4.2.4 Critical point and the continuum limit

The lower-most singularity located at  $\xi = \xi_N^s$  is associated with the de-condensation of the “last” counterion from the charged cylinder. As shown above, this singularity occurs at unity ( $\xi_N^s = 1$ ) when  $\Delta \rightarrow \infty$  and is thus independent of the number of counterions. It therefore gives the exact location of the 2D critical point as  $\xi_c = 1$  when the continuum (thermodynamic) limit  $N \rightarrow \infty$  is approached, which coincides with the mean-field prediction. Note that in analogy with the method used in Section 3.6.2,  $\xi_c$  can also be derived from the asymptotic value of the energy maximum location, Eq. (4.22), for  $l = N$ , when  $\Delta$  and  $N$  both tend to infinity.

Equations (4.23)-(4.25) represent the asymptotic results when the system size increases to infinity but the number of particles,  $N$ , is finite. In the converse limiting case, i.e. when  $\Delta$  is *large* and *fixed* but  $N$  increases to infinity (continuum limit), all singularities smoothen except for the one, which represents the critical point. The limiting energy curve for  $N \rightarrow \infty$  may be obtained as follows. First note that the width of the energy jump around each singularity

tends to zero as indicated by Eq. (4.23). Secondly, the spacing between singular points  $\xi_l^s$  (and thus the width of regular regions for  $\xi > 1$ ) tends to zero (as  $\sim 1/N$ ) as  $N$  increases. Therefore, the energy at a given Manning parameter  $\xi$  between two successive singularities,  $\xi_{l+1}^s < \xi < \xi_l^s$ , is approximately given by  $\tilde{E} \simeq \tilde{E}(\xi = \xi_l^s)$ , where the right hand side is obtained from Eq. (4.19) as  $\tilde{E}(\xi = \xi_l^s) = \Delta/\xi_l^s$ . This implies that

$$\lim_{N \rightarrow \infty} \tilde{E} = \frac{\Delta}{\xi} \quad (4.26)$$

for  $\xi \geq 1$  and sufficiently large  $\Delta$ . For small Manning parameter  $\xi < 1$ , there are no singularities and from Eq. (4.19), I obtain

$$\lim_{N \rightarrow \infty} \tilde{E} = 2\xi\Delta \times \lim_{N \rightarrow \infty} \sum_{l=1}^N \frac{1}{N\xi_l^s} = \xi\Delta \quad (4.27)$$

for large  $\Delta$ . These limiting results can also be obtained using Eq. (4.21).

The predicted energy curve in the continuum limit therefore coincides with the universal form obtained within the mean-field theory in Section 3.3.3 (see Eq. (3.60)). The heat capacity in this limit follows from Eq. (3.80), and exhibits a universal jump at  $\xi_c = 1$  in agreement with Eq. (3.61).

#### 4.2.5 The condensed fraction

The preceding results enable us to calculate the limiting condensed fraction of counterions,  $\alpha(\xi)$ , as well when  $\Delta \rightarrow \infty$  and  $N \rightarrow \infty$ . For a given Manning parameter,  $\xi$ , and number of particles,  $N$ , the condensed fraction  $\alpha_N(\xi)$  is given by the number of singularities located below  $\xi$ , i.e.

$$\alpha_N(\xi) \equiv 1 - \frac{l}{N} \quad \text{for } \xi_{l+1}^s < \xi < \xi_l^s. \quad (4.28)$$

This fraction is trivially zero for  $\xi < \xi_c = 1$  as  $\Delta \rightarrow \infty$ . Using Eqs. (4.16) and (4.28), I obtain the condition

$$\alpha_N(\xi) - \frac{1}{N} < 1 - \frac{1}{\xi} < \alpha_N(\xi), \quad (4.29)$$

which in the limit of infinite number of counterions yields

$$\alpha(\xi) \equiv \lim_{N \rightarrow \infty} \alpha_N(\xi) = 1 - \frac{1}{\xi}. \quad (4.30)$$

This is nothing but the mean-field or Manning condensed fraction,  $\alpha_M = 1 - 1/\xi$  (Section 3.6.1). The finite-ion-number correction to this limiting value follows from Eq. (4.29) as

$$\alpha_N(\xi) - \alpha(\xi) \sim N^{-1}. \quad (4.31)$$



## Chapter 5

# Strong-Coupling Interactions

Electrostatic interaction between charged macromolecules (macroions), such as polyelectrolytes (like DNA) and colloidal particles, is a key factor determining the global phase behavior of charged solutions. Macroions in solutions are often like-charged and thus the bare interaction between them is repulsive. However the mobile neutralizing counterions that maintain electroneutrality of the solution screen the bare charges of macroions and typically reduce the bare interactions between them. Still in many instances, the resultant effective interactions appear to be repulsive, which is often favored from a technological point of view, e.g., when stabilization of colloidal dispersions is important.

In recent years, however, mounting evidence from both experiments [31, 33, 34, 127, 128, 129, 130, 131, 132, 133, 134, 135, 136] and numerical simulations [137, 138, 139, 140, 141, 142, 143, 144, 145, 146, 147, 148, 149, 150, 151, 152, 153, 154, 155, 44, 45, 46, 157, 55, 158] shows that in certain physical conditions, like-charged macroions can strongly *attract* each other via effective forces of electrostatic origin. Most notably, like-charge attraction appears to be responsible in formation of dense packages of DNA molecules (DNA condensates) [30, 31], bundles of stiff charged polymers (such as F-actin) [33, 34, 135] and large aggregates of charged colloidal particles [150, 151, 152, 153]. Interestingly, such attractive forces emerge only in strongly charged (or more precisely, *strongly coupled*) systems, i.e. when macroions are highly charged (with surface charge densities up to  $1e/\text{nm}^2$  as in the DNA system), neutralizing counterions are multivalent, or when the temperature or the dielectric constant of the medium is low. Such strong-coupling attractive interactions are typically much stronger than the usual attractive van-der-Waals interactions and may thus have significant practical implications where, for instance, multivalent counterions are present.

The phenomenon of like-charge attraction indeed contrasts the standard picture available from mean-field theories [18, 1, 2, 3], such as Poisson-Boltzmann theory, which predict purely repulsive like-charge interactions [188, 189, 190]. The main scenarios which are put forward to explain this phenomenon go beyond the mean-field level by accounting for electrostatic correlations that are neglected within mean-field approximation [20, 137, 138, 139, 140, 141, 142, 143, 144, 145, 146, 147, 148, 149, 150, 151, 152, 153, 154, 155, 44, 45, 46, 157, 55, 158, 159, 161, 162, 163, 164, 165, 166, 167, 168, 169, 170, 50, 171, 172, 173, 174, 175, 48, 176, 177, 178, 179, 49, 180, 181, 43, 182, 54, 35, 183, 184, 185, 186, 187]. Recent theoretical attempts include integral-equation methods [143, 159], perturbative improvement of the mean-field theory including Gaussian-fluctuations theories [20, 161, 162, 163, 164, 165, 166, 167, 168, 169, 170, 50, 171, 172], and local density functional theory [174, 175], which compare

well with numerical simulations and all exhibit attraction. These methods are, however, mostly applicable for large separations between macroions or for low coupling strength (the so-called *high-temperature* regime), and can not characterize the closely packed bound-state between like-charged macroions. An alternative approach was triggered by Rouzina and Bloomfield [48] with the insight that counterions form two-dimensional highly correlated layers at macroionic surfaces for large coupling strength (the so-called *low-temperature* regime). Such structural correlations give rise to attractive interactions of mainly energetic origin [176, 177, 178, 179, 49, 180, 181, 43, 182, 54] and can account for the closely packed bound-state of like-charged macroions [45, 46, 55, 176, 177, 178, 179, 49, 180, 181, 43, 182, 54].

This chapter deals with this latter regime of strong coupling. The general physical mechanism that leads to like-charge attraction in this regime is reviewed in Chapter 2. Here I present a systematic analysis of the effective interaction between a pair of like-charged rods and a pair of like-charged spheres [35, 54, 55] using the asymptotic strong-coupling (SC) theory [43, 44], which describes the limit of large coupling parameters ( $\Xi \rightarrow \infty$ ). This asymptotic theory involves a simple analytical expression for the leading-order free energy containing both energetic and entropic contributions from counterions. It therefore represents a finite-temperature theory. The energetic contribution exhibits a long-range attractive force between macroions, which scales as  $\sim d^{-1}$  for two charged rods and as  $\sim d^{-2}$  for two charged spheres located at distance  $d$  from each other. The SC attraction is independent of temperature and prevails as the dominant component when the zero-temperature limit is taken (formally, this limit is achieved by taking the limit  $\mu \rightarrow 0$ , where  $\mu$  is the Gouy-Chapman length). At finite temperatures, the entropic contributions that are incorporated via a single-particle partition function trigger de-condensation of counterions for small radius of curvature of macroions (or small Manning parameter) as discussed in Chapters 2 and 3. This leads to a bare repulsion between macroions. Hence within the SC theory, one can determine both regimes of attraction and repulsion between macroions.

It is shown that when attraction is dominant, macroions form a closely packed bound-state with small surface-to-surface separation of the order of the counterion diameter (plus a term of the order of the Gouy-Chapman length). For charged spheres, these results agree with recent simulations on a semi-quantitative level [54, 35]. For two charged rods, a systematic comparison with Molecular Dynamics simulations reveals a good quantitative agreement between the SC theory and simulations at sufficiently large coupling strength [55]. I will also study the repulsion-dominated as well as the crossover regime, where a binding-unbinding transition is found to occur for both charged rods and charged spheres. This regime does not correspond to large electrostatic correlations between particles, but it is, nonetheless, captured systematically within the SC formalism (see the Discussion).

## 5.1 Strong-coupling theory: General formalism

Consider a system of fixed rigid macroions with charge distribution  $-\sigma(\mathbf{x})e$ , and a number of  $N$  oppositely charged counterions of diameter  $\sigma_{ci}$  and charge valency  $+q$ . All charges interact via Coulombic interaction  $v(\mathbf{x}) = 1/|\mathbf{x}|$ , and the electroneutrality condition is assumed to hold globally in the system. Hence, one always has

$$Nq = \int d\mathbf{x} \sigma(\mathbf{x}). \quad (5.1)$$

As before, I shall use a dimensionless representation which is obtained by rescaling spatial coordinates as  $\tilde{\mathbf{x}} = \mathbf{x}/\mu$  with  $\mu = 1/(2\pi q\ell_B\sigma_s)$  being the Gouy-Chapman length, where  $\sigma_s$  is the surface charge density of macroions (see Eqs. (2.3) and (2.14)). The electroneutrality condition (5.1), when written in rescaled units, relates the coupling parameter to the number of counterions through

$$\tilde{\mathcal{A}} \equiv \int d\tilde{\mathbf{x}} \tilde{\sigma}(\tilde{\mathbf{x}}) = 2\pi\Xi N, \quad (5.2)$$

where  $\tilde{\mathcal{A}}$  is the rescaled area of macroions covered by electric charges, and  $\Xi = 2\pi q^3\ell_B^2\sigma_s$  is the electrostatic coupling parameter (see Eq. (2.4)).

As shown in Appendix A, for large coupling parameter  $\Xi \gg 1$ , the grand-canonical partition function of the system,  $\mathcal{Z}_g$ , adopts a series expansion in powers of  $1/\Xi$  as [44, 43]

$$\mathcal{Z}_g(\Lambda) = \mathcal{Z}_0 \sum_{j=0}^{\infty} \frac{1}{j!} \left( \frac{\Lambda}{2\pi\Xi} \right)^j \left[ \prod_{k=1}^j \int d\tilde{\mathbf{x}}_k \tilde{\Omega}(\tilde{\mathbf{x}}_k) \right] \times \exp \left\{ -\Xi \sum_{n<m}^j v(\tilde{\mathbf{x}}_n - \tilde{\mathbf{x}}_m) - \sum_{i=1}^j \tilde{u}(\tilde{\mathbf{x}}_i) \right\}, \quad (5.3)$$

where  $\Lambda$  is the rescaled fugacity and the function  $\tilde{\Omega}(\tilde{\mathbf{x}})$  takes geometrical constraints into consideration, e.g., restricts the positions of mobile counterions to an appropriate region in space.

Equation (5.3) is in fact nothing but a virial expansion with respect to the counterionic degrees of freedom. The zeroth-order term,

$$\mathcal{Z}_0 = e^{-\tilde{U}_0/\pi\Xi}, \quad (5.4)$$

gives the contribution of fixed macroions in the absence of counterions, where

$$\tilde{U}_0 = \frac{1}{8\pi} \int d\tilde{\mathbf{x}} d\tilde{\mathbf{x}}' \tilde{\sigma}(\tilde{\mathbf{x}}) v(\tilde{\mathbf{x}} - \tilde{\mathbf{x}}') \tilde{\sigma}(\tilde{\mathbf{x}}') \quad (5.5)$$

is the rescaled zero-particle interaction energy. The first-order term in Eq. (5.3) is the partition function in the presence of a single counterion interacting with macroions via the one-particle interaction energy,

$$\tilde{u}(\tilde{\mathbf{x}}) = -\frac{1}{2\pi} \int d\tilde{\mathbf{x}}' v(\tilde{\mathbf{x}} - \tilde{\mathbf{x}}') \tilde{\sigma}(\tilde{\mathbf{x}}'). \quad (5.6)$$

Higher-order terms involve the two-particle interaction,  $v(\tilde{\mathbf{x}} - \tilde{\mathbf{x}}')$ , that enters in the non-perturbative form of  $\exp(-\Xi v)$ .

The *canonical strong-coupling (SC) theory* is obtained as an asymptotic theory from the above expansion, Eq. (5.3), in the limit  $\Xi \rightarrow \infty$ . As shown below, the leading-order contribution to the *canonical* free energy of the system for  $\Xi \rightarrow \infty$  contains only the single-particle terms.

### 5.1.1 The strong-coupling free energy

To calculate the SC free energy, I start from the grand-canonical free energy

$$\mathcal{Q}_g(\Lambda) = -k_B T \ln \mathcal{Z}_g(\Lambda), \quad (5.7)$$

where  $\mathcal{Z}_g$  is given by Eq. (5.3). The Legendre transformation,

$$\mathcal{F}_N = Nk_B T \ln \Lambda + \mathcal{Q}_g(\Lambda), \quad (5.8)$$

provides us with the canonical free energy,  $\mathcal{F}_N$ . The rescaled fugacity,  $\Lambda$ , in Eq. (5.8) is calculated from

$$N = \Lambda \frac{\partial \ln \mathcal{Z}_g}{\partial \Lambda} \quad (5.9)$$

in terms of  $\Xi$  and other rescaled geometrical factors. (Note that  $N$  can be eliminated using Eq. (5.2).) In general, one may propose the following expression for  $\Lambda$  in the large coupling limit  $\Xi \gg 1$ ,

$$\Lambda = \Lambda_0 + \frac{\Lambda_1}{\Xi} + \frac{\Lambda_2}{\Xi^2} + \dots, \quad (5.10)$$

where  $\Lambda_0, \Lambda_1, \dots$  are determined from Eq. (5.9) using Eqs. (5.2), (5.3)-(5.6).<sup>1</sup> It is easy to verify that, for instance,

$$\Lambda_0 = \frac{\tilde{\mathcal{A}}}{\int d\tilde{\mathbf{x}} \tilde{\Omega}(\tilde{\mathbf{x}}) e^{-\tilde{u}(\tilde{\mathbf{x}})}}, \quad (5.11)$$

$$\Lambda_1 = \frac{\tilde{\mathcal{A}}^2 \int d\tilde{\mathbf{x}} d\tilde{\mathbf{x}}' \tilde{\Omega}(\tilde{\mathbf{x}}) \tilde{\Omega}(\tilde{\mathbf{x}}') e^{-\tilde{u}(\tilde{\mathbf{x}}) - \tilde{u}(\tilde{\mathbf{x}}')} [1 - e^{-\Xi v(\tilde{\mathbf{x}} - \tilde{\mathbf{x}}')}]}{2\pi \left[ \int d\tilde{\mathbf{x}} \tilde{\Omega}(\tilde{\mathbf{x}}) e^{-\tilde{u}(\tilde{\mathbf{x}})} \right]^3}. \quad (5.12)$$

Inserting this into Eq. (5.8), one obtains  $\mathcal{F}_N$ , which also admits a large-coupling expression as

$$\frac{\mathcal{F}_N}{k_B T} = \frac{\mathcal{F}_1}{\Xi} + \frac{\mathcal{F}_2}{\Xi^2} + \dots \quad (5.13)$$

The coefficient of the leading-order term reads

$$\mathcal{F}_1 = \frac{\tilde{U}_0}{\pi} - \frac{\tilde{\mathcal{A}}}{2\pi} \ln \int d\tilde{\mathbf{x}} \tilde{\Omega}(\tilde{\mathbf{x}}) e^{-\tilde{u}(\tilde{\mathbf{x}})} + C_0, \quad (5.14)$$

in which  $C_0 = (\tilde{\mathcal{A}}/2\pi) \ln \tilde{\mathcal{A}} - \tilde{\mathcal{A}}/2\pi$  is a constant. The free energy coefficient  $\mathcal{F}_1$  (which may be regarded as the rescaled SC free energy), yields the *strong-coupling free energy* of the system as

$$\frac{\mathcal{F}_N^{\text{SC}}}{k_B T} = \frac{\mathcal{F}_1}{\Xi}. \quad (5.15)$$

This term generates the leading contribution to the effective forces between macroions, which will be examined for two charged rods and spheres in the following sections.

Note that when this asymptotic SC theory is applied to realistic systems of *finite* coupling parameter, one should always determine the regime of parameters, where higher-order correction terms are relatively small. These terms have been calculated analytically for systems composed of planar charged walls in Refs. [44, 43, 45], but for charged rods and spheres, analytical calculations become very difficult. I shall instead use a simple well-established criterion: two apposed like-charge surfaces become strongly coupled when the typical lateral distance between counterions at the surfaces becomes larger than or comparable to the surface-surface separation (see Section 2.4.3). This criterion, which was first introduced by Rouzina and Bloomfield [48], has been confirmed analytically for charged walls [43] and numerically for both planar and curved surfaces [44, 45, 46, 148, 150, 151, 152, 55].

One should also note that the virial expansion (5.3) can systematically incorporate non-electrostatic pair interactions between particles as well. Thus, the SC free energy (5.14)

<sup>1</sup>In general, the proposed expansion, Eq. (5.10), may also involve additional logarithmic terms [43].



may be easily generalized to include, for instance, the excluded-volume interaction between particles. Clearly, only the macroion-counterion excluded-volume interaction enters in the leading-order free energy (via the interaction energy term,  $\tilde{u}(\tilde{\mathbf{x}})$ ). In what follows, I shall assume a hard-core excluded-volume repulsion between counterions (of finite diameter  $\sigma_{\text{ci}}$ ) and macroions. Therefore (due to the exponential factor  $\exp(-\tilde{u})$ ), overlapping configurations do not contribute to the spatial integral in Eq. (5.14) and the effect of counterion size is incorporated into the geometry function  $\tilde{\Omega}$ , which, for cylindrical and spherical macroions of radius  $R_0$ , leads simply to a hard-core radius of

$$R = R_0 + \sigma_{\text{ci}}/2. \quad (5.16)$$

For a given amount of macroion charge, equation (5.16) implies a reduced surface charge density, and thus an increased Gouy-Chapman length,  $\mu$ , as compared to the case with point-like counterions. The following results are presented in units of the Gouy-Chapman length and the counterion diameter explicitly appears only when the actual units are restored (see, e.g., Eqs. (5.33) and (5.52) below).

## 5.2 Two like-charged rods

In this section, I will focus on the interaction between two identical parallel like-charged rods of linear charge density  $-\tau e$ , bare radius  $R_0$  and infinite length  $H$  that are located at axial separation of  $d$  from each other (Figure 5.1). The rods are confined in a rectangular box of edge size  $L$  together with  $N$  neutralizing  $q$ -valent counterions; hence, one has  $qN = 2\tau H$ . The Gouy-Chapman length associated with this system reads

$$\mu = \frac{1}{2\pi q \ell_{\text{B}} \sigma_{\text{s}}} = \frac{R}{q \ell_{\text{B}} \tau}, \quad (5.17)$$

where  $\sigma_{\text{s}} = \tau/(2\pi R)$  is the surface charge density and  $R$  is the hard-core radius defined via Eq. (5.16). Clearly, the rescaled rod radius,  $\tilde{R} = R/\mu$ , is identical with the *Manning parameter*, i.e.

$$\tilde{R} = \xi = q \ell_{\text{B}} \tau. \quad (5.18)$$

The zero-particle and single-particle interaction terms (5.5) and (5.6) are obtained as

$$\frac{\tilde{U}_0}{\tilde{H}} = -2\pi \tilde{R}^2 \ln \tilde{d}, \quad (5.19)$$

$$\tilde{u}(\tilde{x}, \tilde{y}) = 2\tilde{R} (\ln \tilde{r}_1 + \ln \tilde{r}_2), \quad (5.20)$$

where  $\tilde{H} = N\Xi/(2\xi)$  (from the electroneutrality condition), and

$$\tilde{r}_{1,2} = [(\tilde{x} \pm \tilde{d}/2)^2 + \tilde{y}^2]^{1/2} \quad (5.21)$$

are radial distances from the rods axes. Inserting the above expressions into Eq. (5.14), one ends up with the SC free energy (per number of counterions), Eq. (5.15), as

$$\frac{\mathcal{F}_N^{\text{SC}}}{Nk_{\text{B}}T} = -\tilde{R} \ln \tilde{d} - \ln I, \quad (5.22)$$

where

$$I(\tilde{d}, \tilde{R}, \tilde{L}) \equiv \int d\tilde{x} d\tilde{y} \tilde{\Omega} \exp \left[ -2\tilde{R} (\ln \tilde{r}_1 + \ln \tilde{r}_2) \right], \quad (5.23)$$

in which  $\tilde{\Omega} = \tilde{\Omega}(\tilde{x}, \tilde{y}; \tilde{d}, \tilde{R}, \tilde{L})$  specifies the volume available for counterions, i.e., it is unity inside the box (excluding the two rods of hard-core radius  $\tilde{R}$ ) and zero elsewhere.

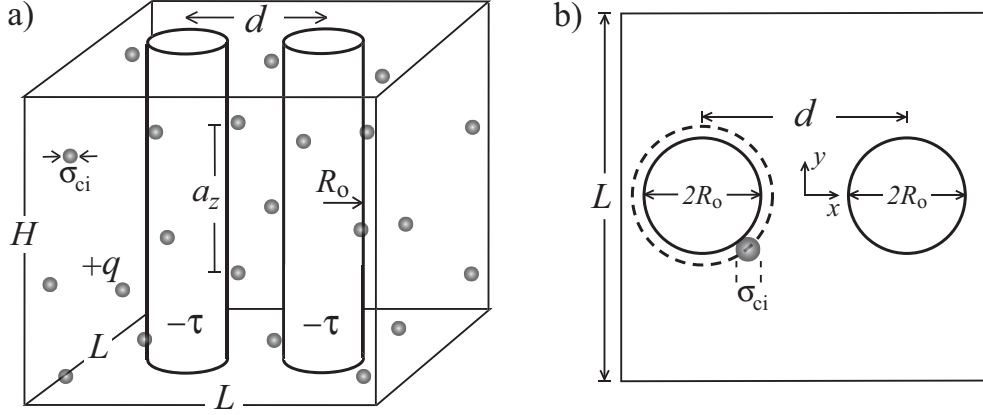


Figure 5.1: a) Two identical parallel charged rods of bare radius  $R_0$  (and infinite length  $H$ ) are considered at the axial separation  $d$  and in a square box of lateral edge size  $L$ , which also contains neutralizing counterions of charge valency  $+q$ . Dashed circle in the top view b) shows the closest approach distance. The frame of coordinates is chosen in the mid-way between the rods with  $z$ -axis being parallel to their axes.  $a_z$  is the typical distance between counterions at surface that will be considered in Section 5.2.3.

### 5.2.1 Threshold of attraction

The first term in Eq. (5.22) is the bare electrostatic repulsion between the rods. The energetic and entropic contributions from counterions is incorporated on the leading order in the single-particle partition function  $I$ , which can generate an effective rod-rod attraction. In order to examine the onset of attraction, let us consider first the limit of infinite box size  $\tilde{L}/\tilde{R} \rightarrow \infty$ . In this limit, the counterionic integral (5.23) scales with the box size as  $I \sim \tilde{L}^{2-4\tilde{R}}$ , which may be seen simply by rescaling the spatial coordinates with  $L$  as  $x \rightarrow x/L$ , etc. Thus for  $\tilde{R} < 1/2$ ,  $I$  diverges and consequently, the distribution function of counterions,  $\sim \exp(-\tilde{u})/I$ , vanishes indicating de-condensation of counterions from the two rods.<sup>2</sup> The counterion-mediated force between the rods,  $\sim \partial \ln I / \partial d$ , tends to zero as well; thus two unconfined rods merely repel each other for  $\tilde{R} < 1/2$ . In contrast for  $\tilde{R} > 1/2$ , counterionic distribution function remains finite indicating that  $\tilde{R} = 1/2$  is the onset of counterion condensation in this system in agreement with the results due to Ray and Manning [53]. Intuitively, one expects that the attraction appears above this threshold, since right at the condensation threshold, there is an unbalanced bare rod-rod repulsion, which can be compensated once a finite fraction of counterions is condensed around the rods.

Now assuming that the SC free energy has only one local minimum, which will be verified by numerical evaluation below, the attraction threshold can be determined from the large-separation behavior of the free energy, i.e. for  $\tilde{d} \gg \tilde{d}_{\min}$ , where  $\tilde{d}_{\min} = 2\tilde{R}$  is the minimum axial separation. To this end, I rescale the spatial coordinates as

$$\tilde{x}' = \frac{\tilde{x}}{\tilde{d}}, \quad \tilde{y}' = \frac{\tilde{y}}{\tilde{d}}. \quad (5.24)$$

<sup>2</sup> The SC counterionic density profile is obtained as  $\tilde{\rho}_{\text{SC}}(\tilde{\mathbf{x}}) = \Lambda_0 \tilde{\Omega}(\tilde{\mathbf{x}}) \exp(-\tilde{u}(\tilde{\mathbf{x}}))$  (see Ref. [43] and Appendix A), where according to Eq. (5.11),  $\Lambda_0 = \tilde{A}/I$ .

Consequently, the integral  $I$  in Eq. (5.23) scales as

$$I(\tilde{d}, \tilde{R}) = \tilde{d}^{2-4\tilde{R}} J\left(\frac{\tilde{R}}{\tilde{d}}, \tilde{R}\right), \quad (5.25)$$

where  $J$  is a dimensionless integral given by

$$J = 2 \int_{\tilde{x}' > 0} d\tilde{x}' d\tilde{y}' \tilde{\Omega}' \left[ \left( \tilde{x}' + \frac{1}{2} \right)^2 + (\tilde{y}')^2 \right]^{-\tilde{R}} \left[ \left( \tilde{x}' - \frac{1}{2} \right)^2 + (\tilde{y}')^2 \right]^{-\tilde{R}}, \quad (5.26)$$

where I have made use of the symmetry property of the integrand upon the reflection with respect to the plane  $\tilde{x}' = 0$ , and thus the corresponding integral is taken only over the half-space  $\tilde{x}' > 0$  excluding a disk of radius  $\tilde{R}/\tilde{d}$  centered at  $(\tilde{x}' = +1/2, \tilde{y}' = 0)$  (this is formally accounted for by the geometry function  $\tilde{\Omega}'$ ). For very large  $\tilde{d}/\tilde{d}_{\min}$ , the radius of the disk tends to zero and the limiting behavior of the integral in Eq. (5.26) is determined by the contributions from the boundary regions, which vary depending on whether  $\tilde{R}$  is smaller or larger than 1.

For Manning parameter  $\tilde{R} < 1$ , the contribution from the boundary region around the disk vanishes, and the integral in Eq. (5.26) is dominated by its outer boundary, which gives only a constant independent of  $\tilde{d}$ . Therefore, the prefactor of  $J$  in Eq. (5.25) yields the leading  $\tilde{d}$ -dependence of  $I$  for large axial separations. Substituting this into Eq. (5.22), I obtain the large-separation form of the SC free energy as

$$\frac{\mathcal{F}_N^{\text{SC}}}{Nk_{\text{B}}T} \simeq -(2 - 3\tilde{R}) \ln \tilde{d}. \quad (5.27)$$

For  $\tilde{R} > 1$ , on the other hand, the integral in Eq. (5.26) is dominated by the boundary region around the disk yielding  $J \sim \tilde{d}^{2\tilde{R}-2}$  for very large  $\tilde{d}/\tilde{d}_{\min}$ , which leads to the following attractive tail for the SC free energy,

$$\frac{\mathcal{F}_N^{\text{SC}}}{Nk_{\text{B}}T} \simeq \tilde{R} \ln \tilde{d}. \quad (5.28)$$

Therefore, as clearly seen from Eqs. (5.27) and (5.28), two unconfined rods experience an attractive force at large separations, when the Manning parameter,  $\tilde{R}$ , becomes larger than the threshold

$$\tilde{R}_c = \frac{2}{3}. \quad (5.29)$$

The onset of attraction between two like-charged rods has also been considered in a number of recent studies. Analysis of Ray and Manning [53] based on the classical counterion-condensation model predicts attraction for  $\tilde{R} > 1/2$ . It should be noted, however, that the attraction mechanism involved in their theory is not based on electrostatic correlations, but features a mean-field covalence-like binding process. Arenzon et al.'s study [177, 182] based on a structural-correlations theory (which also accounts for counterion condensation) predicts attraction for  $\tilde{R} > 2$ . Numerical simulations [145, 157, 55, 158], on the other hand, give attraction for the range of Manning parameters  $\tilde{R} > 0.8$ , but have not yet specified the attraction threshold precisely (see Section 5.2.3 below).

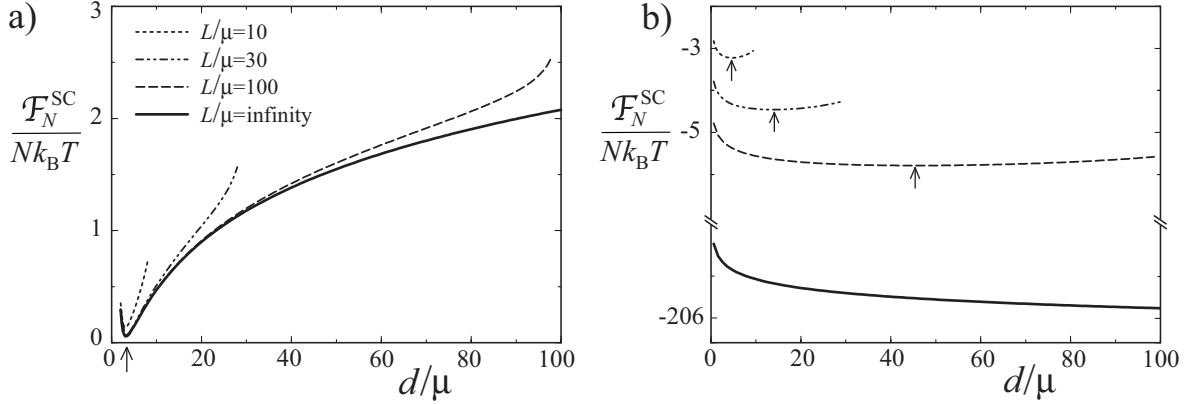


Figure 5.2: The strong-coupling free energy of the two-rod system, Eq. (5.22), as a function of the rescaled axial distance,  $\tilde{d} = d/\mu$ , for Manning parameters a)  $\tilde{R} = 1.0$  and b)  $\tilde{R} = 0.3$  and for several box sizes indicated on the graph. Arrows show the approximate location of the free energy minimum.

### 5.2.2 Equilibrium axial distance

I shall now consider the attraction and repulsion regimes for two like-charged rods in a finite confining box (Figure 5.1). The typical form of the SC free energy as a function of the axial separation,  $\tilde{d}$  (which is calculated numerically from Eq. (5.22)) is shown in Figure 5.2 for both large ( $\tilde{R} > \tilde{R}_c = 2/3$ ) and small ( $\tilde{R} < \tilde{R}_c = 2/3$ ) Manning parameters.

For large Manning parameter  $\tilde{R}$  (see, e.g.,  $\tilde{R} = 1$  in Figure 5.2a), the free energy exhibits a long-range attraction and a pronounced global minimum at a small axial separation  $\tilde{d}_* \simeq 2\tilde{R}$ , which, as seen, depend little on the confining box size,  $\tilde{L}$ . This is because counterions are mostly localized in the proximity of the rods and, particularly, in the narrow intervening region between them as it can be verified directly using the SC counterionic distribution function. One can thus employ a saddle-point approximation to evaluate the counterionic integral (5.23) for  $\tilde{R} \gg 1$  (Appendix E.1), which gives the approximate form of  $\mathcal{F}_N^{\text{SC}}$  around its minimum as

$$\frac{\mathcal{F}_N^{\text{SC}}}{Nk_B T} \simeq 3\tilde{R} \ln \tilde{d} - \ln(\tilde{d} - 2\tilde{R}). \quad (5.30)$$

The first term in Eq. (5.30) contributes a dominant energetic attractive force, which is independent of temperature, while the second term generates a repulsive component which is proportional to temperature,  $T$  (Appendix E.1). Thus for  $\Xi \rightarrow \infty$  and  $\tilde{R} \rightarrow \infty$  (which formally corresponds to the zero-temperature limit), the SC theory predicts that the attractive force increases (in agreement with results in Refs. [145, 168]), and saturates to the limiting value

$$\frac{F_{\text{rods}}^{\text{SC}}(d)}{H} \simeq -\frac{e^2 \tau^2}{2\pi\epsilon\epsilon_0} \times \begin{cases} 1/d & d \gg 2R, \\ 3/d & d \simeq 2R, \end{cases} \quad (5.31)$$

(per unit length of the rods  $H$  and in actual units) for large and small axial separations respectively. Here I have used Eqs. (5.28) and (5.30), and that  $F_{\text{rods}}^{\text{SC}} = -\partial \mathcal{F}_N^{\text{SC}} / \partial d$ .

The rescaled *equilibrium* axial separation,  $\tilde{d}_*$ , maintained by such a long-range attraction,

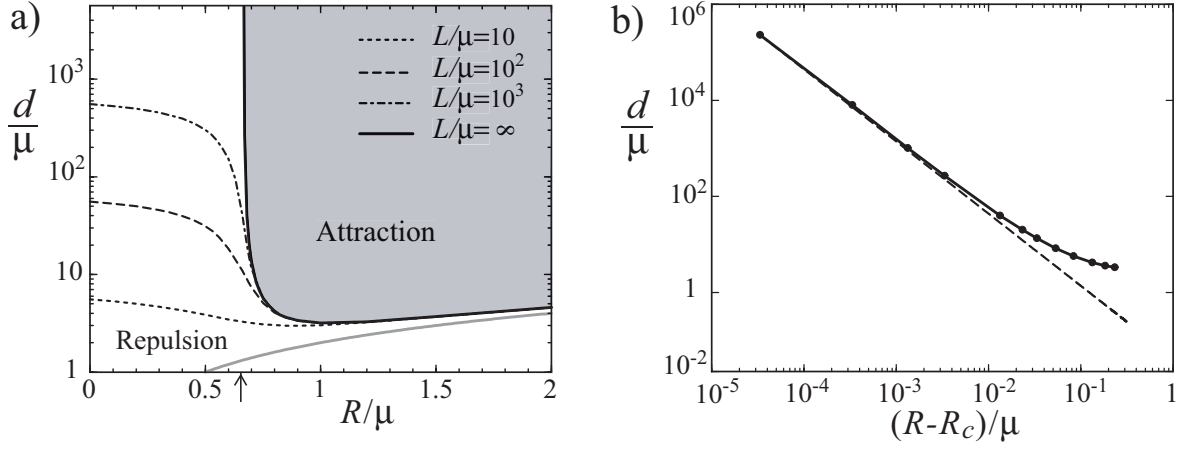


Figure 5.3: a) Regimes of attraction and repulsion for two like-charged rods according to the asymptotic SC theory. The curves show the rescaled equilibrium axial separation,  $\tilde{d}_* = d_*/\mu$ , as a function of the Manning parameter,  $\tilde{R} = R/\mu$ , for confining boxes of different size as indicated on the graph. The curves are obtained numerically by minimization of the free energy (5.22). The thick gray curve corresponds to the contact axial distance  $d = d_{\min} = 2R$ . The unbinding transition of unconfined rods occurs at the threshold Manning parameter  $\tilde{R}_c = 2/3$  (shown by an arrow). b) The equilibrium axial separation of unconfined rods (solid curve with symbols) diverges algebraically in the vicinity of the threshold,  $\tilde{R}_c$ , according to Eq. (5.35). Dashed line shows a power-law fit with the slope  $-3/2$ .

follows by minimizing Eq. (5.30) with respect to  $d$  as

$$\tilde{d}_* \simeq 2\tilde{R} + \frac{2}{3} + \mathcal{O}\left(\frac{1}{\tilde{R}}\right) \quad \text{when } \tilde{R} \gg 1. \quad (5.32)$$

Restoring actual units in Eq. (5.32) and using Eqs. (5.16) and (5.17), one obtains the actual equilibrium surface-to-surface separation of the rods as

$$\delta_* \equiv d_* - 2R_0 \simeq \sigma_{\text{ci}} + \frac{2}{3}\mu + \mathcal{O}(\mu^2), \quad (5.33)$$

when the Manning parameter is sufficiently large (or the Gouy-Chapman length,  $\mu$ , is small). This distance is about the counterion diameter,  $\sigma_{\text{ci}}$ , and indicates a closely packed bound-state for the two rods.

For small Manning parameter  $\tilde{R} < \tilde{R}_c = 2/3$ , on the other hand, qualitatively different features arise (see, e.g.,  $\tilde{R} = 0.3$  in Figure 5.2b). In this case, the effective interaction between the rods exhibits a significant dependence upon the size of the confining box, which is a direct consequence of the de-condensation of counterions. For  $\tilde{R} \ll 1$ , the equilibrium axial separation is obtained approximately as (Appendix E.1)

$$\tilde{d}_* \simeq \frac{\tilde{L}}{\sqrt{\pi}}, \quad (5.34)$$

which tends to infinity with  $\tilde{L} \rightarrow \infty$ , indicating a purely repulsive force between unconfined rods.

In brief, one may specify the attraction and repulsion regimes of two like-charged rods by plotting the equilibrium axial separation  $\tilde{d}_*$  as a function of the Manning parameter, as shown in Figure 5.3a for several different box sizes. The region below each curve shows the repulsion regime and above that is the attraction regime. (These results are obtained by numerical minimization of the full SC free energy, Eq. (5.22).) When the Manning parameter is lowered down to the attraction threshold  $\tilde{R}_c = 2/3$ , the two rods tend to unbind from each other as  $L$  increases to infinity. A continuous unbinding transition occurs in the limit  $L \rightarrow \infty$  (solid curve), which exhibits a universal scaling exponent for the diverging axial distance

$$\tilde{d}_* \sim (\tilde{R} - \tilde{R}_c)^{-\alpha} \quad (5.35)$$

(shown separately in Figure 5.3b), where within our numerical errors

$$\alpha = 3/2. \quad (5.36)$$

### 5.2.3 Comparison with numerical simulations

Several numerical simulations have recently been reported on charged rods [145, 157, 55, 158] and also on more detailed models, which incorporate the charge pattern of DNA [144, 155]. In general, attraction is found for intermediate to large Manning parameter and coupling parameter, which is typically achieved by taking multivalent counterions [145, 157, 55, 158] or small Bjerrum lengths [55].

The emergence of a closely packed bound-state of like-charged rods is established within the simulations [145, 157, 55, 158]. It results from a balance between repulsion at small distances (close to the contact) and attraction at intermediate to large separations. These features agree with the SC predictions on a qualitative level. A quantitative comparison between simulations and the SC theory is meaningful only in the range of parameters where the theory is expected to be valid. Specifically, for a system with finite coupling parameter (e.g., with  $\Xi \sim 10 - 100$ , which is typically the case in the simulations [145, 157, 55]), the SC results (strictly valid only for  $\Xi \rightarrow \infty$ ) are applicable when higher-order correction terms in the  $1/\Xi$ -expansion (5.13) are relatively small. Recall that these correction terms include higher-order electrostatic, as well as counterion-counterion excluded-volume effects (Section 5.1). Here, I first introduce two criteria identifying the regime where these effects are small, and then present a quantitative comparison with recent simulations.

#### Regime of applicability of SC results

For highly charged rods, excluded-volume interactions between counterions may become significant as attraction is accompanied by accumulation of counterions in the narrow intervening region between the rods. At large couplings, counterions tend to line up on opposing surfaces of the rods and along the rods axes forming a correlated inter-locking pattern [157] (see the illustration in Figure 5.1a). The typical distance between counterions at the surface,  $a_z$ , may be estimated from the local electroneutrality condition,  $q = \tau a_z$ , yielding

$$a_z = \frac{q}{\tau}, \quad (5.37)$$

which agrees closely with the results obtained in recent simulations [157]. It is expected that when  $a_z$  is smaller than the counterion diameter,  $\sigma_{ci}$ , i.e.

$$a_z < \sigma_{ci}, \quad (5.38)$$

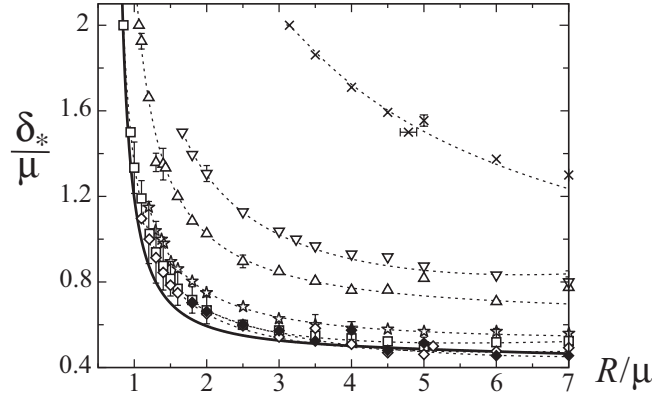


Figure 5.4: Rescaled equilibrium surface-to-surface separation of two like-charged rods,  $\delta_*/\mu = (d_* - 2R)/\mu$ , as a function of Manning parameter,  $\tilde{R} = R/\mu$ . Symbols are the simulation data reported in Ref. [55] for the Rouzina-Bloomfield parameters (from top):  $\gamma_{RB} = 3$  (crosses), 10 (triangle-downs), 15 (triangle-ups), 30 (stars), 40 (squares), 50 (open diamonds) and 60 (filled diamonds). The solid curve is the strong-coupling prediction. Dashed curves are guides to the eye.

excluded-volume repulsions between counterions become important, and the accumulation of counterions between the rods according to the SC mechanism is prohibited. Consequently, the effective electrostatic interaction between the rods may drastically be affected [157].

The importance of higher-order electrostatic effects may be examined in a qualitative fashion using the Rouzina-Bloomfield criterion as demonstrated in Section 2.4.3. Namely, the strong-coupling attraction is expected to emerge when the surface-to-surface distance of the rods,  $\delta = d - 2R_0$ , becomes smaller than the typical distance between counterions at opposing surfaces,  $a_z$ , Eq. (5.37) [148, 150, 151, 152, 48, 43, 45]. Defining the dimensionless *Rouzina-Bloomfield parameter* as

$$\gamma_{RB} = \frac{a_z}{\delta} = \frac{q}{\tau\delta}, \quad (5.39)$$

the strong-coupling attraction regime may be specified by

$$\gamma_{RB} > 1. \quad (5.40)$$

### Numerical simulations

In order to bring out electrostatic features of the like-charge attraction and avoid complications arising from volume interactions [157], I will concentrate on the Molecular Dynamics simulations of the two-rod system performed by Arnold and Holm [55]. In this study, volume interactions between counterions are excluded, but counterions still retain a soft-core excluded-volume repulsion with the rods [55]. The SC results presented in the preceding sections deal with a similar system with the difference that counterion-rod volume interactions were assumed to be of hard-core nature (Section 5.1). The simulation model has a geometry similar to what I have sketched in Figure 5.1 (with periodic boundary conditions employed in  $z$  direction), except that the outer box is cylindrical. (The outer box diameter in simulations is chosen as  $8d$ ; thus for final comparison in Figure 5.4, the theoretical curves are also re-calculated using a similar constraint but using, for simplicity, a square box of edge size

$L = 8d$ . The results are not affected by the box size in the considered range of Manning parameters.) In the simulations, rods are kept at fixed actual surface-to-surface distance,  $\delta$ , with fixed linear charge density,  $\tau$ , and counterion valency,  $q$ , but the Bjerrum length and the rods radius,  $R$ , are varied. Hence, the Gouy-Chapman length,  $\mu = R/(q\ell_B\tau)$ , varies accordingly allowing to span various regimes of coupling parameter and Manning parameter.

In Figure 5.4, the simulation results (symbols) for the equilibrium surface-to-surface distance of rods are shown in rescaled units and as a function of the Manning parameter. The Rouzina-Bloomfield parameter  $\gamma_{\text{RB}}$ , Eq. (5.39), is fixed for each simulation data set. This parameter is related to the coupling parameter,  $\Xi = 2\pi q^3 \ell_B^2 \sigma_s$ , via

$$\Xi = \tilde{R} \tilde{\delta} \gamma_{\text{RB}}, \quad (5.41)$$

and thus gives a measure of deviations from the asymptotic SC limit, as clearly supported by the simulation data in Figure 5.4: the simulated equilibrium axial separation decreases upon increasing  $\gamma_{\text{RB}}$  (from about 3 up to 60) and approaches the strong-coupling curve, which represents a closely packed bound-state of the two rods. The agreement becomes quantitative for the Rouzina-Bloomfield parameter as large as  $\gamma_{\text{RB}} = 50$  and 60 for the whole range of Manning parameters studied in the simulations. Note that, for instance, for a moderate Manning parameter of  $\xi = 3.0$ ,  $\Xi$  increases from 18 for cross symbols up to about 100 for filled diamonds.

Due to convergence limitations, the simulations so far have been limited to the range of Manning parameters  $\tilde{R} > 0.8$  [55]. Nonetheless, the excellent convergence of the data to the SC curve suggests an attraction threshold of about  $\tilde{R}_c = 2/3$  as predicted in Section 5.2.1.

### 5.3 Two like-charged spheres

In this section, I will consider the interaction between two identical like-charged spheres of bare radius  $R_0$  and charge  $-Ze$  that are located at center-to-center distance of  $d$  from each other (Figure 5.5). The spheres are confined in a *cubic* box of edge size  $L$  together with  $N$  neutralizing  $q$ -valent counterions; hence  $Nq = 2Z$ . The Gouy-Chapman length associated with this system is

$$\mu = \frac{1}{2\pi q \ell_B \sigma_s} = \frac{2R^2}{\ell_B q Z}, \quad (5.42)$$

where  $\sigma_s = Z/(4\pi R^2)$  is the surface charge density and  $R$  is the hard-core sphere radius, Eq. (5.16). In analogy with the cylindrical case (see Eq. (5.18)), I shall refer to the ratio between the radius of curvature and the Gouy-Chapman length,

$$\tilde{R} = \frac{R}{\mu} = \frac{\ell_B q Z}{2R}, \quad (5.43)$$

as the *Manning parameter* for charged spheres (see Section 2.3).

To determine the SC effective interaction between spheres, Eq. (5.14), I will follow similar lines as in the preceding sections. The zero-particle and one-particle interaction energies, Eqs. (5.5) and (5.6), are obtained here as

$$\tilde{U}_0 = 4\pi \frac{\tilde{R}^4}{\tilde{d}}, \quad (5.44)$$

$$\tilde{u}(\tilde{x}, \tilde{y}, \tilde{z}) = -2\tilde{R}^2 \left( \frac{1}{\tilde{r}_1} + \frac{1}{\tilde{r}_2} \right), \quad (5.45)$$



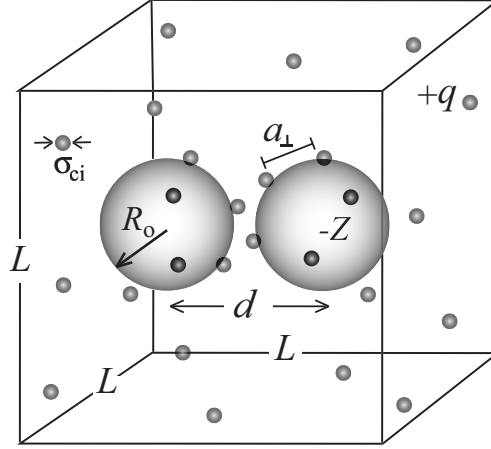


Figure 5.5: Two identical charged spheres of bare radius  $R_0$  and charge  $-Ze$  are considered at center-to-center distance  $d$  in a cubic box of edge size  $L$ , which also contains neutralizing counterions of charge valency  $+q$  (and diameter  $\sigma_{ci}$ ).  $a_{\perp}$  is the typical distance between counterions at the surface that will be considered in Section 5.3.2.

where  $\tilde{r}_{1,2} = [(\tilde{x} \pm \tilde{d}/2)^2 + \tilde{y}^2 + \tilde{z}^2]^{1/2}$  are radial distances from the spheres centers. The SC free energy (5.14) is thus obtained as

$$\frac{\mathcal{F}_N^{\text{SC}}}{Nk_B T} = \frac{\tilde{R}^2}{\tilde{d}} - \ln I, \quad (5.46)$$

where

$$I(\tilde{d}, \tilde{R}, \tilde{L}) \equiv \int d\tilde{x} d\tilde{y} d\tilde{z} \tilde{\Omega} \exp \left[ 2\tilde{R}^2 \left( \frac{1}{\tilde{r}_1} + \frac{1}{\tilde{r}_2} \right) \right], \quad (5.47)$$

in which  $\tilde{\Omega}(\tilde{x}, \tilde{y}, \tilde{z}; \tilde{d}, \tilde{R}, \tilde{L})$  specifies the region accessible for counterions, that is the volume inside the cubic box excluding the two spheres of hard-core radius  $R$ .

The first term in Eq. (5.46) is the bare repulsion between the spheres, and the second term contains energetic and entropic contributions from counterions on the leading order. This term reproduces the binding-unbinding behavior of counterions at charged spheres. It can generate an effective attraction between the spheres as well. To demonstrate this, I first consider two spheres in the limit of infinite box size  $\tilde{L} \rightarrow \infty$ . In this limit, the single-particle partition function,  $I$ , diverges with the box volume as  $I \sim \tilde{V} = \tilde{L}^3$  since the integrand in (5.47) is always positive and bigger than one. Thus the distribution function of counterions around the spheres,  $\sim \exp(-\tilde{u})/I$  (see footnote 2), and also the component of the force contributed by counterions,  $\sim \partial \ln I / \partial \tilde{d} \sim \tilde{L}^{-2}$ , vanish indicating complete de-condensation of counterions and a purely repulsive interaction between unconfined spheres as expected. (Recall from Chapter 2 that spherical macroions can not bind their counterions in an unconfined geometry.) In contrast, it turns out that in a finite confining box, two like-charged spheres can attract each other provided that their Manning parameter is sufficiently large.

Figures 5.6a-d show the typical form of the SC free energy for two spheres in a box, which is calculated numerically (using Monte-Carlo integration methods) from Eq. (5.46). As seen, for small Manning parameter  $\tilde{R}$ , the long-range sphere-sphere repulsion is dominant (Figure 5.6a). But as the Manning parameter exceeds a threshold value of  $\tilde{R}_c^{(1)}$  (which is  $\tilde{R}_c^{(1)} \simeq 3.3$  for  $\tilde{L} =$

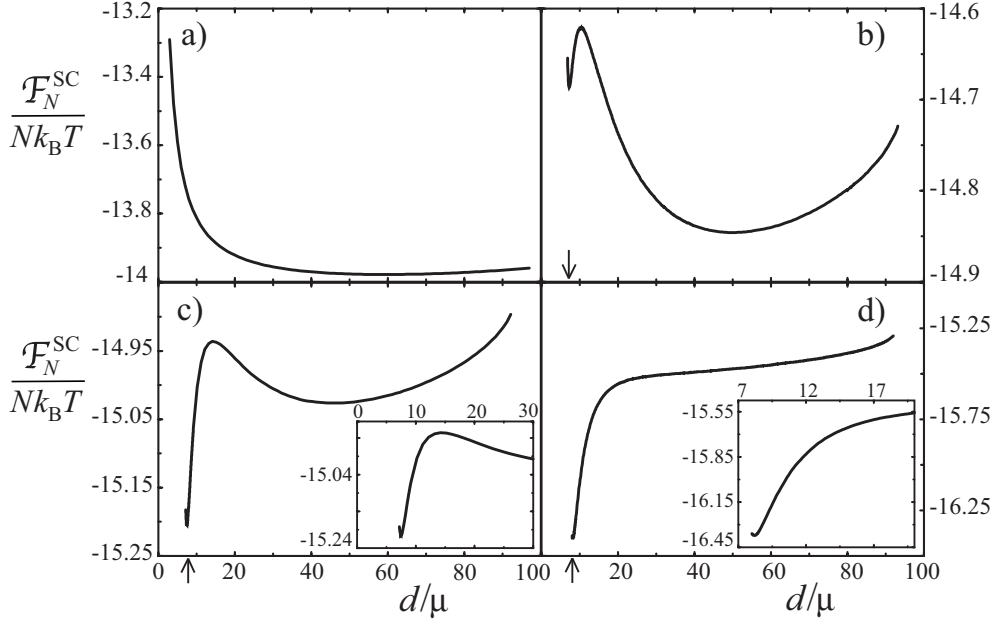


Figure 5.6: The SC free energy of the two-sphere system, Eq. (5.46), plotted as a function of the rescaled center-to-center distance,  $\tilde{d} = d/\mu$ , for different Manning parameters: a)  $\tilde{R} = 1.5$ , b)  $\tilde{R} = 3.4$ , c)  $\tilde{R} = 3.6$  and d)  $\tilde{R} = 4.0$ . The size of the confining box is  $\tilde{L} = 100$  in rescaled units. The insets show a closer view of the small-separation local minimum, the location of which is marked by an arrow. A potential barrier is found in the range  $\tilde{R}_c^{(1)}(\tilde{L}) < \tilde{R} < \tilde{R}_c^{(2)}(\tilde{L})$  (b and c), where  $\tilde{R}_c^{(1)} \simeq 3.3$  and  $\tilde{R}_c^{(2)} \simeq 3.8$  for  $\tilde{L} = 100$ .

100 in the figure), a local minimum is developed at small separations indicating a short-range attraction and a meta-stable bound-state (Figure 5.6b). This attraction regime is separated from the large-distance repulsion regime by a pronounced potential barrier (Figures 5.6b and c). For increasing Manning parameter, the attractive local minimum becomes deeper than the large-distance minimum, and the potential barrier disappears beyond a second threshold of  $\tilde{R}_c^{(2)}$  (which is  $\tilde{R}_c^{(2)} \simeq 3.8$  for  $\tilde{L} = 100$ )—Figure 5.6d. These features indicate a *discontinuous* unbinding transition between a closely packed bound-state and a repulsion-dominated state of two like-charged spheres by varying the Manning parameter. Note that similar features as above are obtained for box sizes that are larger than  $\tilde{L} \simeq 20$ ; for a smaller box size, the attraction regime disappears and only the shallow large-distance minimum is obtained.

A digram representing different regimes of attraction and repulsion for two spheres is shown in Figure 5.7, where I have plotted the locations of the minima (solid curves) of the strong-coupling free energy, Eq. (5.46), as well as the location of its maximum (dashed curves), as a function of the Manning parameter,  $\tilde{R}$ , for fixed  $\tilde{L} = 100$ . The upper branch represents the shallow repulsion-dominated minimum, which is strongly sensitive to the box size. For small  $\tilde{R} \ll 1$ , the equilibrium center-to-center distance increases linearly with the box size as

$$\tilde{d}_* \simeq \sqrt[3]{\frac{3}{4\pi}} \tilde{L}, \quad (5.48)$$

when  $\tilde{L} \rightarrow \infty$  (see Appendix E.2). In contrast, the small-separation minimum (the lower

branch) is nearly independent of the box size. It is maintained by a strong attractive interaction mediated by counterions that tend to accumulate in the intervening region between the spheres. For large  $\tilde{R} \gg 1$ , the approximate form of the SC free energy at small separations around its minimum can be calculated using a saddle-point analysis, which gives (Appendix E.2)

$$\frac{\mathcal{F}_N^{\text{SC}}}{Nk_{\text{B}}T} \simeq -7\frac{\tilde{R}^2}{\tilde{d}} - \ln(\tilde{d} - 2\tilde{R}). \quad (5.49)$$

For increasing Manning parameter to infinity (or decreasing temperature to zero), the repulsive contribution (second term in Eq. (5.49)) vanishes and the energetic attraction (first term in Eq. (5.49)), which is independent of temperature, dominates. The resultant limiting force between spheres at small separation ( $d \simeq 2R$ ) is given by

$$F_{\text{spheres}}^{\text{SC}}(d) = -7\frac{Z^2e^2}{4\pi\epsilon\epsilon_0d^2} \quad (5.50)$$

in actual units, which agrees with the results obtained in other works [179]. The rescaled equilibrium center-to-center distance is obtained from Eq. (5.49) as

$$\tilde{d}_* \simeq 2\tilde{R} + \frac{4}{7} + \mathcal{O}\left(\frac{1}{\tilde{R}}\right) \quad \text{when } \tilde{R} \gg 1. \quad (5.51)$$

Restoring the actual units, one finds the actual equilibrium surface-to-surface separation as

$$\delta_* \equiv d_* - 2R_0 \simeq \sigma_{\text{ci}} + \frac{4}{7}\mu + \mathcal{O}(\mu^2), \quad (5.52)$$

using Eqs. (5.16) and (5.42). Note that this result is obtained for sufficiently large Manning parameter (or small Gouy-Chapman length,  $\mu$ ) and thus predicts an equilibrium surface separation of about the counterion diameter  $\sigma_{\text{ci}}$ .

### 5.3.1 Attraction threshold

The strong-coupling attraction regime for two like-charged spheres may be specified by  $\tilde{R} > \tilde{R}_c^{(1)}$ , where the threshold Manning parameter  $\tilde{R}_c^{(1)}$  actually depends on the confining box size, i.e.  $\tilde{R}_c^{(1)} = \tilde{R}_c^{(1)}(\tilde{L})$ . As shown in the inset of Figure 5.7, the calculated values of  $\tilde{R}_c^{(1)}$  (symbols) exhibit a logarithmic dependence on the box size, which is roughly given by

$$\tilde{R}_c^{(1)} = a + b \ln \tilde{L}, \quad (5.53)$$

where  $a \simeq 0.55$  and  $b \simeq 0.6$  (the fitted function (5.53) is shown by a solid curve). The weak dependence of the attraction threshold on the confinement size can explain the stability of compact clusters of spheres in quite large confinement volumes  $\tilde{L} \gg 1$  [146, 148, 150, 151, 152], since the Manning parameter only needs to exceed a moderate value ( $\sim \ln \tilde{L}$ ) for like-charged spheres to fall into the attraction-dominated regime.

### 5.3.2 Comparison with numerical simulations

Several simulations [146, 147, 148, 150, 151, 152, 153, 154] have recently considered the effective electrostatic attraction of like-charged spheres in the strong coupling regime (e.g., using multivalent counterions or in some cases, low dielectric constants [148] or low temperatures

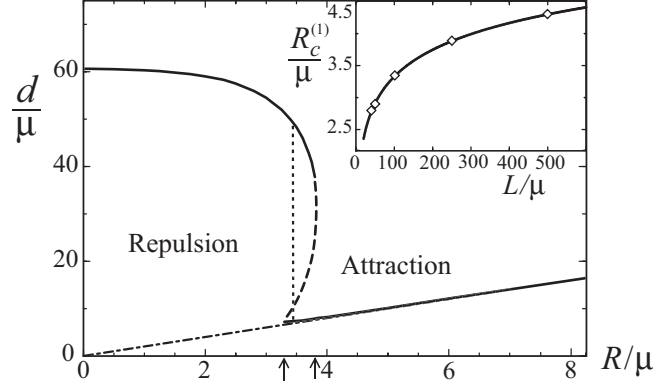


Figure 5.7: Regimes of attraction and repulsion for two like-charged spheres according to the asymptotic SC theory. The solid curves show the rescaled equilibrium center-to-center distance between spheres as a function of the Manning parameter,  $\tilde{R} = R/\mu$ , for a confining cubic box of rescaled size  $\tilde{L} = 100$ . The dashed curve corresponds to the maximum of the SC free energy and the dotted vertical line shows the Manning parameter for which the values of the two minima of the free energy are equal, i.e.  $\tilde{R} \simeq 3.5$ . The locations of threshold Manning parameters  $\tilde{R}_c^{(1)} \simeq 3.3$  and  $\tilde{R}_c^{(2)} \simeq 3.8$  are shown by two arrows. The dot-dashed line shows the contact separation  $d = d_{\min} = 2R$ . Inset: The attraction threshold  $\tilde{R}_c^{(1)}$  (symbols) increases weakly with the rescaled box size,  $\tilde{L}$ , displaying a logarithmic dependence as given by Eq. (5.53) (shown by the solid curve).

[154]). The strength of attractive force is sufficiently large that leads to closely packed bound-states (including large aggregates) between like-charged spheres [146, 147, 148, 150, 151, 152, 153, 154]. The bound-state corresponds to an attractive small-separation minimum in the potential of mean-force between spheres [146, 147, 150, 151, 152], which is separated by a pronounced potential barrier from a repulsion regime at large separations (see, e.g., Fig. 1 in Ref. [146]). On the other hand, it was shown that the attractive minimum and the potential barrier are not robust and exhibit a dependence upon the size of the confinement volume [146]: the depth of the attractive minimum and at the same time, the height of the potential barrier, decreases with increasing volume leading to a long-range repulsion between spheres in a sufficiently large confining box as expected. The qualitative form of the simulated interaction potential [146] indeed agrees with the SC results shown in Figure 5.6. Note also that in agreement with simulations [146], the SC results imply that for a given Manning parameter between the two thresholds  $\tilde{R}_c^{(1)} < \tilde{R} < \tilde{R}_c^{(2)}$ , the height of the free energy barrier decreases and the effective attraction diminishes by increasing the box size. The existence of a potential barrier in the interaction potential of *confined* spheres can result in meta-stable bound-states between spheres [154] and also indicates a first-order phase transition (phase separation between a dilute and an aggregated phase) in the thermodynamic limit [146, 150, 151, 152].

Table 5.1 presents typical parameters from some of recent simulations. In the two last columns, I compare the SC prediction for the equilibrium surface-to-surface separation between spheres (in actual units),  $\delta_* = d_* - 2R_0$ , with the simulation results,  $\delta_{\text{sim}}$  (if explicitly measured), which follow from the location of the minimum of the simulated potential of mean force or equivalently, from the pair distribution function of spheres. The values of  $\delta_*$  are calculated by numerical evaluation of the full SC free energy (5.46) for the corresponding

simulation parameters, in which I have also accounted for the finite size of counterions (Section 5.1). (Note that the analytical expression (5.52) gives an approximate value for  $\delta_*$ , which is valid only up to the first order in  $\mu$ .) As seen, there is a reasonable semi-quantitative agreement between the theoretical predictions and the simulation results. In fact, the equilibrium surface-to-surface distance in these simulations appears to be about the counterion diameter (see the Discussion in Ref. [151, 152]). This also follows from the strong-coupling prediction, Eq. (5.52), because for highly charged spheres, the Gouy-Chapman length is indeed small as compared with the counterion diameter.

In the table, I also show the estimated values for the typical separation between counterions at the sphere surfaces,  $a_\perp$  (see the illustration in Figure 5.5). This quantity is set by the local electroneutrality condition,  $\pi a_\perp^2 \sim q/\sigma_s$ , as

$$a_\perp \simeq R \sqrt{\frac{4q}{Z}} \quad (5.54)$$

up to a geometric factor of the order of one. As seen,  $a_\perp$  is larger than the Gouy-Chapman length ( $\mu \sim 1\text{\AA}$ ) in these simulations leading to a large coupling parameter,  $\Xi$ . Recall that the ratio between these two length scales is related to  $\Xi$  as  $\tilde{a}_\perp = a_\perp/\mu \sim (2\Xi)^{1/2}$  (see Chapter 2), where the coupling parameter,  $\Xi = 2\pi q^3 \ell_B^2 \sigma_s$ , for charged spheres reads

$$\Xi = \frac{q^3 \ell_B^2 Z}{2R^2}. \quad (5.55)$$

Moreover, the strong-coupling (Rouzina-Bloomfield) attraction criterion,

$$\delta < a_\perp, \quad (5.56)$$

is also fulfilled as the equilibrium sphere separation,  $\delta_{\text{sim}}$ , appears to be smaller than  $a_\perp$ . These observations indicate that higher-order electrostatic effects that enter in the sub-leading terms of the  $1/\Xi$ -expansion of the free energy (Section 5.1) are relatively small. In fact, the excluded-volume repulsion between counterions, which enters through these higher-order terms, is also expected to be small in these simulations, since the lateral separation of counterion at spheres is larger than the counterion size,  $\sigma_{\text{ci}}$ . Therefore, the simulation parameters indeed cover the regime, where the asymptotic strong-coupling theory is expected to be valid.

## 5.4 Conclusion and discussion

In this chapter, I investigate the effective electrostatic interaction between like-charged cylindrical and spherical macroions in the regime of large coupling parameter,  $\Xi$ , which is achieved for large counterion valency, large charge densities on macroions, low dielectric constants, or for low temperatures. In this regime, interactions between macroions are dominated by strong counterionic correlations: counterions form highly correlated layers at macroions giving rise to an energetic counterion-mediated attraction. For  $\Xi \rightarrow \infty$ , the leading-order contribution to the interaction free energy is calculated via the strong-coupling theory, which is obtained from a systematic  $1/\Xi$ -expansion series (virial expansion). It represents a finite-temperature theory incorporating both energetic effects (which are responsible for the strong-coupling attraction) as well as the entropic contribution from counterions. The latter enables the SC theory to reproduce the de-condensation of counterions at small Manning parameters and thus yield

Simulation	$q$	$Z$	$\ell_B(\text{\AA})$	$R(\text{\AA})$	$\sigma_{ci}(\text{\AA})$	$L(\text{\AA})$	$\mu(\text{\AA})$	$\tilde{R}$	$\Xi$	$\tilde{R}_c^{(1)}$	$a_\perp(\text{\AA})$	$\delta_{sim}(\text{\AA})$	$\delta_*(\text{\AA})$
Ref. [146]	2	10	7.01	7	3.3	50-200	1.07	8.1	26	2.8-3.7	7.7	2.5	3.41
Ref. [147]	2	20	7.14	10	4	$10^2$	1.01	11.9	28	3.3	7.5	4	4.10
Ref. [148]	2	32	112	48.9	4.4	$10^2$	0.73	70.1	615	3.3	25.5	–	4.41
Ref. [150]	3	60	7.15	20	4	$10^2$	0.75	29.2	85	3.3	9.8	4	4.05
Ref. [153]	3	12	7.15	10	2	$10^2$	0.94	11.7	68	3.3	11.0	–	2.09

Table 5.1: Parameters from simulations on highly charged spheres:  $q$  is the charge valency of counterions with diameter  $\sigma_{ci}$ ,  $Z$  is the charge valency of spheres with radius  $R$ , and  $\ell_B$ ,  $\mu$ ,  $\xi$  and  $\Xi$  are the Bjerrum length, the Gouy-Chapman length, Eq. (5.42), the Manning parameter, Eq. (5.43), and the coupling parameter, Eq. (5.55), respectively.  $L$  is the confining box size and  $\tilde{R}_c^{(1)}$  is the estimated attraction threshold (Section 5.3.1). The last two columns show the equilibrium surface-to-surface distance obtained in these simulations,  $\delta_{sim}$  (if explicitly measured), and the corresponding SC prediction,  $\delta_*$ . Some of the numbers are given up to the order of magnitude, and the extracted values of  $\delta$  from simulations have a typical resolution of about 1Å. Note that in estimating the values of  $\Xi$ ,  $\mu$  and  $a_\perp$ , the finite size of counterions is also accounted for assuming that they have hard-core volume interactions with macroions [147, 148, 150, 151, 152, 153]—see Section 5.1.

a consistent picture for the whole range of Manning parameters. Note however that in this latter regime, counterionic correlations vanish and the macroions repel each other.

For sufficiently large Manning parameter  $\tilde{R} = R/\mu$ , the SC theory predicts a closely packed bound-state between macroions maintained by a long-range attractive force, which varies with distance,  $d$ , as  $\sim d^{-1}$  for two rods, and as  $\sim d^{-2}$  for two spheres (this force is of constant strength for charged plates—see Chapter 2). As shown, the SC predictions for the attraction regime and the closely packed bound-state of two like-charged rods agree quantitatively with recent numerical simulations for elevated coupling strength (e.g., for  $\Xi \sim 10^2$ ) [55]. For charged spheres, the SC predictions (for equilibrium bound-state separation and the effective interaction potential) show a qualitative agreement with the simulations [146, 147, 150, 151, 152, 153]. Note that since numerical simulations can only handle systems with a *finite* coupling parameter, the agreement with the SC theory (strictly valid for  $\Xi \rightarrow \infty$ ) is limited to the regime determined by the Rouzina-Bloomfield criterion, that is small surface-to-surface separation as compared with the counterion spacing at the apposed surfaces of macroions (Chapter 2). In this regime, a dominate energetic coupling is mediated by *single* counterions sandwiched between macroions, which gives rise to a single-particle structure for the SC free energy.

For decreasing Manning parameter, the counterion-induced attraction weakens against the bare repulsion, and macroions exhibit an unbinding transition. For charged rods, this transition is found to be continuous. It occurs at a universal value of the Manning parameter  $\tilde{R}_c = 2/3$  in an infinitely large confinement volume and displays a power-law behavior for diverging axial distance as  $d_* \sim (\tilde{R} - \tilde{R}_c)^{-3/2}$ . Therefore,  $\tilde{R}_c = 2/3$  represents a universal attraction threshold for two *unconfined* rods. Charged spheres, on the contrary, only exhibit attraction in a finite confining box, where the transition between attraction and repulsion regimes is found to be non-universal (volume dependent) and discontinuous due to a potential barrier in the interaction free energy. The attraction threshold for two spheres increases

logarithmically with the box volume, which indicates that the bound-state of strongly coupled spheres is highly stable against changes in the confinement volume as observed also in recent simulations [146, 148, 150, 151, 152].

The SC attraction regime can be realized in experiments by choosing a coupling parameter of the order  $\Xi \sim 10^2$ , and a Manning parameter of the order  $\tilde{R} \sim 10$  for charged spheres and  $\tilde{R} > 1$  for charged rods. For instance, in aqueous solutions of DNA (with radius  $R_0 \simeq 10\text{\AA}$  and linear charge density  $\tau e \simeq 6 e/\text{nm}$ ), one has  $\tilde{R} \simeq 8$  and  $\Xi \simeq 25$  in the presence of divalent counterions, and  $\tilde{R} \simeq 12$  and  $\Xi \simeq 80$  for trivalent counterions such as spermidine. In colloidal dispersions, an aqueous solution of highly charged surfactant micelles of, for example, typical radius  $R_0 \simeq 20\text{\AA}$  and charge valency  $Z \simeq 60$  represents the Manning parameter and the coupling parameter of the order of  $\tilde{R} \simeq 30$  and  $\Xi \simeq 100$  for trivalent counterions.

Here I did not investigate possible thermodynamic phase transitions triggered by attractive strong-coupling forces. There has been indication of an attraction-induced phase separation in the system of like-charged spheres from recent numerical simulations [146, 150, 151, 152, 153]. To study these transitions, one should account for additional entropic contribution from fluctuating macroion-macroion distance coordinate, which are not considered within the present study. This provides an interesting subject for the application of the SC theory in the future.

Another interesting problem is to examine the influence of additional salt on the interactions in the strong-coupling limit. Qualitatively, one can associate the size of the confinement box considered in the present study with the Debye screening length. Thus, addition of salt is expected to matter only close to the unbinding threshold of macroions. Other subjects which are relevant for the interaction between macroions include the effect of finite polymer stiffness, the discrete charge pattern of macroions [144, 155, 173, 176, 177, 179, 180, 156], and bundling of many charged polymers [31, 33, 34, 149, 168, 179, 186].





## Chapter 6

# Polyelectrolyte Brushes: Non-linear osmotic regime

Polyelectrolyte brushes are layers of charged polymer chains that are densely end-grafted onto a surface. Since charged brushes typically trap their counterions and form a layer of very high internal ionic concentration, their structure and behavior is rather insensitive to the amount of externally added salt. This gives rise to a wide range of applications for stabilization and surface functionalization of charged and neutral colloids [15, 191]. In recent years, polyelectrolyte brushes have been subject of extensive investigations both theoretically [192, 193, 16, 194, 195, 196, 197, 198, 199, 200, 201, 202, 203, 204, 205, 206] and experimentally [207, 208, 209, 210, 211, 212, 213, 214, 215, 216, 217], which have revealed the detailed phase behavior of these systems. Of particular importance is the behavior of the equilibrium height of the brush layer (brush thickness) as a function of the grafting density. One may distinguish a few scaling regimes for this quantity, which result from the interplay between steric, entropic and electrostatic contributions.

In strongly charged brushes, i.e. when both grafting density and charge fraction of polyelectrolyte chains are sufficiently large, most of the counterions are trapped inside the brush. For not too high grafting densities, the repulsive osmotic pressure of counterions is the major effect that tends to swell the chains and balances their elastic stretching pressure. This regime is known as the *osmotic brush regime*. According to standard scaling theories [16, 194], the equilibrium thickness of the osmotic brush is independent of the grafting density. For very large grafting densities, steric effects dominate over electrostatic interactions and the excluded-volume repulsions (in good solvent conditions) balance the elastic pressure on the chains, leading to the so-called quasi-neutral brush regime [194, 199]. The effects of excluded-volume interactions have also been studied in poor solvent conditions [195]. On the other hand, for larger charge fractions or large Bjerrum lengths, the electrostatic correlation between mobile counterions and oppositely charged monomers comes into play and generates a strong attractive pressure on the chains, which leads to the collapsed brush regime [194, 203, 204, 205].

In weakly charged brushes with small grafting density and charge fraction of the chains, the counterion cloud extends far beyond the brush height and their osmotic pressure becomes irrelevant against uncompensated electrostatic repulsion between charged monomers. This results in the charged or Pincus brush regime, where the elastic and the electrostatic pressures are balanced [16].

In this chapter, I shall concentrate on the salt-free osmotic brushes on a planar grafting surface and in the *weak-coupling* regime, that is at moderate to small Bjerrum lengths and low counterion valency, where electrostatic correlations are negligible. This regime has been extensively studied by experimental as well as numerical methods. In particular for osmotic brushes, it has been shown both in experiments [216, 217] and simulations [206] that the brush thickness varies weakly with the grafting density, a trend which contrasts the standard scaling results [16, 194]. These scaling theories are based on two main assumptions: i) the charges of both monomers and counterions are assumed to be distributed uniformly inside the brush, and ii) the chain elasticity is treated within the linear (Gaussian) approximation.

Here I will present a mean-field cell-model study [103] as well as a non-linear scaling theory [216], which demonstrate that the observed behavior for the osmotic brush, which will be referred to as the *non-linear osmotic brush regime*, may be explained on a semi-quantitative level by incorporating non-linear effects that go beyond the standard scaling description. Namely, I will account for the laterally non-uniform distribution of monomers and counterions inside the brush as well as the non-linear elasticity of the chains (as required by their strong stretching in the osmotic regime). While inhomogeneous distribution of counterions inside the brush matters at intermediate to small grafting densities, the self-volume occupied by highly stretched and laterally localized polymer chains plays an important role at large grafting densities. This volume remains inaccessible to surrounding counterions. It is assumed to be conserved, which is a simple way to account for the coupling between lateral and longitudinal degrees of freedom: as chains shrink (at a fixed grafting density), the available volume for counterions decreases accordingly, leading to an enhanced osmotic pressure.

In Section 6.1, I shall focus on the non-linear scaling description of the brush, in which, for simplicity, the inhomogeneous charge distributions inside the brush is neglected, but the polymer self-volume as well as the non-linear elasticity is taken into account. This leads to a linearly increasing brush height with the grafting density which is compared with both experiments [216, 217] and simulations [206, 216] displaying a reasonable agreement. Next, I will present a mean-field cell model (Section 6.2) to improve upon the non-linear scaling theory by accounting for *lateral* electrostatic effects (including lateral variation of the counterionic density profile around polyelectrolyte chains) within the framework of the non-linear Poisson-Boltzmann theory. While the non-linear scaling theory is only applicable at large grafting densities, the present mean-field analysis can account for the brush behavior in the whole range of grafting densities (as long as the osmotic condition is preserved, e.g., using sufficiently long chains). It displays a non-monotonic dependence on the grafting density: At moderate grafting densities, the brush height is found to increase with a weaker rate than what predicted by the scaling analysis, due to an interplay between lateral electrostatics and the conservation of the polymer volume. At small grafting densities, the volume constraint becomes irrelevant and the mean-field cell model predicts re-stretching of the chains due to an increasing electrostatic pressure acting on the chains. The dependence of the brush thickness on the grafting density in this limit is regulated by the counterion-condensation process around the chains.

An inhomogeneous distribution of counterions in lateral directions has been recently observed both in simulations [204, 205, 206] and experiments [210, 212, 214, 215]. Experimental data on spherical charged brushes indicate that the counterion distribution around single chain indeed follows the the non-linear PB predictions as obtained within the cylindrical-cell-model approach [37, 38]. On the other hand, chains are found to be stretched up to 60-80% of their contour length [206, 208, 209, 210, 212, 214, 216, 217], which necessitates the use of

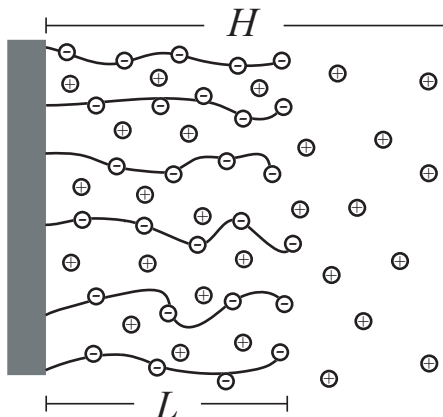


Figure 6.1: Schematic geometry of a charged brush with  $L$  and  $H$  denoting the brush height and the height of the counterion layer, respectively.

non-linear elasticity models [200, 202]. But it should be noted that the elasticity model by itself does not generate a grafting-density dependence for the brush height [202].

## 6.1 Non-linear scaling theory for the osmotic brush

An analytical theory for polyelectrolyte brushes relies on a number of simplifying assumptions. The full theoretical problem is intractable because the degrees of freedom of the polymer chains and the neutralizing mobile counterions are coupled. The schematic geometry of the brush system is visualized in Figure 6.1: the polymer chains are assumed to extend in average to a distance  $L$  from the anchoring surface, and the counterions in general form a layer with a thickness  $H$ . As will be shown later, for strongly charged brushes, the counterion layer height is typically very close to the polymer layer height.

To establish a *scaling theory*, I start by constructing the total free energy of the brush *per unit area* as

$$\mathcal{F}_{\text{tot}} = \mathcal{F}_{\text{chain}} + \mathcal{F}_{\text{ci}} + \mathcal{F}_{\text{int}}, \quad (6.1)$$

which is a sum of separate contributions from polymer chains,  $\mathcal{F}_{\text{chain}}$ , contributions from the counterions,  $\mathcal{F}_{\text{ci}}$ , and an electrostatic interaction term which couples polymers and counterions,  $\mathcal{F}_{\text{int}}$ . The main contribution to the polymer free energy comes from the elastic response due to the stretching of chains, hence  $\mathcal{F}_{\text{chain}} \simeq \mathcal{F}_{\text{elas}}$ . For a freely-jointed-chain model, the elastic free energy has a purely entropic origin and can be calculated exactly (Section 6.2.3). Here only the asymptotic expressions for weak and for strong stretching is needed, which read (per unit area)

$$\frac{\mathcal{F}_{\text{elas}}}{k_{\text{B}}T} \simeq \begin{cases} 3\rho_{\text{a}}L^2/(2N_m b_0^2) & L \ll N_m b_0, \\ -N_m \rho_{\text{a}} \ln(1 - L/N_m b_0) & L \simeq N_m b_0, \end{cases} \quad (6.2)$$

which are proportional to the grafting density,  $\rho_{\text{a}}$ . Here  $N_m$  denotes the number of monomers per chain and  $b_0$  is taken as the center-to-center distance between monomers along the polymer backbone (equal to diameter for spherical monomers). For a fully stretched chain,  $L$  equals

the contour length  $L_0 = N_m b_0$ . The weak-stretching term is the standard linear (Gaussian-chain) elasticity [16, 194]. For the highly stretched situations typically encountered in highly charged brushes, the strong-stretching term (second relation in Eq. (6.2)) is more appropriate and leads to a few changes in the results as will be explained later.

The counterion free energy,  $\mathcal{F}_{\text{ci}}$ , contains entropic contributions (due to the confinement of the counterions inside a layer of thickness  $H$ ) as well as energetic contributions from inter-counterionic interactions. For high grafting densities, entropy of confinement of counterions is the dominant effect (Sections 6.2.4 and 6.3). To estimate this later quantity, I shall employ a free-volume approximation very much in the spirit of the van-der-Waals equation of state for the liquid-gas system. For this I assume an effective hard-core volume of  $v_{\text{eff}}$  for a single polyelectrolyte chain, which reduces the free volume available for counterions inside the brush. The entropic free energy of counterions thus reads (per unit area)

$$\frac{\mathcal{F}_{\text{ci}}}{k_{\text{B}}T} = \rho_{\text{a}} N_m f \left[ \ln \left( \frac{\rho_{\text{a}} N_m f}{H - \rho_{\text{a}} v_{\text{eff}}} \right) - 1 \right], \quad (6.3)$$

where  $f$  is the charge fraction of the chains. Note that throughout this section, I will assume that monomers and counterions are *monovalent* particles. Generalization to multivalent particles is straight forward and will be considered in Section 6.2.

This free-volume theory takes the hard-core interactions between the polymer monomers and the counterions into account in a non-linear fashion. In the limit of vanishing polymer self-volume,  $v_{\text{eff}} \rightarrow 0$ , one recovers the standard ideal entropy expression. As the volume available for the counterions in the brush, which per polymer is  $H/\rho_{\text{a}}$ , approaches the self-volume of the polymers,  $v_{\text{eff}}$ , the free energy expression (6.3) diverges, that means, the entropic prize for that scenario becomes infinitely large. The self-volume of the polymers is roughly independent of the brush height (i.e. remains constant as the chain extension varies), and can be written in terms of the monomer hard-core (or effective) diameter  $\sigma_{\text{eff}}$  and the polymer contour length  $N_m b_0$  as,  $v_{\text{eff}} = N_m b_0 \sigma_{\text{eff}}^2$  (note that  $\sigma_{\text{eff}}$  takes into account the monomer and the counterion diameters, and that the monomers may be bulky with a lateral dimension larger than  $b_0$ ). This leads to the final expression

$$\frac{\mathcal{F}_{\text{ci}}}{k_{\text{B}}T} = \rho_{\text{a}} N_m f \left[ \ln \left( \frac{\rho_{\text{a}} N_m f}{H - \rho_{\text{a}} N_m b_0 \sigma_{\text{eff}}^2} \right) - 1 \right]. \quad (6.4)$$

Finally, the electrostatic interaction between polyelectrolytes and counterions is considered on the mean-field level. For the scaling analysis in this section, I assume the charges are *smearred out* over the brush region ( $0 < z < L$ ) and over the polymer-free region ( $L < z < H$  with  $z$  measuring the direction perpendicular to the anchoring surface. For this situation,  $\mathcal{F}_{\text{int}}$  has been calculated using a box-model in Ref. [203] and reads

$$\frac{\mathcal{F}_{\text{int}}}{k_{\text{B}}T} = \frac{2\pi}{3} \ell_{\text{B}} (\rho_{\text{a}} N_m f)^2 \frac{(H - L)^2}{H}. \quad (6.5)$$

An electrostatic attractive force arises when the counterion layer extends over the polymer layer, i.e. when  $H > L$ . This is the driving force that keeps the counterions inside the brush layer. This force will be important in order to estimate when counterions start to leave the brush as will be discussed later [216]. Note that the above estimate for  $\mathcal{F}_{\text{int}}$  is valid as long as electrostatic correlations (that are neglected within mean-field theory and can indeed lead to an additional attractive pressure on the chains [203]) are small, i.e. for moderate to small

Bjerrum lengths (e.g.,  $\ell_B = e^2/(4\pi\epsilon\epsilon_0k_B T) \sim 1$  nm, which is the typical case for aqueous solutions in room temperature) and for low-valency counterions [43].

The standard osmotic brush regime [16, 194] results from balancing the elastic stretching term for small stretching,  $L \ll N_m b_0$ , Eq. (6.2), with the counterion entropy in the absence of a polymer self-volume (which is Eq. (6.4) in the limit of  $\sigma_{\text{eff}} \rightarrow 0$ ), and for  $H = L$ . The result from minimizing the resulting free energy with respect to the brush height  $L$  gives the optimal height  $L_*$  as [16, 194]

$$\frac{L_*}{N_m b_0} \simeq \sqrt{\frac{f}{3}}. \quad (6.6)$$

It is clear that for fully charged polymers ( $f = 1$ ), the predicted stretching in Eq. (6.6) goes beyond the assumption of weak stretching.

In the strongly stretched osmotic brush regime, one may choose the strong stretching version of the chain elasticity in Eq. (6.2) and balance it with the counterion entropy for vanishing polymer self-volume and for the case  $H = L$  (Eq. (6.4)). The result is

$$\frac{L_*}{N_m b_0} \simeq \frac{f}{1+f}, \quad (6.7)$$

which is the large-stretching analogue of Eq. (6.6). The maximal stretching predicted from this equation is obtained for  $f = 1$  and corresponds to 50% of the contour length. This height is considerably smaller than what is observed in simulations and experiments (Figures 6.2 and 6.3). Moreover, the predicted brush height in Eq. (6.7) does not depend on the grafting density. It transpires that something is missing in the above scaling description. This something is proposed to be the entropic pressure which increases as the volume within the brush is progressively more filled up by the polymer self-volume. The fact that the non-linear elasticity of the chains by itself does not lead to a grafting-density dependence for the brush height has also been noted in previous studies [200, 202].

To demonstrate the *non-linear osmotic brush regime*, I combine the strong stretching (non-linear) version of the chain elasticity in Eq. (6.2) with the counterion entropy, Eq. (6.4), in the presence of a finite polymer self-volume and for  $H = L$ . Minimizing the combined free energy with respect to  $L$ , the equilibrium brush height is obtained as

$$\frac{L_*}{N_m b_0} \simeq \frac{f + \rho_a \sigma_{\text{eff}}^2}{1+f}, \quad (6.8)$$

which exhibits a linear dependence on the grafting density. In the limit of maximal grafting density  $\rho_a \sigma_{\text{eff}}^2 \rightarrow 1$ , that is close packing, the brush height reaches the maximal value  $L_0 = N_m b_0$ , as one would expect: Compressing the brush laterally increases the vertical height and finally leads to a totally extended chain structure.

One main approximation in the preceding analysis is the assumption that all counterions stay localized in the brush layer, i.e.  $H = L$ , which will be analyzed critically now. To get a feeling for the involved forces, I will first consider the confinement of a layer of counterions at a planar charged surface. I take the electrostatic interaction energy (6.5) for an infinitely thin brush layer  $L = 0$  and balance it with the confinement entropy (6.4) for  $\sigma_{\text{eff}} = 0$ , which yields the optimal counterion layer height  $H_* = 3/(2\pi\ell_B N_m f \rho_a) = 3\mu$ . This result has the same scaling as the Gouy-Chapman length  $\mu = 1/(2\pi\ell_B N_m f \rho_a)$ , a measure of the extend of counterion layers [1, 2], and thus shows that the scaling approach reproduces the result from the exact analysis of the Poisson-Boltzmann approach (see Chapter 2). Next, I will consider

the counterion layer in the presence of a finite brush height  $L$ . I will therefore minimize the sum of the electrostatic interaction energy, Eq. (6.5), and the counterion confinement entropy, Eq. (6.4), with respect to the counterion layer height  $H$  for vanishing polymer diameter  $\sigma_{\text{eff}} = 0$ , and obtain the result (to first order in powers of  $[H_* - L]/L$ )

$$H_* = L + 3\mu/2. \quad (6.9)$$

This gives the counterion layer height corresponding to the results in Eqs. (6.6) and (6.7) for the brush height. Since for a typical highly charged brush, the Gouy-Chapman length,  $\mu$ , is of the order of one Angstrom or less, the counterion layer basically has the same height as the brush layer. In other words, the counterions are completely trapped inside the brush for vanishing polymer radius, in agreement with the simulation results shown in Figure 6.2. Now I perform the same estimate for finite polymer volume. Minimizing the sum of the electrostatic interaction energy (6.5) and the counterion confinement entropy (6.4) for finite  $L$  and finite  $\sigma_{\text{eff}}$ , one finds (to first order in powers of  $[H_* - L]/L$ )

$$H_* = L + \frac{3\mu}{2(1-\eta)}, \quad (6.10)$$

where  $\eta = \rho_a \sigma_{\text{eff}}^2 N_m b_0 / L$  measures the ratio of the polymer excluded-volume  $v_{\text{eff}} = \sigma_{\text{eff}}^2 N_m b_0$  and the volume in the brush available for a single polymer  $L/\rho_a$ , and thus the degree of close-packing in the brush. For a grafting density of  $\rho_a = 0.1 \text{ nm}^{-2}$ , a polymer length of  $L = 15 \text{ nm}$  and a monomer number of  $N_m = 136$  (and monovalent particles), as used in the experiments (see below), one obtains a Gouy-Chapman length of  $\mu = 1/(2\pi\ell_B N_m f \rho_a) \simeq 0.01 \text{ nm}$ . Therefore, even for a close-packing fraction of 99%, i.e. for  $\eta = 0.99$ , the difference between the counterion layer height and the brush height is only about a nanometer, which is rather negligible compared to the total brush height. This argument reflects the strong electrostatic interaction between the brush and the counterion layer in the osmotic regime, and it shows that the underlying assumption that all counterions are trapped inside the brush is justified, even for cases where the non-linear osmotic pressure is rather large and leads to a brush height very close to full extension of the chains.

### 6.1.1 Comparison with Molecular Dynamics simulations

Computer simulations have been performed extensively to investigate polyelectrolyte brushes both at strong [203, 204, 205] and low [206] electrostatic couplings.

Here I shall consider simulations performed at low electrostatic coupling, which exhibit the osmotic brush regime [206]. The simulation model adopts a freely-jointed bead-chain model (using the so-called finite extensible non-linear elastic potential) for polymer chains end-grafted onto a rigid surface (with monomers and counterions modeled as soft spheres of equal diameter  $\sigma_{\text{ci}} = \sigma_{\text{m}} = \sigma$  using a repulsive Lennard-Jones potential). All particles are monovalent ( $q_{\text{m}} = q = 1$ ) and moderate values are chosen for the Bjerrum length, i.e.  $\ell_B \sim \sigma$ . The average bond length,  $b_0$ , (which is the result of the interplay between soft LJ repulsion and the bond potential) is almost unaffected by the electrostatic repulsions and roughly equals the particle diameter,  $b_0 = 0.98\sigma$  [206, 103].

Figure 6.2a shows a snapshot from the simulations of a fully charged brush at large grafting density  $\rho_a = 0.12\sigma^{-2}$ . Simulated density profiles of monomers and counterions in normal direction are shown in Figure 6.2b, which indicate that both monomers and counterions

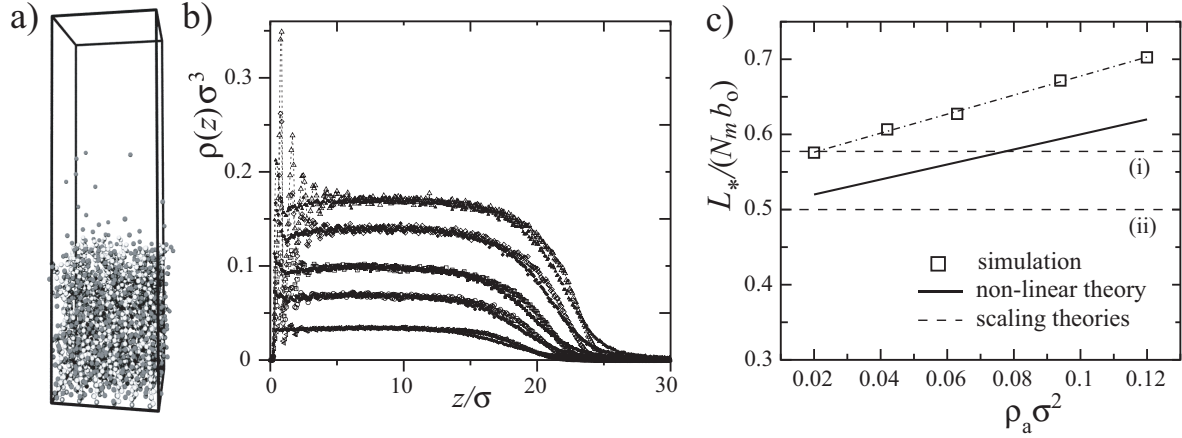


Figure 6.2: a) A snapshot of the simulated polyelectrolyte brush at grafting density of  $\rho_a = 0.12\sigma^{-2}$  (from Refs. [206, 216]). Monomers are shown by light gray and counterions by dark gray spheres. b) Simulated density profiles,  $\rho(z)$ , of monomers (open symbols) and counterions (filled symbols) as a function of the distance from the anchoring surface,  $z$ , for grafting densities (from bottom to top):  $\rho_a\sigma^2 = 0.020$  (triangle-left), 0.042 (circles), 0.063 (squares), 0.094 (diamonds), and 0.12 (triangle-up). c) Simulated brush height (symbols) as a function of grafting density [216]. The solid line represents the prediction of the non-linear scaling theory, Eq. (6.8), with  $\sigma_{\text{eff}}^2 = 2\sigma^2$ . The dashed lines (i) and (ii) show the scaling predictions (6.6) and (6.7), respectively, and the dot-dashed line is guide to the eye. Here the brush is composed of 36 fully charged chains ( $f = 1$ ) of  $N_m = 30$  monomers (contour length of  $L_0/\sigma = 29.4$ ) at  $\ell_B = \sigma$ .

follow very similar nearly-step-like profiles with uniform amplitude inside the brush, which increases with the grafting density (the monomers show a short-range ordering close to the anchoring plane, which is not relevant in the present study). Thus counterions are mostly confined in the polyelectrolyte layer and as, one may observe, the chains are stretched up to about 60%-70% of their contour length.

In Figure 6.2c, the simulation results for the brush height (symbols) are shown along with the prediction of the non-linear scaling theory, Eq. (6.8) (solid line), for moderate to large grafting densities. (Note that I have used  $\sigma_{\text{eff}}^2 = 2\sigma^2$ , which corresponds to an approximate two-dimensional square-lattice packing of monomers and counterions on two interpenetrating sublattices.) As seen, the non-linear scaling prediction qualitatively captures the slow increase of the brush height with grafting density. The deviations from the simulation data may result in part from additional effects such lateral inhomogeneity of counterion distribution around the chains and the intermediate-stretching elasticity of the chains, which go beyond the scaling level and will be taken into account in Section 6.2. An important factor, however, is the way one estimates the effective self-volume of the polymer, or in other words, the estimate for the free volume available for counterions inside the brush, which can explain the deviations between the preceding theoretical prediction and the simulations. This will be discussed using the mean-field cell model in Section 6.2.5 [103].

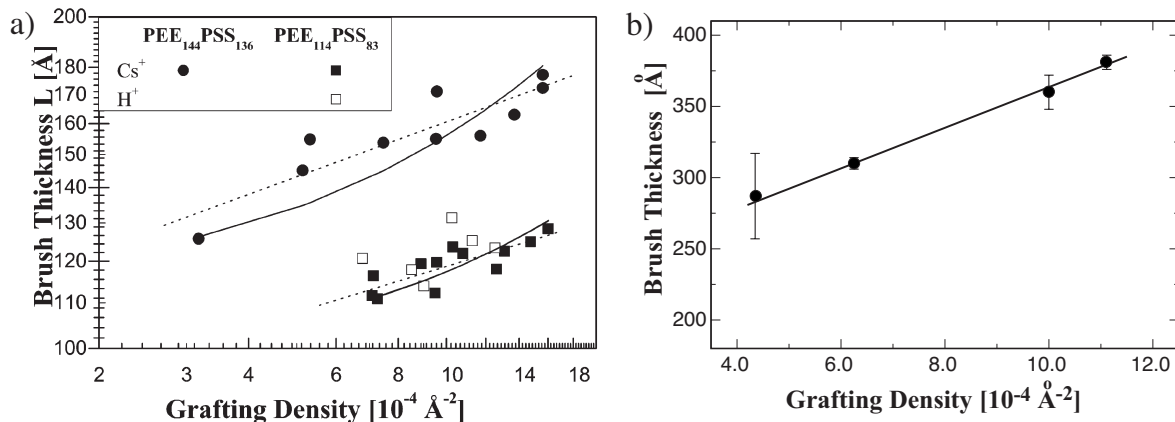


Figure 6.3: a) The experimentally measured height of the osmotic  $\text{PSS}_{136}$  (circles) and  $\text{PSS}_{83}$  (squares) brushes as a function of grafting density from Ref. [216]. The brush contains either 1 mM CsCl salt (filled symbols) or only clean water at  $\text{pH}=5.5$  (open symbols). The dashed lines are power-law fits with the exponents 0.17 and 0.13, respectively. The solid lines are fits to Eq. (6.8). Fits were only made to the filled symbols. b) The experimental results (symbols) for the height of the salt-free osmotic  $\text{PSS}_{356}$  brush as a function of grafting density from Ref. [217]. The solid line shows a fit to the non-linear scaling prediction, Eq. (6.8).

### 6.1.2 Comparison with experiments

The predictions of the non-linear osmotic brush have also been compared with recent experimental data [216, 217]. In a set of experiments [216], the brush height has been measured using monolayers of the diblock copolymers poly-(ethyl ethylene) $_{144}$ poly(styrene sulfonic acid) $_{136}$  (or  $\text{PEE}_{144}\text{PSS}_{136}$ ) and also poly-(ethyl ethylene) $_{114}$ poly(styrene sulfonic acid) $_{83}$  (or  $\text{PEE}_{114}\text{PSS}_{83}$ ) at the air-water interface. The PSS block is soluble in (and extends into) the water phase forming a highly charged brush layer. The grafting density of the PSS brush may be changed by lateral compression and the height of the layer (brush height) is measured using x-ray reflectivity techniques. The brush height is studied in clean water or in the presence of small amount of added salt (1 mM CsCl) that is used for contrast enhancement.

As shown in Figure 6.3a, the data clearly indicate a weak increase of the PSS brush height with grafting density. The brush height is found to be stretched up to 60% of the contour length (which is about  $340 \text{ \AA}$  for  $\text{PEE}_{144}\text{PSS}_{136}$  using a monomer size of about  $2.5 \text{ \AA}$ ). In order to compare with the non-linear scaling predictions, the data for the brush height,  $L$ , are fitted to Eq. (6.8) with the following preselected parameters: monomer size  $b_0 = 2.5 \text{ \AA}$  and number of (the PSS block) monomers  $N_m = 136$  and  $N_m = 83$  for  $\text{PEE}_{144}\text{PSS}_{136}$  and  $\text{PEE}_{114}\text{PSS}_{83}$  systems respectively. The charge fraction (of the PSS block) is estimated as  $f = 0.49$  and  $f = 0.85$  for the two cases respectively, an estimate which accounts also for ion chemical binding inside the brush [216]. The only free parameter is thus  $\sigma_{\text{eff}}$ , which serves as a fit parameter to account for the effective area occupied by a compressed polymer chain. Very similar values are obtained for  $\sigma_{\text{eff}}$  for both systems, i.e.  $\sigma_{\text{eff}} = 13.84 \text{ \AA}$  and  $13.96 \text{ \AA}$  respectively, leading to a minimum chain area of about  $\sigma_{\text{eff}}^2 = 193 \text{ \AA}^2$ . This value is of the same order as the minimum area which a compressed PSS chain with a radius of  $r_m = 6 \text{ \AA}$  occupies, i.e.  $\pi r_m^2 / 0.91 = 124 \text{ \AA}^2$  (assuming a hexagonal lattice). Clearly, the fitted effective



excluded-volume is larger since it also takes into account the finite volume of the counterions which might or might not be hydrated.

In a different set of experiments [217], the osmotic brush height has been measured as function of the grafting density using neutron reflectivity measurements on a monolayer of charged diblock copolymers consisting of poly-(tert-butylstyrene)<sub>63</sub>poly(styrene sulfonate)<sub>356</sub> (or PtBS<sub>63</sub>PSS<sub>356</sub>). Here also the brush height is found to increase weakly with the grafting density, which as shown in Ref. [217], agrees with the present non-linear scaling prediction. In Figure 6.3b, these data are shown (filled symbols) together with a fit to Eq. (6.8) with  $\sigma_{\text{eff}}$  being the only fit parameter (other parameters are chosen as  $b_0 = 2.5\text{\AA}$  for the PSS block with  $N_m = 356$  monomers and a charge fraction of  $f = 0.33$  as estimated in Ref. [217]). As seen, a good fit is obtained by choosing  $\sigma_{\text{eff}} = 14.60\text{\AA}$  corresponding to a minimum effective area of about  $\sigma_{\text{eff}}^2 = 213\text{\AA}^2$  per PSS chain, which is close to the values obtained in the experiments discussed above. Note again that this value incorporates the finite volume of counterions as well.

In brief, the above results demonstrate that the non-linear scaling predictions can capture the non-linear osmotic behavior observed in experiments on a semi-quantitative level.

## 6.2 Non-linear mean-field theory for the osmotic brush

In the preceding scaling analysis, I assumed that the polymer and counterion charges are smeared out in the brush and thus, in particular, neglected the lateral inhomogeneities in the distribution of charges that built up due to the interactions between charged polymers and counterions (see, e.g., Eq. (6.5)). In order to account for these latter effects on the mean-field level, I shall apply a cell-model approach [21, 36, 37, 38, 104] to calculate the electrostatic contribution to the free energy of the osmotic brush. I will also consider the full stretching free energy of the chains based on the freely-jointed-chain model rather than using only the limiting strong-stretching expression, Eq. (6.2).

### 6.2.1 The cell model

To calculate electrostatic contributions, I will model a polyelectrolyte chain in the brush as a cylindrical rod with a uniform linear charge density,  $-\tau e$ . For a chain consisting of  $N_m$  spherical monomers with equal diameter  $b_0$ , one has  $\tau L = q_m f N_m$ , where  $f$  is the charge fraction of the chain,  $-q_m$  is the valency of charged monomers, and  $L$  is the chain length (end-point height from the anchoring surface), which is equal to the rod height. Each polyelectrolyte rod is symmetrically enclosed in a cylindrical unit cell with radius  $D$ , which is determined by the grafting density  $\rho_a$ . The chain length,  $L$ , is assumed to be much larger than the cell radius,  $L \gg D$ . As discussed before, I will assume that the total volume of the rod is constant, i.e.,  $R^2 L = R_0^2 L_0$ , where  $L_0 = N_m b_0$  and  $R_0$  stand for the length and radius associated with its fully stretched conformation. Note that  $R_0$  can generally be different from the radius of the monomers as there are different possibilities to choose a cylindrical rod model for a polyelectrolyte chain (see Section 6.2.5) [103]. In the following sections, I shall focus on a model with  $R_0 = b_0/2$  (Figure 6.4a).

Electroneutrality condition is satisfied in each *unit cell* due to the presence of a fixed number of counterions,  $N$ , with charge valency  $+q$  and radius  $r_c$ , i.e.  $\tau L = q_m f N_m = qN$  (here  $q_m$ ,  $q$  and  $\tau$  are defined to be positive).

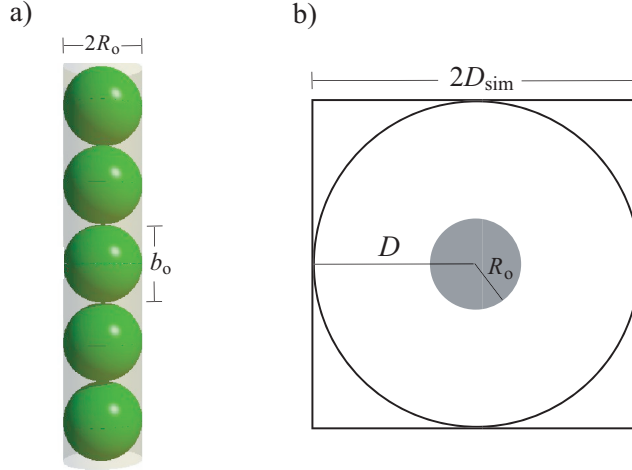


Figure 6.4: The model used for the polyelectrolyte chain (a) and the cylindrical unit cell (b) as discussed in the text. The unit cell boundary in the simulations is shown by a square.

Note that in the simulation model discussed in Section 6.1.1, grafting points form a square lattice with the lattice spacing of  $2D_{\text{sim}}$  and thus, a grafting density of  $\rho_a = 1/(4D_{\text{sim}}^2)$ . Since the analytical solution for the counterion distribution is only available for a cylindrical unit cell, one has to map the square simulation box to a cylindrical box. (In experiments, the grafting-point distribution is highly irregular and thus different from both simulation and analytical models.) There are different ways to adopt a cylindrical unit cell for such a planar brush (Section 6.2.5) [103]. In the following analysis, I will choose a cylindrical cell with the diameter,  $2D$ , equal to the lattice spacing of the square lattice, i.e.  $D = D_{\text{sim}}$ , as shown in Figure 6.4b. The grafting density for this model reads  $\rho_a = 1/(4D^2)$ .

### 6.2.2 The electrostatic free energy

In the mean-field or Poisson-Boltzmann (PB) approximation, the electrostatic correlations between neighboring cells, and also between counterions in a cell, are entirely neglected and the study of the system is thus reduced to a single-cell study (note that the electric field at the boundary of the cell vanishes by virtue of the electroneutrality condition). This approximation is valid for weakly coupled systems, i.e. at moderate or small Bjerrum lengths and for low-valency counterions (see Chapter 2) [43].

The canonical PB free energy of the counterion-cylinder system may be obtained systematically from a saddle-point approximation [50] and reads (see Appendix A)

$$\frac{\mathcal{F}^{\text{PB}}}{k_{\text{B}}T} = -\frac{1}{4\pi\ell_{\text{B}}q^2} \int d\mathbf{x} \left[ \frac{1}{2}(\nabla\psi)^2 + \frac{2\xi}{R}\delta(r-R)\psi(\mathbf{x}) \right] - N \ln \left[ \int_{R \leq r \leq D} d\mathbf{x} e^{-\psi(\mathbf{x})} \right], \quad (6.11)$$

where  $\xi = ql_{\text{B}}\tau$  is the Manning parameter, and the global electroneutrality condition implies

$$\xi L = Nq^2\ell_{\text{B}}. \quad (6.12)$$

The rescaled electric potential  $\psi$  (in units of  $k_{\text{B}}T/qe$ ) fulfills the PB equation as

$$\nabla^2\psi = -\kappa^2 e^{-\psi(\mathbf{x})} \quad (6.13)$$

in the cylindrical region  $R \leq r \leq D$ , where  $\kappa^2 = 4\pi\ell_B q^2 N / \int_{R \leq r \leq D} d\mathbf{x} \exp(-\psi)$  is an unspecified factor the value of which will be fixed once the reference point of the potential is specified.<sup>1</sup> This equation may be solved for  $\psi$  using the boundary conditions [37, 38]

$$\left(r \frac{d\psi}{dr}\right)_{r=R} = 2\xi \quad \text{and} \quad \left(r \frac{d\psi}{dr}\right)_{r=D} = 0 \quad (6.14)$$

as discussed in Chapter 3. The solution for  $\psi(r)$  and thus the PB free energy takes different functional forms depending on whether  $\xi$  lies below or above the Alfrey-Fuoss threshold  $\Lambda_{\text{AF}}$ . For a polyelectrolyte rod with *fixed radius*,  $R$ , one has [37, 38]

$$\Lambda_{\text{AF}} = \frac{\ln(D/R)}{1 + \ln(D/R)}, \quad (6.15)$$

while in the present model with the constant volume constraint,  $\Lambda_{\text{AF}}$  has to be determined from a transcendental equation (see below).

For  $\xi \leq \Lambda_{\text{AF}}$ , the electrostatic free energy per number of monomers reads

$$\frac{\mathcal{F}^{\text{PB}}}{N_m k_B T} = \frac{q_m f}{q} \left\{ -\frac{1}{\xi} \left[ (1+\beta^2) \ln \frac{D}{R} + \ln \left( \frac{(\xi-1)^2 - \beta^2}{1-\beta^2} \right) + \xi \right] + \ln[(\xi-1)^2 - \beta^2] + c(R) \right\} \quad (6.16)$$

(up to an irrelevant additive constant), while for  $\xi \geq \Lambda_{\text{AF}}$ , one has

$$\frac{\mathcal{F}^{\text{PB}}}{N_m k_B T} = \frac{q_m f}{q} \left\{ -\frac{1}{\xi} \left[ (1-\beta^2) \ln \frac{D}{R} + \ln \left( \frac{(\xi-1)^2 + \beta^2}{1+\beta^2} \right) + \xi \right] + \ln[(\xi-1)^2 + \beta^2] + c(R) \right\}, \quad (6.17)$$

where  $c(R) = -\ln(2\pi\ell_B f q q_m N_m R^2)$  and  $\beta$  is an integration constant, which is determined from the transcendental equation

$$\xi = \begin{cases} \frac{1-\beta^2}{1-\beta \coth(-\beta \ln \frac{D}{R})} & \xi \leq \Lambda_{\text{AF}}, \\ \frac{1+\beta^2}{1-\beta \cot(-\beta \ln \frac{D}{R})} & \xi \geq \Lambda_{\text{AF}}. \end{cases} \quad (6.18)$$

Note also that  $R$  represents the actual radius of the polyelectrolyte rod and thus in the present model is related to the Manning parameter,  $\xi$ , through

$$R(\xi) = R_0 \sqrt{\xi/\xi_0}. \quad (6.19)$$

This dependence is induced by the volume constraint  $R^2 L = R_0^2 L_0$ , and the fact that the total charge of the rod is conserved, i.e.

$$\xi L = \xi_0 L_0, \quad (6.20)$$

where  $\xi_0 = q q_m f \ell_B / b_0$  is the Manning parameter associated with the fully stretched conformation of the rod. In the above formulation, counterions have been taken as point-like

<sup>1</sup>The electroneutrality condition entails that the canonical free energy, Eq. (6.11), be invariant under the gauge transformation  $\psi \rightarrow \psi + \psi_0$ . As a consequence, the PB free energy, Eqs. (6.16) and (6.17), is independent of  $\kappa^2$ .

particles. To account for finite counterion radius,  $r_c$ , one may define the hard-core rod radius as

$$R_{\text{hc}}(\xi) = r_c + R_0 \sqrt{\xi/\xi_0} \quad (6.21)$$

to be used instead of  $R$  in the preceding equations. For  $\xi = \xi_0$ , one has  $R_{\text{hc}}(\xi) = r_c + R_0$ , which compares with the effective polymer diameter  $\sigma_{\text{eff}}$  in Section 6.1.

Note that  $\xi$  is limited from above and below due to the geometrical constraints  $R_{\text{hc}} \leq D$  and  $L \leq L_0$  respectively. As a result, one observes that

$$\xi_0 \leq \xi \leq \xi_u, \quad (6.22)$$

where

$$\xi_u = \xi_0 (D - r_c)^2 / R_0^2. \quad (6.23)$$

Finally, note that the threshold Manning parameter,  $\Lambda_{\text{AF}}$ , at which the functional form of the solution to the PB equation is changed, is determined from

$$\Lambda_{\text{AF}} = \frac{\ln D/R_{\text{hc}}(\Lambda_{\text{AF}})}{1 + \ln D/R_{\text{hc}}(\Lambda_{\text{AF}})}, \quad (6.24)$$

in which  $R_{\text{hc}}(\Lambda_{\text{AF}})$  is given by Eq. (6.21).<sup>2</sup>

### 6.2.3 The elastic free energy

I will adopt a freely-jointed-chain (FJC) model to calculate the elastic contribution to the total free energy of the osmotic brush. The exact free energy of such a chain model has a purely entropic origin and is obtained as (see Appendix F.1)

$$\frac{\mathcal{F}^{\text{FJC}}}{N_m k_B T} = -\ln \frac{\sinh y}{y} + y \coth y - 1, \quad (6.25)$$

where  $N_m$  is the number of monomers and  $y$  is found from

$$\frac{L}{L_0} = \coth y - \frac{1}{y}, \quad (6.26)$$

where the chain end-to-end distance,  $L$ , corresponds to the actual rod height within the cell model. The FJC model generates the linear weak-stretching result ( $L \ll N_m b_0$ ) as

$$\frac{\mathcal{F}^{\text{FJC}}}{N_m k_B T} \simeq \frac{3L^2}{2(N_m b_0)^2} \quad (6.27)$$

corresponding to a Gaussian-chain elasticity. On the other hand, it accounts for the finite extensibility of the chain yielding the strong-stretching ( $L \simeq N_m b_0$ ) non-linear elasticity as (see Appendix F.1)

$$\frac{\mathcal{F}^{\text{FJC}}}{N_m k_B T} \simeq -\ln\left(1 - \frac{L}{N_m b_0}\right) + \text{const.} \quad (6.28)$$

---

<sup>2</sup> It is easy to check that the Alfrey-Fuoss threshold,  $\Lambda_{\text{AF}}$ , tends to the Manning critical value  $\xi_M = 1$  [20, 39], when  $D \rightarrow \infty$ , or  $R_0$  and  $r_c \rightarrow 0$ . In the present model,  $\Lambda_{\text{AF}}$  may be smaller or larger than  $\xi_0$ , but it never exceeds  $\xi_u$ , i.e.  $\Lambda_{\text{AF}} < \xi_u$ . Also it never becomes larger than one as seen from Eq. (6.24). Therefore, in a system with  $\xi_0 > 1$ , one will always have the above-threshold condition  $\xi \geq \xi_0 > \Lambda_{\text{AF}}$  implied by Eq. (6.22). Similar situation occurs when  $D \rightarrow R_0 + r_c$ , since in this case one has  $\xi_u \rightarrow \xi_0$ , and hence, again  $\Lambda_{\text{AF}}$  lies below  $\xi_0$ .

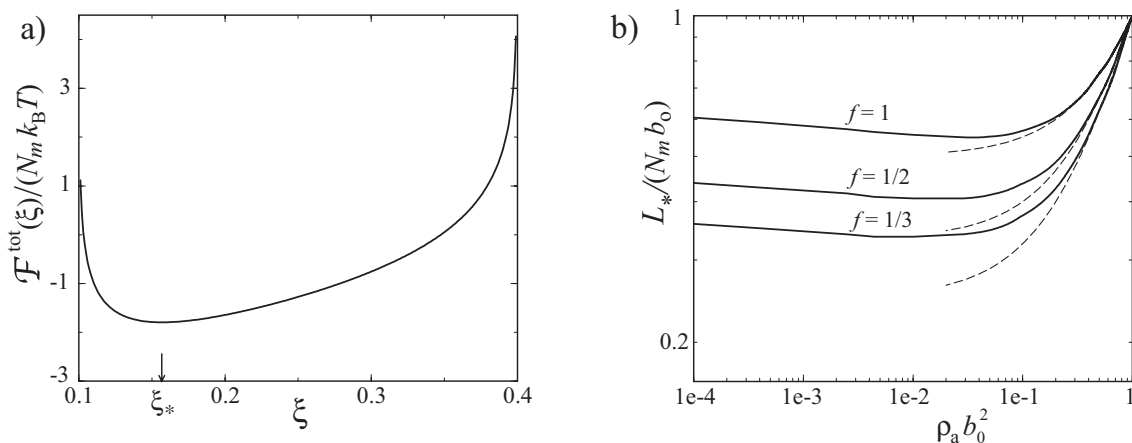


Figure 6.5: a) Typical free energy of the mean-field cell model, Eq. (6.29), plotted as a function of the Manning parameter,  $\xi$ , for  $f = 1$ ,  $\ell_B = 0.1b_0$ ,  $q = q_m = 1$ ,  $r_c = b_0/2$ , and  $D = 1.5b_0$ . In this case, the lower and upper bounds for  $\xi$  are  $\xi_0 = 0.1$  and  $\xi_u = 0.4$ , respectively. The arrow shows the location of the optimal Manning parameter  $\xi_* \simeq 0.16$ . b) Log-log plot of the rescaled optimal height of the brush as a function of the grafting density for  $\ell_B = 0.1b_0$ ,  $q = q_m = 1$ , point-like counterions and various charge fractions as indicated on the graph (solid curves). Dashed lines are the asymptotic behavior obeying Eq. (6.32) for large grafting densities.

### 6.2.4 Optimal brush height and its limiting behavior

The total free energy of the brush *per unit cell* is the sum of the electrostatic and elastic free energies obtained in Eqs. (6.16) or (6.17) and (6.25), i.e.

$$\mathcal{F}^{\text{tot}} = \mathcal{F}^{\text{PB}} + \mathcal{F}^{\text{FJC}}. \quad (6.29)$$

This compares with the scaling free energy (6.1), where the interaction and counterionic contributions (*per unit area*), i.e.  $\mathcal{F}_{\text{ci}} + \mathcal{F}_{\text{int}}$ , are now incorporated in the cell-model PB free energy,  $\mathcal{F}^{\text{PB}}$ .

The total free energy can be viewed as a function of the effective Manning parameter of the system,  $\xi$ , which varies according to the brush height  $L$  (see Eq. (6.20)). The typical form of  $\mathcal{F}^{\text{tot}}$  is shown in Figure 6.5a as a function of  $\xi$ , where other parameters are fixed as  $f = 1$ ,  $\ell_B = 0.1b_0$ ,  $q = q_m = 1$ ,  $r_c = b_0/2$ , and  $D = 1.5b_0$ . Recall that the effective Manning parameter,  $\xi$ , is bounded from below by  $\xi_0$ , and from above by  $\xi_u$ , which are here  $\xi_0 = 0.1$  and  $\xi_u = 0.4$ . The total free energy increases for small and large  $\xi$  and has a minimum at an intermediate Manning parameter,  $\xi_*$ , which corresponds to an optimal brush height  $L_* = \xi_0 L_0 / \xi_*$ .

The reason for this behavior is that by decreasing  $\xi$  down to  $\xi_0$ , the chain becomes highly stretched and its elastic free energy diverges due to its finite extensibility (see Eq. (6.28)). For large  $\xi \rightarrow \xi_u$ , on the other hand, the available space for counterions decreases (since  $R_{\text{hc}} \rightarrow D$ ), and the translational entropy due counterion confinement diverges.

In this section, I will focus on the generic predictions of the present mean-field cell model for the brush height,  $L_*$ , as a function of grafting density,  $\rho_a$ . To this end, I will take counterions as point-like particles ( $r_c = 0$ ) with charge valencies  $q = q_m = 1$ . More general results will be given in the following section.

Figure 6.5b shows the optimal brush height plotted as a function of  $\rho_a$  for the Bjerrum length  $\ell_B = 0.1b_0$ , and for three different values of the charge fraction  $f = 1, 1/2$  and  $1/3$  (solid curves). As seen, both at large and small grafting densities, the brush height increases and eventually tends to its maximum value  $L_0 = N_m b_0$ . Also a lower bound is predicted for the equilibrium height of the brush depending on the charge fraction and the Bjerrum length. For  $f > 1/2$  and  $\ell_B/b_0 \sim 0.1$ , this lower bound is about 50% of the contour length indicating that the chains remain increasingly stretched over a wide range of grafting densities. The limiting behavior of the brush height with grafting density can be understood both by the asymptotic expansion of the free energy (Appendix F.2) and by simple physical arguments as I will present now.

In the limit of large grafting densities  $\rho_a \rightarrow \rho_a^{\max}$  (with  $\rho_a^{\max} = 1/b_0^2$  being the maximum grafting density here), one deals with small cell radius, i.e.  $D/R_0 \rightarrow 1$ , where  $R_0 = b_0/2$  (recall from Section 6.2.1 that in the present model  $\rho_a b_0^2 = R_0^2/D^2$ ). In this limit, the dominant contribution to the PB free energy comes from the confinement entropy of counterions inside the cell, which may be approximated by that of an ideal gas of particles (see Appendix F.2), i.e.

$$\frac{S_{\text{ci}}}{N_m k_B} \simeq f \ln[\pi(D^2 - R^2)L], \quad (6.30)$$

where  $R$  is defined in Eq. (6.19). Therefore, osmotic pressure of counterions becomes the major repulsive pressure swelling the rod against stretching pressure of the elasticity. In this limit, the chain has a large extension and its elastic free energy per number of monomers is given by Eq. (6.28), i.e.

$$\frac{\mathcal{F}_{\text{elas}}}{N_m k_B T} \simeq -\ln(1 - L/L_0). \quad (6.31)$$

Balancing the longitudinal pressures due to these two opposing contributions using  $\partial/\partial L(\mathcal{F}_{\text{elas}} - TS_{\text{ci}}) = 0$  at fixed cell radius  $D$ , I obtain

$$\frac{L_*(\rho_a)}{L_0} \simeq \frac{f + \rho_a b_0^2}{1 + f}, \quad (6.32)$$

which is equivalent to Eq. (6.8) obtained within the non-linear scaling theory in Section 6.1.

The expression given by Eq. (6.32) is plotted in Figure 6.5b for the charge fractions  $f = 1, 1/2, 1/3$  (dashed curves) together with the results obtained from minimization of the full free energy in Eq. (6.29) (solid curves). The coincidence is evident at large grafting densities. The linear dependence on the grafting density in Eq. (6.32) is induced by the conserved polymer volume constraint. The weaker dependence and deviations from Eq. (6.32) observed at lower grafting densities (e.g., at about  $\rho_a b_0^2 \sim 0.1$ , which approximately corresponds to the simulated regime) result from lateral electrostatic effects, which become significant and generate a minimum for the brush at intermediate grafting densities.

For very small grafting densities  $\rho_a b_0^2 \ll 1$  (or equivalently  $D/R_0 \gg 1$ ), the present model is applicable for very long chains, since only in this case, counterions will be confined within the brush (see the Discussion). In this limit, the brush height shows different asymptotic behavior depending on whether the optimal Manning parameter,  $\xi_*$ , is below or above the Alfrey-Fuoss threshold  $\Lambda_{\text{AF}} \simeq 1$ , Eq. (6.24). First I will consider the case with  $\xi_* < \Lambda_{\text{AF}}$ . For the parameters chosen in Figure 6.5b ( $\ell_B = 0.1b_0, q_m = q = 1$ ), this condition holds for  $\rho_a b_0^2 < 0.1$ , as can be checked from Eq. (6.24). In this case, the counterion cloud is highly diluted as counterions are de-condensed (Chapter 3) and there will be no electrostatic

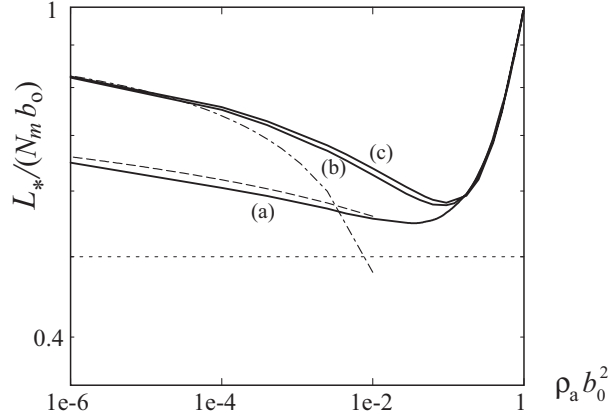


Figure 6.6: Log-log plot of the rescaled optimal height of the brush as a function of grafting density. Solid curves show the results obtained from the minimization of the full free energy, Eq. (6.29), with  $f = 1$ ,  $q = q_m = 1$ , and point-like counterions, for a)  $\ell_B = 0.1b_0$  ( $\xi_0 = 0.1$ ), b)  $\ell_B = 0.7b_0$  ( $\xi_0 = 0.7$ ) and c)  $\ell_B = 1.2b_0$  ( $\xi_0 = 1.2$ ). The dashed and dot-dashed curves show the asymptotic estimates at small grafting densities for the cases a) (using Eq. (6.34)) and c) (Eq. (6.38)) respectively. The dotted line shows the brush height in the absence of lateral effects for  $f = 1$  (Eq. (6.39)).

screening on the bare electrostatic potential of the rod  $\psi(r) = 2\xi \ln(r/R)$ . This potential is used to calculate the electrostatic energy per unit cell as

$$\frac{U_{\text{elec}}}{N_m k_B T} \simeq f \xi \ln \frac{D}{R}. \quad (6.33)$$

The entropic contribution of counterions may still be accounted for using Eq. (6.30). Consequently, the electrostatic free energy of the system,  $\mathcal{F}_{\text{elec}} \simeq U_{\text{elec}} - T S_{\text{ci}}$ , is obtained as

$$\frac{\mathcal{F}_{\text{elec}}}{N_m k_B T} \simeq f(\xi - 2) \ln \frac{D}{R} \quad (6.34)$$

for very large  $D/R_0$ . This expression can be derived also by expanding the PB free energy (6.16) in powers of  $R/D$  as shown in Appendix F.2.

Using Eqs. (6.34) and (6.19), the longitudinal electrostatic pressure can be calculated by differentiating  $\mathcal{F}_{\text{elec}}$  with respect to  $L = \xi_0 L_0 / \xi$ . Balancing this with the elastic pressure from Eq. (6.31), one obtains the equilibrium brush height which has to be calculated numerically and is shown in Figure 6.6 (dashed curve) for  $f = 1$  and  $\ell_B = 0.1b_0$ . In the Figure, I also show the results from minimization of the full free energy, Eq. (6.29) (solid curve a). The plot is made for  $\rho_a$  down to  $10^{-6}b_0^{-2}$ . For vanishingly small grafting densities  $\rho_a b_0^2 \rightarrow 0$ , the entropic contribution becomes negligible compared with the bare electrostatic repulsion between monomers, and the equilibrium brush height behaves asymptotically as

$$\frac{L_*(\rho_a)}{L_0} \simeq \frac{f \ln \rho_a b_0^2}{f \ln \rho_a b_0^2 - 2\xi_0^{-1}}. \quad (6.35)$$

This function is not shown in Figure 6.6, because it is valid for smaller grafting densities.

In the second scenario, i.e. when the optimal Manning parameter becomes larger than the threshold  $\xi_* > \Lambda_{\text{AF}} \simeq 1$ , bare electrostatic interactions are partially screened as a result

of the counterion condensation process (Chapter 3). The PB electrostatic potential (up to some logarithmic corrections) reduces to the bare electrostatic potential of a rod with critical Manning parameter  $\xi_M = 1$ , i.e.,  $\psi(r) = 2\ln(r/R)$ , when  $D/R_0 \rightarrow \infty$ . The electrostatic energy per unit cell can be estimated using this potential as

$$\frac{U_{\text{elec}}}{N_m k_B T} \simeq \frac{f}{\xi} \ln \frac{D}{R}. \quad (6.36)$$

To estimate entropic contributions in this case, I shall adopt the counterion-condensation picture [20, 39] that only a fraction of  $1/\xi$  of counterions are unbound and may contribute to the entropic pressure. Thus, the corresponding ideal-gas entropy of counterions,  $S_{\text{ci}}$  in Eq. (6.30), may be corrected by such a factor and used, together with Eq. (6.36), to obtain the leading term of the electrostatic free energy per unit cell,  $\mathcal{F}_{\text{elec}} \simeq U_{\text{elec}} - TS_{\text{ci}}$ , as

$$\frac{\mathcal{F}_{\text{elec}}}{N_m k_B T} \simeq -\frac{f}{\xi} \ln \frac{D}{R}. \quad (6.37)$$

This expression may be obtained by a limiting expansion of the PB free energy (6.17)–see Appendix F.2. Calculating the longitudinal electrostatic pressure from Eq. (6.37) and balancing it with the non-linear stretching pressure from Eq. (6.31), I obtain

$$\frac{L_*(\rho_a)}{L_0} \simeq 1 + \frac{2\xi_0}{f \ln \rho_a b_0^2}. \quad (6.38)$$

The asymptotic expression, Eq. (6.38), is shown in Figure 6.6 (dot-dashed curve) along with the result from minimization of the full free energy, Eq. (6.29) (solid curve c) for a system with  $f = 1$  and  $\ell_B = 1.2b_0$  ( $\xi_0 = 1.2$ ) for which the optimal Manning parameter,  $\xi_*$ , remains always above the Alfrey-Fuoss threshold (see footnote 2). As seen, the above asymptotic estimate, Eq. (6.38), becomes accurate for  $\rho_a b_0^2 < 10^{-4}$ . Similar behavior is obtained within the present model for the whole range of Bjerrum lengths; see, e.g., the result for  $f = 1$  and  $\ell_B = 0.7b_0$  ( $\xi_0 = 0.7$ ) in Figure 6.6 (solid curve b).

The preceding results on the low-grafting-density behavior of the brush thickness demonstrate the important role of lateral electrostatic effects (especially that of lateral distribution of counterions), which are systematically included in the PB free energy and generate re-stretching of the chains at small grafting densities. In this limit, the constant volume constraint becomes unimportant. Both for weakly charged ( $\xi_0 < 1$ ) and highly charged chains ( $\xi_0 > 1$ ), lateral electrostatic contributions produce a repulsive longitudinal force acting on the chains, which increases logarithmically by decreasing the grafting density (Eqs. (6.34) and (6.37)). In particular, for highly charged chains, the force is independent of the brush height, i.e.  $-\partial\mathcal{F}_{\text{elec}}/\partial L \sim \ln D/R$  (using Eqs. (6.37) and (6.20)), which is a direct consequence of the electrostatic screening due to condensation of counterions. In any case, the increase of the brush height, which converges to the contour length, is logarithmically weak. If lateral effects are neglected, the brush height remains independent of the grafting density and reads

$$\frac{L_*}{L_0} = \frac{f}{1+f}, \quad (6.39)$$

which is shown by a dotted line in Figure 6.6. This result follows from Eqs. (6.30), (6.31) and neglecting the volume constraint (compare with Eq. (6.7) in the non-linear scaling theory in Section 6.1).



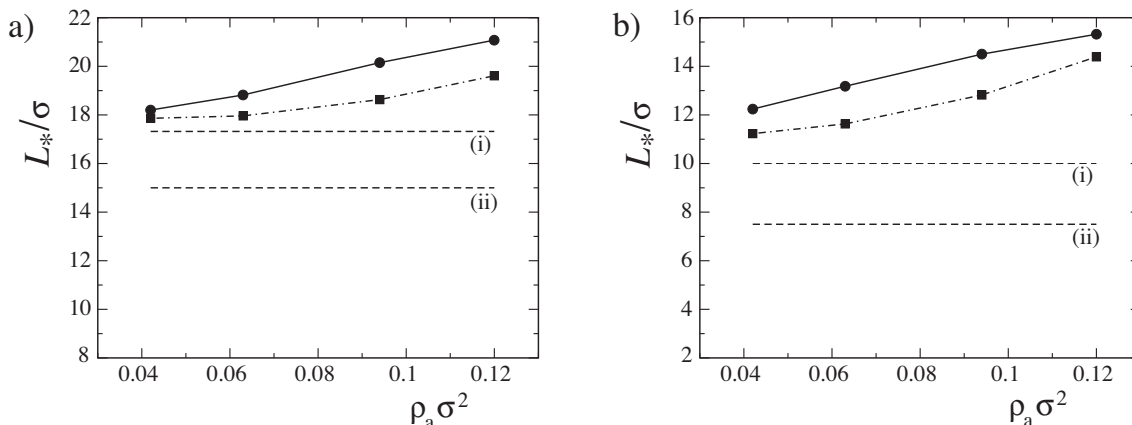


Figure 6.7: Brush height as a function of the grafting density for polyelectrolyte chains of  $N_m = 30$  monomers (contour length  $L_0 \simeq 30\sigma$ ). Circles show the simulation data and squares are the predictions of the present mean-field cell model for a) charge fraction  $f = 1$  and the Bjerrum length  $\ell_B = \sigma$ , and b) charge fraction  $f = 1/3$  and  $\ell_B \simeq 2\sigma$ . The dotted lines (i) and (ii) show the scaling predictions, Eqs. (6.6) and (6.7), with Gaussian and non-linear elasticity respectively.

Finally, I emphasize that the non-monotonic behavior of the brush thickness is not influenced by the elasticity model and qualitatively similar features are obtained when a Gaussian chain elasticity is used.<sup>3</sup>

### 6.2.5 Comparing mean-field results with simulations

The predictions of the mean-field model presented above are compared with simulation results [206] in Figure 6.7 (the details of the simulation model are described briefly in Section 6.1.1). Theoretical points are obtained by minimization of the total free energy (6.29) taking into account the polymer volume conservation and the finite size of the counterions using  $r_c = b_0/2$  (here  $q = q_m = 1$  and I assume  $b_0 = \sigma$  while comparing with the simulation data). As seen, the theoretical predictions (squares) qualitatively capture the trend observed in the simulations (circles). The main source of quantitative deviations between the theory and the simulations may be associated with the estimate of the free volume accessible for counterions in the cell-model approach, i.e. the results vary depending on the way the simulated system is mapped to a cylindrical cell model (Section 6.2.1). This gives a measure of the systematic errors of the present model, which as shown in Ref. [103], turns out to be of the order of the deviations from the simulation data. To elucidate this point, I consider here a slightly different version of the cell model, in which the polyelectrolyte rod is chosen such that it has the same *volume* as the polymer chain (rather than having the same radius as chosen so far). In this case, the radius of the fully stretched rod is slightly smaller and reads  $R_0 = \sqrt{2/3}b_0/2$  as shown in Figure 6.8a. Also I will choose the cylindrical cell such that it has the same volume as the

<sup>3</sup>For instance, by replacing the FJC elasticity with the Gaussian chain elasticity (6.27), the brush height is found to increase logarithmically by decreasing  $\rho_a b_0^2$  as  $L_*/L_0 \sim -\ln \rho_a b_0^2$  in the low-grafting-density regime and for highly charged chains. The elasticity model affects the magnitude of the chain stretching and also the particular dependence of the brush height on the grafting density. For chains of finite length, the correct limiting behavior is obtained if the finite extensibility of the chain is accounted for, e.g., using the FJC model.

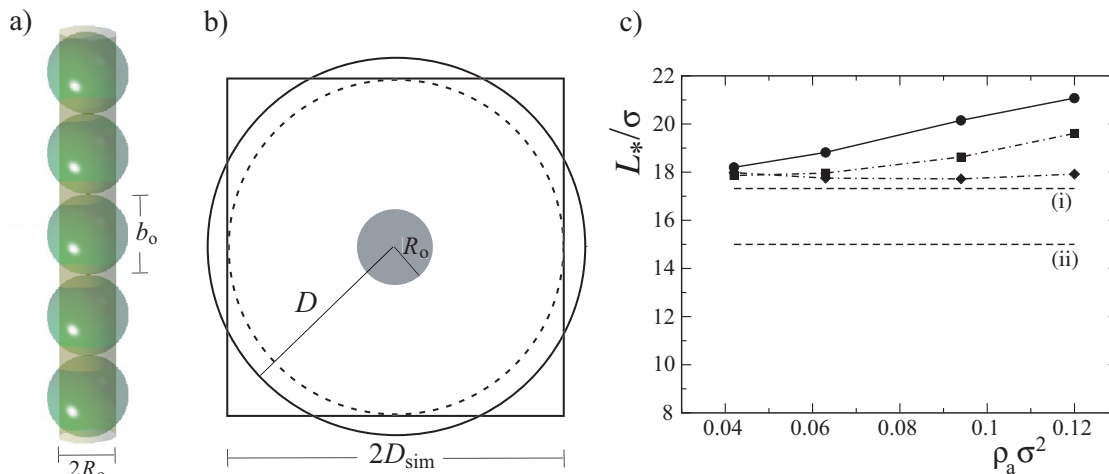


Figure 6.8: A different version of the cell model adopted for the simulated brush system with a) a polyelectrolyte rod and b) a cylindrical unit cell (solid circle) that occupy the same volumes as the (fully stretched) polyelectrolyte chain and the square unit cell within the simulations respectively; i.e. one has here  $R_0 = \sqrt{2/3}b_0/2$  and  $D = 2D_{\text{sim}}/\sqrt{\pi}$ . This unit cell has a larger free volume for counterions as compared with the model considered in the previous section, which adopts a larger rod radius and a smaller outer cylinder radius (shown by a dashed circle)—compare Figure 6.4. c) The brush height (diamonds) calculated using the cell model shown in a) and b) is compared with the theoretical results presented in the previous section (squares) and the simulations (circles). Parameters are the same as in Figure 6.7a. The dotted lines (i) and (ii) are the scaling predictions (6.6) and (6.7), respectively.

simulation (square) unit cell. This implies a cell radius of  $D = 2D_{\text{sim}}/\sqrt{\pi}$  (Figure 6.8b). In brief, the new choice of the cell model gives a larger volume for counterions, which lowers their osmotic pressure. The results for the brush height are calculated (for  $f = 1$ ,  $\ell_B = \sigma$ , and  $q = q_m = 1$ ) using the full free energy (6.29), finite counterion size ( $r_c = b_0/2$ ) and the volume constraint as before (diamonds in Figure 6.8c). As expected, the results appear to be somewhat smaller than previous ones (squares in Figures 6.7 and 6.8c). Note also that the results for the new model lie around the minimum of the brush height, which occurs at intermediate grafting densities (see Figure 6.5b). The difference between the two models represents the systematic error-bars of the cell model, indicating also that the simulation data agree with the cell-model predictions within these errors-bars.

Yet some of the differences may still be associated with excluded-volume effects and lateral wiggling of the polyelectrolyte chains in the simulations, which are accounted for here in a simple fashion using the polymer volume conservation. They can play a role at large grafting densities, where the validity of the cell-model approach might break down.

### 6.3 Conclusion and Discussion

In this chapter, strongly charged polyelectrolyte brushes are investigated in the non-linear osmotic regime using a non-linear scaling analysis as well as a mean-field (Poisson-Boltzmann) cell model.

In the simulations [206] as well as in recent experiments [216, 217] on dense osmotic brushes, it has been observed that the brush height varies weakly with the grafting density. In this situation, polyelectrolyte chains are strongly stretched and counterions are mostly confined within the brush layer. The observed behavior for the brush height does not agree with the standard scaling analysis [16, 194], which yields a brush height independent of the grafting density.

The present non-linear scaling analysis indicates that the self-volume of the polymer chains, which is neglected in previous studies, plays an important role at large grafting densities and generates a *linear* dependence on the grafting density. This volume is inaccessible for counterions, and is effectively conserved. It therefore couples the osmotic pressure of counterions in the brush to the variations of the chains extension.

Furthermore, I have considered additional corrections to the scaling results using a mean-field analysis by incorporating i) the non-linear Poisson-Boltzmann theory, which includes lateral electrostatic effects (including non-uniform distribution of counterions in the brush), and ii) the non-linear elasticity of the chains (that are typically strongly stretched in the osmotic regime) using a freely-jointed-chain model. The predictions of the present study have been compared with both experiments and simulations and display a semi-quantitative agreement with them. While non-linear elasticity models have been accounted for in the past [200, 202], previous studies have commonly assumed that charges are smeared out and uniformly distributed in the brush. The present mean-field cell-model study shows that laterally inhomogeneous distribution of polymers (which are highly localized) and that of counterions become increasingly important as the grafting density is lowered: They lead to a weak dependence on the grafting density and a minimum for the brush height at intermediate grafting densities. At small grafting densities, they result in the re-stretching of the chains.

Here I have neglected the excluded-volume repulsion between counterions and also the non-uniform distribution of counterions in the direction normal to the anchoring plane, which results from partial diffusion of counterions outside the brush layer. The former effect may play a role at large grafting densities, while the latter is expected to become important at low grafting densities and for short chains (see below). Both effects are partially present in the simulations and experiments. In Section 6.1, I have shown that the diffusion of counterions outside the brush layer is expected to be negligible in the regime of parameters considered in the simulations and experiments. This is in fact verified directly in the simulations (see Figure 6.2). In what follows, I will first show that the excluded-volume repulsion between counterions is negligible, and then provide an estimate for the minimum chain length which is necessary to keep counterions inside the brush.

Possible contribution from excluded-volume repulsions between counterions may be estimated from the second-virial contribution to the total free energy, which may be written (per unit cell) as

$$\frac{\mathcal{F}_{v2}}{N_m k_B T} = \frac{1}{2N_m} v_2 \bar{\rho}_{ci}^2 V_{cell} = \frac{1}{2} v_2 \frac{N_m f^2}{\pi(D^2 - R^2)L}, \quad (6.40)$$

where  $v_2 > 0$  is the effective virial coefficient of counterions (for good solvent condition), and  $\bar{\rho}_{ci}$  is their average density in a unit cell of volume  $V_{cell} = \pi(D^2 - R^2)L$ . The longitudinal

pressure coming from the second-virial contribution,  $\pi_{v_2}^{\text{Long}}$ , is calculated by differentiating Eq. (6.40) with respect to  $L$ , the brush height. Comparing the result with the longitudinal osmotic pressure  $\pi_{\text{os}}^{\text{Long}} \sim f/L$  (Eq. (6.30)), one finds

$$\frac{\pi_{v_2}^{\text{Long}}}{\pi_{\text{os}}^{\text{Long}}} \sim \frac{v_2/2\pi b_0^3}{L/N_m f b_0} \left( \frac{4\rho_a b_0^2}{1 - 4\rho_a b_0^2} \right), \quad (6.41)$$

where the volume exclusion (closest approach distance) between counterions and monomers is also accounted for. For largest grafting densities used in the simulations, e.g.,  $\rho_a b_0^2 \sim 0.1$ , and for fully charged chains  $f = 1$  (where  $L/L_0 \sim 2/3$ ), one has  $\pi_{v_2}^{\text{Long}}/\pi_{\text{os}}^{\text{Long}} \sim (1/10)v_2/v_2^{\text{hc}}$ , where  $v_2^{\text{hc}} = \pi b_0^3/6$  is the hard-core second virial coefficient. If one takes  $v_2 \sim v_2^{\text{hc}}$ , the excluded-volume pressure of counterions, which is neglected in the present study, is found to be almost one order of magnitude smaller than their osmotic pressure. This ratio is even smaller for smaller charge fractions and grafting densities, which cover the experimental regime as well.

In general, counterions tend to leave the brush when the effective charge density of the polyelectrolyte layer,  $N_m f \rho_a$ , is small, i.e. at small grafting densities, small charge fractions or for short chains. To prevent this situation, one should choose the parameters such that the height of the counterion layer, which is roughly given by the effective Gouy-Chapman length of the brush layer,  $\mu = 1/(2\pi\ell_B N_m f \rho_a)$ , is smaller than the brush height  $L_*$  (note that here I concentrate on monovalent particles). Comparing  $\mu$  with the scaling prediction (6.6) for  $L_*$ , one finds that the osmotic condition,  $L_* > \mu$ , is ensured if the number of monomers is larger than the threshold

$$N_m^* = f^{-3/4} (\rho_a b_0^2)^{-1/2} \left( \frac{b_0}{\ell_B} \right)^{1/2}. \quad (6.42)$$

One notes that for  $f \sim 1$  and  $\ell_B \sim b_0$ , this condition corresponds to the overlapping threshold for neighboring chains, that is when  $\rho_a L_0^2 \sim 1$ , where  $L_0 = N_m b_0$  is the contour length. To give a numerical estimate for  $N_m^*$ , I use the simulation parameters ( $\ell_B = b_0$  for fully charged chains,  $f = 1$ ): at grafting densities as small as  $\rho_a b_0^2 \sim 10^{-6}$ , Eq. (6.42) gives  $N_m^* \sim 10^3$ , while for  $\rho_a b_0^2 \sim 10^{-2}$  it gives  $N_m^* \simeq 10$ . Note that the latter case coincides with the minimum grafting density used in the simulations, where polyelectrolyte chains bear  $N_m = 30$  monomers (see Section 6.1.1).

Another mechanism which may become relevant (and invalidate the assumptions of the present theory) at small charge fractions and small grafting densities is the formation of mushroom conformations due to shrinkage of the chains onto the anchoring plane. To prevent this, one has to take long chains with  $N_m > N_m^{**} = (\rho_a b_0^2)^{-1}$ , which is a more stringent condition on  $N_m$ , i.e.  $N_m^{**} > N_m^*$ . This corresponds to the Gaussian size of the polyelectrolyte chains,  $N_m^{1/2} b_0$ , being larger than the distance between neighboring chains in the brush,  $\rho_a^{-1/2}$ . (Note that I have assumed a Gaussian polymer to obtain an upper bound estimate for  $N_m^{**}$ .) At small grafting density of the order  $\rho_a b_0^2 \sim 10^{-6}$ , one has  $N_m^{**} \sim 10^6$ , a quite large value, and for  $\rho_a b_0^2 \sim 10^{-2}$ , one obtains  $N_m^{**} \sim 100$ . In brief the low-grafting-density regime, where the brush height has been predicted to increase with decreasing grafting density, may be observed in experiments and simulations by choosing long enough chains.

An interesting problem is to extend the present results to include the variation of the counterionic density profile in the direction normal to the anchoring plane and at low grafting densities. A previous study [201] predicts that if this effect is accounted for using the non-linear PB equation, the brush height monotonically decreases by lowering the grafting

density provided that the concentration of counterions (and that of monomers) is assumed to be smeared out laterally. The present results predict a re-increase of the brush height by lowering the grafting density, when the counterion profile is assumed to be uniform in normal direction, and allowed to adopt a laterally inhomogeneous form according to the non-linear PB equation. An extended approach should, therefore, examine the interplay between these two mechanisms.



## Chapter 7

# Charged Polymers in Electric Field

Understanding the dynamic behavior of charged polymers has become a major topic in polymer research mainly because in many practically relevant applications, one indeed deals with dynamical properties of polymers in solution [19]. A most notable example is electrophoresis, which has developed over the last several decades as a very powerful technique in separation and characterization of biomolecules and colloids [19, 218, 219, 220, 221]. In electrophoretic experiments, charged particles are studied subject to an external electric field and in particular, one measures the (electrophoretic) mobility of particles from their stationary-state drift velocity in response to the electric field. For charged polymers, the electrophoretic mobility appears to be dependent in a rather complex way on a number of factors such as chain contour length (or number of monomers) [220, 221, 222, 223, 224, 225, 226] and surrounding conditions such as ionic strength [223]. In general, the structural properties of polymers, such as stiffness, global chain conformation and even specific details such as charge pattern along the backbone [70, 73], as well as the nature of interactions with solvent particles and surrounding counterions all appear to have a remarkable influence on electrophoresis of charged polymers [58, 100, 165, 219, 220, 227, 228, 229, 230, 231, 232, 233]. Indeed, the interconnection between these factors has made it very difficult to establish a thorough theoretical understanding of polymer electrophoresis and there remains still numerous unsolved issues [73, 220, 221, 223, 224].

Classical theories for dynamics of charged polymers are built upon simple models in which, for instance, the polymer chain is modeled as a uniformly charged cylinder [165, 219, 228, 229, 230] or a line of discrete charges [58]. More complicated charge patterns that can capture structural details are exceedingly more difficult to study on an analytical level. The parameters that enter such theories (e.g., the linear charge density of polymer and the Manning parameter) reflect an effective or coarse-grained description of microscopic details.

Recent capillary electrophoresis experiments however reveal a markedly different behavior for polymer mobility when charge pattern of the backbone is changed [73]. One of the parameters that can be adjusted carefully using synthetic chains is the charge spacing (distance between two subsequent charged monomers along the backbone), which is related to the effective linear charge density or the Manning parameter. It is shown [73] that when the charge spacing is varied while the effective Manning parameter is kept fixed (e.g., by controlling the solvent dielectric constant), polymers exhibit different electrophoretic responses to the external driving field. Similar trend is observed when the counterion size is changed. These effects clearly go beyond the standard theoretical modeling of polymers and reflect the importance

of specific features and local structural details.

In this chapter, I aim to study certain aspects of the stationary-state electrophoretic mobility of charged polymers within a coarse-grained theoretical model, which can still account for structural details of the polymer chains in a simple fashion. For this I shall use Brownian Dynamics simulations (as well as simple analytical methods) and consider only long extended flexible polymers with spherical monomers together with neutralizing counterions both in the presence and absence of hydrodynamic interactions mediated by solvent medium. Short polymer chains may undergo folding-unfolding transitions [232, 233] and display orientational motions [234] and more complex conformational changes that go beyond the scope of the present study (long chain length is mimicked in the simulations using periodic boundary conditions along the central polymer axis). Moreover, the dynamics of counterions in the presence of an infinite polymer chain has not yet been examined numerically, while some of the classical theoretical works are in fact developed for such a system [58, 165, 219, 228, 229, 230]. This system is particularly interesting since counterion condensation emerges strictly at long extended charged polymers [39] (see also Chapter 3).

In this study, I shall consider several different charge patterns for the polymer chain by varying the charge spacing and the monomer size while keeping the effective linear charge density, the Bjerrum length and thus the Manning parameter fixed by increasing the monomer charge valency. Thereby, I demonstrate that the structural details can indeed substantially affect the mobility of particles both in free-draining situation (i.e. without hydrodynamic interactions) and in a hydrodynamic medium. In particular, the monomer and counterion mobility (along the polymer central axis) both reduce upon increasing the polymer charge spacing, which, in the free-draining situation, can be understood analytically in terms of a simple model incorporating driven diffusion of counterions in a periodic potential generated by the charge pattern of the polymer chain. I will also demonstrate how condensation of counterions influence dynamics of monomers and counterions in both cases. (Note that unlike the discussion in Chapter 3, where statics of counterion condensation is studied in the asymptotic infinite-dilution limit, here only small confining volumes per polymer are considered.) An interesting result is that hydrodynamic effects lead to a reduction in the population of condensed counterions (hydrodynamic *evaporation*), which becomes more enhanced upon increasing the electric field. This can be related to a large friction force on counterions in this case as compared with the free-draining situation. Hydrodynamic forces generated by the polymer chain in fact reverse the counterion mobility, i.e. counterions are dragged along with the charged polymer. Yet in contrast to the main assumption in the standard counterion-condensation model [58], mobility of condensed counterions turns out to be lower (in magnitude) than the monomer mobility. In the free-draining case, by contrast, counterions always tend to move in their proper direction in the electric field.

## 7.1 Model and methods

In the following dynamics simulations, I consider a single flexible charged polymer chain consisting of  $N_m$  spherical monomers of radius  $r_m$  of which a fraction  $f$  is charged with charge valency  $-q_m$ , and with a regular distribution along the backbone. I employ a cell model in which the polymer is centered and confined with its neutralizing counterions in a square box of lateral edge size  $L$  and height  $H$ . The box contains  $N$  counterions of radius  $r_c$



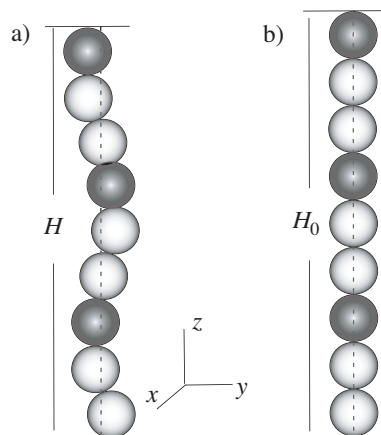


Figure 7.1: Schematic view of a flexible polymer composed of charged and neutral spherical monomers (in black and light gray respectively). Fluctuations (a) cause the projected polymer end-to-end distance,  $H$ , to be generally different from the contour length  $H_0 = 2N_m r_m$  (b). Central polymer axis is shown by a dashed vertical line.

and charge valency  $+q$  to ensure the electroneutrality condition, i.e.

$$qN = f q_m N_m. \quad (7.1)$$

(Note that  $q_m$  and  $q$  are defined to be positive.) In order to mimic an infinite polymer chain, I choose the box height  $H$  to be equal to the projected end-to-end distance of the polymer along its central axis ( $z$  axis) and implement periodic boundary conditions by replicating the main simulation box infinitely many times in that direction. Therefore, the box height is instantaneously updated during the simulations according to length fluctuations of the polymer (Figure 7.1). For the parameters chosen in this work, however, the length variation is typically only a small percentage of the polymer contour length,  $H_0 = 2N_m r_m$ , and does not lead to an appreciable effect.

### 7.1.1 Interactions

The following interactions are accounted for in the present model. Charged particles are supposed to interact with the bare Coulomb interaction

$$\frac{U_Q}{k_B T} = \ell_B \sum_{\langle ij \rangle} \frac{q_i q_j}{|\mathbf{x}_i - \mathbf{x}_j|}, \quad (7.2)$$

where the sum runs over all particle pairs in the main simulation box and their periodic images in  $z$  direction. Here  $q_i$  and  $\mathbf{x}_i$  refer to the charge valency and the position of particle  $i$ . Summation over periodic images in Eq. (7.2) leads to infinite summation series over Coulomb interaction ( $\sim 1/|\mathbf{x}|$ ). In dynamics simulations, one in fact needs to calculate summation series over inter-particle forces ( $\sim 1/|\mathbf{x}|^2$ ), which are rapidly convergent and can be calculated with high accuracy using the methods developed by Lekner [110] and Sperb [111] (see Appendix D).

Charged particles also experience a constant external electric field,  $\mathbf{E} = E \hat{z}$ , in  $z$  direction specified by the interaction potential

$$\frac{U_{\text{ext}}}{k_{\text{B}}T} = - \sum_i \left( \frac{q_i e}{k_{\text{B}}T} \right) E z_i. \quad (7.3)$$

Monomers and counterions are modeled as soft spheres using an excluded-volume potential

$$U_{\text{LJ}} = \sum_{\langle ij \rangle} U_{\text{LJ}}^{ij}, \quad (7.4)$$

where  $U_{\text{LJ}}^{ij}$  is the shifted Lennard-Jones potential

$$\frac{U_{\text{LJ}}^{ij}}{k_{\text{B}}T} = \begin{cases} \epsilon \left[ \left( \frac{\sigma_{ij}}{|\mathbf{x}_{ij}|} \right)^{12} - 2 \left( \frac{\sigma_{ij}}{|\mathbf{x}_{ij}|} \right)^6 + 1 \right] & |\mathbf{x}_{ij}| \leq \sigma_{ij} \\ 0 & |\mathbf{x}_{ij}| \geq \sigma_{ij}, \end{cases} \quad (7.5)$$

between each two particles  $i$  and  $j$  of center-to-center distance  $|\mathbf{x}_{ij}| = |\mathbf{x}_i - \mathbf{x}_j|$ . Here  $\epsilon$  determines the strength of repulsion (in units of  $k_{\text{B}}T$ ) and  $\sigma_{ij}$  is taken as the sum of radii, i.e.  $\sigma_{ij} = r_i + r_j$  (one has  $r_i = r_c$  if particle  $i$  is a counterion and  $r_i = r_m$  if it is a monomer). Note that such a soft potential maintains an equilibrium separation of  $|\mathbf{x}_{ij}|_{\text{eq}} = \sigma_{ij}$  for two particles when other forces are absent.

Finally, to ensure the connectivity of the polymer chain, a Gaussian (or linear) elasticity potential is used as

$$\frac{U_{\text{elas}}}{k_{\text{B}}T} = \frac{K}{2} \sum_{\langle ij \rangle} \left( |\mathbf{x}_i - \mathbf{x}_j| - 2r_m \right)^2, \quad (7.6)$$

where the sum runs over nearest neighbors of the chain monomers only. This potential represent a *flexible* chain with a bond stiffness  $K$ .

### 7.1.2 Rescaled parameters

In order to proceed, it is convenient to use a dimensionless representation. I conventionally rescale the length scales with the counterion radius, e.g., as

$$\tilde{\mathbf{x}} = \frac{\mathbf{x}}{r_c}. \quad (7.7)$$

In rescaled units

$$\tilde{r}_m = \frac{r_m}{r_c} \quad (7.8)$$

gives the size ratio between monomers and counterions and is a key parameter to demonstrate structural details. Other relevant rescaled parameters are the charge fraction,  $f$ , and the charge valency ratio

$$\tilde{q}_m = \frac{q_m}{q}. \quad (7.9)$$

The strength of electrostatic interactions in the system is typically determined by two independent dimensionless parameters, namely, the Manning parameter

$$\xi = \frac{f q_m q \ell_{\text{B}}}{2 r_m} \quad (7.10)$$

and the *counterionic* Coulomb parameter

$$\Gamma_c = \frac{q^2 \ell_B}{2r_c}. \quad (7.11)$$

This latter parameter can be expressed in terms of other dimensionless parameters as  $\Gamma_c = \xi \tilde{r}_m / (\tilde{q}_m f)$ . Recall that the Manning parameter determines the binding state of counterions to the polymer chain and regulates the counterion-condensation process (Chapters 2 and 3). The counterionic coupling parameter, on the other hand, gives the strength of Coulomb repulsions between two counterions at contact and is a measure of electrostatic correlations among counterions. Note also that Eq. (7.10) represents Manning parameter of a fully extended chain, i.e. with all monomers being in contact and aligned in  $z$  direction (Figure 7.1b).

In rescaled representation, the external field reads

$$\tilde{E} = \frac{qer_c E}{k_B T}, \quad (7.12)$$

which is varied in the simulations over a range of  $\tilde{E} \sim 0.1 - 10$  in order to bring out both linear- and non-linear-response features in the present theoretical model. For comparison, note that  $\tilde{E} = 0.5$  corresponds to an electric field of about  $E \sim 10^6$  V/m if one takes nanometer-size particles of valency  $q = 3$ , which is close to realistic values.

Other rescaled parameters that will be fixed in the present study are the Lennard-Jones energy parameter,  $\epsilon$ , which is typically chosen as unity, and the stiffness parameter  $\tilde{K} = Kr_c^2 / (k_B T)$ , which is chosen as  $\tilde{K} = 100$  corresponding to a narrow distribution of polymer bond lengths.

### 7.1.3 Langevin Brownian Dynamics

To investigate the stationary-state dynamics of the polymer-counterion system, I shall employ the position Langevin equation both in the absence and in the presence of hydrodynamic interactions. The former case is referred to as *free-draining* (or self-diffusing) dynamics and corresponds to the situation where the velocity of a particle is determined only by the force acting on it. In general, however, the velocity of a given particle in a fluid medium is not simply proportional to the forces acting on that particle, but depends on the forces acting on other particles as well. This is because the force acting on a given particle causes a long-range flow field in solvent (which is treated here as a continuum medium) and thereby affects the velocities of other particles [235]. This kind of interaction mediated by solvent flow is referred to as *hydrodynamic interaction* and will be accounted for in the following simulations as well. The comparison between these two cases for particle dynamics allows one to identify the role of electro-friction and hydrodynamic effects separately.

#### Free-draining dynamics

The free-draining position Langevin equation yields the velocity of the  $i$ -th particle at time  $t$  as [12, 13, 236]

$$\dot{\mathbf{x}}_i = -\mu_0^i \nabla_{\mathbf{x}_i} U_{\text{tot}} + \boldsymbol{\zeta}_i(t), \quad (7.13)$$

where

$$U_{\text{tot}} = U_Q + U_{\text{ext}} + U_{\text{LJ}} + U_{\text{elas}} \quad (7.14)$$

is the total interaction potential of the system (thus  $-\nabla_{\mathbf{x}_i} U_{\text{tot}}$  is nothing but the total force acting on particle  $i$ ), and  $\zeta_i(t)$  is a time-dependent noise term, which mimics random collisions with microscopic solvent particles. The above equation represents dissipative dynamics of the system at sufficiently long times where inertia effects are relaxed [13, 17]. Here  $\mu_0^i$  is the bare particle mobility (or self-mobility) which is inversely proportional to the friction coefficient  $\eta$  as

$$\mu_0^i = \frac{1}{6\pi\eta r_i}. \quad (7.15)$$

The noise term  $\zeta_i(t)$  is chosen as a Gaussian-distributed uncorrelated (white) noise with zero mean value  $\langle \zeta_i(t) \rangle = 0$ , and the two-point correlation function

$$\langle \zeta_{i\nu}(t) \zeta_{j\nu'}(t') \rangle = 2D_0^i \delta_{ij} \delta_{\nu\nu'} \delta(t - t'), \quad (7.16)$$

where  $\nu$  and  $\nu'$  represent different Cartesian components. To ensure an equilibrium distribution function according to the Boltzmann weight at long times (for zero external field), the self-diffusion constant  $D_0^i$  must fulfill the Einstein's relation [9], i.e.

$$D_0^i = \mu_0^i k_B T. \quad (7.17)$$

In numerical simulations [237], the Langevin equation is used in a discretized form using a finite, sufficiently small time step  $\Delta t$ . Thus, for example, the equation for  $z$  component of the position vector of the  $i$ -th particle at time  $t = (n + 1) \Delta t$  reads

$$\tilde{z}_i(n + 1) = \tilde{z}_i(n) - \tilde{\mu}_0^i \left( \frac{\partial \tilde{U}_{\text{tot}}}{\partial \tilde{z}_i} \right)_n + \sqrt{2\tilde{\mu}_0^i} \tilde{\zeta}_{iz}(n) \quad (7.18)$$

for the integral number  $n$  and in rescaled units (similar equations hold for  $x$  and  $y$  components). Here I have defined  $\tilde{U}_{\text{tot}} = U_{\text{tot}}/(k_B T)$ , and

$$\tilde{\mu}_0^i = \frac{D_0^i \Delta t}{r_c^2} \quad (7.19)$$

as the rescaled self-mobility (or dimensionless time step) of particle  $i$ . The discrete noise term is rescaled as  $\tilde{\zeta}_{i\nu}(n) = \zeta_{i\nu}(n)/\sqrt{2D_0^i/\Delta t}$  representing thus a random Gaussian distribution with zero mean and unit variance, i.e.  $\langle \tilde{\zeta}_{i\nu}(n) \rangle = 0$  and

$$\langle \tilde{\zeta}_{i\nu}(n) \tilde{\zeta}_{j\nu'}(n') \rangle = \delta_{ij} \delta_{\nu\nu'} \delta_{nn'}. \quad (7.20)$$

The Langevin equation is supplemented with an initial condition for particle positions. I choose the initial conditions such that all monomers are aligned in  $z$  direction and the chain length equals the contour length (Figure 7.1b). But counterion locations are chosen at random in the simulation box. The rescaled time step  $\tilde{\mu}_0^i$  is typically chosen as  $\tilde{\mu}_0^i = 10^{-3}/\tilde{r}_i$  (with  $\tilde{r}_i = 1$  for counterions and  $\tilde{r}_i = \tilde{r}_m$  for monomers), which provides a good compromise between accuracy and efficiency.

### Hydrodynamic interactions

Hydrodynamic interactions between particles may be modeled in the simulations as follows. For macromolecular systems, it is commonly assumed that the fluid motion is incompressible

and creeping [6]. In other words, the flow field around particles can be described by the *linearized* Navier-Stokes equation, known as Stokes equation, corresponding to the so-called low-Reynolds-number regime [235]. Hence, the deterministic part of the velocity at the position of particle  $i$  can be obtained from linear superposition of velocities generated by forces acting on all particles as [235]

$$\mathbf{v}_i = \sum_j \hat{\mathbf{M}}_{ij} \cdot \mathbf{F}_j, \quad (7.21)$$

where the sum runs over *all* particles,  $\mathbf{F}_j$  is the force acting on particle  $j$ , and  $\hat{\mathbf{M}}_{ij}$  is the (hydrodynamic) *mobility tensor* for a pair of particles  $i$  and  $j$ , which depends on the distance between these particles, i.e.  $\mathbf{x}_{ij} = \mathbf{x}_i - \mathbf{x}_j$ . The Langevin equation may thus be written as [238]

$$\dot{\mathbf{x}}_i = - \sum_j \hat{\mathbf{M}}_{ij} \cdot (\nabla_{\mathbf{x}_j} U_{\text{tot}}) + \sum_j \nabla_{\mathbf{x}_i} \cdot \hat{\mathbf{D}}_{ij} + \boldsymbol{\zeta}_i(t), \quad (7.22)$$

where now the zero-mean Gaussian noise term has the following two-point correlation function

$$\langle \boldsymbol{\zeta}_i(t) \boldsymbol{\zeta}_j(t') \rangle = 2\hat{\mathbf{D}}_{ij} \delta(t - t'), \quad (7.23)$$

with the *diffusion tensor*  $\hat{\mathbf{D}}_{ij}$  being related to the mobility tensor by virtue of the fluctuation-dissipation theorem (generalized Einstein's relation) as

$$\hat{\mathbf{D}}_{ij} = k_B T \hat{\mathbf{M}}_{ij}. \quad (7.24)$$

Note that since the friction in the system leads to dissipation of energy, the mobility or diffusion tensor is positive definite.

The case with no hydrodynamic interactions is reproduced when the off-diagonal terms of the mobility tensor are zero and one has only the self terms, i.e.  $\hat{\mathbf{M}}_{ij} = \mu_0^i \delta_{ij} \hat{\mathbf{I}}$ , where  $\hat{\mathbf{I}}$  is the three-dimensional unity matrix.

Numerous studies in past have considered the systematic derivation of the hydrodynamic tensor,  $\hat{\mathbf{M}}_{ij}$ , for spherical particles of finite size [239, 240].  $\hat{\mathbf{M}}_{ij}$  can in general be written as an expansion in inverse powers of the center-to-center distance between particles,  $\mathbf{x}_{ij} = \mathbf{x}_i - \mathbf{x}_j$ . Assuming no-slip (stick) boundary condition on particle surfaces and on the leading order (in inverse powers of distance  $1/|\mathbf{x}_{ij}|$ ), the hydrodynamic tensor is given by

$$\hat{\mathbf{M}}_{ii} = \mu_0^i \hat{\mathbf{I}} \quad (7.25)$$

for same particle ( $i = j$ ), and for different *non-overlapping* particles as

$$\hat{\mathbf{M}}_{ij} = \frac{1}{8\pi\eta |\mathbf{x}_{ij}|} \left[ \left( 1 + \frac{\sigma_{ij}^{(2)}}{3|\mathbf{x}_{ij}|^2} \right) \hat{\mathbf{I}} + \left( 1 - \frac{\sigma_{ij}^{(2)}}{|\mathbf{x}_{ij}|^2} \right) \hat{\mathbf{x}}_{ij} \hat{\mathbf{x}}_{ij} \right] \quad \text{for } |\mathbf{x}_{ij}| > \sigma_{ij}, \quad (7.26)$$

where  $\hat{\mathbf{x}}_{ij} = \mathbf{x}_{ij}/|\mathbf{x}_{ij}|$ ,  $\sigma_{ij} = r_i + r_j$  and  $\sigma_{ij}^{(2)} = r_i^2 + r_j^2$ . When particles overlap, i.e.  $|\mathbf{x}_{ij}| < \sigma_{ij}$ , the above expression for  $\hat{\mathbf{M}}_{ij}$  is no longer valid. In this case, a positive-definite expression was obtained by Rotne and Prager [239] as

$$\hat{\mathbf{M}}_{ij} = \frac{1}{6\pi\eta a} \left[ \left( 1 - \frac{9|\mathbf{x}_{ij}|}{32a} \right) \hat{\mathbf{I}} + \left( \frac{3|\mathbf{x}_{ij}|}{32a} \right) \hat{\mathbf{x}}_{ij} \hat{\mathbf{x}}_{ij} \right] \quad \text{for } |\mathbf{x}_{ij}| < \sigma_{ij}, \quad (7.27)$$

which is valid only for *equal-size* particles with  $r_i = r_j = a$ . In the simulations with equal-size particles, I will therefore use Eqs. (7.25)-(7.27) to incorporate hydrodynamic interactions.

For non-equal size particles, however, I shall only employ Eq. (7.25) and the non-overlapping expression (7.26), but make use of a larger excluded-volume repulsion strength between particles (typically with  $\epsilon = 5$ ), such that the particle overlapping is suppressed and the positive-definiteness of the mobility tensor is not violated.

For the purpose of numerical simulations, equation (7.22) should be used in a discretized form [237, 238]. But first note that the second term on the right hand side of this equation is zero since the mobility tensor as given above is divergenceless, i.e.

$$\sum_j \nabla_{\mathbf{x}_i} \cdot \hat{\mathbf{D}}_{ij} = 0. \quad (7.28)$$

Thus using a sufficiently small time step  $\Delta t$ , one obtains

$$\mathbf{x}_i(n+1) = \mathbf{x}_i(n) - \sum_j \left[ \hat{\mathbf{M}}_{ij} \cdot (\nabla_{\mathbf{x}_j} U_{\text{tot}}) \right]_n \Delta t + \zeta_i(n) \Delta t, \quad (7.29)$$

where the discretized zero-mean Gaussian random force,  $\zeta_i$ , has the two-point correlation function

$$\langle \zeta_i(n) \zeta_j(n') \rangle = 2 \hat{\mathbf{D}}_{ij} \frac{\delta_{nn'}}{\Delta t}. \quad (7.30)$$

In rescaled units, one has

$$\tilde{\mathbf{x}}_i(n+1) = \tilde{\mathbf{x}}_i(n) - \sum_j \left[ \hat{\mathbf{M}}'_{ij} \cdot (\nabla_{\tilde{\mathbf{x}}_j} \tilde{U}_{\text{tot}}) \right]_n + \sqrt{6} \tilde{\zeta}_i(n), \quad (7.31)$$

where  $\tilde{\zeta}_i(n) = \zeta_i(n) \Delta t / (\sqrt{2} r_c)$ ,  $\hat{\mathbf{M}}'_{ij} = \hat{\mathbf{M}}_{ij} \Delta t / r_c^2$ , and thus

$$\langle \tilde{\zeta}_i(n) \tilde{\zeta}_j(n') \rangle = \hat{\mathbf{D}}'_{ij} \delta_{nn'}, \quad (7.32)$$

where I have defined  $\hat{\mathbf{D}}'_{ij} = \hat{\mathbf{D}}_{ij} \Delta t / r_c^2$ . Note that a random Gaussian noise with the correlation function (7.32) may be generated numerically from Gaussian distributed random numbers with zero mean and *unit* variance using the Cholesky decomposition method as described in detail by Ermak et al. [238].

In the simulations, I will use minimal-image scheme to determine hydrodynamic interactions between particles and their periodic images, because a closed-form formula for the computation of the square root of the hydrodynamic tensor (involved in the Cholesky decomposition method) [241] is not available when incorporating infinite periodic images. This approximation is expected to be valid because only systems with small lateral extensions are considered here, where hydrodynamic interactions are expected to be screened at distances comparable to the box height. By contrast, Coulomb interactions are evaluated using infinite periodic images along the polymer central axis (Appendix D).

#### 7.1.4 Models for charge pattern

In order to bring out the effects due to local structural details of polymers, I shall consider five different models for charge pattern of a polymer chain. These are obtained by varying the charge fraction  $f$ , the charge valency ratio,  $\tilde{q}_m = q_m/q$ , and the size ratio,  $\tilde{r}_m = r_m/r_c$ , between monomers and counterions. Note that these parameters are changed such that the system retains *the same* Bjerrum length,  $\ell_B$ , and the effective linear charge density for the

polymer chain,  $\tau = q_m f / (2r_m)$ , as well as the same Manning parameter,  $\xi$ , in all different models. I will use counterions of the same charge valency and radius in these models. Therefore, when an effective description is considered (i.e. by mapping a polymer chain to a uniformly charged line or cylinder of given radius), all these models appear to be *equivalent*; hence, one can isolate the effects due only to the polymer charge distribution and ions sizes.

Different polymer models used in the present study are as follows (Figure 7.2):

- model A: all monomers are charged,  $f = 1$ , and have the same charge and radius as counterions,  $\tilde{q}_m = \tilde{r}_m = 1$ .
- model B<sub>1</sub>: every second monomer is charged,  $f = 1/2$ , but with a valency twice that of counterions (in magnitude),  $\tilde{q}_m = 2$ . All monomers have the same radius as counterions,  $\tilde{r}_m = 1$ .
- model B<sub>2</sub>: every third monomer is charged,  $f = 1/3$ , with  $\tilde{q}_m = 3$ , but again  $\tilde{r}_m = 1$ .
- model C<sub>1</sub>: all monomers are charged,  $f = 1$ , but they are twice as big as counterions,  $\tilde{r}_m = 2$ , and bear a charge valency twice the counterion valency,  $\tilde{q}_m = 2$ .
- model C<sub>2</sub>: all monomers are charged,  $f = 1$ , but they are three times larger than counterions,  $\tilde{r}_m = 3$ , and bear a charge valency three times as large,  $\tilde{q}_m = 3$ .

## 7.2 Simulations results

### 7.2.1 Counterion distribution

Figure 7.2 shows typical snapshots from Brownian Dynamics simulations for the five different models introduced above (recall that all these polymer models have the same effective linear charge density). Here the Manning parameter is chosen as  $\xi = 4.0$ , the rescaled electric field (in  $z$  direction upward) is  $\tilde{E} = 3.0$ , and particle dynamics is free draining. As may be seen from the snapshots, counterions tend to accumulate more densely around polymer models with *smaller* monomer size (note that some counterions always tend to diffuse to large distances from the polymer which are not shown in the snapshots). In order to quantify the distribution of counterions, I shall consider the radial density profile,  $\rho(r)$ , of counterions averaged in  $z$  direction and calculated directly from the simulations.

Figure 7.3a shows the rescaled density profile  $\tilde{\rho}(\tilde{r}) = \rho(r)r_c^3$  for different models and in the absence (no HI) and presence (HI) of hydrodynamic interactions. Note that here  $r$  is the radial distance from the polymer central axis (in  $xy$  plane) and  $r_c$  the counterionic radius. The Manning parameter is  $\xi = 4.0$ , the rescaled external field is  $\tilde{E} = 3.0$  (as in Figure 7.2), and the density profiles are normalized to the total number of counterions,  $N$ . In general, the data show a peak at radial distance  $\tilde{r} \simeq \tilde{r}_m + 1$ , which corresponds to the closest approach distance of counterions from monomers. Below this distance, counterion density reduces due mainly to volume exclusion from monomers. But still since the chain is flexible and there is sizable chain wiggling for small monomer size (models A, B<sub>1</sub> and B<sub>2</sub>), counterions have a finite chance to appear at the polymer central axis and thus their density at  $\tilde{r} = 0$  is not zero. The reduction of counterion density near the polymer with increasing monomer-counterion size ratio,  $\tilde{r}_m$ , is clearly seen from the figure both with and without hydrodynamic interactions (compare models C<sub>1</sub> and C<sub>2</sub> with other models). This may be understood by

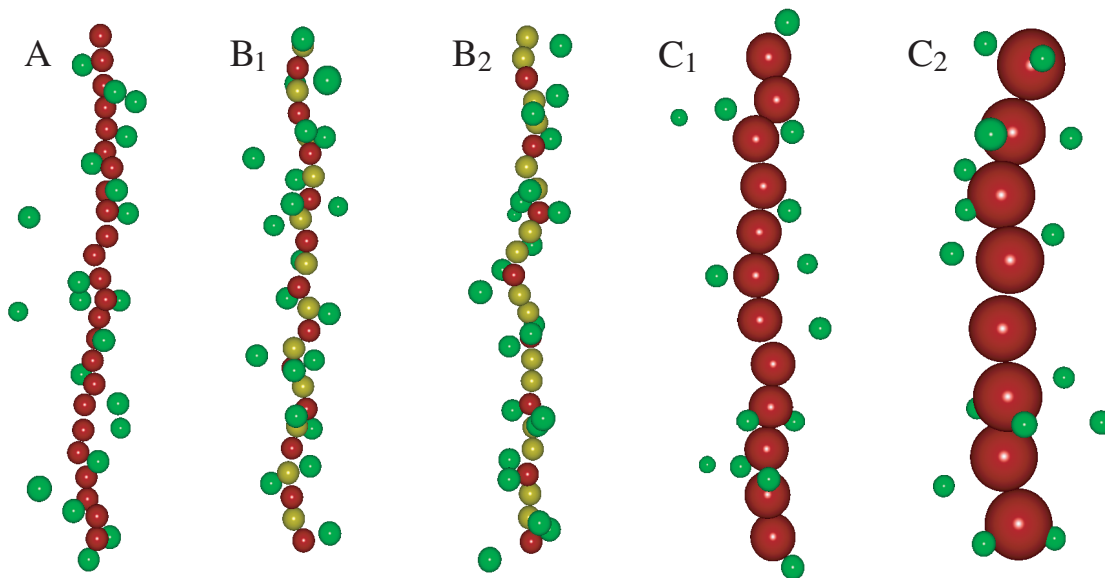


Figure 7.2: Typical snapshots from the Brownian Dynamics simulation of a charged polymer and counterions. Charged monomers are shown in dark gray and neutral monomers are shown in light gray. In models A,  $C_1$  and  $C_2$  all monomers are charged but have different sizes, namely, the same size as counterions in A and twice and three times as large in  $C_1$  and  $C_2$ . In models  $B_1$  and  $B_2$ , monomers have the same size as counterions, but the charge fraction changes, i.e. every second and every third monomer is charged in  $B_1$  and  $B_2$  respectively. Note that all models have the same effective linear charge density and Manning parameter, which is achieved by changing the charge valency of monomers, i.e. in model A, counterions and monomer have the same valency but monomer valency is twice (three times) the counterion valency in models  $B_1$  and  $C_1$  ( $B_2$  and  $C_2$ ). Here Manning parameter is  $\xi = 4.0$ , the electric field strength (in  $z$  direction upward) is  $\tilde{E} = 3.0$ , the lateral box edge size is  $\tilde{L} = 60 + 2\tilde{r}_m$  (with  $\tilde{r}_m = r_m/r_c$ ) and hydrodynamic interactions are switched off.

noting that although polymers have the same linear charge density, their effective surface charge density, and thereby their effective surface field which attracts counterions, reduces sizably with increasing  $\tilde{r}_m$ .

Comparing the data in Figures 7.3a indicates that hydrodynamic interactions lead to dilution of the counterionic atmosphere in the immediate vicinity of the polymer chain, as the density peak height in this case (HI) is systematically lower. In Figure 7.3b, I show the radial density of counterions in the presence of hydrodynamic interactions and for increasing electric field in model  $B_2$ . As clearly seen, the counterionic density reduces further around the polymer chain as the electric field becomes larger. Such effects are almost negligible in the absence of hydrodynamic interactions (data not shown; see, e.g., Figure 7.4b below).

### 7.2.2 Hydrodynamic “evaporation” mechanism

To examine the field-driven dilution of the counterionic cloud in more detail, I consider an integrated quantity,  $\alpha$ , which is obtained by integrating the density profile up to a certain distance,  $\tilde{r}_*$ , from the central polymer axis (and dividing by the total number of counterions).



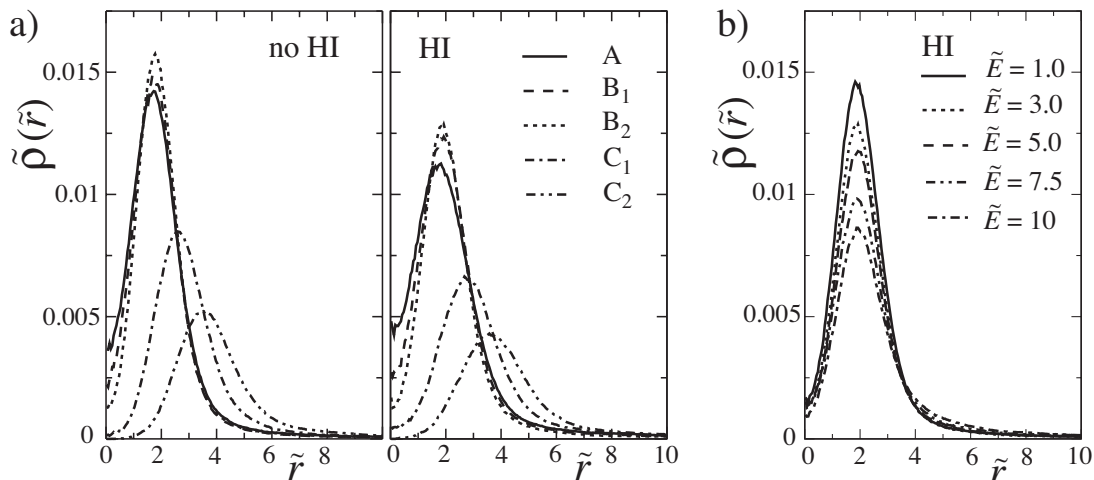


Figure 7.3: a) Radial density profile of counterions averaged in  $z$  direction and in rescaled units  $\tilde{\rho}(\tilde{r}) = \rho(r)r_c^3$  as a function of rescaled radial distance from the polymer central axis,  $\tilde{r}$ , for various models with the following parameters:  $\xi = 4.0$ ,  $\tilde{E} = 3.0$  (in  $z$  direction) and  $\tilde{L} = 60 + 2\tilde{r}_m$ . The graph on the left (no HI) represents free-draining results, while the graph on the right (HI) shows the data with hydrodynamic interactions included. b) The same as a) but in the presence of hydrodynamic interactions and for model B<sub>2</sub> and various rescaled electric field strength as indicated on the graph. (These results are obtained with  $N = 24$  counterions and  $N_m = 24$  monomers in models A, B<sub>1</sub> and B<sub>2</sub>, and  $N_m = 12$  and 8 monomers in models C<sub>1</sub> and C<sub>2</sub> under periodic boundary conditions in  $z$  direction.)

Connecting this quantity with the so-called *condensed fraction* of counterions requires a criterion for  $\tilde{r}_*$ . For this purpose, I consider the cumulative density profile  $n(\tilde{r})$  of counterions, which gives the number of counterions within a cylindrical shell of radius  $\tilde{r}$ . Typical examples for  $n(\tilde{r})$  are shown in Figure 7.4a from free-draining dynamics simulations of models C<sub>1</sub> and C<sub>2</sub> (note that the radial distance  $0 \leq \tilde{r} \leq \sqrt{2}\tilde{L}/2$  in a square box of edge size  $\tilde{L}$ ). The short-distance increasing part of the profile (till it reaches a shoulder) is taken here as the condensed layer; it typically corresponds to distances smaller than  $\tilde{r}_* = 4 + \tilde{r}_m$ , and thus represents a cylindrical shell around the polymer axis that can accommodate *two* layers of counterions. In fact since the Manning parameter is large here ( $\xi = 4.0$ ), the result is not strongly dependent on the choice of  $\tilde{r}_*$ . (Recall from equilibrium studies in Chapter 3 that in the infinite-dilution limit,  $\tilde{L} \rightarrow \infty$ , one can provide a systematic definition for the condensed fraction using the Poisson-Boltzmann equation.)

The results for the condensed fraction,  $\alpha$ , are shown in Figure 7.4b with (HI) and without (no HI) hydrodynamic interactions. As expected, for vanishing electric field, the condensed fraction agrees with the equilibrium Manning limiting value,  $\alpha_M = 1 - 1/\xi$  for  $\xi > 1$  (i.e.  $\alpha_M = 0.75$  for  $\xi = 4.0$ ), which is shown by a dot-dashed line in the graph. In fact, the free-draining and the hydrodynamic results also coincide for vanishing electric field, which reflects the basic point that equilibrium properties of the system do not depend on hydrodynamic interaction between particles. For models C<sub>1</sub> and C<sub>2</sub>, which have larger monomers,  $\alpha$  is typically smaller due to the lower density of counterions near the surface as discussed before.

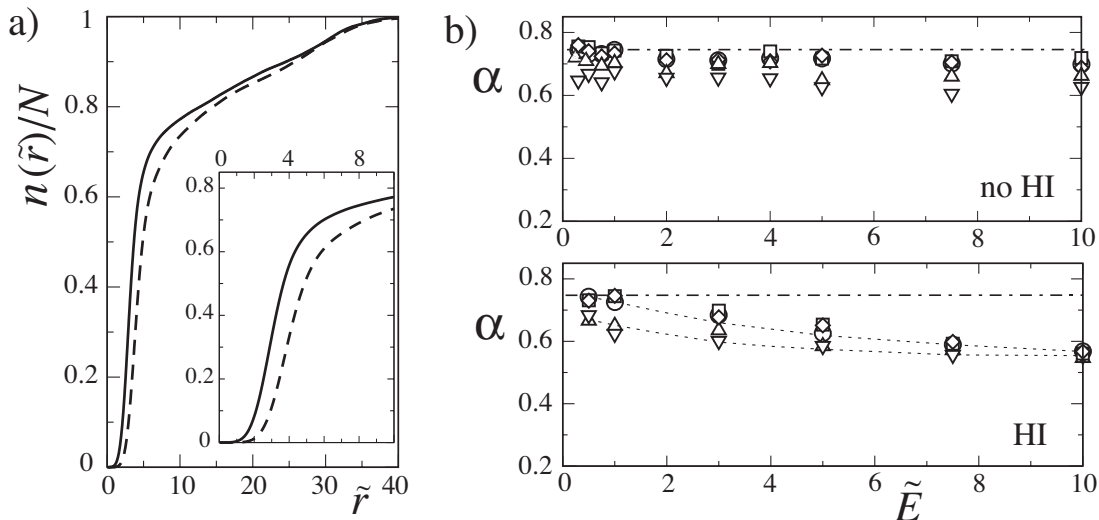


Figure 7.4: a) Cumulative radial density of counterions,  $n(\tilde{r})$ , as a function of distance from the central polymer axis,  $\tilde{r}$ , for models  $C_1$  (solid curve) and  $C_2$  (dashed curve) in the absence of hydrodynamic interactions (for  $\tilde{E} = 3.0$  and  $\xi = 4.0$ ). Inset shows a closer view of the data for small distances. b) Condensed fraction of counterions as defined in the text (Section 7.2.2) as a function of the electric field with (HI) and without (no HI) hydrodynamic interactions. Symbols show different models: A (circles),  $B_1$  (squares),  $B_2$  (diamonds),  $C_1$  (triangle-ups),  $C_2$  (triangle-downs), and dotted lines are guides to eyes. Manning parameter is  $\xi = 4.0$  and other parameters are as in Figure 7.3. The equilibrium Manning limiting value is shown by a horizontal dot-dashed line. Error-bas are of the order of the symbol size.

When particle do not interact hydrodynamically, the condensed ratio remains almost the same at various electric fields. However, in agreement with the observation in previous section, the condensed fraction is smaller and systematically decreases for growing external field strength,  $\tilde{E}$ , when hydrodynamic interactions are taken into account. A comparison of numerical values suggest that up to 10% of counterions are driven away or *evaporate* as a result of hydrodynamic interactions. As will be discussed later, this mechanism allows the system to reduce the friction. Note that because charged monomers drift in opposite direction to the external field, they tend to drag condensed counterions along, that is opposite to their proper direction, which causes a considerable friction.

### 7.2.3 Electrophoresis: Mobility in an external field

In this section, I shall focus on the stationary-state mobility of particles under the action of an external field. The average mobility of a charged particle  $i$  due to an electric field in  $z$  direction,  $\mathbf{E} = E \hat{\mathbf{z}}$ , is defined here as

$$\mu_i = \frac{\langle \dot{z}_i(t) \rangle}{q_i e E}, \quad (7.33)$$

where  $q_i e$  is the charge and  $\dot{z}_i$  is the velocity of the particle in  $z$  direction. In the absence of interactions between particles, the mobility tends to the bare mobility of the particle, i.e.

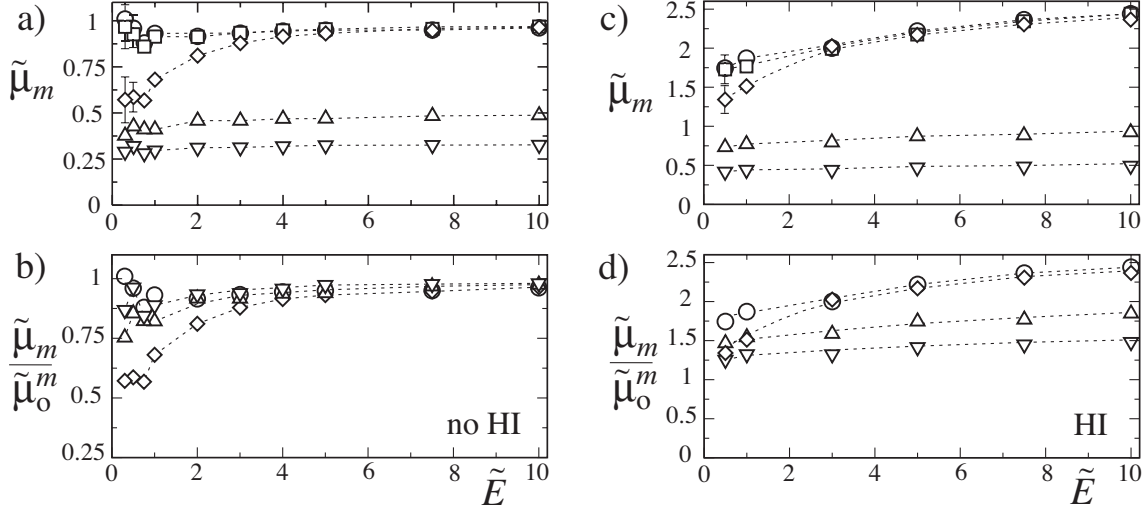


Figure 7.5: Rescaled mobility of monomers,  $\tilde{\mu}_m$ , Eq. (7.35), in the absence (a) and presence (c) of hydrodynamic interactions as a function of the rescaled external field,  $\tilde{E}$ . Symbols show different models: A (circles), B<sub>1</sub> (squares), B<sub>2</sub> (diamonds), C<sub>1</sub> (triangle-ups) and C<sub>2</sub> (triangle-downs). b) and d) are the same data (excluding model B<sub>1</sub>) in which the mobility is rescaled with the bare value  $\tilde{\mu}_0^m = \tilde{r}_m^{-1}$ , Eq. (7.36). Here the Manning parameter is  $\xi = 4.0$  and other parameters are as in Figure 7.3. Dotted lines are guides to eyes. Error-bars if not shown are smaller than the symbol size.

$\mu_i \rightarrow \mu_0^i$  (Eq. (7.15)), as may directly be seen from the Langevin equation (7.13).

### Mobility of monomers

The average mobility of monomers can be calculated in the simulations from the discrete form

$$\mu_m = -\frac{1}{q_m e f N_m E \Delta t} \overline{\sum_{i=1}^{N_m} [z_i(n+1) - z_i(n)]}, \quad (7.34)$$

where the sum runs over all monomers in the simulation box and the bar sign denotes time average in the simulations after proper relaxation time. Note that in the above expression, the denominator equals the total external force acting on the polymer (per simulation box), that is  $q_m e f N_m E$ , and thus the ratio  $\mu_p \equiv \mu_m / N_m$  is nothing but the average *polymer mobility*.<sup>1</sup>

In order to proceed, I rescale the mobility with the bare value for counterions,  $\mu_0^c = 1/(6\pi\eta r_c)$ , Eq. (7.15). Thus in rescaled units

$$\tilde{\mu}_m \equiv \frac{\mu_m}{\mu_0^c} = -\frac{1}{\tilde{q}_m f N_m \tilde{E} \tilde{\mu}_0^c} \overline{\sum_{i=1}^{N_m} [\tilde{z}_i(n+1) - \tilde{z}_i(n)]}. \quad (7.35)$$

In Figure 7.5, the rescaled monomer mobility is plotted as a function of the rescaled electric field for different polymer models. In the absence of hydrodynamic interactions and

<sup>1</sup>In literature, the quantity  $\mu_p$  is referred to as the inverse electrophoretic friction coefficient [58], and the polymer *electrophoretic mobility* is defined as  $Q_p \mu_p$  with  $Q_p = q_m e f N_m$  being the total polymer charge. In the present study, the polymer charge per unit length is kept fixed, and thus I will drop the charge prefactor and refer to definition (7.34) as the mobility.

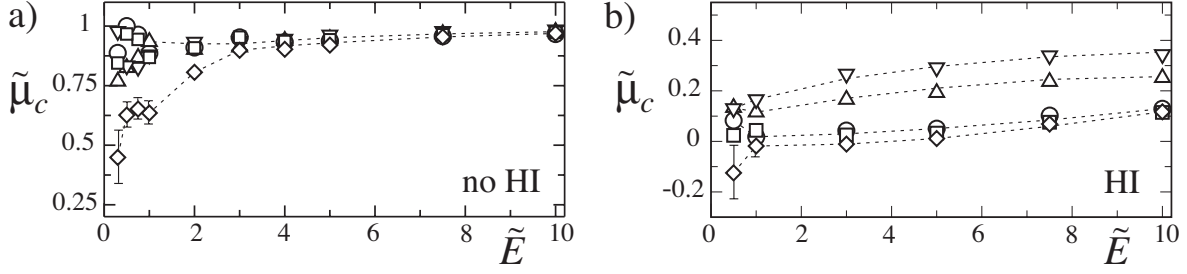


Figure 7.6: Rescaled mobility of counterions,  $\tilde{\mu}_c$ , in the absence (a) and presence (b) of hydrodynamic interactions as a function of the rescaled external field,  $\tilde{E}$ . Here Manning parameter is  $\xi = 4.0$ . Symbols and other parameters are as in Figure 7.5. For the sake of clarity, the error-bars are only shown for model  $B_2$ , which has the largest values for the error-bars.

for increasing electric field (Figure 7.5a), the monomer mobility tends to the bare value,

$$\tilde{\mu}_0^m = \frac{\mu_0^m}{\mu_0^c} = \tilde{r}_m^{-1}, \quad (7.36)$$

which is unity for models A,  $B_1$  and  $B_2$ , where monomers have the same size as counterions, but is smaller for larger monomers (by a factor of two and three in models  $C_1$  and  $C_2$  respectively). This may be seen more clearly in Figure 7.5b, where I have plotted  $\tilde{\mu}_m/\tilde{\mu}_0^m$  for models A,  $B_2$ ,  $C_1$  and  $C_2$ . The observed trend at high electric field resembles the so-called Wien effect, which has originally been studied for simple electrolyte solutions [242].

For small and intermediate external fields ( $\tilde{E} \sim 1$ ), the data show larger error-bars reflecting larger thermal fluctuations effects against the driving external force. In this regime, there are remarkable deviations from the large-field value  $\tilde{\mu}_m/\tilde{\mu}_0^m \simeq 1$ , which are more pronounced for model  $B_2$  with higher charge spacing along the backbone. In this case, the mobility is reduced down to 60% of the bare value at small electric fields  $\tilde{E} \sim 1$ . These free-draining features can be understood using a simple theoretical model as will be shown in Section 7.2.5 below.

The monomer mobility changes dramatically when hydrodynamic interactions are included (Figure 7.5c). In this case,  $\tilde{\mu}_m$  is substantially larger (by a factor of about two for the parameters chosen in the figure) as compared with free-draining case shown in Figure 7.5a. The data also indicate that the mobility in the three models with small monomer size ( $\tilde{r}_m = 1$ ) does not saturate within the considered range of electric field  $\tilde{E} < 10$ , while the mobility of larger monomers appears to be weakly dependent on the field strength. An enhanced mobility for monomers in a hydrodynamic medium is indeed expected because of a phenomenon known as *hydrodynamic entraining effect*: Because monomers are almost aligned and move in the same direction, the flow field generated by each monomer enhances the mobility of the others that follow it (corresponding to a lower effective friction experienced by those monomers).

Interestingly, enhancement of the mobility due to hydrodynamic effects is stronger for small monomers (models A,  $B_1$  and  $B_2$ ) as follows from Figure 7.5d, where I have rescaled the monomer mobility with the bare value, Eq. (7.36). Therefore, unlike the free-draining case, the size of monomers in a hydrodynamic medium has an important influence on their mobility, which reflects the non-linear nature of hydrodynamic interactions.

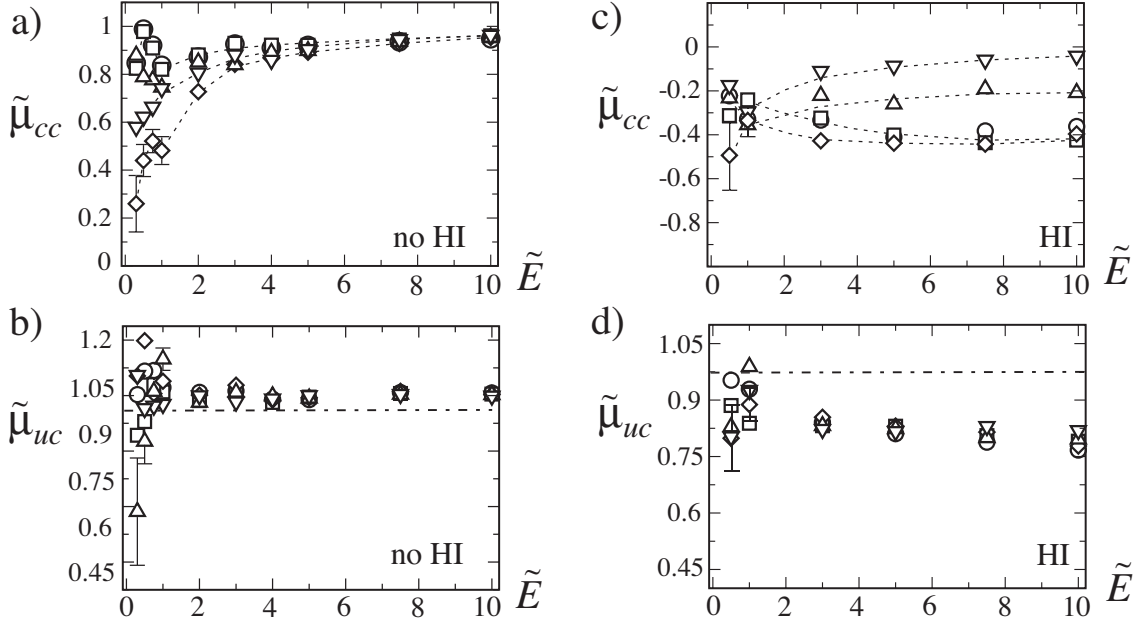


Figure 7.7: Rescaled mobility,  $\tilde{\mu}_{cc}$ , of condensed and that of de-condensed counterions,  $\tilde{\mu}_{uc}$ , as a function of the rescaled external field,  $\tilde{E}$ , in the absence (no HI) and presence (HI) of hydrodynamic interactions. Here Manning parameter is  $\xi = 4.0$ . Symbols and other details are as in Figure 7.5. For clarity, error-bars are shown only for a single set, which represents typical error-bars for other data sets as well.

### Mobility of counterions

In the present model, counterions are positively charged and prefer to move in the same direction as the electric field, while charged monomers drift in the opposite direction. This generates a considerable friction between monomers and the surrounding counterion cloud, which is the reason behind the reduction of mobilities at low electric fields. The data in Figure 7.6 show the rescaled average mobility of counterions,  $\tilde{\mu}_c$ , defined as

$$\tilde{\mu}_c \equiv \frac{\mu_c}{\mu_0^c} = \frac{1}{\tilde{\mu}_0^c N \tilde{E}} \sum_{i=1}^N \overline{[\tilde{z}_i(n+1) - \tilde{z}_i(n)]}, \quad (7.37)$$

as a function of  $\tilde{E}$ . As expected, the mobility of free-draining counterions (Figure 7.6a) tends to the bare value  $\tilde{\mu}_0^c = 1$  for large electric fields. For free-draining counterions, the average mobility actually almost coincides with that of monomers (when size difference is also accounted for), i.e.

$$\tilde{\mu}_c \simeq \frac{\tilde{\mu}_m}{\tilde{\mu}_0^m} \quad (7.38)$$

within the simulation error-bars (compare Figures 7.5a and 7.6a; see also Figure 7.10 below). This reflects a fundamental symmetry of the present model, that is, since the total charge of monomers equals that of counterions (due to electroneutrality in the simulation box), the total force from the external field acting on monomers and counterions are also the same. On

average, the internal forces in  $z$  direction also balance leading to almost equal mobilities for counterions and monomers.

When hydrodynamic interactions are present (Figure 7.6b), this symmetry does not hold and counterions show distinctly different (and indeed *smaller*) average mobility as compared with the free-draining case, indicating stronger drag forces acting on counterions. This is in contrast to the strong entraining effect which is obtained for monomers (compare Figure 7.5c). Note that, in particular, counterion mobility in Figure 7.6b vanishes and even becomes negative at small to intermediate fields in models with small monomer size.

To get more insight into the dynamic behavior of counterions, mobility of condensed,  $\tilde{\mu}_{cc}$ , and de-condensed,  $\tilde{\mu}_{uc}$ , counterions are considered separately in Figure 7.7 (the mobility is rescaled with the bare value as in Eq. (7.37)). The discrimination between such two population of counterions is made based on the criterion explained before, i.e. the condensation shell is defined as a cylindrical shell around the polymer that can accommodate two layers of counterions. For sufficiently large fields and in the free-draining case (a and b), counterions located either close or far away from the polymer show similar mobility as the effects due to inter-particle interactions are relatively small. For de-condensed counterions (Figure 7.7b), the mobility remains close to the bare mobility,  $\tilde{\mu}_0^c = 1$  (shown by a dot-dashed horizontal line), almost in the whole range of the electric fields (except for quite small values where large fluctuations appear). Condensed counterions (Figure 7.7a), show systematically smaller values at intermediate to small fields, especially in model B<sub>2</sub> with large charge spacing along the polymer. Since at the chosen value of Manning parameter ( $\xi = 4.0$ ), more than half of the counterions are condensed (Figure 7.4b), the overall mobility of counterions is dominated by condensed ones, and thus reduces the total counterion mobility at low fields as already seen in Figure 7.6a. It is important to note that the mobility of free-draining condensed counterions is positive, which means that they glide along the polymer, an effect seen in previous simulation of short polymers as well [232, 233].

When hydrodynamic forces are in action (Figures 7.7c), condensed counterion are found to be dragged along with the monomers as their mobility becomes *negative*. For the chosen parameters in the figure, this occurs for all values of the field strength  $\tilde{E} < 10$ , and in all five different models, but mobility in the presence of large monomers (models C<sub>1</sub> and C<sub>2</sub>) is expectedly larger. In the present case, even de-condensed counterions show a smaller mobility (75% of the bare value) for large electric fields (Figure 7.7d), which reflects the fact that the opposing flow field generated by the motion of monomers is long-ranged. Note that the mobility of condensed counterions is still very different (smaller in magnitude) from that of monomers (compare Figure 7.5c), which contrasts the assumption in previous theoretical works that condensed counterions form a layer that moves as a single body with the polymer chain [58]. Again the substantial reduction and sign change in the total mobility of counterions (Figure 7.6b) is due to the fact that more than half of the counterions are condensed for the chosen parameters as indicated from the data in Figure 7.4b. As discussed in Section 7.2.2, counterion density near the polymer decreases when hydrodynamic interactions are included. Given the preceding results for the mobility, this process can be understood as a mechanism to reduce the friction between particles in the system.

#### 7.2.4 Counterion condensation and electrophoretic mobility

The data presented in the preceding section are obtained for a typically large Manning parameter (i.e.  $\xi = 4.0$ ), where, as shown, most of the counterions are highly bound to the charged

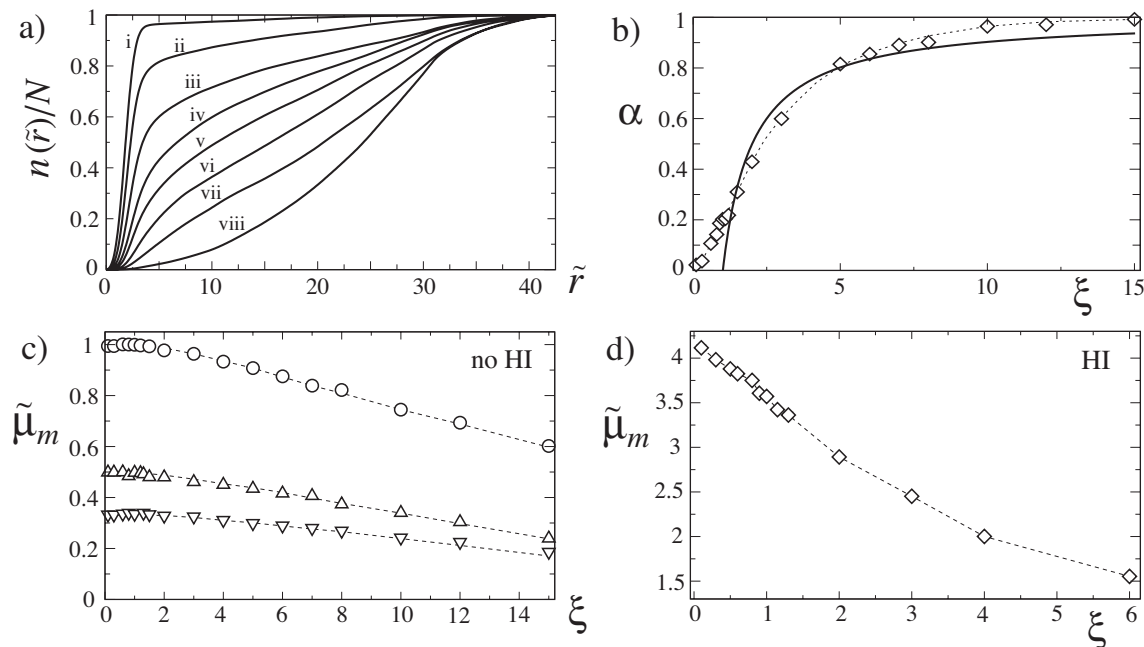


Figure 7.8: a) Cumulative density profile,  $n(\tilde{r})$ , of free-draining counterions in model A and at electric field  $\tilde{E} = 3.0$  for various Manning parameters (from top):  $\xi = 10.0, 5.0, 3.0, 2.0, 1.5, 1.0, 0.6$  and  $0.1$  (curves labeled by i-viii respectively). b) The simulated condensed fraction corresponding to the situation in a) as a function of Manning parameter (symbols). The solid curve shows the equilibrium Manning limiting value. c) Rescaled mobility of monomers,  $\tilde{\mu}_m$ , in the absence of hydrodynamic interactions and d) in the presence of hydrodynamic interactions as a function of Manning parameter at electric field  $\tilde{E} = 3.0$ . In c) symbols are data for models A (circles),  $C_1$  (triangle-ups) and  $C_2$  (triangle-downs) and in d) symbols represent data for model A. Error-bars are smaller than the symbol size and other parameters are as in Figure 7.5.

polymer. By changing the Manning parameter, the degree of counterion binding varies and one expects remarkable changes in the mobility. In Figure 7.8a, the cumulative density profile of counterions is shown for various Manning parameters and at fixed external electric field  $\tilde{E} = 3.0$ . For decreasing Manning parameter, the general form of the profile changes, especially the short-distance region in which the cumulative density rapidly increases (conventionally defined as the condensed layer) disappears, reflecting counterion de-condensation. These features agree with the results in Chapter 3, where counterion-condensation process is studied in equilibrium condition. As it was shown, the universal and critical features associated with the counterion-condensation transition (CCT), which is predicted to occur at the critical Manning parameter  $\xi_c = 1$ , appear in the limit of very large confinement volumes. Here the simulated system is considered in rather small confining box (rescaled confining box size of  $\tilde{L} = 60 + 2\tilde{r}_m$ ), and the transition to the complete de-condensation regime is expected to be highly suppressed. This is seen from the data in Figure 7.8b, where the condensed fraction appears to almost smoothly crossover to zero for decreasing  $\xi$  instead of vanishing sharply at  $\xi = 1$  (compare with Figure 3.4 in Chapter 3). In the figure, I also show the (equilibrium) Manning limiting value, i.e.  $\alpha_M = 1 - 1/\xi$  for  $\xi > 1$  and zero otherwise (solid

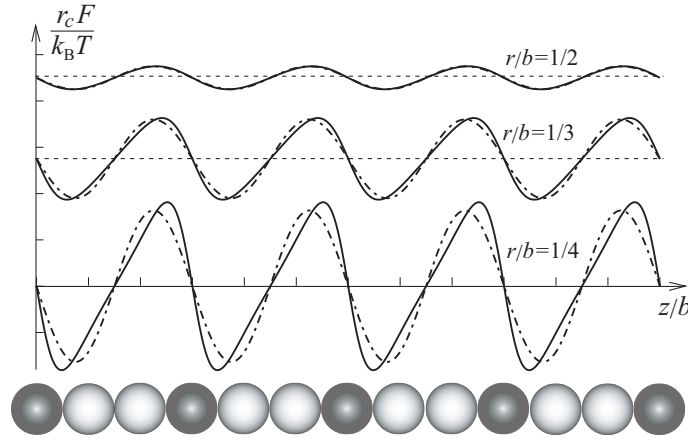


Figure 7.9: The  $z$  component of the electrostatic force generated by an *infinite* array of charges (aligned in  $z$  direction) at different radial distances  $r$  from the central axis as indicated on the graph. Charged monomers are schematically shown by dark spheres. The charge spacing is  $b/r_c = 6.0$  and the Manning parameter is chosen as  $\xi = 4.0$ . The solid curves represent the force profile given by Eq. (7.40) (including up to 10 terms in the series) and the dot-dashed curves give the approximate sinusoidal profile, Eq. (7.41). For clarity, the force profiles are shifted by a constant and the horizontal lines display the zero level.

curve). Note that the differences between this result and the data (symbols) at intermediate  $\xi$  is mostly due to non-equilibrium dynamic effects, because, as shown before (Figure 7.4), the counterion density deviates from its equilibrium value and gives a smaller condensed fraction even at electric fields as small as  $\bar{E} = 3.0$  as considered here. At large  $\xi$ , finite-ion-number effects come into play in the simulations and counterions all appear to be condensed (note that here the number of counterions is  $N = 24$  and thus, for instance, at  $\xi = 15$  less than a single counterion, i.e.  $N/\xi$ , is predicted to be de-condensed according to the Manning limiting law).

In Figure 7.8c and d, the data obtained for average monomer mobility are shown as a function of Manning parameter,  $\xi$ . In both free-draining (c) and hydrodynamic (d) situation, there appears a rather smooth crossover in the data when Manning parameter increases beyond the predicted threshold  $\xi_c = 1$  [39]. In the former case, the mobility,  $\tilde{\mu}_m$ , remains close to the bare value,  $\tilde{\mu}_0^m = \tilde{r}_m^{-1}$  (Eq. (7.36)) in the de-condensation regime, indicating weak counterion-monomer interactions and thus small electro-friction effects. While in the condensation regime ( $\xi > 1$ ),  $\tilde{\mu}_m$  decreases slowly (and almost linearly) with increasing  $\xi$ . In the hydrodynamic case, by contrast, mobility increases for decreasing Manning parameter in the de-condensation regime. But due to larger friction effects in this case, the decay of  $\tilde{\mu}_m$  with increasing counterion condensation (increasing  $\xi$ ) is found to be stronger as compared with the free-draining case.

### 7.2.5 Self-diffusion at a charge array: An analytical approach

The generic behavior of mobility of counterions and monomers in the free-draining situation can be understood using a simple analytical model as I present now.

In order to study electro-friction effects on an analytical level, I neglect the flexibility



of the polymer chain and focus on an infinitely long, fixed and rigid array of  $q_m$ -valency charges with spacing  $b$ . I will then consider a single counterion (of charge valency  $q$ ), which diffuses in the vicinity of this charge array under the action of an external electric field in  $z$  direction parallel to the array axis (charges are assumed to be point-like and interact only via bare Coulomb potential). As will be demonstrated below, this simple model can provide quantitative information about the mobility of particles at various distances from the polymer giving further insight into the behavior observed in the simulations.

### Force profile of a charge array

The  $z$  component of the Coulombic force generated by the array at a radial distance  $r$  from its axis is given by

$$F_z(r, z) = -\frac{qq_m e^2}{4\pi\epsilon\epsilon_0} \sum_{m=-\infty}^{+\infty} \frac{z - mb}{[r^2 + (z - mb)^2]^{3/2}}, \quad (7.39)$$

where  $(r = 0, z = mb)$  gives the location of charged monomers for  $m = -\infty, \dots, +\infty$  (Figure 7.9). The summation in the above equation is convergent and can be mapped to rapidly-converging and equivalent series formulae containing special functions (Appendix D). For instance, one obtains

$$F_z(r, z) = -\frac{qq_m e^2}{4\pi\epsilon\epsilon_0 b^2} \left[ 8\pi \sum_{m=1}^{+\infty} m K_0 \left( 2\pi m \frac{r}{b} \right) \sin \left( 2\pi m \frac{z}{b} \right) \right], \quad (7.40)$$

where  $K_0(x)$  is the modified Bessel function of the second kind, which decays exponentially for large  $x$  (as  $\sim \exp(-x)/\sqrt{x}$ ) but diverges logarithmically for small  $x$ . The above representation is therefore rapidly convergent when the radial distance  $r$  from the polymer axis is sufficiently large. The resultant force profile is periodic in  $z$  direction and the amplitude of the force modulation decreases with increasing  $r$  (Figure 7.9).

The problem of driven diffusion of a counterion near a charged polymer is therefore reduced to the problem of Brownian motion in a periodic potential under the action of a constant external field. To proceed further, I truncate the series in Eq. (7.40) after the first term, and therefore consider only a sinusoidal force profile as

$$F_z(r, z) \simeq -A(r) \sin \left( 2\pi \frac{z}{b} \right), \quad (7.41)$$

where the amplitude  $A(r) = [2qq_m e^2 / (\epsilon\epsilon_0 b^2)] K_0(2\pi r/b)$ . In fact, the above sinusoidal profile (dot-dashed curves in Figure 7.9) closely follows the full force profile (7.40) generated by the array (solid curves in the figure) at distances  $\tilde{r} > 1$ , which is due to the rapidly decaying behavior of the Bessel function. The above approximation allows for an analytical solution for the mobility of counterions as follows.

### Average counterion mobility

The Langevin equation (7.13) for a counterion drifted by an electric field  $E$  in  $z$  direction and at a radial distance  $r$  may be written in rescaled form as

$$\dot{w}(t) = \mu'_0 \left( F' - A'(r) \sin w \right) + \zeta'(t), \quad (7.42)$$

where the variables and parameters are rescaled as follows:  $w(t) = 2\pi z(t)/b$  is the rescaled position of the counterion along  $z$  axis,  $\mu'_0 = 4\pi^2\mu_0^c/b^2$  is a rescaled bare mobility and  $\zeta'(t)$  is the rescaled zero-mean white noise with the two-point correlation function of the form

$$\langle \zeta'(t) \zeta'(t') \rangle = 2\mu'_0 k_B T \delta(t - t'). \quad (7.43)$$

The force terms in Eq. (7.42) contain two rescaled coefficients, namely,

$$F' = qeEb/(2\pi), \quad (7.44)$$

which represents the external field, and

$$\frac{A'(r)}{k_B T} = 4\xi K_0\left(2\pi \frac{r}{b}\right), \quad (7.45)$$

which identifies the counterion-polymer interaction with  $\xi = qq_m \ell_B/b$  being the Manning parameter. The rescaled average counterion mobility as defined in Eq. (7.37) may be written here as

$$\tilde{\mu}_c = \frac{\langle \dot{w} \rangle}{\mu'_0 F'} = 1 - \chi^{-1}(r) \langle \sin w \rangle, \quad (7.46)$$

using Eq. (7.42), where

$$\chi(r) = \frac{F'}{A'(r)}. \quad (7.47)$$

Clearly, at very large radial separation  $r$ , the interaction coefficient  $A'(r)$  vanishes (due to exponentially decaying Bessel function) and therefore,  $\chi^{-1}(r)$  tends to zero. Consequently, average mobility  $\mu_c$ , Eq. (7.46), tends to the rescaled bare value for counterion, i.e.  $\tilde{\mu}_c \rightarrow 1$ .

In order to calculate the mobility for arbitrary Manning parameter,  $\xi$ , electric field,  $E$ , and radial separation  $r$ , one needs to calculate  $\langle \sin w \rangle$  in Eq. (7.46). This problem has in fact been solved for a similar Langevin equation (with periodic potential) in a different context [243, 244, 245]. The solution may be written in terms of modified Bessel functions of imaginary order as

$$\tilde{\mu}_c = 1 + \chi^{-1}(r) \operatorname{Im} \left\{ \frac{I_{1+iF'/(2k_B T)}\left(\frac{A'(r)}{2k_B T}\right)}{I_{iF'/(2k_B T)}\left(\frac{A'(r)}{2k_B T}\right)} \right\}. \quad (7.48)$$

Using this equation and Eqs. (7.44) and (7.45), one can calculate the average mobility as a function of  $\xi$  and  $E$ .

In Figure 7.10a, I have plotted  $\tilde{\mu}_c$  as obtained from Eq. (7.48) for fixed Manning parameter  $\xi = 4.0$ , fixed charge spacing  $b/r_c = 6$  (corresponding to model B<sub>2</sub>) and for various radial distance  $\tilde{r} = r/r_c$  (as indicated on the graph), as function of the rescaled electric field  $\tilde{E} = qeEr_c/(k_B T)$ . I also show simulation data (symbols) for the mobility of counterions, condensed counterions and monomers in model B<sub>2</sub> and for Manning parameter  $\xi = 4.0$ . As seen, the predicted mobility (7.48) substantially decreases at small electric fields (corresponding to linear response regime) when  $r/r_c$  is small, i.e. when counterion moves close to the polymer axis. The reason for this behavior is that the counterion should penetrate through periodic potential barriers generated by the array which hinder its motion (Figure 7.9). While at large separations or at sufficiently large electric fields, the free particle mobility is reproduced as expected. Note that the preceding theoretical model deals with diffusion of a single particle,

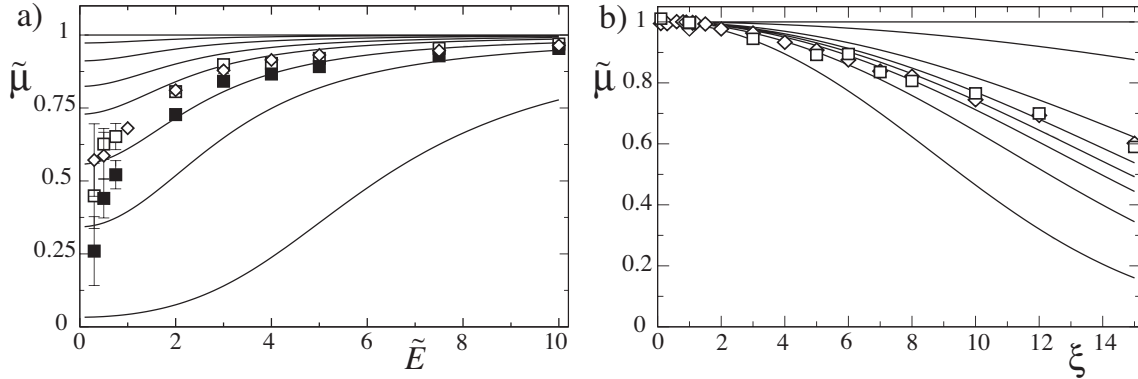


Figure 7.10: a) Rescaled mobility of free-draining counterions (solid curves) calculated from the charge-array model, Eq. (7.48), representing driven diffusion at radial distances (from top)  $\tilde{r} = 10.0, 3.0, 2.5, 2.2, 2.0, 1.75, 1.5$  and  $1.0$  from the central polymer axis. Here Manning parameter and the charge spacing are fixed as  $\xi = 4.0$ , and  $b/r_c = 6$ . Symbols show simulated mobility of counterions (open squares), condensed counterions (filled squares) and monomers (diamonds) for  $\xi = 4.0$  and in model B<sub>2</sub>. b) The same quantity as in a) but here for fixed electric field  $\tilde{E} = 3.0$ , fixed charge spacing  $b/r_c = 2$  and various Manning parameters at radial distances (solid curves from top)  $\tilde{r} = 10.0, 3.0, 2.5, 2.4, 2.35, 2.3, 2.2$  and  $2.0$ . Symbols show simulated mobility of counterions (open squares) and monomers (diamonds) for  $\tilde{E} = 3.0$  and in model A.

and ignores interactions between counterions as well as the chain fluctuations. Yet, as seen, it nicely captures the general trend observed in the simulations on a qualitative level. In fact, the data coincide with the theoretical curves obtained for diffusion at radial distance  $\tilde{r} \simeq 2$ , which in the simulations, corresponds to the location of the peak of the density profile (Figure 7.3, model B<sub>2</sub>).

In Figure 7.10b, a similar comparison is made in which the electric field is fixed ( $\tilde{E} = 3.0$ ) but Manning parameter is varied. Both data and theoretical curves correspond to model A with  $b/r_c = 2$ . Again the results of the above model qualitatively explain the trend observed in the simulations, i.e. for increasing Manning parameter the mobility of particles decreases due to stronger counterion-polymer interactions. The coincidence occurs again for a reasonable value of radial distance ( $\tilde{r} \simeq 2$ ) chosen in the analytical solution (7.48).

### 7.3 Conclusion and discussion

Using Brownian Dynamics simulation techniques, I investigate the stationary-state dynamics of charged polymers and counterions in an external electric field and for various charge patterns for the polymer chain.

In order to eliminate finite-length effects and capture counterion condensation, I have used an infinite polymer chain, which is mimicked in the simulations using periodic boundary conditions. Both free-draining dynamics and hydrodynamic interactions between particles are studied. In general, the polymer shows an enhanced electrophoretic mobility in the presence of hydrodynamic interactions, which can be understood based on the hydrodynamic entraining effect, i.e. since monomers are aligned and move in the same direction, the generated flow

field enhances their mobility. In contrast, counterion mobility substantially decreases in the presence of long-ranged hydrodynamic effects, because counterions motion (in the opposite direction relative to monomers) is strongly hindered by the monomers flow field. Interestingly, counterions close to the polymer (condensed counterions) are dragged along with the polymer in this case. But in contrast to the assumption in the standard counterion-condensation model [58], they have a lower absolute mobility. Another important result is that hydrodynamic effects lead to partial evaporation of condensed counterions, and cause notable deviations from the Manning limiting value for the condensed fraction, which is more enhanced at large electric fields.

In the free-draining case, condensed counterions mobility, although reduces due to interaction with the polymer, still remains positive. At low Manning parameters or for large external fields, counterion mobility is close to the bare value as expected. But as the Manning parameter increases beyond unity, where counterion-condensation effects start to become important, the mobility decreases almost linearly with the Manning parameter. As shown, the general behavior of free-draining mobility can be understood qualitatively based on a single-particle diffusion model in the presence of a periodic potential generated by an array of charges, which approximately represents the electrostatic potential due to the polymer.

In the simulations, I have considered five different models, in which the charge spacing and the monomer size differ, but the effective linear charge density (and the Manning parameter) is kept fixed. As shown, increasing the charge spacing highly suppresses the mobility of charged particles at large Manning parameter. The reason is that the mobility (which roughly represents inverse effective friction coefficient) is dominated by interactions between condensed counterions and monomers, which, as shown within the charge-array model, lead to large friction for large charge spacing. This signifies the role of local structural details as observed also in recent electrophoretic experiments [73]. Therefore, the electrophoretic behavior of charged polymers (at moderate to large Manning parameters) can not be described on a quantitative level unless charge pattern is correctly incorporated.

In the present study, I have not accounted for the effects of co-ions, which are expected to change the overall mobility of particles in the system in a remarkable fashion. In fact, co-ions are drifted by the electric field in the opposite direction as compared with counterions, which, in a hydrodynamic medium, leads to screening of hydrodynamic interactions over a length scale comparable to the Debye screening length. One can also incorporate more complex structures for the polymer chain in the simulations, e.g., using monomers of different size in a chain or using side groups. These issues will be addressed in the future.

## Appendix A

# Field Theory for Macroions in an Ionic Solution

In this appendix, I will present a field theoretical formalism for the equilibrium properties of a classical charged system consisting of fixed macroions of charge distribution  $-\sigma(\mathbf{x})e$  in an ionic mixture (electrolyte) of  $n + 1$  different ionic species that are all immersed in a continuum medium of dielectric constant  $\varepsilon$  and at temperature  $T$ . In order to reproduce the results presented in the text for the counterion-only solutions as a special case, I shall distinguish one of the counterionic species (of charge valency  $+q$  and total number  $N$ ) from the other  $n$  “salt” ionic species (labeled by Greek indices  $\alpha = 1, \dots, n$  and of charge valencies  $z_\alpha$  and total numbers  $N_\alpha$ ). The limiting theories of mean field (Poisson-Boltzmann) and strong coupling (SC) will be derived afterwards as two complementary asymptotic cases.

The configurational Hamiltonian of the mixture reads

$$\begin{aligned} \frac{\mathcal{H}}{k_B T} &= \frac{\ell_B}{2} \int d\mathbf{x} d\mathbf{x}' [q\hat{\rho}(\mathbf{x}) + \hat{\rho}_s(\mathbf{x}) - \sigma(\mathbf{x})] v(\mathbf{x} - \mathbf{x}') [q\hat{\rho}(\mathbf{x}') + \hat{\rho}_s(\mathbf{x}') - \sigma(\mathbf{x}')] \\ &\quad - \frac{\ell_B}{2} [q^2 N + \sum_{\alpha=1}^n z_\alpha^2 N_\alpha] v(0), \end{aligned} \quad (\text{A.1})$$

where  $\ell_B = e^2/(4\pi\varepsilon\varepsilon_0 k_B T)$  is the Bjerrum length,  $v(\mathbf{x}) = 1/|\mathbf{x}|$  is the Coulomb interaction in three dimensions, and I have defined

$$\hat{\rho}_s(\mathbf{x}) = \sum_{\alpha=1}^n z_\alpha \hat{\rho}_\alpha(\mathbf{x}), \quad \hat{\rho}_\alpha(\mathbf{x}) = \sum_{i=1}^{N_\alpha} \delta(\mathbf{x}_i^\alpha - \mathbf{x}), \quad \hat{\rho}(\mathbf{x}) = \sum_{i=1}^N \delta(\mathbf{x}_i - \mathbf{x}), \quad (\text{A.2})$$

in which  $\hat{\rho}_\alpha$  and  $\hat{\rho}$  are the number density operators associated with the salt ionic species (located at positions  $\{\mathbf{x}_i^\alpha\}$ ) and  $q$ -counterions (located at  $\{\mathbf{x}_i\}$ ), respectively. The canonical partition function of the system is written as

$$\mathcal{Z}_{N, N_\alpha} = \left[ \frac{1}{N!} \prod_{i=1}^N \int \frac{d\mathbf{x}_i}{(\lambda_t)^\alpha} \Omega(\mathbf{x}_i) \right] \left[ \prod_{\alpha=1}^n \frac{1}{N_\alpha!} \prod_{i=1}^{N_\alpha} \int \frac{d\mathbf{x}_i^\alpha}{(\lambda_t^\alpha)^\alpha} \Omega_\alpha(\mathbf{x}_i^\alpha) \right] \exp \left\{ - \frac{\mathcal{H}}{k_B T} \right\}, \quad (\text{A.3})$$

where the integrals are taken over positions of mobile particles and the geometry functions  $\Omega(\mathbf{x})$  and  $\Omega_\alpha(\mathbf{x})$  specify the available space for these particles (with  $\lambda_t^\alpha = h/\sqrt{2\pi m_\alpha k_B T}$  and  $\lambda_t = h/\sqrt{2\pi m k_B T}$  being the corresponding thermal wave-lengths).

The partition function (A.3) can be mapped to a field theory by means of a Hubbard-Stratonovich transformation, which may be done by inserting the identities

$$\int \mathcal{D}\rho_s \delta(\rho_s - \hat{\rho}_s) = \int \mathcal{D}\rho_s \mathcal{D}\varphi_s e^{i \int_{\mathbf{x}} \varphi_s (\rho_s - \hat{\rho}_s)} = 1, \quad (\text{A.4})$$

$$\int \mathcal{D}\rho \delta(\rho - \hat{\rho}) = \int \mathcal{D}\rho \mathcal{D}\varphi e^{i \int_{\mathbf{x}} \varphi (\rho - \hat{\rho})} = 1, \quad (\text{A.5})$$

where  $\{\rho_s(\mathbf{x}), \varphi_s(\mathbf{x})\}$  and  $\{\rho(\mathbf{x}), \varphi(\mathbf{x})\}$  are some conjugate fluctuating fields. One thus finds

$$\begin{aligned} \mathcal{Z}_{N, N_\alpha} = & \int \left[ \mathcal{D}\rho \mathcal{D}\varphi \mathcal{D}\rho_s \mathcal{D}\varphi_s \right] e^{-V[\rho, \varphi, \rho_s, \varphi_s]} \times \frac{1}{N!} \left[ \int \frac{d\mathbf{x}}{a^3} \Omega(\mathbf{x}) e^{-i\varphi} \right]^N \\ & \times \prod_{\alpha=1}^n \frac{1}{N_\alpha!} \left[ \int \frac{d\mathbf{x}}{a_\alpha^3} \Omega_\alpha(\mathbf{x}) e^{-iz_\alpha \varphi_s} \right]^{N_\alpha}, \end{aligned} \quad (\text{A.6})$$

where I have defined  $a^3 = \lambda_t^3 \exp[-q^2 \ell_B v(0)/2]$ ,  $a_\alpha^3 = (\lambda_t^\alpha)^3 \exp[-z_\alpha^2 \ell_B v(0)/2]$ , and

$$V[\rho, \varphi, \rho_s, \varphi_s] = \frac{\ell_B}{2} \int_{\mathbf{x}, \mathbf{x}'} [q\rho(\mathbf{x}) + \rho_s(\mathbf{x}) - \sigma(\mathbf{x})] v(\mathbf{x} - \mathbf{x}') [q\rho(\mathbf{x}') + \rho_s(\mathbf{x}') - \sigma(\mathbf{x}')] - i \int_{\mathbf{x}} (\rho\varphi + \rho_s \varphi_s). \quad (\text{A.7})$$

In order to proceed, it is convenient to consider the grand-canonical partition function

$$\mathcal{Z}_g(\lambda, \{\lambda_\alpha\}) = \sum_{N=0}^{\infty} \lambda^N \left( \prod_{\alpha=1}^n \sum_{N_\alpha=0}^{\infty} \lambda_\alpha^{N_\alpha} \right) \mathcal{Z}_{N, N_\alpha}, \quad (\text{A.8})$$

where  $\{\lambda_\alpha\}$  and  $\lambda$  are fugacities associated with salt ionic species and  $q$ -counterions, respectively. The Gaussian integrals over  $\rho$  and  $\rho_s$  fields can easily be evaluated and one arrives at a single-field representation, that is

$$\mathcal{Z}_g(\hat{\lambda}, \{\hat{\lambda}_\alpha\}) = \int \frac{\mathcal{D}\varphi}{\mathcal{Z}_v} \exp \{ -\mathcal{S}[\varphi] \}, \quad (\text{A.9})$$

where  $\mathcal{Z}_v \sim (\text{Det } v)^{1/2}$  involves vacuum-fluctuations contribution, and

$$\begin{aligned} \mathcal{S}[\varphi] = & \frac{1}{2q^2 \ell_B} \int_{\mathbf{x}, \mathbf{x}'} \varphi(\mathbf{x}) v^{-1}(\mathbf{x} - \mathbf{x}') \varphi(\mathbf{x}') - \int_{\mathbf{x}} \left[ \frac{i}{q} \sigma(\mathbf{x}) \varphi(\mathbf{x}) + \hat{\lambda} \Omega(\mathbf{x}) e^{-i\varphi} + \sum_{\alpha} \hat{\lambda}_\alpha \Omega_\alpha(\mathbf{x}) e^{-iz_\alpha \varphi/q} \right] \\ = & \int_{\mathbf{x}} \left[ \frac{1}{8\pi q^2 \ell_B} \left( \nabla \varphi(\mathbf{x}) \right)^2 - \frac{i}{q} \sigma(\mathbf{x}) \varphi(\mathbf{x}) - \hat{\lambda} \Omega(\mathbf{x}) e^{-i\varphi} - \sum_{\alpha} \hat{\lambda}_\alpha \Omega_\alpha(\mathbf{x}) e^{-iz_\alpha \varphi/q} \right], \end{aligned} \quad (\text{A.10})$$

is the *effective Hamiltonian*, in which I have used the inverse Coulomb operator  $v^{-1}(\mathbf{x}) = -\nabla^2 \delta(\mathbf{x})/4\pi$  in three dimensions, and rescaled the fugacities as  $\hat{\lambda} \equiv \lambda a^{-3}$  and  $\hat{\lambda}_\alpha \equiv \lambda_\alpha a_\alpha^{-3}$ .

In general, density profile of particles at macroions and the effective interaction between macroions in the ionic mixture can be derived from Eq. (A.9). For instance, the average number of particles is given by

$$\langle N \rangle = \hat{\lambda} \frac{\partial \ln \mathcal{Z}_g(\hat{\lambda}, \{\hat{\lambda}_\alpha\})}{\partial \hat{\lambda}} = \int d\mathbf{x} \bar{\rho}(\mathbf{x}), \quad (\text{A.11})$$

$$\langle N_\alpha \rangle = \hat{\lambda}_\alpha \frac{\partial \ln \mathcal{Z}_g(\hat{\lambda}, \{\hat{\lambda}_\alpha\})}{\partial \hat{\lambda}_\alpha} = \int d\mathbf{x} \bar{\rho}_\alpha(\mathbf{x}), \quad (\text{A.12})$$

where the number density profile of  $q$ -counterions and that of salt species  $\alpha$  is

$$\bar{\rho}(\mathbf{x}) = \hat{\lambda} \Omega(\mathbf{x}) \left\langle e^{-i\varphi} \right\rangle, \quad \bar{\rho}_\alpha(\mathbf{x}) = \hat{\lambda}_\alpha \Omega_\alpha(\mathbf{x}) \left\langle e^{-iz_\alpha \varphi/q} \right\rangle. \quad (\text{A.13})$$

### Dimensionless representation

I shall proceed using a dimensionless representation by rescaling the spatial coordinates as  $\tilde{\mathbf{x}} = \mathbf{x}/\mu$  with the Gouy-Chapman length associated with  $q$ -counterions, that is  $\mu = 1/(2\pi q\ell_B\sigma_s)$ , assuming that macroions have a uniform surface charge density of  $\sigma_s$ . One thus obtains

$$Z_g(\Lambda, \{\Lambda_\alpha\}) = \int \frac{\mathcal{D}\varphi}{Z_v} \exp \left\{ -\frac{\tilde{\mathcal{S}}[\varphi]}{\Xi} \right\}, \quad (\text{A.14})$$

where the rescaled effective Hamiltonian reads

$$\tilde{\mathcal{S}}[\varphi] = \frac{1}{2\pi} \int_{\tilde{\mathbf{x}}} \left[ \frac{1}{4} \left( \nabla_{\tilde{\mathbf{x}}} \varphi(\tilde{\mathbf{x}}) \right)^2 - i\tilde{\sigma}(\tilde{\mathbf{x}})\varphi(\tilde{\mathbf{x}}) - \Lambda\tilde{\Omega}(\tilde{\mathbf{x}}) e^{-i\varphi} - \sum_{\alpha} \Lambda_{\alpha}\tilde{\Omega}_{\alpha}(\tilde{\mathbf{x}}) e^{-i\gamma_{\alpha}\varphi} \right], \quad (\text{A.15})$$

in which  $\tilde{\sigma}(\tilde{\mathbf{x}}) = \mu\sigma(\mathbf{x})/\sigma_s$ ,  $\tilde{\Omega}(\tilde{\mathbf{x}}) = \Omega(\mathbf{x})$ ,  $\tilde{\Omega}_{\alpha}(\tilde{\mathbf{x}}) = \Omega_{\alpha}(\mathbf{x})$ , and  $\Lambda = 2\pi\hat{\lambda}\mu^3\Xi$  and  $\Lambda_{\alpha} = 2\pi\hat{\lambda}_{\alpha}\mu^3\Xi$  are the rescaled fugacities. As seen, the theory involves the following dimensionless parameters (besides possible geometrical parameters characterizing macroions shape): i) the *electrostatic coupling parameter* associated with  $q$ -counterions,

$$\Xi = 2\pi q^3 \ell_B^2 \sigma_s, \quad (\text{A.16})$$

and ii) the charge valency ratios,

$$\gamma_{\alpha} = \frac{z_{\alpha}}{q}, \quad (\text{A.17})$$

with  $\alpha = 1, \dots, n$ . The asymptotic theories of mean field and strong coupling can be obtained by taking appropriate limits of  $\Xi$  and  $\gamma_{\alpha}$ .

### A.1 Weak-coupling limit: Mean-field theory

The weak-coupling limit is obtained when both  $\Xi$  and  $|\gamma_{\alpha}|$  become small. This situation may be realized experimentally using low-valency ions at weakly charged surfaces. In the limit  $\Xi \rightarrow 0$ , the integral in Eq. (A.14) is dominated by the saddle-point solution of the effective Hamiltonian,  $\varphi_{\text{PB}}$ , which is obtained from the saddle-point equation  $\delta\tilde{\mathcal{S}}[\varphi]/\delta\varphi|_{\varphi_{\text{PB}}} = 0$ . Hence,

$$\frac{1}{2} \nabla_{\tilde{\mathbf{x}}}^2 \varphi_{\text{PB}} = -i\tilde{\sigma}(\tilde{\mathbf{x}}) + i\Lambda\tilde{\Omega}(\tilde{\mathbf{x}}) e^{-i\varphi_{\text{PB}}} + i \sum_{\alpha} \Lambda_{\alpha}\gamma_{\alpha}\tilde{\Omega}_{\alpha}(\tilde{\mathbf{x}}) e^{-i\gamma_{\alpha}\varphi_{\text{PB}}}, \quad (\text{A.18})$$

which is nothing but the well-known Poisson-Boltzmann (PB) equation for the rescaled mean-field potential,  $\varphi_{\text{PB}}$ . The mean-field (PB) theory obtained for  $\Xi \rightarrow 0$  does not include fluctuation and correlation effects, which become relevant at finite values of  $\Xi$ . They can be accounted for using a loop expansion around the saddle-point solution (see, e.g., Ref. [50] and references therein). The loop expansion however breaks down at large  $\Xi \gg 1$ , where higher-order corrections become large and require a different approach (see Section A.2 below).

#### PB theory with counterions only

When no additional salt is present, the PB equation (A.18) is reduced to

$$\tilde{\nabla}_{\tilde{\mathbf{x}}}^2 \psi = 2\tilde{\sigma}(\tilde{\mathbf{x}}) - \tilde{\kappa}^2 \tilde{\Omega}(\tilde{\mathbf{x}}) e^{-\psi(\tilde{\mathbf{x}})}, \quad (\text{A.19})$$

where  $\psi = i\varphi_{\text{PB}}$  and  $\tilde{\kappa}^2 = 2\Lambda$ . In the *canonical* ensemble with  $N$  counterions, one has

$$N = \Lambda \frac{\partial \ln \mathcal{Z}_g(\Lambda, 0)}{\partial \Lambda} = \frac{1}{2\pi\Xi} \int d\tilde{\mathbf{x}} \tilde{\rho}_{\text{PB}}(\tilde{\mathbf{x}}) \quad (\text{A.20})$$

using Eqs. (A.11), (A.14) and (A.15), where

$$\tilde{\rho}_{\text{PB}}(\tilde{\mathbf{x}}) = \frac{\tilde{\kappa}^2}{2} \tilde{\Omega}(\tilde{\mathbf{x}}) e^{-\psi(\tilde{\mathbf{x}})} \quad (\text{A.21})$$

is the rescaled PB density profile of counterions. Note that the electroneutrality condition implies that  $\int d\mathbf{x} \sigma(\mathbf{x}) = Nq$ , or in rescaled units  $\tilde{\mathcal{A}} \equiv \int d\tilde{\mathbf{x}} \tilde{\sigma}(\tilde{\mathbf{x}}) = 2\pi N\Xi$ , where, assuming that macroion charges are distributed over their surfaces,  $\tilde{\mathcal{A}}$  is nothing but the rescaled area of macroions. Using this, the normalization prefactor of the density profile is obtained as

$$\frac{\tilde{\kappa}^2}{2} = \frac{\tilde{\mathcal{A}}}{\int d\tilde{\mathbf{x}} \tilde{\Omega}(\tilde{\mathbf{x}}) e^{-\psi(\tilde{\mathbf{x}})}}. \quad (\text{A.22})$$

Note that in general the density profile in rescaled units,  $\tilde{\rho}(\tilde{\mathbf{x}})$ , are related to the actual density profile,  $\rho(\mathbf{x})$  (Eq. (A.13)), via

$$\tilde{\rho}(\tilde{\mathbf{x}}) = \frac{\rho(\mathbf{x})}{2\pi\ell_B\sigma_s^2}. \quad (\text{A.23})$$

Restoring the actual units in Eq. (A.19), one recovers the standard PB equation

$$\nabla^2 \psi_{\text{elec}}(\mathbf{x}) = \frac{\sigma(\mathbf{x})e}{\varepsilon\varepsilon_0} - \frac{q\rho_{\text{PB}}(\mathbf{x})e}{\varepsilon\varepsilon_0}, \quad (\text{A.24})$$

where  $\psi_{\text{elec}} = k_B T \psi / qe$  is the actual mean-field electrostatic potential field, and

$$\rho_{\text{PB}}(\mathbf{x}) = \rho_0 e^{-qe\psi_{\text{elec}}/k_B T} \quad (\text{A.25})$$

is the actual PB density profile of counterions with  $\rho_0 = N / \int d\mathbf{x} \Omega(\mathbf{x}) \exp(-qe\psi_{\text{elec}}/k_B T)$ .

### PB free energy with counterions only

The canonical PB free energy,  $\mathcal{F}_N^{\text{PB}}$ , is obtained by inserting the PB solution,  $\psi = i\varphi_{\text{PB}}$ , into the grand-canonical partition function (A.14) and then using a Legendre transformation as

$$\mathcal{F}_N^{\text{PB}} = Nk_B T \ln \left( \frac{\Lambda a^3}{2\pi\mu^3\Xi} \right) + \mathcal{Q}_g^{\text{PB}}(\Lambda), \quad (\text{A.26})$$

where  $\mathcal{Q}_g^{\text{PB}}(\Lambda) = -k_B T \ln \mathcal{Z}_g(\Lambda, [\psi(\tilde{\mathbf{x}})])$  is the grand-canonical free energy and  $\Lambda$  is calculated from Eq. (A.20) (note that the argument of the logarithm on the right hand side is nothing but the actual fugacity  $\lambda$ ). It is straight-forward to show that

$$\frac{\mathcal{F}_N^{\text{PB}}}{Nk_B T} = -\frac{1}{\tilde{\mathcal{A}}} \int d\tilde{\mathbf{x}} \left[ \frac{1}{4} (\nabla_{\tilde{\mathbf{x}}} \psi)^2 + \tilde{\sigma}(\tilde{\mathbf{x}}) \psi(\tilde{\mathbf{x}}) \right] - \ln \left[ \frac{1}{\tilde{\mathcal{A}}} \int d\tilde{\mathbf{x}} \tilde{\Omega}(\tilde{\mathbf{x}}) e^{-\psi(\tilde{\mathbf{x}})} \right] - \ln \left( \frac{\mu^3 \tilde{\mathcal{A}}}{Na^3} \right) - 1, \quad (\text{A.27})$$

and in actual units

$$\frac{\mathcal{F}_N^{\text{PB}}}{k_B T} = - \int d\mathbf{x} \left[ \frac{(\nabla_{\mathbf{x}} \psi)^2}{8\pi q^2 \ell_B} + \frac{1}{q} \sigma(\mathbf{x}) \psi(\mathbf{x}) \right] - N \ln \left[ \int \frac{d\mathbf{x}}{a^3} \Omega(\mathbf{x}) e^{-\psi(\mathbf{x})} \right] + (N \ln N - N). \quad (\text{A.28})$$



## A.2 Strong-coupling limit

It has been shown in previous works [44, 43] that in the limit  $\Xi \rightarrow \infty$ , an asymptotic theory, known as the strong-coupling (SC) theory, may be derived for counterions at charged objects, which can account for the correlation effects at large coupling strength [35] (Chapter 5). In what follows, I will apply the same approach to derive the SC theory for macroions in an ionic mixture. It will be assumed that the coupling parameter associated with  $q$ -counterions is large  $\Xi \rightarrow \infty$ , but the valency ratio of bathing salt ions to  $q$ -counterions is small,  $|\gamma_\alpha| < 1$ . In other words, ionic species  $\alpha = 1, \dots, n$  (additional salt) are weakly coupled to macroions, while the  $q$ -counterions are strongly coupled to them. Moreover, the coupling between salt co-ions and  $q$ -counterions is also assumed to be weak, which can be valid, for instance, when the  $q$ -counterions are bulky (with small effective surface charge density) [129], although here ions are all assumed to be point-like.

The preceding assumptions allow one to treat the contribution from additional salt within a linearization (Debye-Hückel) approximation by expanding the last term in Eq. (A.15) up to the second-order in  $\gamma_\alpha \varphi$ , which yields

$$\mathcal{S}[\varphi] \simeq \mathcal{S}_0[\varphi] - \frac{\Lambda}{2\pi} \int_{\tilde{\mathbf{x}}} \tilde{\Omega}(\tilde{\mathbf{x}}) e^{-i\varphi}, \quad (\text{A.29})$$

where the Gaussian part of the effective Hamiltonian reads

$$\mathcal{S}_0[\varphi] = \frac{1}{2\pi} \int_{\tilde{\mathbf{x}}} \left[ \frac{1}{4} (\nabla_{\tilde{\mathbf{x}}} \varphi)^2 - i \left( \tilde{\sigma}(\tilde{\mathbf{x}}) - \sum_{\alpha} \Lambda_{\alpha} \tilde{\Omega}_{\alpha}(\tilde{\mathbf{x}}) \gamma_{\alpha} \right) \varphi + \frac{1}{2} \left( \sum_{\alpha} \Lambda_{\alpha} \tilde{\Omega}_{\alpha}(\tilde{\mathbf{x}}) \gamma_{\alpha}^2 \right) \varphi^2 \right] + \mathcal{E}_0, \quad (\text{A.30})$$

in which  $\mathcal{E}_0 = -\frac{1}{2\pi} \sum_{\alpha} \Lambda_{\alpha} \tilde{V}_{\alpha}$ , where  $\tilde{V}_{\alpha} = \int d\tilde{\mathbf{x}} \tilde{\Omega}_{\alpha}(\tilde{\mathbf{x}})$ . In order to proceed with an analytic approach, I assume that the salt ions (and not the  $q$ -counterions) are present in all space (of total volume  $V$ ), i.e.  $\tilde{\Omega}_{\alpha}(\tilde{\mathbf{x}}) = 1$  and thus  $\tilde{V}_{\alpha} = \tilde{V}$ .

The non-linear part of the effective Hamiltonian (A.29) may be handled for large  $\Xi$  using the standard strong-coupling approach [43], i.e. by employing a perturbative expansion in Eq. (A.14) of the integrand in powers of  $\Lambda/\Xi$ , which gives

$$\mathcal{Z}_g = \left\langle \exp \left[ \frac{\Lambda}{2\pi\Xi} \int_{\tilde{\mathbf{x}}} \tilde{\Omega}(\tilde{\mathbf{x}}) e^{-i\varphi} \right] \right\rangle_0 = \sum_{j=0}^{\infty} \frac{1}{j!} \left( \frac{\Lambda}{2\pi\Xi} \right)^j \int \left[ \prod_{k=1}^j d\tilde{\mathbf{x}}_k \tilde{\Omega}(\tilde{\mathbf{x}}_k) \right] \left\langle e^{-i \sum_{k=1}^j \varphi(\tilde{\mathbf{x}}_k)} \right\rangle_0, \quad (\text{A.31})$$

where the subindex 0 indicates averaging with respect to the Gaussian part,  $\mathcal{S}_0[\varphi]$ . The averages in Eq. (A.31) may be calculated in a straight-forward manner as

$$\left\langle e^{-i \sum_{k=1}^j \varphi(\tilde{\mathbf{x}}_k)} \right\rangle_0 = \frac{\mathcal{Z}_{\text{DH}}}{\mathcal{Z}_v} \exp \left[ -\frac{1}{8\pi^2\Xi} \int_{\tilde{\mathbf{x}}} \chi(\tilde{\mathbf{x}}) v_{\text{DH}}(\tilde{\mathbf{x}} - \tilde{\mathbf{x}}') \chi(\tilde{\mathbf{x}}') - \frac{\mathcal{E}_0}{\Xi} \right], \quad (\text{A.32})$$

where  $\chi(\tilde{\mathbf{x}}) = \tilde{\sigma}(\tilde{\mathbf{x}}) - \sum_{\alpha} \Lambda_{\alpha} \gamma_{\alpha} - 2\pi\Xi \sum_{k=1}^j \delta(\tilde{\mathbf{x}} - \tilde{\mathbf{x}}_k)$ , and  $\mathcal{Z}_{\text{DH}} \sim (\text{Det } v_{\text{DH}})^{1/2}$  with  $v_{\text{DH}}$  being the Debye-Hückel (screened Coulomb) interaction

$$v_{\text{DH}}(\tilde{\mathbf{x}}) = 4\pi \left[ (-\nabla^2 + \tilde{\kappa}_s^2) \delta(\tilde{\mathbf{x}}) \right]^{-1} = \frac{e^{-\tilde{\kappa}_s |\tilde{\mathbf{x}}|}}{|\tilde{\mathbf{x}}|}, \quad (\text{A.33})$$

in which  $\tilde{\kappa}_s^2 = 2 \sum_{\alpha} \Lambda_{\alpha} \gamma_{\alpha}^2$  is the rescaled inverse Debye screening length due to the bathing salt ions. In actual units, one has  $\kappa_s^2 = (\tilde{\kappa}_s/\mu)^2 = 4\pi \ell_B \sum_{\alpha} z_{\alpha}^2 \lambda_{\alpha}$ .

Using the above results in Eq. (A.31), one obtains the following expression

$$\mathcal{Z}_g = A_0 e^{-\tilde{U}_s/\pi\Xi} \left[ 1 + \frac{\Lambda}{2\pi\Xi} \int d\tilde{\mathbf{x}} A_1(\tilde{\mathbf{x}}) e^{-\tilde{u}_s(\tilde{\mathbf{x}})} + \mathcal{O}\left(\frac{\Lambda}{2\pi\Xi}\right)^2 \right], \quad (\text{A.34})$$

where  $\tilde{U}_s$  and  $\tilde{u}_s$  are screened zero-particle and one-particle interaction terms,

$$\tilde{U}_s = \frac{1}{8\pi} \int d\tilde{\mathbf{x}} d\tilde{\mathbf{x}}' \tilde{\sigma}(\tilde{\mathbf{x}}) v_{\text{DH}}(\tilde{\mathbf{x}} - \tilde{\mathbf{x}}') \tilde{\sigma}(\tilde{\mathbf{x}}'), \quad (\text{A.35})$$

$$\tilde{u}_s(\tilde{\mathbf{x}}) = -\frac{1}{2\pi} \int d\tilde{\mathbf{x}}' v_{\text{DH}}(\tilde{\mathbf{x}} - \tilde{\mathbf{x}}') \tilde{\sigma}(\tilde{\mathbf{x}}'). \quad (\text{A.36})$$

Note that  $\tilde{U}_s$  represents the bare interactions between fixed macroions (i.e. when no  $q$ -counterions are present) and  $\tilde{u}_s$  gives the interaction energy of a single  $q$ -counterion with macroions. Higher-order terms include multi-particle contributions. The prefactors  $A_0$  and  $A_1(\tilde{\mathbf{x}})$  are given by

$$A_0 = \frac{\mathcal{Z}_{\text{DH}}}{\mathcal{Z}_v} \exp \left\{ -\frac{\mathcal{E}_0}{\Xi} + \frac{(\sum_\alpha \Lambda_\alpha \gamma_\alpha)}{8\pi^2 \Xi} \int_{\tilde{\mathbf{x}}, \tilde{\mathbf{x}}'} v_{\text{DH}}(\tilde{\mathbf{x}} - \tilde{\mathbf{x}}') \left( 2\tilde{\sigma}(\tilde{\mathbf{x}}) - \sum_\alpha \Lambda_\alpha \gamma_\alpha \right) \right\} \quad (\text{A.37})$$

$$A_1(\tilde{\mathbf{x}}) = \exp \left\{ -\frac{(\sum_\alpha \Lambda_\alpha \gamma_\alpha)}{2\pi} \int_{\tilde{\mathbf{x}}'} v_{\text{DH}}(\tilde{\mathbf{x}} - \tilde{\mathbf{x}}') - \frac{1}{2} \Xi v_{\text{DH}}(\tilde{0}) \right\}. \quad (\text{A.38})$$

Clearly, the preceding expansion in powers of  $\Lambda/\Xi$  is nothing but the virial expansion for  $q$ -counterions at fixed charged objects in the presence of added salt. The *asymptotic SC theory* is represented by the leading-order term of the expansion (A.34), which becomes formally exact when  $\Xi \rightarrow \infty$ .

The counterion-only case (no added salt) considered in Chapter 5 [43] follows directly from Eq. (A.34) when the limit  $\kappa_s \rightarrow 0$  (or  $\lambda_\alpha \rightarrow 0$ ) is taken, in which case the DH interaction,  $v_{\text{DH}}(\tilde{\mathbf{x}})$ , reduces to bare Coulomb interaction  $v(\tilde{\mathbf{x}}) = 1/|\tilde{\mathbf{x}}|$ , and one has  $A_0 \rightarrow 1$  and  $A_1 \rightarrow \exp[-\Xi v(\tilde{0})/2]$ . The full form of the resultant series expansion is given in Eq. (5.3), in which  $\tilde{U}_0 = \lim_{\kappa_s \rightarrow 0} \tilde{U}_s$ ,  $\tilde{u} = \lim_{\kappa_s \rightarrow 0} \tilde{u}_s$  and the fugacity is again rescaled as  $\Lambda \rightarrow \Lambda \exp[-\Xi v(\tilde{0})/2]$ . In order to obtain the canonical strong-coupling theory, one needs to evaluate the fugacity  $\Lambda$  from  $N = \Lambda \partial \ln \mathcal{Z}_g(\Lambda, 0)/\partial \Lambda$ . In general,  $\Lambda$  adopts a large-coupling series expansion as

$$\Lambda = \Lambda_0 + \frac{\Lambda_1}{\Xi} + \frac{\Lambda_2}{\Xi^2} + \dots, \quad (\text{A.39})$$

where  $\Lambda_0, \Lambda_1, \dots$  are calculated in text (see the notes in Section 5.1.1). In particular, one has

$$\Lambda_0 = \frac{\tilde{\mathcal{A}}}{\int d\tilde{\mathbf{x}} \tilde{\Omega}(\tilde{\mathbf{x}}) e^{-\tilde{u}(\tilde{\mathbf{x}})}}, \quad (\text{A.40})$$

where  $\tilde{u}$  is defined in Eq. (5.6). Using the preceding results in Eq. (A.13), one obtains the asymptotic SC density profile of counterions in rescaled units as

$$\tilde{\rho}_{\text{SC}}(\tilde{\mathbf{x}}) = \Lambda_0 \tilde{\Omega}(\tilde{\mathbf{x}}) e^{-\tilde{u}(\tilde{\mathbf{x}})}. \quad (\text{A.41})$$

# Appendix B

## Notes on the Onsager instability

Here I briefly discuss the singularities associated with the Onsager instability, which, as demonstrated in Section 3.2.1, represents the binding-unbinding transition of a single counterion in the presence of a charged cylindrical boundary. The rescaled energy,  $\tilde{E} = E_N/(Nk_B T)$ , and excess heat capacity,  $\tilde{C} = C_N/(Nk_B)$ , of this system can be calculated from the single-particle partition function, Eq. (3.17). The results in fact coincide with those obtained in Chapter 4 by choosing  $N = 1$  (see also Figures 4.3 and 4.2). The energy and the excess heat capacity are thus obtained as

$$\tilde{E} \simeq \frac{2\xi\Delta \exp[2(1-\xi)\Delta]}{\exp[2(1-\xi)\Delta] - 1} - \frac{\xi}{1-\xi}, \quad (\text{B.1})$$

$$\tilde{C} \simeq \frac{\xi^2}{(1-\xi)^2} - \frac{\Delta^2 \xi^2}{\sinh^2[2(1-\xi)\Delta]}, \quad (\text{B.2})$$

for large  $\Delta \gg 1$ . Both  $\tilde{E}$  and  $\tilde{C}$  become singular at the critical Manning parameter  $\xi_c = 1$  when  $\Delta \rightarrow \infty$ . For finite large  $\Delta$ , this singular point appears in the form of a pronounced peak near the critical point. The approximate location of the energy peak  $\xi_*^E$  is obtained as (see Chapter 4)

$$\xi_*^E \simeq 1 - \frac{1}{\sqrt{2\Delta}}, \quad (\text{B.3})$$

for  $\Delta \gg 1$ , which shows a different asymptotic convergency (from below) to the critical value  $\xi_c = 1$  as compared with the mean-field result, Eq. (3.82). The heat capacity peak is located above the critical Manning parameter and is given by

$$\xi_*^C \simeq 1 + \frac{5}{\Delta^2}. \quad (\text{B.4})$$

In the limit  $\Delta \rightarrow \infty$ , the heat capacity diverges at the critical point from above and below displaying the algebraic divergency

$$\tilde{C} \sim \zeta^{-2} \quad (\text{B.5})$$

where  $\zeta = 1 - 1/\xi$ . The left tail of energy (for  $\xi < \xi_*^E$ ) goes to infinity linearly with  $\Delta$  as  $\tilde{E} \simeq 2\xi\Delta + \xi/(\xi - 1)$ , but its right tail shows a power-law divergency as

$$\tilde{E} \sim \zeta^{-1}. \quad (\text{B.6})$$

Note that these behavior are distinctly different from those obtained in the simulations with many particles (Section 3.6.2) and within the mean-field theory (Section 3.3).



# Appendix C

## Mean-Field Theory for Charged Cylinders: Asymptotic results

This Appendix is devoted to asymptotic analysis of the mean-field Poisson-Boltzmann (PB) results for counterions at a charged cylinder. In particular, I will derive the asymptotic form of the scaling functions and order parameters associated with the counterion-condensation transition as used in Chapters 3.

As discussed in Chapter 3, the PB solution for counterions at a single charged cylinder involves an integration constant  $\beta$ , which is determined from the transcendental equation (3.26), depending on whether the Manning parameter  $\xi$  is larger or smaller than the Alfrey-Fuoss threshold  $\Lambda_{AF}$ , Eq. (3.24). It depends on  $\xi$  and the lateral extension factor  $\Delta = \ln(D/R)$  and tends to one from below for increasing  $\Delta$  to infinity. All other quantities within the PB theory may be expressed in terms of  $\beta$ . A general discussion has been given by Fuoss et al. [38] for the overall behavior of  $\beta$ . Here, I first review some of the previous results and then obtain the finite-size-scaling relations for  $\beta$  near the PB critical Manning parameter,  $\xi_c^{PB} = 1$ , and for large  $\Delta \gg 1$ . The asymptotic behavior of the PB order parameters and the PB potential and density profile for counterions will also be discussed.

### C.1 Limiting behavior of $\beta$ for large $\Delta$

**Small Manning parameter  $\xi < \Lambda_{AF}$ :**

The integration constant  $\beta$  vanishes at  $\xi = \Lambda_{AF}$  and tends to unity,  $\beta \rightarrow 1^-$ , for small  $\xi \rightarrow 0^+$ , as it can be checked easily from Eq. (3.26) (I arbitrarily choose  $\beta \geq 0$ ) [38]. Further inspection shows that in this regime,  $\beta \rightarrow (\xi - 1)^-$  when  $\Delta \rightarrow \infty$  [38]. Hence for  $\Delta \gg 1$ , one can propose the following form

$$\beta^2 \simeq (\xi - 1)^2(1 - x), \quad (\text{C.1})$$

where  $x$  is a small function of  $\xi$  and  $\Delta$ . To determine  $x$ , one may rearrange the first equation in (3.26) as

$$\beta\Delta = \frac{1}{2} \ln \frac{1 - \beta}{1 + \beta} - \frac{1}{2} \ln \frac{(\xi - 1) + \beta}{(\xi - 1) - \beta}. \quad (\text{C.2})$$

and use this together with Eq. (C.1) to obtain

$$x \simeq \frac{4\xi}{2 - \xi} e^{2(\xi - 1)\Delta}, \quad (\text{C.3})$$

which reproduces Eq. (3.31) in the text.

### Large Manning parameter $\xi > \Lambda_{\text{AF}}$ :

For large Manning parameter  $\xi > \Lambda_{\text{AF}}$ ,  $\beta$ , Eq. (3.26), tends to a finite upper bound  $\beta_\infty = \pi/\Delta$ , when  $\xi \rightarrow \infty$  [38]. Thus for  $\Delta \rightarrow \infty$ ,  $\beta$  vanishes for the whole range of Manning parameters  $\xi > \Lambda_{\text{AF}} \simeq 1$  as used frequently in the text (see, e.g., Eq. (3.42)).

## C.2 Finite-size scaling for $\beta$ close to $\xi_c^{\text{PB}}$ :

Of particular importance is the behavior of  $\beta$  close to  $\xi_c^{\text{PB}} = 1$ . (Since always  $\Lambda_{\text{AF}} \leq 1$ , I restrict the discussion only to the regime  $\xi > \Lambda_{\text{AF}}$ ). Analysis of Eq. (3.26) shows that for sufficiently large  $\Delta$ , one has  $\beta \simeq \pi/(2\Delta)$  right at the critical point  $\xi_c^{\text{PB}} = 1$ . One may then perform a Taylor expansion around  $\xi_c^{\text{PB}}$  to obtain the approximate form of  $\beta$  for small  $\zeta = 1 - \xi_c^{\text{PB}}/\xi$  as

$$\beta(\zeta, \Delta) = \frac{\pi}{2\Delta} + \frac{2}{\pi}\zeta - \frac{8\Delta}{\pi^3}\zeta^2 + \mathcal{O}(\zeta^3), \quad (\text{C.4})$$

which remains valid for  $\zeta\Delta < \pi^2/4$ . This relation clearly indicates a scale-invariant form for  $\beta$  when  $\Delta \gg 1$ . Comparing this with Eq. (3.50), I find the approximate form of the scaling function  $\mathcal{B}(u)$  as

$$\mathcal{B}(u) \simeq \frac{\pi}{2} + \frac{2}{\pi}u - \frac{8}{\pi^3}u^2, \quad (\text{C.5})$$

where  $u = \zeta\Delta < \pi^2/4$ . In particular, one has  $\mathcal{B}(u) \rightarrow \pi/2$  as  $u \rightarrow 0$ .

The asymptotic behavior of  $\mathcal{B}(u)$  for  $u \rightarrow \infty$  (or equivalently  $\Delta \rightarrow \infty$  for finite  $\zeta$ ) can be obtained using a different series expansion, since in this limit  $\beta$  becomes singular at  $\xi_c^{\text{PB}} = 1$  and the above expansion breaks down. This is because  $\beta$  is always singular (with an infinite first derivative) at  $\Lambda_{\text{AF}}$  which tends to the critical Manning parameter [38]. I thus perform an expansion around  $\xi = \Lambda_{\text{AF}}$ , which yields  $\beta \simeq \sqrt{3\zeta/\Delta}$ . This gives the asymptotic form of the scaling function as

$$\mathcal{B}(u) \simeq \sqrt{3u} \quad u \rightarrow \infty. \quad (\text{C.6})$$

## C.3 The PB cumulative density profile

The PB cumulative density of counterions,  $n_{\text{PB}}(y)$ , is defined through Eq. (3.72). It can be easily shown that  $n_{\text{PB}}(y)$  is a monotonically increasing function of  $y = \ln(r/R)$ , i.e.  $dn_{\text{PB}}/dy \geq 0$  [75]. It is therefore bounded by its boundary values  $n_{\text{PB}}(0) = 0$  and  $n_{\text{PB}}(\Delta) = N$  (see Figure 3.3).

For  $\xi > \Lambda_{\text{AF}}$ ,  $n_{\text{PB}}(y)$  has an inflection point the location of which,  $y_* = \ln(r_*/R)$ , follows from equation  $d^2n_{\text{PB}}/dy^2 = 0$  as  $y_* = \tan^{-1}[(\xi - 1)/\beta]/\beta$ . It is easy to check (using the results in Appendix C.1) that  $y_* \simeq \Delta/2$  for large  $\xi$  and that  $y_* \rightarrow 0$  for  $\xi \rightarrow 1$  ( $y_*$  becomes negative for smaller values). For  $\xi < \Lambda_{\text{AF}}$ , on the other hand, the cumulative density,  $n_{\text{PB}}(y)$ , vanishes for  $y < \Delta$  as  $\Delta \rightarrow \infty$ , as can be checked by inserting the approximate expression (C.1) for  $\beta$  into Eq. (3.72).

Note that the main quantities of interest within the PB theory can be expressed solely in terms of the cumulative density profile. This includes the PB potential field  $\psi_{\text{PB}}$  and the

order parameters  $S_n^{\text{PB}}$ . Using the definitions of these quantities (Section 3.3), I obtain the following relations (which are valid for all  $\xi$ )

$$\psi_{\text{PB}}(y) = 2\xi \left( y - \frac{1}{N} \int_0^y n_{\text{PB}}(y') dy' \right) \quad (\text{C.7})$$

$$S_n^{\text{PB}} = \frac{1}{\xi^n} \int_0^\Delta dy e^{-ny} \left( \frac{1}{N} \frac{dn_{\text{PB}}}{dy} \right). \quad (\text{C.8})$$

## C.4 Asymptotic behavior of $S_n$ within PB theory

### Small Manning parameter $\xi < \Lambda_{\text{AF}}$ :

For  $\xi < \Lambda_{\text{AF}} \simeq 1$ , the order parameters,  $S_n$ , vanish as  $\Delta \rightarrow \infty$  indicating complete decondensation of counterions. To demonstrate this, I use Eq. (C.8), which, for  $\Delta \gg 1$ , can be written as

$$\xi^n S_n^{\text{PB}} = \frac{n}{N} \int_0^\Delta dy e^{-ny} n_{\text{PB}}(y) + \mathcal{O}(e^{-n\Delta}). \quad (\text{C.9})$$

Since the cumulative density is bounded by the number of counterions,  $N$ , and tends to zero at any finite  $y$  for  $\xi < \Lambda_{\text{AF}} \simeq 1$  (Appendix C.3), one obtains  $S_n^{\text{PB}} \rightarrow 0$  in this regime as  $\Delta \rightarrow \infty$ .

### Large Manning parameter $\xi > \Lambda_{\text{AF}}$ :

Consider the exact mean-field expression for  $S_n^{\text{PB}}$ , Eq. (3.40). The integrand in Eq. (3.40) is the product of an exponentially decaying factor with an inverse-squared sine-function, which has a series of divergencies at  $y_m = (m\pi - \epsilon)/\beta$  for integer  $m$  and  $\epsilon \equiv \cot^{-1}[(\xi - 1)/\beta]$ . For  $\Delta \rightarrow \infty$ , it follows from Appendix C.1 that  $\beta \rightarrow 0$  when  $\xi > \Lambda_{\text{AF}} \simeq 1$  implying  $\epsilon \rightarrow 0$ . In this limit,  $\epsilon$  may be expanded as

$$\epsilon \simeq \frac{\beta}{\xi - 1} - \frac{\beta^3}{3(\xi - 1)^3} + \mathcal{O}(\beta^5). \quad (\text{C.10})$$

The location of singularities,  $y_m$ , tend to infinity with increasing  $\Delta$  except for  $m = 0$  for which one has  $y_0 = -\epsilon/\beta \rightarrow -1/(\xi - 1)$  using Eq. (C.10). The quantity  $S_n^{\text{PB}}$  in Eq. (3.40) is therefore dominated by the lower bound of the integral (around  $y = 0$ ) due to the exponentially-decaying integrand. To derive the asymptotic form of  $S_n^{\text{PB}}$  for large  $\Delta$ , one can expand the integrand either around the lower limit of the integral  $y = 0$  or around the singular point  $y_0$ . Both procedures lead to the same scaling relation (3.42) for  $S_n$  in the strict limit of  $\Delta \rightarrow \infty$  when  $\xi$  is *close* to the critical value  $\xi_c^{\text{PB}} = 1$ . But only the second procedure leads to a correct result when  $\xi$  increases beyond the critical value. This is because for large  $\xi$ , the singularity at  $y_0 \sim -1/(\xi - 1)$  approaches zero rendering the expansion around  $y = 0$  a poor approximation.

By expanding the integrand around  $y = 0$  (up to the first order in  $y$ ), I obtain from Eq. (3.40) that

$$S_n^{\text{PB}} \simeq \frac{\beta^2}{\xi^{n+1} \sin^2 \epsilon} \int_0^\Delta dy e^{-(n+2\xi-2)y} \simeq \frac{\beta^2 + (\xi - 1)^2}{\xi^{n+1}(n + 2\xi - 2)}. \quad (\text{C.11})$$

This relation reproduces Eq. (3.41) in the text, which, as explained above, is valid for  $\xi$  close to  $\xi_c^{\text{PB}} = 1$ .

For larger values of  $\xi$ , I expand the integrand in (3.40) around  $y_0 = -\epsilon/\beta$ , which yields

$$S_n^{\text{PB}} \simeq \frac{\beta/\epsilon}{\xi^{n+1}} \left[ 1 - \frac{n\epsilon}{\beta} e^{n\epsilon/\beta} \Gamma\left(0, \frac{n\epsilon}{\beta}\right) \right], \quad (\text{C.12})$$

where  $\Gamma(a, b)$  is the incomplete Gamma function. This relation provides a quite good approximation for  $S_n$  for large  $\Delta$  and in the whole range of  $\xi > \xi_c^{\text{PB}} = 1$ . In particular, when the limit  $\Delta \rightarrow \infty$  is taken, it yields the correct result for  $S_n(\xi, \Delta \rightarrow \infty)$  (see Eq. (C.22) below).

## C.5 PB potential, counterion density and free energy

The preceding results for  $\beta$  may be used to obtain the asymptotic form of the rescaled PB potential field,  $\psi = \psi_{\text{PB}}(\tilde{r})$ , Eq. (3.25), the counterionic density profile,  $\tilde{\rho}_{\text{PB}}(\tilde{r})$ , Eq. (3.27), and that of the PB free energy,  $\mathcal{F}_N^{\text{PB}}$ , Eqs. (3.54) and (3.54), when  $\Delta$  tends to infinity.

### Small Manning parameter $\xi < \Lambda_{\text{AF}}$ :

For  $\xi < \Lambda_{\text{AF}} \simeq 1$ , I use the large- $\Delta$  expansion for  $\beta$  given by Eqs. (C.1) and (C.3), where  $x$  is a small parameter. Up to the leading order, the PB potential  $\psi_{\text{PB}}(\tilde{r})$  (first relation in Eq. (3.25)) is obtained from a series expansion as

$$\psi_{\text{PB}}(\tilde{r}) = 2\xi \ln \frac{\tilde{r}}{R} + \mathcal{O}\left(e^{2(\xi-1)\Delta}\right). \quad (\text{C.13})$$

Similar expansion may be performed for the density profile (first relation in Eq. (3.27)), which shows that the density profile asymptotically tends to zero as

$$\tilde{\rho}_{\text{PB}}(\tilde{r}) = \left(\frac{\tilde{r}}{R}\right)^{-2\xi} \times \mathcal{O}\left(e^{2(\xi-1)\Delta}\right) \rightarrow 0. \quad (\text{C.14})$$

Derivation of the limiting form of the PB free energy, Eq. (3.55), may be done in the same way and yields Eq. (3.59) for  $\xi \leq \xi_c^{\text{PB}} = 1$ .

### Large Manning parameter $\xi > \Lambda_{\text{AF}}$ :

For large  $\xi > \Lambda_{\text{AF}} \simeq 1$ , one may use the fact that  $\beta$  itself becomes small for large  $\Delta$  and vanishes for increasing  $\Delta \rightarrow \infty$  (Appendix C.1). Hence, the second expression for the potential field in Eq. (3.25) may be expanded for small  $\beta$ , which gives

$$\psi_{\text{PB}}(\tilde{r}) = 2 \ln \frac{\tilde{r}}{R} + 2 \ln \left[ 1 + (\xi - 1) \ln \frac{\tilde{r}}{R} \right] + \mathcal{O}(\Delta^{-2}). \quad (\text{C.15})$$

A similar expansion may be performed for the density profile (second relation in Eq. (3.27)), which gives

$$\tilde{\rho}_{\text{PB}}(\tilde{r}) = \frac{(\xi - 1)^2}{\xi^2} \left(\frac{\tilde{r}}{R}\right)^{-2} \left[ 1 + (\xi - 1) \ln \frac{\tilde{r}}{R} \right]^{-2} + \mathcal{O}(\Delta^{-2}). \quad (\text{C.16})$$

Finally, the PB free energy expression (3.54), when expanded for small  $\beta$ , yields the limiting expression in Eq. (3.59) for  $\xi \geq \xi_c^{\text{PB}}$ .



## C.6 PB solution in an unbounded system ( $\Delta = \infty$ )

In the present study, I have assumed that the counterion-cylinder system is bounded laterally ensuring the normalization of density profile,  $\tilde{\rho}_{\text{PB}}(\tilde{r})$ , to the total number of counterions,  $N$ , even in the limit  $\Delta \rightarrow \infty$ . In a strictly unbounded system (with  $\Delta = \infty$ ), the normalization property of density is not preserved, since a finite fraction of counterions escape to infinity. In this case, the PB equation (3.18) can be solved by relaxing the normalization condition (3.21). Assuming the boundary conditions at the cylinder surface as  $\psi_{\text{PB}}^\infty(\tilde{R}) = 0$  and  $\tilde{R}[d\psi_{\text{PB}}^\infty(\tilde{r} = \tilde{R})/d\tilde{r}] = 2\xi$ , one finds [105]

$$\psi_{\text{PB}}^\infty(\tilde{r}) = \begin{cases} 2\xi \ln \frac{\tilde{r}}{\tilde{R}} & \xi \leq \xi_c^{\text{PB}} = 1, \\ 2 \ln \frac{\tilde{r}}{\tilde{R}} + 2 \ln \left[ 1 + (\xi - 1) \ln \frac{\tilde{r}}{\tilde{R}} \right] & \xi \geq \xi_c^{\text{PB}} = 1. \end{cases} \quad (\text{C.17})$$

Also  $\tilde{\kappa}^2 = \tilde{\rho}_{\text{PB}}^\infty(\tilde{R}) = 0$  for  $\xi \leq \xi_c^{\text{PB}} = 1$  and  $\tilde{\kappa}^2/2 = (\xi - 1)^2/\xi^2$  otherwise. Hence using Eq. (3.23), the density profile (for  $\tilde{R} \leq \tilde{r} \leq \tilde{D}$ ) in a strictly unbounded system is obtained as

$$\tilde{\rho}_{\text{PB}}^\infty(\tilde{r}) = \begin{cases} 0 & \xi \leq 1, \\ \frac{(\xi-1)^2}{\xi^2} \left[ \frac{\tilde{r}}{\tilde{R}} \right]^{-2} \left[ 1 + (\xi - 1) \ln \frac{\tilde{r}}{\tilde{R}} \right]^{-2} & \xi \geq 1, \end{cases} \quad (\text{C.18})$$

which has the same form as given in Eqs. (3.32) and (3.34). But now  $\tilde{\rho}_{\text{PB}}^\infty(\tilde{r})$  is normalized to the condensed fraction of counterions,  $\alpha_{\text{M}}$  (Eq. (3.71)), i.e.

$$\int_{\tilde{R}}^{\infty} d\tilde{r} \tilde{r} \tilde{\rho}_{\text{PB}}^\infty(\tilde{r}) = \alpha_{\text{M}} \xi = \begin{cases} 0 & \xi \leq \xi_c^{\text{PB}} = 1, \\ \xi - 1 & \xi \geq \xi_c^{\text{PB}} = 1 \end{cases} \quad (\text{C.19})$$

(compare with Eq. (3.29)). The order parameters in the unbounded system,  $S_n^{\text{PB},\infty}$ , may be calculated using  $\tilde{\rho}_{\text{PB}}^\infty$ . For  $\xi > \xi_c^{\text{PB}} = 1$ , I obtain

$$S_n^{\text{PB},\infty} = \frac{1}{\xi^n} \left[ 1 - \frac{n}{\xi - 1} e^{n/(\xi-1)} \Gamma\left(0, \frac{n}{\xi - 1}\right) \right]. \quad (\text{C.20})$$

In the vicinity of the critical point ( $\xi \rightarrow 1^+$ ), the order parameter obeys the scaling relation

$$S_n^{\text{PB},\infty}(\zeta) \sim \frac{\zeta}{n}, \quad (\text{C.21})$$

which exhibits a different exponent as compared with the quantity  $S_n^{\text{PB}}(\zeta, \Delta \rightarrow \infty)$  in Eq. (3.42). This is again due to the difference in normalization factor, which enters in  $S_n$  through Eq. (3.38) (note the order in which the integration and the infinite-system limit are taken). In general, the order parameter  $S_n^{\text{PB}}(\zeta, \Delta \rightarrow \infty)$  is obtained by multiplying  $S_n^{\text{PB},\infty}(\zeta)$  with the condensed fraction  $\alpha_{\text{M}}$ , as

$$S_n^{\text{PB}}(\zeta, \Delta \rightarrow \infty) = \alpha_{\text{M}} S_n^{\text{PB},\infty}(\zeta). \quad (\text{C.22})$$



# Appendix D

## Periodic Cell Model: Summation techniques for simulations in 3D

### D.1 Counterions at charged cylinders: MC simulations

As stated in Section 3.5.2, the periodic boundary conditions used in the simulations in 3D lead to summation of Coulombic interactions ( $v(\mathbf{x}) = 1/|\mathbf{x}|$ ) over all periodic images. The resultant summation series are convergent for an *electroneutral* system and can be mapped to fast-converging series, which can be handled easily in the simulations [110, 111]. In what follows, I derive the convergent expressions for the configurational Hamiltonian (3.3).

The main simulation box (of height  $H$  and containing  $N$  counterions) is replicated infinitely many times in  $z$  direction generating a series of  $M \rightarrow \infty$  image boxes labeled with  $m = -M/2, \dots, -1, 0, 1, \dots, +M/2$  (with  $m = 0$  being the main box). The Hamiltonian (3.3) consists of three parts  $\mathcal{H}_N = \mathcal{H}_{\text{ci}} + \mathcal{H}_{\text{int}} + \mathcal{H}_{\text{self}}$ , namely, counterion-counterion interaction,  $\mathcal{H}_{\text{ci}}$ , counterion-cylinder interaction,  $\mathcal{H}_{\text{int}}$ , and the cylinder self-energy,  $\mathcal{H}_{\text{self}}$ , that will be analyzed separately. Here I use actual units and in the end, transform the results to the rescaled form.

#### $\mathcal{H}_{\text{int}}$ and $\mathcal{H}_{\text{self}}$ terms

The counterion-cylinder interaction part per simulation box reads  $\mathcal{H}_{\text{int}}/(Mk_{\text{B}}T) = \sum_{\alpha=1}^N u(r_{\alpha})$ , where using  $\sigma(\mathbf{x}) = \sigma_s \delta(r - R)$ , one has

$$u(r_{\alpha}) = -q\ell_{\text{B}} \int v(\mathbf{x} - \mathbf{x}_{\alpha}) \sigma(\mathbf{x}) d\mathbf{x} = 2\xi \ln\left(\frac{r_{\alpha}}{R}\right) + c_0 \quad (\text{D.1})$$

with  $\alpha$  running only over the counterions within the main box. The constant term is given by

$$c_0 = -q\ell_{\text{B}} \int v(\mathbf{x} - \mathbf{x}_0) \sigma(\mathbf{x}) d\mathbf{x}, \quad (\text{D.2})$$

where  $\mathbf{x}_0$  belongs to the cylinder surface.  $c_0$  may be written in terms of the cylinder self-energy,

$$\frac{\mathcal{H}_{\text{self}}}{Mk_{\text{B}}T} = \frac{\ell_{\text{B}}}{2} \int \sigma(\mathbf{x}) v(\mathbf{x} - \mathbf{x}') \sigma(\mathbf{x}') d\mathbf{x} d\mathbf{x}'. \quad (\text{D.3})$$

Using the electroneutrality condition  $\tau H = qN$  (per box), one can show that  $\beta\mathcal{H}_{\text{self}}/(Mk_{\text{B}}T) = -Nc_0/2$ . Thus, one has

$$\frac{1}{Mk_{\text{B}}T} \left( \mathcal{H}_{\text{int}} + \mathcal{H}_{\text{self}} \right) = 2\xi \sum_{\alpha=1}^N \ln \left( \frac{r_{\alpha}}{R} \right) + C_0, \quad (\text{D.4})$$

where  $C_0 = -\beta\mathcal{H}_{\text{self}}/M$  is a constant (see Eq. (3.4)), which diverges logarithmically with  $M$ . This can be seen from the asymptotic behavior of the self-energy for large  $M$  (or large  $MH/R$ ), i.e.

$$\begin{aligned} \frac{\mathcal{H}_{\text{self}}/(k_{\text{B}}T)}{\tau^2\ell_{\text{B}}MH} &= \int_0^{2\pi} d\theta d\theta' \int_{-\frac{MH}{2}}^{\frac{MH}{2}} \frac{dz dz'/(2MH)}{\sqrt{(z-z')^2 + 4R^2 \sin^2 \frac{\theta-\theta'}{2}}} \\ &\simeq a_0 + \ln \left( \frac{MH}{R} \right) + \mathcal{O} \left( \frac{R}{MH} \right)^2, \end{aligned} \quad (\text{D.5})$$

where  $a_0 \simeq \ln 2 - 1$ . This logarithmic divergency is cancelled by a similar divergent term coming from the interaction between counterions as shown below.

### $\mathcal{H}_{\text{ci}}$ term and the Lekner-Sperb formulae

The contribution from counterionic interactions (per box and for large  $M$ ) can be written as

$$\frac{\mathcal{H}_{\text{ci}}}{Mk_{\text{B}}T} = \frac{q^2\ell_{\text{B}}}{2M} \sum_{i \neq j} v(\mathbf{x}_i - \mathbf{x}_j) = \frac{q^2\ell_{\text{B}}}{2H} \left[ \sum_{\alpha \neq \beta=1}^N S_M \left( \frac{\mathbf{x}_{\alpha} - \mathbf{x}_{\beta}}{H} \right) + NS_M^0 \right], \quad (\text{D.6})$$

where  $i$  and  $j$  run over *all* counterions (including periodic images), while  $\alpha$  and  $\beta$  run over counterions in the main simulation box. One also has  $S_M^0 = 2 \sum_{m=1}^{M/2} m^{-1}$  and

$$S_M \left( \frac{\mathbf{x}_{\alpha} - \mathbf{x}_{\beta}}{H} \right) = \sum_{m=-M/2}^{M/2} \left[ \rho_{\alpha\beta}^2 + (\zeta_{\alpha\beta} + m)^2 \right]^{-1/2}, \quad (\text{D.7})$$

where  $\rho_{\alpha\beta} = [(x_{\alpha} - x_{\beta})^2 + (y_{\alpha} - y_{\beta})^2]^{1/2}/H$  and  $\zeta_{\alpha\beta} = (z_{\alpha} - z_{\beta})/H$ . Note that  $S_M^0$ , in particular, represents the interaction between a counterion and its periodic images, which are lined up in  $z$  direction. This series diverges and may be written as  $S_M^0 = 2 \ln(M/2) + 2\mathbf{C}_e$  for  $M \rightarrow \infty$ , where  $\mathbf{C}_e = 0.577215\dots$  is the Euler's constant. In this limit,  $S_M$  is also divergent, but it may be split into a convergent and a divergent part as

$$S_M = S_M^0 + S_{\text{LS}}(\rho_{\alpha\beta}, \zeta_{\alpha\beta}) + 2(\ln 2 - \mathbf{C}_e), \quad (\text{D.8})$$

in which the convergent series  $S_{\text{LS}}(\rho_{\alpha\beta}, \zeta_{\alpha\beta})$  can be expressed in terms of special functions.

Now inserting the above results for  $S_M$  and  $S_M^0$  into Eq. (D.6), one can see that for  $M \rightarrow \infty$ ,

$$\frac{\mathcal{H}_{\text{ci}}}{Mk_{\text{B}}T} = \frac{q^2\ell_{\text{B}}}{2H} \sum_{\alpha \neq \beta=1}^N S_{\text{LS}}(\rho_{\alpha\beta}, \zeta_{\alpha\beta}) + \xi(\mathbf{C}_e - \ln 2) + \xi N \ln M, \quad (\text{D.9})$$

with a logarithmic divergent term (last term) from the one-dimensional periodicity of the system. Using Eqs. (D.5) and (D.9), it immediately follows that the divergencies in Eqs.

(D.4) and (D.9) cancel each other when the electroneutrality condition is assumed. Thus I obtain the well-defined expression

$$\frac{\mathcal{H}_N}{Mk_{\text{B}}T} = 2\xi \sum_{\alpha=1}^N \ln \left( \frac{r_{\alpha}}{R} \right) + \frac{q^2 \ell_{\text{B}}}{2H} \sum_{\alpha \neq \beta=1}^N S_{\text{LS}}(\rho_{\alpha\beta}, \zeta_{\alpha\beta}) + \xi N h_0, \quad (\text{D.10})$$

where  $h_0 = 1 + \ln(R/2H) + (\mathbf{C}_e - \ln 2)/N$ ; equivalently,

$$\frac{\mathcal{H}_N}{Mk_{\text{B}}T} = 2\xi \sum_{\alpha=1}^N \ln \left( \frac{\tilde{r}_{\alpha}}{\tilde{R}} \right) + \frac{\Xi}{2\tilde{H}} \sum_{\alpha \neq \beta=1}^N S_{\text{LS}}(\tilde{\rho}_{\alpha\beta}, \tilde{\zeta}_{\alpha\beta}) + \xi N h_0, \quad (\text{D.11})$$

in rescaled units, where  $h_0 = 1 + \ln(\xi^2/2\Xi N) + (\mathbf{C}_e - \ln 2)/N$ . The above expression is used to obtain the internal energy and the heat capacity of the system in the Monte-Carlo simulations reported in Section 3.5. The term  $S_{\text{LS}}(\tilde{\rho}_{\alpha\beta}, \tilde{\zeta}_{\alpha\beta})$  may be obtained from Eq. (D.8) using mathematical identities proposed by Lekner [110] and Sperb [111]. It may be written in the form of two formally *identical* series expansion

$$S_{\text{LS}} = \begin{cases} \text{I} : -2 \ln \tilde{\rho}_{\alpha\beta} + 4 \sum_{m=1}^{\infty} K_0(2\pi m \tilde{\rho}_{\alpha\beta}) \cos(2\pi m \tilde{\zeta}_{\alpha\beta}). \\ \text{II} : \sum_{m=1}^{\infty} \binom{-1/2}{m} (\tilde{\rho}_{\alpha\beta})^{2m} \left[ Z(2m+1, 1 + \tilde{\zeta}_{\alpha\beta}) - Z(2m+1, 1 - \tilde{\zeta}_{\alpha\beta}) \right] + \\ \quad + (\tilde{\rho}_{\alpha\beta}^2 + \tilde{\zeta}_{\alpha\beta}^2)^{-1/2} - \Psi(1 + \tilde{\zeta}_{\alpha\beta}) - \Psi(1 - \tilde{\zeta}_{\alpha\beta}) - c_*. \end{cases} \quad (\text{D.12})$$

In the above relations,  $K_0(x)$  is the modified Bessel function of the second kind,  $Z(n, x) = \sum_{k=0}^{\infty} 1/(k+x)^n$  is the Hurwitz Zeta function,  $\Psi(x)$  is the Digamma function, and  $c_* = 2 \ln 2 \simeq 1.386294 \dots$

The series in Eq. (D.12) can be evaluated numerically up to the desired accuracy. Note that the first series (Lekner scheme) involves the Bessel function  $K_0(x)$ , which decays exponentially for large  $x$  (as  $\sim \exp(-x)/\sqrt{x}$ ) but diverges logarithmically for small  $x$ . It is therefore rapidly converging when the radial distance between two given particles,  $\tilde{\rho}_{\alpha\beta}$ , is sufficiently large. I use the following recipe to truncate series I: For  $\tilde{\rho}_{\alpha\beta} > 3$ , I truncate after the third term, for  $1/3 \leq \tilde{\rho}_{\alpha\beta} \leq 3$ , I include  $2 + [3/\tilde{\rho}_{\alpha\beta}]$  terms in the sum (where  $[x]$  refers to the integer part of  $x$ ), and for  $1/4 \leq \tilde{\rho}_{\alpha\beta} < 1/3$ , I sum at least 12 terms. This recipe ensures a *relative* truncation error of about  $|e_r| \sim 10^{-10}$ . For small radial separation  $\tilde{\rho}_{\alpha\beta} < 1/4$  between two particles, series I becomes inefficient and slow. I thus employ the second series expression (Sperb scheme). This series is rapidly converging for small  $\tilde{\rho}_{\alpha\beta}$  provided that  $\tilde{\zeta}_{\alpha\beta}$ , which enters in the argument of the Hurwitz Zeta function, is sufficiently small, namely for  $|\tilde{\zeta}_{\alpha\beta}| \leq 1/2$  [111] (note that in general one has  $|\tilde{\zeta}_{\alpha\beta}| \leq 1$ ). In fact due to the periodicity of the system, the energy expression (D.6) remains invariant under the transformations  $\tilde{\zeta}_{\alpha\beta} \rightarrow 1 - \tilde{\zeta}_{\alpha\beta}$  and  $\tilde{\zeta}_{\alpha\beta} \rightarrow -\tilde{\zeta}_{\alpha\beta}$ , and thus  $\tilde{\zeta}_{\alpha\beta}$  can be always restricted to the range  $|\tilde{\zeta}_{\alpha\beta}| \leq 1/2$ . In this case, I use up to 8 terms in series II. The relative truncation error,  $|e_r|$ , varies for different  $\tilde{\zeta}_{\alpha\beta}$ , e.g., for  $\tilde{\zeta}_{\alpha\beta} \simeq 0.4$  and  $\tilde{\rho}_{\alpha\beta} \simeq 0.25$ , one has  $|e_r| \sim 10^{-7}$ . The error substantially decreases for smaller  $\tilde{\zeta}_{\alpha\beta}$ . The above truncation recipes yield accurate estimates for the interaction energies within the statistical error-bars of the simulations.



# Appendix E

## Strong-Coupling Interactions: Asymptotic analysis

In this appendix, I discuss the asymptotic forms of the strong-coupling free energy as quoted in Chapter 5 for the interaction between two like-charged rods and two like-charged spheres.

### E.1 Two like-charged rods

I will first consider the limit of vanishingly small Manning parameter  $\tilde{R} \ll 1$ . A straightforward expansion of the integral in Eq. (5.22) in powers of  $\tilde{R}$  gives the following expression for the SC free energy (5.22), i.e.

$$\frac{\mathcal{F}_N^{\text{SC}}}{Nk_{\text{B}}T} \simeq -\tilde{R} \ln \tilde{d} + \frac{2\tilde{R}}{\tilde{L}^2} \int_{-\tilde{L}/2}^{\tilde{L}/2} d\tilde{x} d\tilde{y} (\ln \tilde{r}_1 + \ln \tilde{r}_2) - \ln \tilde{L}^2, \quad (\text{E.1})$$

where I have omitted terms that are independent of  $\tilde{L}$  and  $\tilde{d}$  as they are irrelevant in the present discussion. The first two terms in Eq. (E.1) are nothing but the mean energy of the two rods and their counterions, and the last term is the entropic contribution from counterions, which takes an ideal gas form due to the highly de-condensed state of counterion for small  $\tilde{R}$ . (This may be seen more clearly using the electroneutrality condition  $2\tau H = qN$  and restoring the actual units that yields  $\mathcal{F}_N^{\text{SC}}/(k_{\text{B}}T) \simeq -2\ell_{\text{B}}\tau^2 H \ln d + 2\xi N (\ln r_1 + \ln r_2) - N \ln L^2$ . Note also that Manning parameter equals the rescaled radius of rods, Eq. (5.18), thus  $\tilde{R} \rightarrow 0$  implies line charges in the rescaled picture.) The bare repulsive force between the rods scales like  $\sim \tilde{d}^{-1}$ , but the counterion-induced attraction force (coming from the second term) scales as  $\sim \tilde{d}/\tilde{L}^2$ , which becomes vanishingly small as  $\tilde{L} \rightarrow \infty$ . Therefore, the asymptotic free energy (E.1) admits a shallow  $\tilde{L}$ -dependent minimum as seen in Figure 5.2. By minimizing expression (E.1) with respect to  $\tilde{d}$ , the bound-state separation is approximately found as in Eq. (5.34) in the text when  $\tilde{L} \rightarrow \infty$ .

For large  $\tilde{R} > \tilde{R}_c$ , the free energy substantially decreases, when the rods are close to each other (Figure 5.2). Inspection shows that in this situation, the main contribution to the integral  $I$  in Eq. (5.23) comes from the intervening region between the rods ( $-\tilde{d}/2 + \tilde{R} < \tilde{x} < \tilde{d}/2 - \tilde{R}; \tilde{y} \simeq 0$ ). This reflects strong accumulation of counterions in this region for large  $\tilde{R}$ , as it can be checked directly from the counterionic distribution function obtained in the SC

limit. The integral  $I$ , Eq. (5.23), may be rewritten as

$$I = \int d\tilde{x} d\tilde{y} \tilde{\Omega} \exp \left[ -2\tilde{R}g(\tilde{x}, \tilde{y}) \right], \quad (\text{E.2})$$

where  $g(\tilde{x}, \tilde{y}) = \ln \tilde{r}_1 + \ln \tilde{r}_2$ , and  $\tilde{r}_{1,2}$  are radial distances from the rods axes (Eq. (5.21)). It follows that  $(\tilde{x}, \tilde{y}) = (0, 0)$  is the saddle point of  $g$ , thus for sufficiently large  $\tilde{R} \gg 1$ , a saddle-point approximation may be used to calculate  $I$ , which gives (up to some irrelevant prefactors)

$$I \simeq e^{-2\tilde{R} \ln \tilde{d}^2} \times \tilde{d}^2 \times \int_{-1/2+\tilde{R}/\tilde{d}}^{1/2-\tilde{R}/\tilde{d}} d\tilde{x} e^{8\tilde{R}\tilde{x}^2}, \quad (\text{E.3})$$

where I have rescaled the coordinates as  $\tilde{x} \rightarrow \tilde{x}/\tilde{d}$ ,  $\tilde{y} \rightarrow \tilde{y}/\tilde{d}$  (Eq. (5.24)) and assumed that the box size is sufficiently large. Indeed, the above approximation is valid as long as the surface-to-surface separation of rods is sufficiently small, i.e.  $\epsilon = (\tilde{d} - 2\tilde{R})/2\tilde{R} \ll 1$ , since  $g$  is singular at  $(\tilde{x}/\tilde{d}, \tilde{y}/\tilde{d}) = (\pm 1/2, 0)$ . Using Eqs. (E.3) and (5.22), one obtains

$$\frac{\mathcal{F}_N^{\text{SC}}}{Nk_{\text{B}}T} \simeq 3\tilde{R} \ln \tilde{d} - f(\tilde{d}, \tilde{R}), \quad (\text{E.4})$$

where  $f \simeq \ln(\tilde{d} - 2\tilde{R}) + \mathcal{O}(\epsilon)$ . This yields Eq. (5.30) in the text. Note that for large separations, equations (5.27) and (5.28) should be used instead as the correct asymptotic forms of the free energy.

Restoring the actual units in Eq. (E.4), one obtains

$$\frac{\mathcal{F}_N^{\text{SC}}}{k_{\text{B}}T} \simeq 6\ell_{\text{B}}\tau^2 H \ln d - N \ln(d - 2R). \quad (\text{E.5})$$

The first term in Eq. (E.5) represents the attractive interaction energy between two rods mediated by neutralizing counterions that are located (and lined up along the axes) between them with an effective linear charge density of  $+2\tau$ . While the second term may be regarded as a repulsive entropic contribution from counterions.

## E.2 Two like-charged spheres

For small Manning parameter  $\tilde{R} \ll 1$ , one can expand the integral in the SC free energy for two spheres, Eq. (5.46), to get

$$\frac{\mathcal{F}_N^{\text{SC}}}{Nk_{\text{B}}T} \simeq \frac{\tilde{R}^2}{\tilde{d}} - \frac{2\tilde{R}^2}{\tilde{L}^3} \int_{-\tilde{L}/2}^{\tilde{L}/2} d^3\tilde{r} \left( \frac{1}{\tilde{r}_1} + \frac{1}{\tilde{r}_2} \right) - \ln \tilde{L}^3. \quad (\text{E.6})$$

This expression comprises the mean energy of the two spheres with their neutralizing counterions (first two terms) together with the entropic contribution from counterions (last term) that has an ideal-gas form and reflects their highly diluted state. The bare repulsive sphere-sphere force scales as  $\sim \tilde{d}^{-2}$ , while the counterion-induced attraction force (coming from the second term) scales as  $\sim \tilde{d}/\tilde{L}^3$ , which vanishes as  $\tilde{L} \rightarrow \infty$ . The asymptotic free energy (E.6) has a shallow  $\tilde{L}$ -dependent minimum as seen in Figures 5.6a-c. The location of this minimum, Eq. (5.48) in the text, is easily obtained from the asymptotic expression (E.6).

For large  $\tilde{R}$ , the free energy exhibits a local minimum at small center-to-center separations (Figure 5.6d), where the main contribution to the volume integral in Eq. (5.46) comes from



the intervening region between spheres ( $-\tilde{d}/2 + \tilde{R} < \tilde{x} < \tilde{d}/2 - \tilde{R}; \tilde{y} \simeq 0; \tilde{z} \simeq 0$ ). A saddle-point approximation similar to the two-rod system (Eq. (E.3)) may be performed, which gives the asymptotic expression (5.49) in the text for the free energy at sufficiently large  $\tilde{R}$  and small surface-to-surface separation  $\epsilon = (\tilde{d} - 2\tilde{R})/2\tilde{R} \ll 1$ , i.e.

$$\frac{\mathcal{F}_N^{\text{SC}}}{Nk_{\text{B}}T} = -7\frac{\tilde{R}^2}{\tilde{d}} - f(\tilde{d}, \tilde{R}), \quad (\text{E.7})$$

where  $f \simeq \ln(\tilde{d} - 2\tilde{R}) + \mathcal{O}(\epsilon)$ . Restoring the actual units, one obtains

$$\frac{\mathcal{F}_N^{\text{SC}}}{k_{\text{B}}T} \simeq -7\ell_{\text{B}}\frac{Z^2}{d} - N \ln(d - 2R). \quad (\text{E.8})$$

The first term in Eq. (E.8) formally corresponds to the energetic attraction between two spheres mediated by a neutralizing counterion (of charge valency  $q = +2Z$ ) located between them. The second term is a repulsive entropic contribution from counterions.



# Appendix F

## Free Energy of a Charged Brush

As discussed in Chapter 6, the main contributions to the free energy an osmotic brush come from elastic stretching and electrostatic contributions. The former contribution is calculated using a freely-jointed-chain model, the details of which is presented in the following section. The electrostatic contribution is obtained from a cell-model approach; the forthcoming Section F.2 gives a short derivation of the asymptotic results used in the text for this part at small and large grafting densities of the brush.

### F.1 Freely-jointed-chain model

A freely-jointed chain (FJC) consists of  $N_m$  rigid links (monomers), each of fixed length  $b_0$  that can point in any direction independently of each other. The free energy of such a polymer chain is purely entropic and may be obtained by performing calculations in an isobaric ensemble, i.e. assuming that the chain is stretched by applying a constant force  $F$  (in units of  $k_B T$ ). The configuration space of the chain is spanned by a set of angles  $\{\theta_i, \phi_i\}$  specifying orientations of the monomers labeled by  $i = 1, \dots, N_m$  (a spherical frame of coordinates is chosen with  $z$ -axis pointing in the same direction as the force  $F$ ). The partition function of FJC model is

$$\mathcal{Z}_F^{\text{FJC}} = \left[ \int_0^{2\pi} \frac{d\phi}{2\pi} \int_0^\pi \frac{d\theta}{2} \sin \theta e^{b_0 F \cos \theta} \right]^{N_m} = \left[ \frac{e^{b_0 F} - e^{-b_0 F}}{2b_0 F} \right]^{N_m}. \quad (\text{F.1})$$

The extension (end-to-end distance) of the chain,  $L$ , follows from  $L = \partial \ln \mathcal{Z}_F^{\text{FJC}} / \partial F$  as

$$\frac{L}{b_0 N_m} = \coth b_0 F - \frac{1}{b_0 F}. \quad (\text{F.2})$$

Using Legendre transformation one can calculate the isochoric free energy of the system,  $\mathcal{F}^{\text{FJC}} / (k_B T) = -\ln \mathcal{Z}_F^{\text{FJC}} + LF$ , hence

$$\frac{\mathcal{F}^{\text{FJC}}}{N_m k_B T} = -\ln \frac{\sinh b_0 F}{b_0 F} + b_0 F \coth b_0 F - 1, \quad (\text{F.3})$$

which is used together with Eq. (F.2) in Chapter 6.

In the weak-stretching or Gaussian-chain limit  $b_0 F \ll 1$ , the end-to-end distance is obtained from Eq. (F.2) as  $L \simeq N_m b_0^2 F / 3$ , which gives the Gaussian-chain free energy as

$\mathcal{F}^{\text{FJC}}/(N_m k_B T) \simeq 3L^2/2(N_m b_0)^2$ . In the strong-stretching limit  $b_0 F \gg 1$ , a non-linear force-extension relation is reached from Eq. (F.2) as  $L/(b_0 N_m) \simeq 1 - 1/(b_0 F)$ . Using this, one finds the non-linear elastic free energy  $\mathcal{F}^{\text{FJC}}/(N_m k_B T) \simeq -\ln(1 - L/N_m b_0) + \text{const.}$

## F.2 PB free energy: Asymptotic results

**Small grafting densities  $\rho_a b_0^2 \ll 1$ :**

In this case, as discussed in the text, different expressions are obtained for the PB free energy depending on whether the Manning parameter is smaller or larger than the Alfrey-Fuoss threshold  $\Lambda_{\text{AF}} = \ln(D/R)/[\ln(D/R) + 1]$ , Eq. (6.15). Note that within the cell model used for the brush, the grafting density is inversely related to the lateral cell radius  $D$ , i.e.  $\rho_a b_0^2 = (R/D)^2$ . Using the results in Chapter 3 for large  $D/R$ , the PB free energy (per unit cell) is given by

$$\frac{\mathcal{F}^{\text{PB}}}{N_m k_B T} \simeq \begin{cases} f(\xi - 2) \ln(D/R) & \xi \leq \Lambda_{\text{AF}} \simeq 1, \\ -(f/\xi) \ln(D/R) & \xi \geq \Lambda_{\text{AF}} \simeq 1, \end{cases} \quad (\text{F.4})$$

for vanishing grafting density or  $D/R \rightarrow \infty$ . These results confirm Eqs. (6.34) and (6.37) in the text that are obtained using heuristic arguments.

For small Manning parameter  $\xi \leq \Lambda_{\text{AF}} \simeq 1$ , both bare electrostatic energy of the charged rod and entropy of mobile counterions contribute to the free energy as  $f\xi \ln D/R$  and  $-2f \ln D/R$ , respectively. However, for very large  $D/R$ , the longitudinal entropic pressure of counterions becomes vanishingly small as compared with the longitudinal bare electrostatic pressure. This can be seen by differentiation of the corresponding terms of the free energy with respect to the cell volume  $\pi D^2 L$  at fixed cell radius  $D$ . (Note that the longitudinal osmotic pressure is calculated from the free energy as  $\pi_{\text{os}}^{\text{Long}} = -\partial \mathcal{F}^{\text{PB}}/(\pi D^2 \partial L)$ , where  $L$  is related to  $\xi$  via Eq. (6.20) and  $D$  is kept fixed.) In contrast, bare electrostatic and entropic contributions lead to lateral pressures of the same order, as may be seen by differentiating the corresponding terms of the free energy with respect to  $\pi D^2 L$  at fixed rod length  $L$ . This latter result is known as Manning's limiting law for the osmotic coefficient of dilute solutions of weakly charged polyelectrolytes [39], which states that the osmotic coefficient,  $\nu$ , tends to a finite value of  $\nu = 1 - \xi/2$  as the solution becomes highly diluted. This relation can be derived using the cell-model free energy (F.4) by noting that the osmotic coefficient is defined as the ratio between the lateral osmotic pressure acting on the cell boundary,

$$\pi_{\text{os}}^{\text{Lat}}(D) = -\frac{\partial \mathcal{F}^{\text{PB}}}{2\pi D L \partial D} \quad (\text{F.5})$$

and the lateral osmotic pressure of an ideal gas of particles filling the cell under similar conditions, i.e.  $P_{\text{id}} = N/\pi L(D^2 - R^2)$ . Therefore, one obtains

$$\lim_{D/R \rightarrow \infty} \nu = \lim_{D/R \rightarrow \infty} \left( \frac{\pi_{\text{os}}^{\text{Lat}}}{P_{\text{id}}} \right) = 1 - \frac{\xi}{2}. \quad (\text{F.6})$$

For large Manning parameter  $\xi > \Lambda_{\text{AF}} \simeq 1$ , electrostatic repulsions and entropic effects have contributions of the same order of magnitude in the total longitudinal pressure acting on the rod, which can be understood in terms of the counterion-condensation picture [39] as

explained in Section 6.2.4. The Manning limiting law for the (lateral) osmotic coefficient is obtained in this regime (from Eq. (F.5) and second relation in Eq. (F.4)) as

$$\lim_{D/R \rightarrow \infty} \nu = \frac{1}{2\xi}. \quad (\text{F.7})$$

Note that in the cell model used in Chapter 6, the rod radius  $R$  is not fixed but depends on  $\xi$  (see Eq. (6.21)). The preceding discussions still hold for  $D \gg r_c + R_0$ .

**Large grafting densities  $\rho_a b_0^2 \rightarrow 1^-$ :**

In a cell model with fixed  $R$ , the Alfrey-Fuoss threshold  $\Lambda_{\text{AF}} = \ln(D/R)/[\ln(D/R) + 1]$  tends to zero as the grafting density tends to its maximum value, i.e. when  $D/R \rightarrow 1$ . Therefore, for finite values of the Manning parameter  $\xi$ , one has to use Eqs. (6.18) and (6.17) for  $\xi \geq \Lambda_{\text{AF}}$ .

Starting from Eq. (6.18), one can find an approximate expression for  $\beta$  in the limit of  $D/R \rightarrow 1$ . Defining  $\epsilon = D/R - 1$  and expanding Eq. (6.18) for small  $\epsilon$ , one obtains

$$\beta^2 \simeq \xi \left( \frac{1}{\epsilon} + \mathcal{O}(\epsilon^0) \right) - 1. \quad (\text{F.8})$$

Now replacing  $\beta^2$  in Eq. (6.17) and expanding in terms of  $\epsilon$ , one obtains (up to an additive constant independent of  $\epsilon$ )

$$\frac{\mathcal{F}^{\text{PB}}}{N_m k_B T} \simeq -f \ln \epsilon + \mathcal{O}(\epsilon). \quad (\text{F.9})$$

This is the entropic free energy of an ideal gas of particles up to the leading order (compare Eq. (6.30)), which represents the main contribution to the PB free energy at large grafting densities.

In the cell model with constant volume constraint for the charged rod, this limit (namely  $D \rightarrow r_c + R_0$ ) has to be handled with care. In fact, the upper limit on  $\xi$ , that is  $\xi_u$ , Eq. (6.23), tends to the lower limit  $\xi_0$ , Eq. (6.22), and so does the optimal Manning parameter. The Alfrey-Fuoss threshold  $\Lambda_{\text{AF}}$  becomes smaller than  $\xi_0$ , therefore, the system indeed satisfies  $\xi > \Lambda_{\text{AF}}$  condition, so that the above discussion remains valid.



# Bibliography

- [1] E.J. Verwey, J.T.G. Overbeek, *Theory of the Stability of Lyophobic Colloids* (Elsevier, Amsterdam, 1948).
- [2] J. Israelachvili, *Intermolecular and Surface Forces* (Academic Press, London, 1991).
- [3] R.J. Hunter, *Foundations of Colloidal Science* (Clarendon, Oxford, first edition 1987, second edition 2001).
- [4] P.-G. de Gennes, *Scaling Concepts in Polymers Physics* (Cornell University Press, Ithaca, 1979)
- [5] A.Y. Grosberg, A.R. Khokhlov, *Statistical Physics of Macromolecules* (American Institute of Physics, New York, 1994).
- [6] M. Doi, S.F. Edwards, *The Theory of Polymer Dynamics* (Oxford University Press, Oxford, 1986).
- [7] B. Alberts, A. Johnson, J. Lewis, M. Raff, K. Roberts, P. Walter, *Molecular Biology of the Cell* (Garland Science, New York, 2002).
- [8] R. Brown, *Edinburgh New Phil. J.* **5**, 358 (1828).
- [9] A. Einstein, *Ann. Physik*, **17**, 549 (1905); **19**, 371 (1906).
- [10] M. von Smoluchowski, *Ann. Physik*, **21**, 756 (1906).
- [11] J. Perrin, *Atoms* (Constable, London, 1916).
- [12] P. Langevin, *Comptes Rendus* **146**, 530 (1908).
- [13] S. Chandrasekhar, *Rev. Mod. Phys.* **15**, 1 (1943).
- [14] B.V. Derjaguin, L. Landau, *Acta Physicochim. USSR* **14**, 633 (1941).
- [15] D.H. Napper, *Polymeric Stabilization of Colloidal Dispersions* (Academic Press, London, 1983).
- [16] P. Pincus, *Macromolecules* **24**, 2912 (1991).
- [17] P.M.V. Résibois, *Electrolyte Theory* (Harper and Row, New York, 1968).
- [18] P. Debye, E. Hückel, *Physik. Z.* **24**, 185 (1923).

- [19] H. Dautzenberg, W. Jaeger, B.P.J. Kötzt, C. Seidel, D. Stscherbina, *Polyelectrolytes: Formation, characterization and application* (Hanser Publishers, New York, 1994).
- [20] F. Oosawa, *Polyelectrolytes* (Marcel Dekker, New York, 1971).
- [21] C. Holm, P. Kékicheff, R. Podgornik (Editors), *Electrostatic Effects in Soft Matter and Biophysics* (Kluwer Academic Publishers, Dordrecht, 2001).
- [22] A.K. Kleinschmidt, D. Lang, D. Jacherts, R.K. Zahn, *Biochim. Biophys. Acta* **61**, 857 (1962).
- [23] K.K. Kunze, R.R. Netz, *Phys. Rev. Lett.* **85**, 4389 (2000).
- [24] H. Boroudjerdi, R.R. Netz, *Europhys. Lett.* **64**, 413 (2003); *J. Phys.: Condens. Matter* **17**, S1137 (2005).
- [25] H. Boroudjerdi, Y.-W. Kim, A. Naji, R.R. Netz, X. Schlagberger, A. Serr, *Physics Reports* (2005)–in press.
- [26] J.O. Rädler, I. Koltover, T. Salditt, C.R. Safinya, *Science* **275**, 810 (1997).
- [27] J.O. Rädler, I. Koltover, A. Jamieson, T. Salditt, C.R. Safinya, *Langmuir* **14**, 4272 (1998).
- [28] I. Koltover, T. Salditt, J.O. Rädler, C.R. Safinya, *Science* **281**, 78 (1998).
- [29] R.G. Crystal, *Science* **270**, 404 (1995).
- [30] W.M. Gelbart, R.F. Bruinsma, P.A. Pincus, V.A. Parsegian, *Physics Today* (September 2000), pp. 38-44.
- [31] V.A. Bloomfield, *Biopolymers* **31**, 1471 (1991); *Curr. Opin. Struct. Biol.* **6**, 334 (1996).
- [32] O. Lambert, L. Plançon, J.L. Rigaud, L. Letellier, *Mol. Microbiol.* **30**, 761 (1998).
- [33] J.X. Tang, S. Wong, P.T. Tran, P.A. Janmey, *Ber. Bunsenges. Phys. Chem.* **100**, 796 (1996).
- [34] J.X. Tang, T. Ito, T. Tao, P. Traub, P.A. Janmey, *Biochemistry* **36**, 12600 (1997).
- [35] A. Naji, S. Jungblut, A.G. Moreira, R.R. Netz, *Physica A* **352**, 131 (2005).
- [36] A. Katchalsky, *Pure Appl. Chem.* **26**, 327 (1971).
- [37] T. Alfrey, P.W. Berg, H. Morawetz, *J. Polym. Sci.* **7**, 543 (1951).
- [38] R.M. Fuoss, A. Katchalsky, S. Lifson, *Proc. Natl. Acad. Sci. USA* **37**, 579 (1951).
- [39] G.S. Manning, *J. Chem. Phys.* **51**, 924 (1969); **51**, 3249 (1969).
- [40] N. Bjerrum, *Kgl. Danske Videnskab. Selskab. Mat.-fys. Medd.* **7**, 1 (1926).
- [41] G. Gouy, *J. Phys. (Paris)* **9**, 457 (1910).
- [42] D.L. Chapman, *Phil. Mag.* **25**, 475 (1913).



- [43] R.R. Netz, Eur. Phys. J. E **5**, 557 (2001).
- [44] A.G. Moreira, R.R. Netz, Europhys. Lett. **52**, 705 (2000)
- [45] A.G. Moreira, R.R. Netz, Phys. Rev. Lett **87**, 078301 (2001).
- [46] A.G. Moreira, R.R. Netz, Eur. Phys. J. E **8**, 33 (2002).
- [47] M. Baus, J. Hansen, Phys. Rep. **59**, 1 (1980).
- [48] I. Rouzina, V.A. Bloomfield, J. Phys. Chem. **100**, 9977 (1996).
- [49] A.Yu. Grosberg, T.T. Nguyen, B.I. Shklovskii, Rev. Mod. Phys. **74**, 329 (2002).
- [50] R.R. Netz, H. Orland, Eur. Phys. J. E **1**, 203 (2000).
- [51] H. Wennerström, B. Jönsson, P. Linse, J. Chem. Phys. **76**, 4665 (1982).
- [52] Y. Burak, D. Andelman, H. Orland, Phys. Rev. E **70**, 016102 (2004).
- [53] J. Ray, G.S. Manning, Macromolecules **30**, 5739 (1997); Langmuir **10**, 2450 (1994).
- [54] A. Naji, R.R. Netz, Eur. Phys. J. E **13**, 43 (2004).
- [55] A. Naji, A. Arnold, C. Holm, R.R. Netz, Europhys. Lett. **67**, 130 (2004).
- [56] N. Imai, T. Ohnishi, J. Chem. Phys. **30**, 1115 (1959); T. Ohnishi, N. Imai, F. Oosawa, J. Phys. Soc. Japan **15**, 896 (1960).
- [57] G.S. Manning, Biophys. Chem. **7**, 95 (1977).
- [58] G.S. Manning, J. Phys. Chem. **79**, 262 (1975); **85**, 1506 (1981).
- [59] G.S. Manning, Q. Rev. Biophys. **11**, 179 (1978).
- [60] G.S. Manning, Ber. Bunsenges. Phys. Chem. **100**, 909 (1996).
- [61] G.S. Manning, Physica A **231**, 236 (1996).
- [62] A.D. MacGillivray, J. Chem. Phys. **56**, 80 (1972); **56**, 83 (1972); **57**, 4071 (1972); **57**, 4075 (1972).
- [63] G.V. Ramanathan, J. Chem. Phys. **78**, 3223 (1983).
- [64] G.V. Ramanathan, C.P. Woodbury, J. Chem. Phys. **77**, 4133 (1982); **82**, 1482 (1985).
- [65] C.P. Woodbury, G.V. Ramanathan, Macromolecules **15**, 82 (1982).
- [66] B.H. Zimm, M. Le Bret, J. Biomol. Struct. Dyn. **1**, 461 (1983); M. Le Bret, B.H. Zimm, Biopolymers **23**, 287 (1984).
- [67] A. Ikegami, J. Polym. Sci. A **2**, 907 (1964).
- [68] R. Zana et al., J. Chim. Phys. Physicochim. Biol. **68**, 1258 (1971).
- [69] M. Kowblansky, P. Zema, Macromolecules **14**, 166 (1981); **14**, 1448 (1981).

- [70] J.W. Klein, B.R. Ware, *J. Chem. Phys.* **80**, 1334 (1984).
- [71] P. Ander, M. Kardan, *Macromolecules* **17**, 2431 (1984).
- [72] L.M. Penafiel, T.A. Litovitz, *J. Chem. Phys.* **96**, 3033 (1992); **97**, 559 (1992).
- [73] A. Popov, D.A. Hoagland, *J. Polym. Sci. Part B: Polym. Phys.* **42**, 3616 (2004).
- [74] R.G. Winkler, M. Gold, P. Reineker, *Phys. Rev. Lett.* **80**, 3731 (1998).
- [75] M. Deserno, C. Holm, S. May, *Macromolecules* **33**, 199 (2000); M. Deserno, Ph.D. thesis, University of Mainz (2000).
- [76] S. Liu, M. Muthukumar, *J. Chem. Phys.* **116**, 9975 (2002); S. Liu, K. Ghosh, M. Muthukumar, *J. Chem. Phys.* **119**, 1813 (2003).
- [77] Q. Liao, A.V. Dobrynin, M. Rubinstein, *Macromolecules* **36**, 3399 (2003).
- [78] M. Fixman, *J. Chem. Phys.* **70**, 4995 (1979)
- [79] D. Stigter, *J. Phys. Chem.* **82**, 1603 (1978); *Biophys. J.* **69**, 380 (1995).
- [80] P. González-Mozuelos, M. Olvera de la Cruz, *J. Chem. Phys.* **103**, 3145 (1995).
- [81] C.A. Tracy, H. Widom, *Physica A* **244**, 402 (1997).
- [82] Y. Levin, M.C. Barbosa, *J. Phys. II (France)* **7**, 37 (1997).
- [83] P.S. Kuhn, Y. Levin, M.C. Barbosa, *Macromolecules* **31**, 8347 (1998).
- [84] H. Schiessel, P. Pincus, *Macromolecules* **31**, 7953 (1998).
- [85] R.M. Nyquist, B.-Y. Ha, A.J. Liu, *Macromolecules* **32**, 3481 (1999).
- [86] J. Ray, G.S. Manning, *Macromolecules* **32**, 4588 (1999).
- [87] H. Qian, J.A. Schellman, *J. Phys. Chem. B* **104**, 11528 (2000).
- [88] G.S. Manning, *Macromolecules* **34**, 4650 (2001).
- [89] A. Deshkovski, S. Obukhov, M. Rubinstein, *Phys. Rev. Lett.* **86**, 2341 (2001).
- [90] P.L. Hansen, R. Podgornik, V.A. Parsegian, *Phys. Rev. Lett.* **64**, 021907 (2001).
- [91] M.L. Henle, C.D. Santangelo, D.M. Patel, P.A. Pincus, *Europhys. Lett.* **66**, 284 (2004).
- [92] M. Muthukumar, *J. Chem. Phys.* **120**, 9343 (2004).
- [93] I. Borukhov, *J. Polym. Sci. B: Polym. Phys.* **42**, 3598 (2004).
- [94] B. O'Shaughnessy, Q. Yang, *Phys. Rev. Lett.* **94**, 048302 (2005).
- [95] A. Naji, R.R. Netz, *Phys. Rev. Lett.* **95**, 185703 (2005).
- [96] A. Naji, R.R. Netz, submitted to *Phys. Rev. E*; e-print: cond-mat/0508771.

- 
- [97] A.L. Kholodenko, A.L. Beyerlein, Phys. Rev. Lett. **74**, 4679 (1995).
- [98] Y. Levin, Physica A **257**, 408 (1998).
- [99] Y.Y. Suzuki, J. Phys.: Condens. Matter **16**, 2119 (2004).
- [100] R.L. Cleland, Macromolecules **24**, 4386 (1991).
- [101] J. Cardy, *Scaling and Renormalization in Statistical Physics* (Cambridge University Press, Cambridge, 1996).
- [102] J. DeRouchey, R.R. Netz, J.O. Rädler, Eur. Phys. J. E **16**, 17 (2005).
- [103] A. Naji, R.R. Netz, C. Seidel, Eur. Phys. J. E **12**, 223 (2003)
- [104] S. Lifson, A. Katchalsky, J. Polym. Sci. **13**, 43 (1954).
- [105] R.R. Netz, J.-F. Joanny, Macromolecules **31**, 5123 (1998).
- [106] D. Bratko, V. Vlachy, Chem. Phys. Lett. **90**, 434 (1982).
- [107] M. Le Bret, B.H. Zimm, Biopolymers **23**, 271 (1984).
- [108] C.S. Murthy, R.J. Bacquet, P.J. Rossky, J. Phys. Chem. **89**, 701 (1985)
- [109] N. Metropolis et al., J. Chem. Phys. **21**,1087 (1953).
- [110] J. Lekner, Physica A **176**, 485 (1991).
- [111] R. Sperb, Mol. Simul. **20**, 179 (1998).
- [112] A. Arnold, C. Holm, Comput. Phys. Commun. **148**, 327 (2002).
- [113] H. Flyvberg, H.G. Petersen, J. Chem. Phys. **91**, 461 (1989).
- [114] R. Bacquet, P.J. Rossky, J. Phys. Chem. **88**, 2660 (1984)
- [115] S.S. Zakharova et al., J. Chem. Phys. **111**, 10706 (1999)
- [116] A.W.C. Lau, D.B. Lukatsky, P. Pincus, S.A. Safran, Phys. Rev. E **65**, 051502 (2002).
- [117] A.M. Ferrenberg, D.P. Landau, Phys. Rev. B **44**, 5081 (1991).
- [118] M.E. Fisher, M.N. Barber, Phys. Rev. Lett. **28**, 1516 (1972).
- [119] M.N. Barber, Finite-size Scaling, in *Phase Transitions and Critical Phenomena*, edited by C. Domb und J.L. Lebowitz, Vol. 8, Ch. 2 (Academic Press, New York, 1983).
- [120] K. Binder, Z. Phys. B **43**, 119 (1981).
- [121] K. Binder, D.W. Heermann, *Monte Carlo Simulation in Statistical Physics: An Introduction*, (Springer-Verlag, Berlin, 1997).
- [122] V. Privman (Editor), *Finite Size Scaling and Numerical Simulation of Statistical Systems*, (World Scientific, Singapore, 1990).

- [123] Y. Burak, H. Orland, preprint (2005); e-print: cond-mat/0509126.
- [124] R. Das et al., Phys. Rev. Lett. **90**, 188103 (2003).
- [125] B. Jayaram et al., Macromolecules **23**, 3156 (1990).
- [126] M.J. Stevens, K. Kremer, J. Chem. Phys. **103**, 1669 (1995).
- [127] A. Khan, B. Jönsson, H. Wennerström, J. Phys. Chem. **89**, 5180 (1985).
- [128] H. Wennerström, A. Khan, B. Lindman, Adv. Colloid Interface Sci. **34**, 433 (1991).
- [129] D.C. Rau, V.A. Parsegian, Biophys. J. **61**, 246 (1992); **61**, 260 (1992).
- [130] P. Kékicheff, S. Marčelja, T. J. Senden, V. E. Shubin, J. Chem. Phys. **99**, 6098 (1993).
- [131] M. Delsanti, J.P. Dalbiez, O. Spalla, L. Belloni, M. Drifford, ACS Symp. Ser. **548**, 381 (1994).
- [132] M. Olvera de la Cruz, L. Belloni, M. Delsanti, J.P. Dalbiez, O. Spalla, M. Drifford, J. Chem. Phys. **103**, 5781 (1995).
- [133] M. Dubois, T. Zemb, N. Fuller, R.P. Rand, V.A. Parsegian, J. Chem. Phys. **108**, 7855 (1998).
- [134] H.H. Strey, R. Podgornik, D.C. Rau, V.A. Parsegian, Curr. Opin. Struct. Biol. **8**, 309 (1998).
- [135] G.C.L. Wong, A. Lin, J.X. Tang, Y. Li, P.A. Janmey, C.R. Safinya, Phys. Rev. Lett. **91**, 018103 (2003); J.C. Butler, T. Angelini, J.X. Tang, G.C.L. Wong, Phys. Rev. Lett. **91**, 028301 (2003).
- [136] T.E. Angelini, H. Liang, W. Wriggers, G.C.L. Wong, Proc. Natl. Acad. Sci. USA **100**, 8634 (2003)
- [137] L. Guldbbrand, B. Jönsson, H. Wennerström, P. Linse, J. Chem. Phys. **80**, 2221 (1984).
- [138] B. Svensson, B. Jönsson, Chem. Phys. Lett. **108**, 580 (1984).
- [139] D. Bratko, B. Jönsson, H. Wennerström, Chem. Phys. Lett. **128**, 449 (1986).
- [140] L. Guldbbrand, L.G. Nilsson, L. Nordenskiöld, J. Chem. Phys. **85**, 6686 (1986); L.G. Nilsson, L. Guldbbrand, L. Nordenskiöld, Mol. Phys. **72**, 177 (1991).
- [141] C.E. Woodward, B. Jönsson, T. Åkesson, J. Chem. Phys. **89**, 5145 (1988).
- [142] J.P. Valleau, R. Ivkov, G.M. Torrie, J. Chem. Phys. **95**, 520 (1991).
- [143] R. Kjellander, T. Åkesson, B. Jönsson, S. Marčelja, J. Chem. Phys. **97**, 1424 (1992).
- [144] A.P. Lyubartsev, L. Nordenskiöld, J. Phys. Chem. **99**, 10373 (1995).
- [145] N. Grønbech-Jensen, R.J. Mashl, R.F. Bruinsma, W.M. Gelbart, Phys. Rev. Lett. **78**, 2477 (1997).

- [146] N. Grønbech-Jensen, K.M. Beardmore, P. Pincus, *Physica A* **261**, 74 (1998).
- [147] J.W. Wu, D. Bratko, J.M. Prausnitz, *Proc. Natl. Acad. Sci. USA* **95**, 15169 (1998).
- [148] E. Allahyarov, I. D'Amico, H. Löwen, *Phys. Rev. Lett.* **81**, 1334 (1998).
- [149] M.J. Stevens, *Phys. Rev. Lett.* **82**, 101 (1999).
- [150] P. Linse, V. Lobaskin, *Phys. Rev. Lett.* **83**, 4208 (1999).
- [151] P. Linse, V. Lobaskin, *J. Chem. Phys.* **112**, 3917 (2000).
- [152] P. Linse, *J. Chem. Phys.* **113**, 4359 (2000).
- [153] B. Hribar, V. Vlachy, *Biophys. J.* **78**, 694 (2000).
- [154] R. Messina, C. Holm, K. Kremer, *Phys. Rev. Lett.* **85**, 872 (2000); *Europhys. Lett.* **51**, 461 (2000).
- [155] E. Allahyarov, H. Löwen, *Phys. Rev. E* **62**, 5542 (2000).
- [156] A.G. Moreira, R.R. Netz, *Europhys. Lett.* **57**, 911 (2002).
- [157] M. Deserno, A. Arnold, C. Holm, *Macromolecules* **36**, 249 (2003).
- [158] K.-C. Lee, I. Borukhov, W.M. Gelbart, A.J. Liu, M.J. Stevens, *Phys. Rev. Lett.* **93**, 128101 (2004).
- [159] R. Kjellander, S. Marčelja, *Chem. Phys. Lett.* **112**, 49 (1984); *J. Chem. Phys.* **82**, 2122 (1985).
- [160] R. Kjellander, T. Åkesson, B. Jönsson, S. Marčelja, *J. Chem. Phys.* **97**, 1424 (1992).
- [161] F. Oosawa, *Biopolymers* **6**, 1633 (1968).
- [162] P. Attard, R. Kjellander, D.J. Mitchell, *Chem. Phys. Lett.* **139**, 219 (1987); P. Attard, R. Kjellander, D.J. Mitchell, B. Jönsson, *J. Chem. Phys.* **89**, 1664 (1988).
- [163] P. Attard, D.J. Mitchell, B.W. Ninham, *J. Chem. Phys.* **88**, 4987 (1988).
- [164] R. Podgornik, *J. Phys. A: Math. Gen.* **23**, 275 (1990); R. Podgornik, B. Žekš, *J. Chem. Soc., Faraday Trans. II* **84**, 611 (1988).
- [165] J.-L. Barrat, J.-F. Joanny, *Adv. Chem. Phys.* **XCIV**, 1 (1996).
- [166] P.A. Pincus, S.A. Safran, *Europhys. Lett.* **42**, 103 (1998).
- [167] R. Podgornik, V.A. Parsegian, *Phys. Rev. Lett.* **80**, 1560 (1998).
- [168] B.-Y. Ha, A.J. Liu, *Phys. Rev. Lett.* **79**, 1289 (1997); *Phys. Rev. Lett.* **81**, 1011 (1998); *Phys. Rev. E* **58**, 6281 (1998); *Phys. Rev. E* **60**, 803 (1999); *Phys. Rev. Lett.* **83**, 2681 (1999).
- [169] D.B. Lukatsky, S.A. Safran, *Phys. Rev. E* **60**, 5848 (1999).

- [170] M. Kardar, R. Golestanian, *Rev. Mod. Phys.* **71**, 1233 (1999).
- [171] B.-Y. Ha, *Phys. Rev. E* **64**, 031507 (2001).
- [172] A.W.C. Lau, P. Pincus, *Phys. Rev. E* **66**, 041501 (2002).
- [173] O. Gonzalez-Amezcuca, M. Hernandez-Contreras, P. Pincus, *Phys. Rev. E* **64**, 041603 (2001).
- [174] M.J. Stevens, M.O. Robbins, *Europhys. Lett.* **12**, 81 (1990).
- [175] A. Diehl, M.N. Tamashiro, M.C. Barbosa, Y. Levin, *Physica A* **274**, 433 (1999); M.C. Barbosa, M. Deserno, C. Holm, *Europhys. Lett.* **52**, 80 (2000).
- [176] A.A. Kornyshev, S. Leikin, *J. Chem. Phys.* **107**, 3656 (1997); *Phys. Rev. Lett.* **82**, 4138 (1999).
- [177] J.J. Arenzon, J.F. Stilck, Y. Levin, *Eur. Phys. J. B* **12**, 79 (1999); Y. Levin, J.J. Arenzon, J.F. Stilck, *Phys. Rev. Lett.* **83**, 2680 (1999); A. Diehl, H.A. Carmona, Y. Levin, *Phys. Rev. E* **64**, 011804 (2001).
- [178] B.I. Shklovskii, *Phys. Rev. E* **60**, 5802 (1999).
- [179] B.I. Shklovskii, *Phys. Rev. Lett.* **82**, 3268 (1999).
- [180] A. Diehl, H.A. Carmona, Y. Levin, *Phys. Rev. E* **64**, 011804 (2001).
- [181] A.W.C. Lau, D. Levine, P. Pincus, *Phys. Rev. Lett.* **84**, 4116 (2000); A.W.C. Lau, P. Pincus, D. Levine, H.A. Fertig, *Phys. Rev. E* **63**, 051604 (2001).
- [182] Y. Levin, *Rep. Prog. Phys.* **65**, 1577 (2002).
- [183] I. Rouzina, V.A. Bloomfield, *Biophys. J.* **74**, 3152 (1998).
- [184] R. Golestanian, M. Kardar, T.B. Liverpool, *Phys. Rev. Lett.* **82**, 4456 (1999).
- [185] Y. Levin, *Physica A* **265**, 432 (1999)
- [186] T.T. Nguyen, I. Rouzina, B.I. Shklovskii, *J. Chem. Phys.* **112**, 2562 (2000).
- [187] O. Spalla, L. Belloni, *Phys. Rev. Lett.* **74**, 2515 (1995); L. Belloni, *J. Phys.: Condens. Matter* **12**, R549 (2000).
- [188] J.C. Neu, *Phys. Rev. Lett.* **82**, 1072 (1999).
- [189] J.E. Sader, D.Y.C. Chan, *J. Colloid Interface Sci.* **213**, 268 (1999); *Langmuir* **16**, 324 (2000).
- [190] E. Trizac, J.-L. Raimbault, *Phys. Rev. E* **60**, 6530 (1999); E. Trizac, *Phys. Rev. E* **62**, R1465 (2000).
- [191] Y.S. Park, Y. Ito, Y. Imanishi, *Chem. Mater.* **9**, 2755 (1997).
- [192] S.J. Miklavic, S. Marcelja, *J. Phys. Chem.* **92**, 6718 (1988).

- [193] S. Misra, S. Varanasi, P.P. Varanasi, *Macromolecules* **22**, 4173 (1989).
- [194] O.V. Borisov, T.M. Birstein, E.B. Zhulina, *J. Phys. II (Paris)* **1**, 521 (1991).
- [195] R.S. Ross, P. Pincus, *Macromolecules* **25**, 2177 (1992).
- [196] E.B. Zhulina, T.M. Birstein, O.V. Borisov, *J. Phys. II (Paris)* **2**, 63 (1992).
- [197] J. Wittmer, J.-F. Joanny, *Macromolecules* **26**, 2691 (1993).
- [198] R. Israëls, F.A.M. Leermakers, G.J. Fleer, E.B. Zhulina, *Macromolecules* **27**, 3249 (1994).
- [199] O.V. Borisov, E.B. Zhulina, T.M. Birstein, *Macromolecules* **27**, 4795 (1994).
- [200] V.A. Pryamitsyn, F.A.M. Leermakers, G.J. Fleer, E.B. Zhulina, *Macromolecules* **29**, 8260 (1996).
- [201] E.B. Zhulina, O.V. Borisov, *J. Chem. Phys.* **107**, 5952 (1997).
- [202] V.M. Amoskov, V.A. Pryamitsyn, *Polymer Science USSR* **37**, 1198 (1995).
- [203] F.S. Csajka, R.R. Netz, C. Seidel, J.-F. Joanny, *Eur. Phys. J. E* **4**, 505 (2001).
- [204] F.S. Csajka, C.C. van der Linden, C. Seidel, *Macromol. Symp.* **146**, 243 (1999).
- [205] F.S. Csajka, C. Seidel, *Macromolecules* **33**, 2728 (2000); *Macromolecules* **38**, 2022 (2005).
- [206] C. Seidel, *Macromolecules* **36**, 2536 (2003); *Macromolecules* **38**, 2540 (2005).
- [207] Y. Mir, P. Auroy, L. Auvray, *Phys. Rev. Lett.* **75**, 2863 (1995).
- [208] P. Guenoun, A. Schlachli, D. Sentenac, J.M. Mays, J.J. Benattar, *Phys. Rev. Lett.* **74**, 3628 (1995).
- [209] H. Ahrens, S. Förster, C.A. Helm, *Macromolecules* **30**, 8447 (1997).
- [210] H. Ahrens, S. Förster, C.A. Helm, *Phys. Rev. Lett.* **81**, 4172 (1998).
- [211] F. Muller, M. Delsanti, L. Auvray, J. Yang, Y.J. Chen, J.W. Mays, B. Demé, M. Tirrell, P. Guenoun, *Eur. Phys. J. E* **3**, 45 (2000).
- [212] F. Muller, P. Fontaine, M. Delsanti, L. Belloni, J. Yang, Y.J. Chen, J.W. Mays, P. Lesieur, M. Tirrell, P. Guenoun, *Eur. Phys. J. E* **6**, 109 (2001).
- [213] P. Guenoun, F. Muller, M. Delsanti, L. Auvray, Y.J. Chen, J.W. Mays, M. Tirrell, *Phys. Rev. Lett.* **81**, 3872 (1998).
- [214] M. Balastre, F. Li, P. Schorr, J. Yang, J.W. Mays, M.V. Tirrell, *Macromolecules* **35**, 9480 (2002).
- [215] S. Hayashi, T. Abe, N. Higashi, M. Niwa, K. Kurihara, *Langmuir* **18**, 3932 (2002).

- [216] H. Ahrens, S. Förster, C.A. Helm, N.A. Kumar, A. Naji, R.R. Netz, C. Seidel, *J. Phys. Chem. B* **108**, 16870 (2004).
- [217] G. Romet-Lemonne, J. Daillant, P. Guenoun, J. Yang, J.W. Mays, *Phys. Rev. Lett.* **93**, 148301 (2004).
- [218] J. T.G. Overbeek, P.H. Wiersema, in *Electrophoresis: Theory, Methods, and Applications*, M. Bier, Ed. (Academic Press, New York, 1967); Vol. 2.
- [219] D.C. Henry, *Proc. R. Soc. London Ser. A* **133**, 106 (1931).
- [220] J.L. Viovy, *Rev. Mod. Phys.* **72**, 813 (2001).
- [221] G.W. Slater, M. Kenward, L.C. McCormick, M.G. Gauthier, *Curr. Opin. Biotech.* **14**, 58 (2003).
- [222] R.L. Cleland, *Macromolecules* **24**, 4391 (1991).
- [223] D.A. Hoagland, E. Arvanitidou, C. Welch, *Macromolecules* **32**, 6180 (1999).
- [224] A.E. Nkodo, J.M. Garnier, B. Tinland, H. Ren, C. Desruisseaux L.C. McCormick, G. Drouin, G.W. Slater, *Electrophoresis* **22**, 2424 (2001).
- [225] E. Stellwagen, Y. Lu, N.C. Stellwagen, *Biochemistry* **42**, 11745 (2003).
- [226] B. Maier, U. Seifert, J.O. Rädler, *Europhys. Lett.* **60**, 622 (2002).
- [227] D. Long, J.L. Viovy, A. Ajdari, *Phys. Rev. Lett.* **76**, 3858 (1996).
- [228] D. Stigter, *J. Phys. Chem.* **82**, 1417 (1978).
- [229] S.A. Allison, *Macromolecules* **29**, 7391 (1996).
- [230] S.A. Allison, D. Stigter, *Biophys. J.* **78**, 121 (2000).
- [231] M. Muthukumar, *Electrophoresis* **17**, 1167 (1996).
- [232] R.R. Netz, *Phys. Rev. Lett.* **90**, 128104 (2003).
- [233] R.R. Netz, *J. Phys. Chem. B* **107**, 8208 (2003).
- [234] X. Schlagberger, R.R. Netz, *Europhys. Lett.* **70**, 129 (2005).
- [235] J. Happel, H. Brenner, *Low Reynolds Number Hydrodynamics* (Kluwer, Dordrecht, 1991).
- [236] M. Lax, *Rev. Mod. Phys.* **38**, 541 (1966).
- [237] M.P. Allen and D.J. Tildesley, *Computer Simulation of Liquids* (Clarendon Press, Oxford, 1997).
- [238] D.L. Ermak, J.A. McCammon, *J. Chem. Phys.* **69**, 1352 (1978).
- [239] J. Rotne, S. Prager, *J. Chem. Phys.* **50**, 4831 (1969).



- 
- [240] B.U. Felderhof, *Physica A* **89**, 373 (1977).
- [241] W.H. Press, S.A. Teukolsky, W.T. Vetterling, B.P. Flannery, *Numerical Recipes in C* (Cambridge University Press, Cambridge, second edition, 1992).
- [242] Wien, *Ann. Physik*, **83**, 327 (1927).
- [243] V. Ambegaokar, B.I. Halperin, *Phys. Rev. Lett.* **22**, 1364 (1969).
- [244] H. Risken, *The Fokker-Planck Equation* (Springer-Verlag, Berlin, 1989).
- [245] W.T. Coffey, Yu.P. Kalmykov, J.T. Waldron, *The Langevin Equation* (World Scientific, Singapore, 1996).



# List of Publications

1. A. Naji, R. R. Netz, C. Seidel, Non-linear osmotic brush regime: Simulations and mean-field theory, *Eur. Phys. J. E* **12**, 223 (2003).
2. A. Naji, R.R. Netz, Attraction of like-charged macroions in the strong-coupling limit, *Eur. Phys. J. E* **13**, 43 (2004).
3. A. Naji, A. Arnold, C. Holm, R.R. Netz, Attraction and unbinding of like-charged rods, *Europhys. Lett.* **67**, 130 (2004).
4. H. Ahrens, S. Förster, C.A. Helm, N.A. Kumar, A. Naji, R.R. Netz, C. Seidel, The non-linear osmotic brush regime: Experiments, simulations and scaling theory, *J. Phys. Chem. B* **108**, 16870 (2004).
5. A. Naji, R.R. Netz, Counterions at charged cylinders: Criticality and universality beyond mean-field theory, *Phys. Rev. Lett.* **95**, 185703 (2005).
6. A. Naji, S. Jungblut, A.G. Moreira, R.R. Netz, Electrostatic interactions in strongly coupled soft matter, *Physica A* **352**, 131 (2005).
7. H. Boroudjerdi, Y.-W. Kim, A. Naji, R.R. Netz, X. Schlagberger, A. Serr, Statics and dynamics of strongly charged soft matter, *Physics Reports* **416**, 129 (2005).
8. A. Naji, R. Podgornik, Quenched charge disorder and Coulomb interactions, *Phys. Rev. E* **72**, 041402 (2005).
9. A. Naji, R.R. Netz, Scaling and universality in the counterion-condensation transition at charged cylinders, submitted to *Phys. Rev. E*; e-print: cond-mat/0508771.
10. A. Naji, R. R. Netz, C. Seidel, Theoretical approaches to neutral and charged brushes, *Advances in Polymer Science*—in press.
11. P.A. Neff, A. Naji, C. Ecker, R. von Klitzing, A.R. Bausch, Electrical detection of self-assembled polyelectrolyte multilayers by a thin film resistor, preprint (2005); submitted to *Macromolecules*.
12. A. Naji, R.R. Netz, Counterion condensation and electrophoresis of charged polymers, preprint (2005).
13. A. Naji, R.R. Netz, Dynamic field theory for charged systems: Limiting laws of electrolyte conduction revisited, preprint (2005).



# Acknowledgment

The mere fact that my life as a student—an occupation which I had to possess for more than twenty years to acquire a university PhD degree—comes to an end by the completion of this thesis gives me an immense feeling of relief. Yet to begin a new era in my life, I would like to thank all people who helped me during all these years and in particular during my PhD program.

To Prof. Dr. Roland R. Netz I would like to express my gratitude for supervising my PhD program, for proposing interesting research topics and providing me with guidance and constructive criticism both in research and in the presentation of scientific results. Also for providing me with the possibility to attend numerous conferences and workshops which led to a few wonderful collaborations with other groups.

I am grateful to my collaborators and friends, Axel Arnold, Andreas Bausch, Yoram Burak, Christiane Helm, Christian Holm, Petra Neff, Rudi Podgornik, Henri Orland and Christian Seidel, with whom I had the chance to work on several interesting problems some of which indeed appear in this thesis. Special thanks to our group members with whom I attended many wonderful activities and received great help during these years, namely, Alfredo Alexander-Katz, Ourida Azi, Hoda Boroudjerdi, Christian Fleck, Jiri Janecek, Svetlana Jungblut, Woon and Teresa Kim, Manoel Manghi, Andre G. Moreira, Paul Neger, Xaver Schlagberger, Christian Sendner, Andreas Serr, Hirofumi Wada, Thomas Westphal, and our kind secretary in the Technical University of Munich, Ms. Sonja Ortner.

On the other hand, I would like to thank Prof. Dr. Reinhard Lipowsky, director of the Theory Division of the Max-Planck Institute of Colloids and Interfaces, where I started my PhD program in 2001, for giving me the opportunity to work at the Institute. I also thank Martin Brinkmann, Rumiana Dimova, Nicole Jaster, Stefan Klumpp, Julian Shillcock, Ulrich Schwartz, Angelo Valleriani, Sahin Uyaver and Ms. Gudrun Conrad for scientific or technical assistance during my stay in Potsdam-Berlin. This is followed by two fruitful years in the Physics Department of the Ludwig Maximilian University of Munich, where I enjoyed meeting or discussing scientific issues with various people including Prof. Dr. Herbert Wagner, the ex-chair of the Statistical Physics Group, Prof. Dr. Joachim O. Rädler, who kindly accepted to co-referee my thesis, Prof. Dr. Erwin Frey, Prof. Dr. Ivo Sachs, Dr. Ulrich Gerland, Richard Neher, Julia Schwartz, Dominique Gobert, Michael Sindel, Robert Dahlke and Ms. Caroline Lesperance.

Though this thesis represents the results of an intensive four-year PhD research program, the courage and interest to pursue a scientific career, and in particular physics, was given to me by many people during my school or undergraduate studies in Tehran.

Above all I would like to thank my first teachers, my mother and father, Masoumeh and Sohrab, who gave me the basic motivations to become interested in science, simply by providing me with all possible means of doing science as a child, taking from journals, books

and a microscope and even taking their nine-year old to professional observatory programs. I should then thank my dearest friend and wife, Hoda Boroudjerdi, who above everything else is optimistic, patient and courageous. Without her warm support, I am sure I would not have been successful in being simply more optimistic, patient, courageous and complete this thesis in time. More than anyone else, I owe her (who has actually been doing her PhD program in the same group) inspiring discussions about physics and metaphysics that have profoundly changed the way I look at both aspects of life.

# Curriculum Vitae

**Name:** Ali Naji  
**Date of birth:** 11 September 1976  
**Place of birth:** Karaj (Tehran, Iran)

**School:**

1982 - 1987 Elementary school (Shahid Zare), Shahriar, Iran  
1987 - 1990 Guidance school (Shahid Vahedi, Shahriar, and Ebn-e-Sina, Tehran)  
1990 - 1994 High school studies (Alborz High School), Tehran  
Subject: Mathematics and Physics

**Higher education:**

10/1994 - 07/1998 Bachelor of Science (BSc) in Physics,  
Sharif University of Technology, Tehran, Iran  
10/1998 - 01/2000 Master of Science (MSc) in Physics  
Sharif University of Technology, Tehran, Iran  
Thesis title: Compressible Burgers Turbulence in Arbitrary Dimensions  
(Supervisor: Prof. Shahin Rouhani)  
09/2000 - 07/2001 Diploma Degree in Condensed Matter Physics,  
International Centre for Theoretical Physics (ICTP), Trieste, Italy  
Thesis title: Theoretical Studies of Turbulence in a One-Dimensional  
Burgers-Model Analog of Magnetohydrodynamics  
(Passed with Honors; supervisor: Prof. Rahul Pandit)  
08/2001 - 11/2005 Ph.D. in Physics,  
Ludwig Maximilian University (LMU), Munich, Germany  
Thesis title: Counterions at Charged Polymers  
(Magna cum laude; supervisor: Prof. Dr. Roland R. Netz)